Interaction of structure and physical properties in accretionary wedges: examples from the Cascadia and Nankai Trough subduction zones

By

Susanna I. Webb

A dissertation submitted in partial fulfillment of

the requirements for the degree of

Doctor of Philosophy

(Geoscience)

at the

UNIVERSITY OF WISCONSIN–MADISON

2017

Date of final oral examination: 08/01/2017

The dissertation is approved by the following members of the Final Oral Committee:

Harold J. Tobin, Professor, Geoscience

Alan R. Carroll, Professor, Geoscience

Clifford H. Thurber, Professor, Geoscience

Hiroki Sone, Assistant Professor, Geological Engineering

Randolph T. Williams, Post-doctoral Researcher, McGill University

Acknowledgements

First, thanks to my advisor, Harold Tobin, for his support and mentoring throughout my graduate school career. During my time at Wisconsin, I've had some invaluable experiences, both in the lab and out in the field. I truly appreciate his guidance and patience over the course of my graduate school career. I also appreciate his willingness to listen and his ability to make most situations seem way less daunting and more manageable than I initially think they will be. I am truly grateful that he was my advisor; even with all the uncertainty that is inherent in graduate school, he helped make my overall experience a positive one.

Many thanks to my committee, Alan Carroll, Cliff Thurber, Hiroki Sone, and Randy Williams, for helpful comments and guidance and for their time. Their edits have improved this dissertation.

Thanks also to IODP and COAST cruise participants for data collection, processing, and reports. Many thanks to collaborators, including Dana Petersen, Will Fortin, Erik Everson, Katie Kiernan, Graham Kent and Steve Holbrook. This dissertation was made possible by funding from the Geoscience Department's Weeks Research Assistantship and the Mark and Carol Ann Solien Research Assistantship, as well as the US Science Support Program and NSF grant OCE-1334322.

Special thanks to Ben Abernathy, without whom many of the computer-related portions of this work would have been impossible. I appreciate his patience and willingness to explain how, exactly, components of computers and servers work, as well as the hours he has devoted to keeping the Visualization Lab running. It is also thanks to him that I have a grasp on the basics of Linux.

Thank you to Tamara Jeppson, my officemate, research group cohort, and friend for the past six years. Her support has been invaluable in finishing this dissertation; I appreciate all the discussions, not only about research but on almost any conceivable topic (and some inconceivable as well, I'm sure). I am eternally grateful we were able to share the adventures of graduate school.

Thanks to Joe Kington, who introduced me to seismic data, and Joanne Tudge, for her help with well logs, and thanks also to the structure group. Many thanks to my fellow graduate students in the geology department, with special thanks to Nathan Andersen, Tyler Blum, Helen Le Mévèl, Andria Ellis, Andrew Walters, and Chelsea Lancelle for their support and friendship. My undergraduate advisor, Josh Feinberg, and the scientists at the Institute for Rock Magentism at the University of Minnesota oversaw my first forays into research, and I thank them for their patience and encouragement at the start of my academic career.

Thanks also to my family for their incredible support. Thanks to my mother, Jennifer Brand, for her understanding, and the longstanding advice of "done is better than perfect" and "watch for snakes". Thanks to my father, Nick Webb, for his unwavering belief that I am capable of and will succeed at anything I turn my hand to, even when I am sure I won't. And finally to Erik Wipf, whose sacrifices have allowed me to focus my time and effort on finishing my doctorate. After a chance meeting on our first day as freshmen at the University of Minnesota and as our relationship evolved from friendship to marriage, he has been part of my entire journey through higher education. I will never be able to express what his unwavering support has meant to me over the past decade. Thank you, for everything, always.

Table of Contents

List of Figures

Abstract

Subduction zones are capable of producing large, megathrust earthquakes that are sometimes tsunamigenic. Structure and physical properties in the accretionary wedge play a role in how far rupture can propagate and how the wedge deforms coseismically. In areas that cannot be easily sampled, seismic reflection, refraction, and tomography and logging data are used to interpret structure and estimate physical properties at depth, in order to inform our assumptions about the conditions at depth. This dissertation uses seismic reflection data and velocity models in the Cascadia subduction zone to interpret structure, link structure to the broader wedge deformation history, and investigate the presence of overpressure below the wedge. I also examine log data from Nankai to estimate values for bulk moduli and examine trends in porosity and velocity at depth within the inner accretionary wedge.

Chapters 2 and 3 are focused on the central Cascadia subduction zone, offshore Grays Harbor, Washington State. The Cascadia subduction zone is a seismic endmember for subduction zones, with no large interplate earthquakes seismically recorded, although paleoseismology does reveal that the margin has ruptured in large megathrust earthquakes in the past. Structurally, central Cascadia is also anomalous, as it displays dominantly landward vergent faulting in the outer wedge, has a very low wedge taper angle, and contains a broad, lightly deformed lower slope terrace between the inner and outer wedges. Closely spaced, relatively high resolution seismic reflection data were collected as part of the Cascadia Open Access Seismic Transect (COAST) initiative in July 2012, and are used in this study.

In Chapter 2, I present a full structural interpretation of the COAST lines. With this dataset, I can document different structural styles within the landward vergent zone at a smaller scale and with better resolution that was previously available. Two active décollements are interpreted: an upper décollement within the sediment section, and a basal décollement at the sediment-basement interface (within seismic resolution). In areas where the upper décollement is active

~500 m of sediment is being subducted, and the other 2.5 km of the incoming sediments section is incorporated into the wedge. The level of internal deformation in thrust sheets and amount of overlying slope basin sediment correspond to which décollement level is active. Internally deformed thrust sheets with backthrusts are correlated to the presence of thicker slope basins, and faults sole into the upper décollement. In areas bypassed by sediment channels, slope basins are not as thick, thrust sheets show little internal deformation, and faults sole into the sediment-basement interface. These interpretations help delineate the spatial extent of décollements, and suggest that supra-wedge sedimentation may have influenced the development of the wedge, including the formation of the lower slope terrace and the promotion of out of sequence fault activity.

Chapter 3 focuses on the analysis of porosity and pore pressure estimates derived from velocity models used to depth migrate COAST seismic reflection lines. Three lines are analyzed, and the velocity-models are converted to porosity using previously published empirically derived velocity-porosity transforms. In order to calculate excess pore pressure and overpressure ratio, I tested three separate exponential curve fits to undisturbed, normally compacting sediments to construct the initial lithostatic model. Excess pore pressure up to 5 MPa was estimated, with overpressure ratios <0.15. No excess pore pressure was documented in the underthrust sediment section, indicating that if overpressure is present, it is below seismic resolution, and cannot be used to help estimate the updip limit of the seismogenic zone. Excess pore pressure was documented in the incoming sediment section and the footwalls of thrust sheets. There are no anomalies in the hanging walls of faults, including the frontal thrust, indicating that if there is overpressure at depth in the incoming section, the wedge is effectively draining fluids. The analysis of pore pressure shows that 1) if the base of the wedge is weak, which has been theorized to enable landward vergent faulting, it is due to mechanical properties of the sediments or a relatively thin underthrust layer and 2) the Cascadia wedge is relatively well-drained, and thus potentially strong, which can lead to a low wedge taper angle.

Chapter 4 uses data from the Nankai Trough Seismogenic Zone Experiment (NanTroSEIZE) to investigate the physical properties at depths previously unsampled in the inner accretionary wedge. I reprocessed sonic log data to obtain P-wave and S-wave velocity values, and estimated elastic moduli values. The velocity logs were also used to estimate overpressure at depth. The

logs through the deeper section of the accretionary wedge give remarkably constant responses over a depth > 1 km. Based on the logs, some low overpressure is estimated. However, the porosity values measured from core and cuttings continue to decrease, following a normal compaction curve. Structural scenarios and changes in lithology are discussed as possible ways to reconcile the two datasets.

1 Introduction and motivation

Geometry of faults and the physical properties of the materials in and around them affect how seismic rupture will propagate if a fault fails seismically. Faults at subduction zones are capable of producing large, damaging earthquakes, and pose a significant hazard to population centers located near the plate boundaries. The extent and location of rupture affects how much of a seismic hazard an event will be, and whether or not it will be tsunamigenic if the fault is submarine.

Subduction zone megathrust earthquakes nucleate in the locked seismogenic zone which is bordered by transition zones at its updip and downdip limits, where very low frequency earthquakes and episodic tremor and slip can occur [*Obara and Kato*, 2016]. Subduction zone plate boundary faults consist of a locked seismogenic zone with transition zones at its updip and downdip limit. Traditional assumptions were that accretionary wedges overlay (and in fact define) an aseismic portion of the plate boundary fault, and are composed of velocity strengthening material that would inhibit rupture propagation (e.g. [*Hyndman et al.*, 1997]). However, recent large earthquakes, including the 2004 Sumatra and 2011 Tohoku events, have involved slip beneath the accretionary wedge, resulting in large displacement at the seafloor and the production of tsunami [*Lay et al.*, 2005; *Ito et al.*, 2011]. Some low frequency and slow slip events have also been observed in updip areas previously presumed to be aseismic [*Ito and Obara*, 2006; *Obara and Kato*, 2016]. If an accretionary wedge does overly a seismic rather

than aseismic portion of the subduction zone interface, the mechanical properties of the wedge material, as well as its structure, may control how much the wedge could be deformed in a large event [*Lotto et al.*, 2017]. This has large implications for the tsunamigenic potential for a given earthquake.

The properties at the plate boundary are critical to understanding whether or not rupture can propagate beneath the accretionary wedge (e.g. [*Ruff and Kanamori*, 1980; *Schwartz and Ruff*, 1987; *Cloos*, 1992; *Hyndman and Wang*, 1995; *Park et al.*, 2004]). Changes in pore pressure and effective stress at the plate boundary will change the strength and frictional properties on the fault surface, as well as its potential slip behavior [*Moore and Vrolijk*, 1992; *Saffer and Bekins*, 2006; *Ask and Morgan*, 2010]. The updip limit of the seismogenic zone has often been inferred to be where overpressure occurs and the sediment is weak and aseismic [*Saffer and Tobin*, 2011]. The hydrogeology and properties of sediments at the plate boundary have been invoked as a controlling factor at subduction zones worldwide [*von Huene et al.*, 1998; *Calahorrano et al.*, 2008; *Collot et al.*, 2008; *Ranero et al.*, 2008; *Bangs et al.*, 2009; *Barker et al.*, 2009; *Wallace et al.*, 2009; *Park et al.*, 2010]. Locating areas of changing overpressure, and thus effective stress, can help map out the updip limit of the locked zone, domains of mechanical strength, and provide an estimate of frictional locking properties of the plate interface fault system.

Mechanical properties of subducted sediments underneath a wedge are very difficult to determine as samples from depth are generally not available. Properties from fault zone samples indicate that they often have low frictional coefficients and lower elastic moduli than other sedimentary materials, and exhibit velocity strengthening properties, which would tend to inhibit rupture propagation [*Ikari et al.*, 2009; *Ikari and Saffer*, 2011; *Jeppson and Tobin*, 2015]. Frictional properties of clays, even after undergoing mineral transitions, appear to stay relatively

constant [*Saffer et al.*, 2012]. Cementation may have an increasing influence with depth [*Ask and Morgan*, 2010]. However, an examination of the porosity and permeability of samples can help constrain the possible fluid present at depth, and help us estimate overpressure and effective stress.

Overpressure in an accretionary wedge is a balance between fluid escape, compaction, and fluid production. As sediment is buried, it loses porosity and permeability. If it is buried relatively slowly, fluid can usually migrate and escape the wedge; however, if the sediment is buried quickly, the pathways for escape may not be available, and the section is more likely to experience overpressure [*Moore et al.*, 1991; *Moore and Vrolijk*, 1992; *Gamage et al.*, 2011]. Often, subducted sediment can contain fluids that have limited fluid pathways for escape compared to those in the overlying wedge [*Screaton et al.*, 2002, 2009; *Bangs and Gulick*, 2005; *Calahorrano et al.*, 2008]. Drilling through the décollement at the Nankai Trough has shown that the underthrust sediments have a higher porosity than the overthrust, indicating a higher potential for over pressure [*Screaton et al.*, 2002; *Gamage and Screaton*, 2006]. Experimental studies have indicated that permeability may be lower in subducted sediments, which favors the development of overpressure [*Ikari and Saffer*, 2012]. As the sediment is buried, it often undergoes dehydration reactions, which in turn increase the amount of fluid present in the underthrust section [*Saffer and Tobin*, 2011].

Structure and fluids are closely linked in subduction zones. Fluids influence how wedge structure develops, but the presence of faults can alter the fluid budget of a wedge by either allowing or inhibiting drainage. Fault geometry and structure help determine the amount of sediment that is subducted or accreted in the wedge (Figure 1.1) [*von Huene and Scholl*, 1991; *Clift and Vannucchi*, 2004]. The décollement is a detachment surface into which faults sole, and

overlies the underthrust sediment section. If faults sole more closely to the oceanic crust, smaller quantities of sediment will be underthrust than if the décollement is located higher in the stratigraphic section. Accreted sediment deformed by faults has a higher chance of allowing fluid to escape. Underthrust sediment is often assumed to be weaker and more fluid-rich than the overlying wedge, as there are fewer escape pathways for the fluids [*Moore*, 1989; *Moore and Vrolijk*, 1992]. The relative weakness or strength of this section compared to what overlies it influences the eventual wedge development and the material properties at the plate boundary fault [*Screaton et al.*, 2009].

Fluids can in turn exert a control on the type of deformation present in a wedge, as well as its overall structure and taper angle [*Davis et al.*, 1983; *Dahlen*, 1990; *Bilotti and Shaw*, 2005; *Screaton et al.*, 2009; *Kukowski et al.*, 2010; *Saffer*, 2010]. In critical taper theory, wedge taper angle (the sum of its surface angle and the angle of its basal detachment surface) is dependent on the strength of the material in the wedge as well as the friction at its base (Figure 1.2) [*Davis et al.*, 1983; *Dahlen*, 1990; *Suppe*, 2014]. A stronger wedge would result in a lower taper angle, whereas a higher coefficient of basal friction would result in a higher taper angle for the wedge. Structural interpretation of accretionary wedges and their deformation styles inform our assumptions about the strength of materials within and below the wedge.

Here, I present work from two subduction zone study areas that 1) looks at the interplay between structure and conditions at depth for an endmember subduction zone where the updip extent of the seismogenic zone is not well constrained and 2) estimates elastic properties for a previously unsampled wedge domain. These studies will aid in the assessment of seismic hazard analysis at these and potentially other margins.

Chapters 2 and 3 focus on the central Cascadia subduction zone, offshore Grays Harbor, Washington. In Chapter 2, I present the structural interpretation of closely spaced seismic reflection lines. I document two active décollements below the outer wedge, which is characterized by landward vergent faulting. The extent of internal deformation of thrust sheets and the amount of supra-wedge sedimentation are linked to which décollement level is active, leading to a proposed model that calls on heavy supra-wedge sedimentation during the Pleistocene as a driver for wedge development.

In Chapter 3, I used velocity models from pre-stack depth migrations of seismic reflection lines to model pore pressure and overpressure ratio in the central Cascadia margin. No large overpressure ratio values are observed below the wedge, indicating that if overpressure is present, it is not resolvable with current data. The highest, but still modest, pore pressure values occur in the footwalls of thrust faults whose hanging walls show no pore pressure anomalies, indicating that they are well drained. The low to modest amounts of excess pore pressure indicate that the wedge is most likely draining effectively, and may be mechanically strong.

In Chapter 4, I use logging-while-drilling data collected by Integrated Ocean Drilling Program expeditions in the Nankai Trough, Japan, to estimate conditions and elastic moduli within the inner accretionary wedge, a previously unsampled tectonic domain. Initially, I reprocessed the sonic logs to produce both P-wave and S-wave velocity logs. The inner accretionary wedge has elastic moduli values similar to other clay samples from similar depths, but higher than those previously calculated for Nankai Trough samples from shallower depths (e.g. [*Schumann et al.*, 2014]). Sonic log values are relatively constant over 1 km, while porosity values from core and cuttings continue to decrease, indicating perhaps a relatively simple tectonic history, and that the sediment section may be experiencing its peak load at the present time.

1.1 References

Ask, M. V. S., and J. K. Morgan (2010), Projection of mechanical properties from shallow to greater depths seaward of the Nankai accretionary prism, *Tectonophysics*, *482*(1–4), 50–64, doi:10.1016/j.tecto.2009.08.023.

Bangs, N. L. B., and S. P. S. Gulick (2005), Physical Properties along the Developing Decollement in the Nankai Trough: Inferences from 3-D Seismic Reflection Data Inversion and Leg 190 and 196 Drilling Data, *Proc. Ocean Drill. Program, Initial Reports Vol. 190/196*, *190/196*.

Bangs, N. L. B., G. F. Moore, S. P. S. Gulick, E. M. Pangborn, H. J. Tobin, S. Kuramoto, and A. Taira (2009), Broad, weak regions of the Nankai Megathrust and implications for shallow coseismic slip, *Earth Planet. Sci. Lett.*, *284*(1–2), 44–49, doi:10.1016/j.epsl.2009.04.026.

Barker, D. H. N., R. Sutherland, S. A. Henrys, and S. Bannister (2009), Geometry of the Hikurangi subduction thrust and upper plate, North Island, New Zealand, *Geochemistry Geophys. Geosystems*, *10*(2), doi:10.1029/2008GC002153.

Bilotti, F., and J. H. Shaw (2005), Deep-water Niger Delta fold and thrust belt modeled as a critical-taper wedge: The influence of elevated basal fluid pressure on structural styles, *Am. Assoc. Pet. Geol. Bull.*, *89*(11), 1475–1491, doi:10.1306/06130505002.

Calahorrano, A., V. Sallares, J.-Y. Collot, F. Sage, and C. R. Ranero (2008), Nonlinear variations of the physical properties along the southern Ecuador subduction channel: Results from depth-migrated seismic data, *Earth Planet. Sci. Lett.*, *267*(3–4), 453–467, doi:10.1016/j.epsl.2007.11.061.

Clift, P., and P. Vannucchi (2004), Controls on tectonic accretion versus erosion in subduction zones: Implications for the origin and recycling of the continental crust, *Rev. Geophys.*, *42*(2), doi:10.1029/2003RG000127.

Cloos, M. (1992), Thrust-type subduction-zone earthquakes and seamount asperities: a physical model for seismic rupture, *Geology*, *20*(7), 601–604, doi:10.1130/0091-7613(1992)020<0601:TTSZEA>2.3.CO;2.

Collot, J.-Y., W. Agudelo, A. Ribodetti, and B. Marcaillou (2008), Origin of a crustal splay fault and its relation to the seismogenic zone and underplating at the erosional north Ecuador–south Colombia oceanic margin, *J. Geophys. Res.*, *113*(B12), B12102, doi:10.1029/2008JB005691.

Dahlen, F. A. (1990), Critical Taper Model of Fold-And-Thrust Belts and Accretionary Wedges, *Annu. Rev. Earth Planet. Sci.*, *18*, 55–99, doi:10.1146/annurev.ea.18.050190.000415.

Davis, D., J. Suppe, and F. A. Dahlen (1983), Mechanics of Fold-and-Thrust Belts and Accretionary Wedges, *J. Geophys. Res.*, *88*(B2), 1153–1172.

Gamage, K., and E. J. Screaton (2006), Characterization of excess pore pressures at the toe of the Nankai accretionary complex, Ocean Drilling Program sites 1173, 1174, and 808: Results of one-dimensional modeling, *J. Geophys. Res.*, *111*, B04103, doi:10.1029/2004JB003572.

Gamage, K., E. J. Screaton, B. A. Bekins, and I. Aiello (2011), Permeability–porosity relationships of subduction zone sediments, *Mar. Geol.*, *279*(1–4), 19–36, doi:10.1016/j.margeo.2010.10.010.

von Huene, R., and D. W. Scholl (1991), Observations at convergent margins concerning sediment subduction, subduction erosion, and the growth of continental crust, *Rev. Geophys.*, *29*(3), 279–316, doi:10.1029/91RG00969.

von Huene, R., D. Klaeschen, M. Gutscher, and J. Fruehn (1998), Mass and fluid flux during accretion at the Alaskan margin, *GSA Bull.*, *110*(4), 468–482.

Hyndman, R. D., and K. Wang (1995), The rupture zone of Cascadia great earthquake from current deformation and the thermal regime, *J. Geophys. Res.*, *100*(B11), 22133–22154, doi:http://dx.doi.org/10.1029/95JB01970.

Hyndman, R. D., M. Yamano, and D. A. Oleskevich (1997), The seismogenic zone of subduction thrust faults, *Isl. Arc*, *6*(3), 244–260, doi:10.1111/j.1440-1738.1997.tb00175.x.

Ikari, M. J., and D. M. Saffer (2011), Comparison of frictional strength and velocity dependence between fault zones in the Nankai accretionary complex, *Geochemistry, Geophys. Geosystems*, *12*(4), n/a-n/a, doi:10.1029/2010GC003442.

Ikari, M. J., and D. M. Saffer (2012), Permeability contrasts between sheared and normally consolidated sediments in the Nankai accretionary prism, *Mar. Geol.*, *295–298*, 1–13, doi:10.1016/j.margeo.2011.11.006.

Ikari, M. J., D. M. Saffer, and C. Marone (2009), Frictional and hydrologic properties of a major splay fault system, Nankai subduction zone, *Geophys. Res. Lett.*, *36*(20), 1–5, doi:10.1029/2009GL040009.

Ito, Y., and K. Obara (2006), Dynamic deformation of the accretionary prism excites very low frequency earthquakes, *Geophys. Res. Lett.*, *33*(2), doi:10.1029/2005GL025270.

Ito, Y., T. Tsuji, Y. Osada, M. Kido, D. Inazu, Y. Hayashi, H. Tsushima, R. Hino, and H. Fujimoto (2011), Frontal wedge deformation near the source region of the 2011 Tohoku-Oki earthquake, *Geophys. Res. Lett.*, *38*(7), doi:10.1029/2011GL048355.

Jeppson, T. N., and H. J. Tobin (2015), San Andreas fault zone velocity structure at SAFOD at core, log, and seismic scales, *J. Geophys. Res.*, 1–15, doi:10.1002/2015JB012043.Received.

Kukowski, N., J. Greinert, and S. A. Henrys (2010), Morphometric and critical taper analysis of the Rock Garden region, Hikurangi Margin, New Zealand: Implications for slope stability and potential tsunami generation, *Mar. Geol.*, *272*(1–4), 141–153, doi:10.1016/j.margeo.2009.06.004.

Lay, T. et al. (2005), The Great Sumatra-Anadaman Earthquake of 26 December 2004, *Science (80-.).*, *308*(May), 1127–1133, doi:10.1126/science.1112250.

Lotto, G. C., E. M. Dunham, T. N. Jeppson, and H. J. Tobin (2017), The effect of compliant prisms on subduction zone earthquakes and tsunamis, *Earth Planet. Sci. Lett.*, *458*, 1–23, doi:10.1016/j.epsl.2016.10.050.

Moore, J. C. (1989), Tectonics and hydrogeology of accretionary prisms: role of the decollement zone, *J. Struct. Geol.*, *11*(1), 95–106.

Moore, J. C., and P. Vrolijk (1992), Fluids in Accretionary Prisms, *Rev. Geophys.*, *30*(2), 113–135.

Moore, J. C., K. M. Brown, F. Horath, G. R. Cochrane, M. E. MacKay, and G. F. Moore (1991), Plumbing Accretionary Prisms: Effects of Permeability Variations, *Philos. Trans. R. Soc. A Math. Phys. Eng. Sci.*, *335*, 275–288, doi:10.1098/rsta.1991.0047.

Obara, K., and A. Kato (2016), Connecting slow earthquakes to huge earthquakes, *Science (80-.).*, *353*(6296), 253–258.

Park, J.-O., G. F. Moore, T. Tsuru, S. Kodaira, and Y. Kaneda (2004), A subducted oceanic ridge influencing the Nankai megathrust earthquake rupture, *Earth Planet. Sci. Lett.*, *217*(1–2), 77–84, doi:10.1016/S0012-821X(03)00553-3.

Park, J.-O., G. Fujie, L. Wijerathne, T. Hori, S. Kodaira, Y. Fukao, G. F. Moore, N. L. B. Bangs, S. Kuramoto, and A. Taira (2010), A low-velocity zone with weak reflectivity along the Nankai subduction zone, *Geology*, *38*(3), 283–286, doi:10.1130/G30205.1.

Ranero, C. R., I. Grevemeyer, H. Sahling, U. Barckhausen, C. Hensen, K. Wallmann, W. Weinrebe, P. Vannucchi, R. Von Huene, and K. McIntosh (2008), Hydrogeological system of erosional convergent margins and its influence on tectonics and interplate seismogenesis, *Geochemistry, Geophys. Geosystems*, *9*(3), doi:10.1029/2007GC001679.

Ruff, L., and H. Kanamori (1980), Seismicity and the subduction zone process, *Phys. Earth Planet. Inter.*, *23*, 240–252.

Saffer, D. M. (2010), Hydrostratigraphy as a control on subduction zone mechanics through its effects on drainage: an example from the Nankai Margin, SW Japan, *Geofluids*, doi:10.1111/j.1468-8123.2009.00276.x.

Saffer, D. M., and B. A. Bekins (2006), An evaluation of factors influencing pore pressure in accretionary complexes: Implications for taper angle and wedge mechanics, *J. Geophys. Res. Solid Earth*, *111*(4), 1–21, doi:10.1029/2005JB003990.

Saffer, D. M., and H. J. Tobin (2011), Hydrogeology and Mechanics of Subduction Zone Forearcs: Fluid Flow and Pore Pressure, *Annu. Rev. Earth Planet. Sci.*, *39*, 157–186, doi:10.1146/annurev-earth-040610-133408.

Saffer, D. M., D. A. Lockner, and A. Mckiernan (2012), Effects of smectite to illite transformation on the frictional strength and sliding stability of intact marine mudstones, *Geophys. Res. Lett.*, *39*, doi:10.1029/2012GL051761.

Schumann, K., M. Stipp, J. H. Behrmann, D. Klaeschen, and D. Schulte-Kortnack (2014), P and S wave velocity measurements of water-rich sediments from the Nankai Trough, Japan, *J. Geophys. Res. Solid Earth*, 1–15, doi:10.1002/2014JB010978.Received.

Schwartz, S. Y., and L. J. Ruff (1987), Asperity distribution and earthquake occurrence in the southern Kurile Islands arc, *Phys. Earth Planet. Inter.*, *49*(1–2), 54–77, doi:10.1016/0031-9201(87)90132-4.

Screaton, E. J., D. M. Saffer, P. Henry, and S. Hunze (2002), Porosity loss within the underthrust sediments of the Nankai accretionary complex: Implications for overpressures, *Geology*, *30*(1), 19–22, doi:10.1130/0091-7613(2002)030<0019:PLWTUS>2.0.CO;2.

Screaton, E. J. et al. (2009), Interactions between deformation and fluids in the frontal thrust region of the NanTroSEIZE transect offshore the Kii Peninsula, Japan: Results from IODP Expedition 316 Sites C0006 and C0007, *Geochemistry Geophys. Geosystems*, *10*, doi:10.1029/2009GC002713.

Suppe, J. (2014), Fluid overpressures and strength of the sedimentary upper crust, *J. Struct. Geol.*, *69*(PB), 481–492, doi:10.1016/j.jsg.2014.07.009.

Wallace, L. M. et al. (2009), Characterizing the seismogenic zone of a major plate boundary subduction thrust: Hikurangi Margin, New Zealand, *Geochemistry Geophys. Geosystems*, *10*(10), doi:10.1029/2009GC002610.

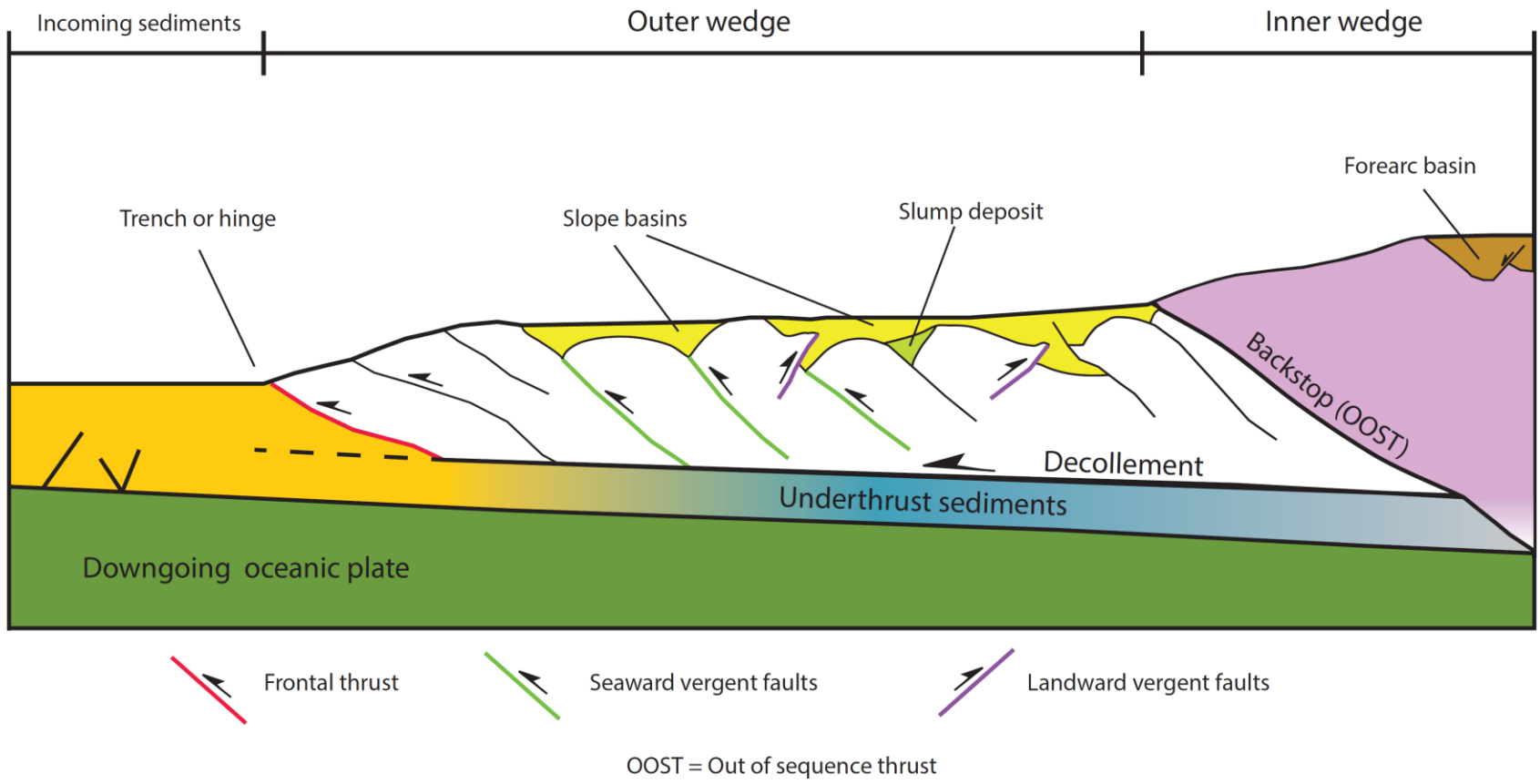

Figure 1.1: Cartoon illustrating and labelling some features of an accretionary wedge. The incoming sediment section is either subducted or underthrust, depending on the depth of the decollement. The accretionary wedge is usually divided into two sections: the actively deforming, compressional outer wedge, and the inner wedge, which often experiences extension. Often, the two domains are separated by an out of sequence thrust (OOST) that acts as a backstop to outer wedge deformation. Deformation styles in the wedge can be varied, with seaward or landward vergent faults that may be blind thrusts buried by slope basin sediments. Out of sequence thrust faulting can sometimes be seen in the outer wedge as well.

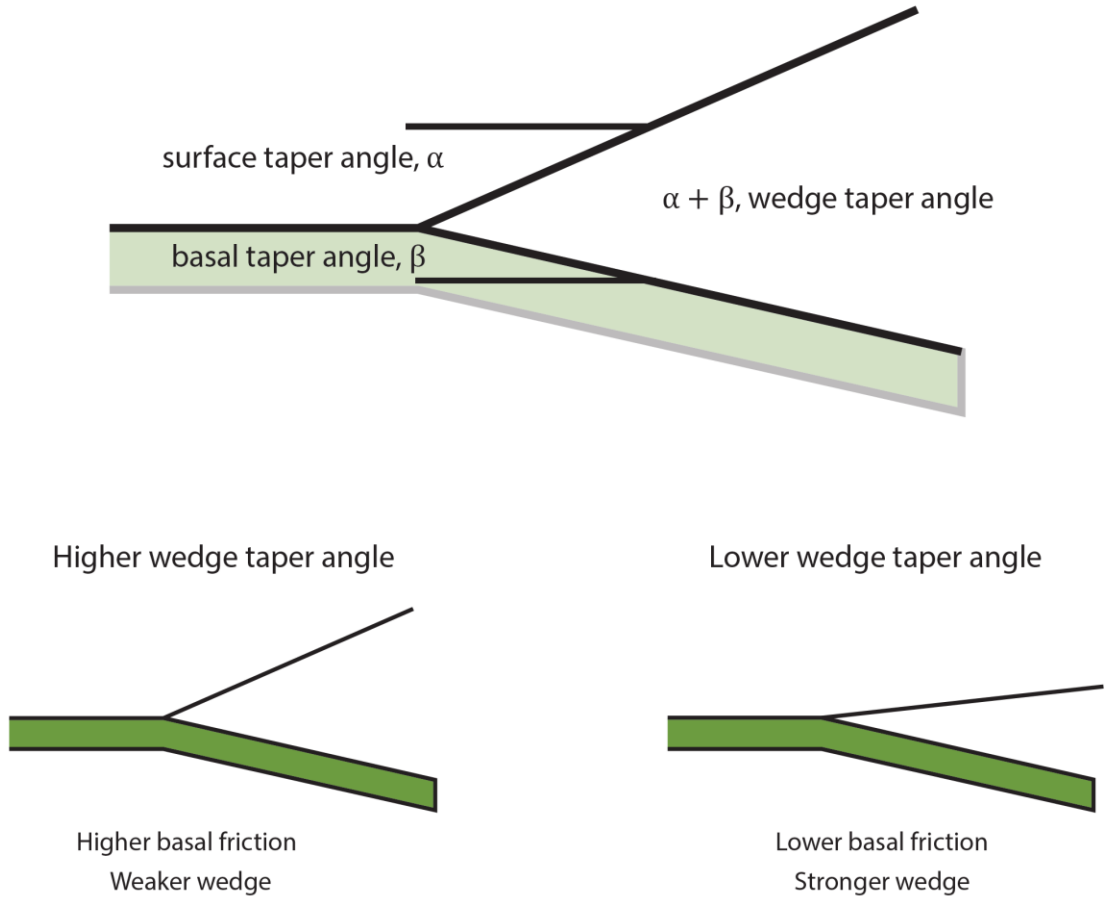

Figure 1.2: Cartoon illustrating the surface, basal, and wedge taper angle, as defined by *Davis et al.* [1983].

2 Structure and wedge development of the Cascadia margin offshore Grays Harbor, Washington

Abstract

When compared globally to other accretionary wedges, the central Cascadia margin is structurally anomalous, with an extremely low wedge taper angle, predominantly landward-vergent thrust faults, and a flat lower slope terrace behind the actively deforming outer wedge. Seismically, the Cascadia margin as a whole is quiescent, with no large interplate seismicity occurring in the recent past, so the updip limit of the seismogenic zone is difficult to define. Here, we present structural interpretation of the Cascadia Open Access Seismic Transect (COAST) dataset, which consists of nine trench-perpendicular and two trench-parallel closely spaced active source seismic reflection lines that image the landward vergent accretionary wedge. By documenting structural changes within the landward vergent zone, we address factors that contributed to wedge development in this area. Thrusts are generally landward vergent, but the amount of internal deformation and fault architecture varies spatially within the survey area. Out of sequence motion on faults is recorded. Thrusts sole either into the sediment basement interface, or into a level ~200 ms TWT above it, with both levels of décollement active in most lines. Very little to no sediment is currently being underthrust at the deformation front, and the amount of sediment present beneath the wedge is relatively thin (≤500 m). Heavy supra-wedge sedimentation has created large interconnected slope basins over most of the outer wedge and the lower slope terrace. The lower slope terrace, the flat region landward of the outer wedge, contains structures that deform the sediment above them, although they may be folds or smaller thrust sheets, as there is not conclusive evidence that they are diapiric. This structural analysis allows us to understand more about wedge development, which may have been influenced by heavy Pleistocene sedimentation, as well as the presence of the Quinault Ridge.

2.1 Introduction

The structure of an accretionary wedge influences how the wedge develops, and can inform our estimates of conditions at depth. Detailed interpretation of active source seismic data can help elucidate how the wedge formed and what factors may have influenced its development. Thrust

fault soling depths can help delineate the location of the plate boundary fault in the shallow subduction zone and the degree to which sediment is subducted. Changes in structure within the wedge may point to changes in the physical properties of the material in the wedge, and differences in mechanical strength between the overlying wedge and the décollement.

Structural styles within a wedge can determine how much sediment is accreted or underthrust [*von Huene and Scholl*, 1991; *Clift and Vannucchi*, 2004]. If faults sole more closely to the oceanic crust, smaller quantities of sediment will be underthrust than if the décollement is located higher in the stratigraphic section. The rate of sedimentation on top of an active wedge can in turn alter structural development by influencing the location of deformation or burying sediments that may not be fully drained (e.g. [*Simpson*, 2004, 2010; *Bilotti and Shaw*, 2005]).

Detailed structural interpretation is necessary to form the framework for discussions of mechanical properties of the wedge, location of the plate boundary fault, and estimates of conditions at depth below the wedge, which in turn can affect the extent of rupture during an earthquake.

2.2 The Cascadia subduction zone

2.2.1 Seismicity

Offshore northern California, Oregon, Washington, and British Columbia, the Juan de Fuca plate subducts shallowly underneath North America at a rate of ~36 to 40 mm/year [*DeMets et al.*, 2010], forming the Cascadia subduction zone (Figure 2.2.1). Cascadia is a seismic outlier among large subduction zones, with almost no interplate seismicity [*Wang et al.*, 2003; *Tréhu et al.*, 2008; *Williams et al.*, 2011; *Wang and Tréhu*, 2016]. There have been no recorded subduction

zone events larger than a magnitude ~4, although paleoseismology indicates that there has been large, margin-scale megathrust rupture in the past, most recently in 1700 CE [*Atwater and Yamaguchi*, 1991; *Benson et al.*, 2001; *Goldfinger et al.*, 2003; *Goldfinger*, 2011; *Atwater et al.*, 2014].

2.2.2 Accretionary wedge structure

The Cascadia margin has a well developed accretionary wedge along its entire length which displays distinct structural styles from north to south. Although the Juan de Fuca plate is relatively young (~8 Ma), voluminous terrestrially-derived sediment covers much of the plate near the subduction zone, causing a thick incoming sediment section, generally > 2 km at the deformation front where the sediment becomes incorporated into the outer wedge [*Griggs and Kulm*, 1970; *Carson*, 1973; *Underwood et al.*, 2005]. These sediments are predominantly Pleistocene turbidites, deposited during glacial periods, overlying some earlier fine grained Pliocene to Pleistocene silty clays [*Kulm et al.*, 1973b; *Carson et al.*, 1986; *Westbrook et al.*, 1994; *Underwood et al.*, 2005]. Several submarine canyons are active across the margin, feeding the Nitinat and Astoria fans, which cover the incoming Juan de Fuca plate [*Carson*, 1973; *Barnard*, 1978]. Most of these canyons are located in the central portion of the Cascadia margin, offshore Washington and northern Oregon. Recent imaging has shown that the incoming sediment section is relatively undeformed before reaching the trench, although small normal faults are present, attributed to plate bending and compaction ([*Han et al.*, 2016]; this study). Along the length of the margin, oblique deformation is expressed as a series of strike-slip faults [*MacKay et al.*, 1992; *Tobin et al.*, 1993; *Goldfinger et al.*, 1997]. Listric normal faults are interpreted in the shallower landward portion of the wedge, indicating this portion of the margin experiences margin-normal extension [*McNeill et al.*, 1997].

The structure of the margin separates it into three zones: northern Cascadia offshore Vancouver Island, southern Cascadia south of ~45 degrees N, and the central zone between the two. These zones are apparent in the bathymetry in Figure 2.2.1, with the northern and southern portions characterized by a narrower accretionary wedge, and the central portion by a broader, low relief accretionary wedge. In the northern portion of the margin, seaward vergent faulting has been interpreted in the relatively narrow wedge [*Davis and Hyndman*, 1989; *Hyndman et al.*, 1993; *Clowes and Hyndman*, 2002]. These seaward vergent faults sole at or close to the oceanic crust, and the incoming sediment section is interpreted as ranging between three to five kilometers thick [*Davis and Hyndman*, 1989]. In the southern Cascadia margin, seismic lines show mixed vergence faults in the toe of the accretionary wedge near 45 degrees N, with a transition to mostly seaward vergent faults in the outer wedge to the south [*MacKay et al.*, 1992]. This wedge is also relatively narrow and has a thick incoming sediment section, up to 3 km thick at the deformation front [*Silver*, 1969; *Tobin et al.*, 1993; *MacKay*, 1995; *Gulick et al.*, 1998; *Fisher et al.*, 1999].

The focus of this study is the central Cascadia margin offshore Washington, where the accretionary wedge structure is dominated by landward vergent faults (e.g [*Silver*, 1972; *Seely*, 1977; *Flueh et al.*, 1998; *Fisher et al.*, 1999; *Adam et al.*, 2004]). Other wedges, most notably Sumatra [*Frederik et al.*, 2015], exhibit landward vergent faulting within the wedge, but central Cascadia has landward-vergent faulting as the dominant fault orientation across the entire outer region of the accretionary wedge [*MacKay et al.*, 1992; *Flueh et al.*, 1998; *von Huene et al.*, 1998; *Fisher et al.*, 1999; *Gerdom et al.*, 2000; *Gutscher et al.*, 2001; *Adam et al.*, 2004]. The wedge is also broader than its northern and southern counterparts, with wider thrust spacing and a very low taper angle (<4°) [*MacKay et al.*, 1992; *MacKay*, 1995; *Gerdom et al.*, 2000].

Seismic interpretation of the transition between the seaward vergent and landward vergent zones documents some doubly vergent thrusts and indicates that a strike slip fault may separate the two zones, but the change in vergence is relatively abrupt [*MacKay et al.*, 1992].

A long standing research question in Cascadia is the origin of landward vergent faulting in the central margin. Very low basal shear stress is required to produce a predominantly landward vergent wedge with such a low taper angle [*Seely*, 1977]. Models have been able to produce seaward and dual vergence, but not a dominantly landward vergent wedge without invoking very specific conditions [*Davis et al.*, 1983; *MacKay*, 1995; *Gutscher et al.*, 2001]. Landward vergence has been attributed to rapid sediment deposition, possibly coupled with a seaward dipping décollement and a strong wedge [*Seely*, 1977; *MacKay*, 1995; *Fisher et al.*, 1999; *Gutscher et al.*, 2001; *Adam et al.*, 2004]. The geometry of such a décollement is due to the conditions necessary in analogue models to produce landward vergent faulting, rather than an interpretation of such a structure from seismic lines. At central Cascadia, large submarine canyons cut across the margin [*Griggs and Kulm*, 1970; *Carson*, 1973]. The two large submarine fans that fill the Cascadia Basin, the Nitinat Fan to the north and the Astoria Fan to the south, overlap offshore the central Cascadia margin (e.g. [*Griggs et al.*, 1969; *Underwood et al.*, 2005]). The development of landward vergent faulting has been attributed to a seaward dipping backstop to the outer wedge and existence of triangle zones such as those seen in continental fold and thrust belts have also been proposed [*Adam et al.*, 2004], as well as viscous layer flow in the lower portion of the wedge [*Gutscher et al.*, 2001]. Many of these hypotheses combine a specific geometry with low basal wedge friction, which has often been tied to the presence of overpressured fluids at depth [*MacKay et al.*, 1992; *Tobin et al.*, 1993; *Adam et al.*, 2004; *Saffer and Bekins*, 2006]. A high thermal gradient between the deformation front and

continental slope leading to a high vertical strain gradient due to plastic deformation has also been proposed as a mechanism that can produce landward vergent faulting in the wedge [*Booth-Rea et al.*, 2008].

In this study, we use newly acquired, closely spaced multichannel seismic (MCS) data to assess spatial variability in structural style and the implications for the temporal evolution within a section of the landward vergent central Cascadia margin. We identify the location and depth of the décollement, the various types of structures, and propose a model for wedge development.

2.3 COAST Survey

Several 2D seismic reflection and refraction surveys have been collected on the Cascadia margin (e.g [*Silver*, 1969, 1972; *Carson*, 1973; *Seely*, 1977; *MacKay et al.*, 1992; *MacKay*, 1995; *McNeill et al.*, 1997; *Adam et al.*, 2004]). The most recent reflection seismic survey on the margin, collected by the R/V *Marcus G. Langseth,* was the 2012 Cascadia Open Access Seismic Transect (COAST) used in this study (Figure 2.2.2, [*Holbrook et al.*, 2012]). Eleven reflection seismic profiles were shot, with nine lines perpendicular to the margin (lines 1 through 9), and two along strike (lines 10 and 11). An 8 km long streamer with 636 channels at a spacing of 12.5 m was used to collect the seismic data. A 36 airgun tuned array was fired every 50 m, recording data at a sample rate of 2 ms. The tow depth for the airgun-streamer array was either 9 m (lines 2, 3A, 4, 6, 8, 9A, 9B, 9C, 10) or 15 m (lines 1, 3, 5, 7, 9, 11); the deeper tow depth was intended to increase the low frequency signal, which is best for imaging deeper structures. Multiple reflection profiles were collected along portions of lines 3 and 9 with different frequency sources and streamer tow depths to compare data from different acquisition parameters; the longest and most complete lines are used here. Common mid-point (CMP) gathers are spaced at 6.25 m.

Data quality of the lines was occasionally compromised by equipment failures and periods of airgun shutdown due to marine mammal presence, which can be seen in the stacked lines. The along-strike lines 10 and 11 are of particularly poor quality, so high resolution multibeam bathymetry is used to correlate structures between lines. The multibeam bathymetry was collected on the COAST cruise using a Kongsberg EM122 system, and processed at Oregon State University [*Beeson,* 2017].

Time migrated stacks of all the lines were prepared on board the ship [*Holbrook et al.*, 2012]. Seismic data were assigned geometry, sorted, and bad traces were edited out of the gathers. Mutes were applied and normal moveout (NMO) functions defined, before the CMP gathers were stacked and migrated (COAST cruise report, 2012). Navigation data from the P1/90 files were added to the stacked lines at Wisconsin. The seafloor multiple is a very strong arrival, close to the oceanic crust reflector in two-way time in many of the lines. Two of the lines (3 and 4) were commercially pre-stack time migrated (PSTM) by GeoTrace. The initial quality control report highlights multiple problems with acquisition, as well as corrupt navigation files. The lines underwent proprietary multiple suppression techniques, including surface related multiple elimination and a radon demultiple, as well as noise attenuation in the frequency domain, which improved imaging of the oceanic crust and other arrivals. After Kirchoff pre-stack time migration, the velocities were reanalyzed, and an NMO correction and mutes were applied to the data before it was filtered through a bandpass filter and rotated to zero phase. GeoTrace provided a processing report, the processed lines, and velocity models for these two lines. Shipboard time migrated stacks as well as the GeoTrace stacks were used to make interpretations for this study.

2.4 Seismic data interpretation

The region covered by the COAST lines can be separated into four tectonic domains: the incoming sediment section, the outer wedge, the lower slope terrace, and the landward accretionary wedge (inner wedge) (Figure 2.2.3). A detailed structural interpretation of each of these is made below (see structural map, Figure 2.2.4). The incoming sediment section can be seen as a flat plain to the west of the accretionary wedge, and is generally undeformed (Figure 2.2.2). The incoming sediment transitions to the outer wedge at the deformation front, but no morphological trench is formed. Because thrusts are landward vergent, the deformation front is defined at the hinge zone of the first frontal thrust where the incoming sediment is incorporated into the frontal thrust sheet. The outer wedge is a low angle, broad, flat section of the wedge that is deformed by large thrust faults. The Quinault Ridge, a prominent symmetrical bathymetric high, separates the outer wedge from the lower slope terrace, a slightly deformed thick sedimentary basin. Landward (eastward) of the lower slope terrace is the steeper portion of the continental slope, then the continental shelf, which includes the forearc basin. This section of the wedge is termed the inner wedge, and is in the extensional regime [*McNeill et al.*, 1997]. The accretionary wedge below this forearc basin is seismically chaotic, and is generally referred to as the "mélange broken formation", or MBF, in previous work [*McNeill et al.,* 1997; *Flueh et al.,* 1998].

Two large submarine channels cut across the study area: the Quinault Canyon and the Willapa Canyon [*Carson*, 1973; *Barnard*, 1978; *Underwood et al.*, 2005] (Figure 2.2.2). The Quinault Canyon incises relatively shallowly into the lower slope terrace across lines 1, 2, 3, and 4, before crossing into the outer wedge slightly to the north of line 5. The Quinault Canyon continues along the back (landward) portion of the outer wedge, incising channels seen in lines 6, 7, and 8

before joining the Willapa Canyon just to the north of line 9, near the center of the line. Line 9 generally follows the trace of the Willapa Canyon as it comes off the continental shelf and cuts perpendicular to the subduction direction before reaching the Cascadia Basin on the Juan de Fuca plate. The canyon does turn slightly toward the south just before the frontal thrust, as can be seen in the bathymetry in Figure 2.2.2. The channel eventually joins with the Cascadia Channel in the Cascadia Basin (Figures 2.2 and 2.4).

2.4.1 Incoming sediments

The incoming sediment section in the COAST lines is, like other areas imaged in Cascadia, over 2000 ms of two way time, which corresponds to approximately 2.5-3 km, assuming incoming sediment velocities of 2500-3000 m/s from GeoTrace PSTM velocities and other velocity models [*MacKay et al.,* 1995; *Everson*, 2014; *Fortin*, 2015] (e.g. Figures 2.3 and 2.5). Beneath this sediment section, the reflector interpreted as the top of the oceanic crust is high amplitude and clearly visible. The crust is generally flat, with the exception of Line 4, where a buried basement high was imaged at the end of the line below the incoming sediment section (Figure 2.2.3). Given the high sedimentation rate and the voluminous sediment deposited by the Nitinat and Astoria fans, basement topography entering the trench is buried, but can be identified through seismic reflection profiles, as well as gravity and magnetic surveys (e.g. [*Gulick et al.,* 1998; *Gerdom et al.,* 2000; *Tréhu et al.*, 2012]).

The incoming sediments are generally undeformed, although there are small normal faults present in most lines (Figure 2.2.5a, indicated by red arrows). The normal faults in the sediment section have small offsets, are generally restricted to the lower half of the sediment package, and sometimes can be seen cutting the oceanic crust reflector (Figure 2.2.5). Offset of the oceanic crust indicates that some faults originate in the crust and propagate upward through the sediment

section. Deformation increases as the section enters the outer wedge. A population of conjugate reverse faults can be seen forming at the deformation front (Figure 2.5b, Figure 2.6), but the dominant initial deformation of the sediment section is with a large landward vergent thrust (Fault A) that forms the frontal thrust of the outer wedge.

2.4.2 The Outer Wedge

As documented by other seismic reflection data interpretations (e.g. [*MacKay et al.*, 1992; *Fisher et al.*, 1999; *Adam et al.*, 2004]), the accretionary wedge in this portion of the Cascadia margin is dominated by landward vergent thrust sheets. Beneath the outer wedge, the oceanic crust reflector has a variable amplitude—in better imaged sections, such as line 3 and 4, the oceanic crust reflector is relatively easy to identify and can be interpreted confidently below the outer wedge (Figures 2.7 and 2.8a). In more deformed areas, such as the landward portion of line 7 and below the Quinault Ridge (see section 4.3.1), the oceanic crust reflector dims and in some cases cannot be easily interpreted (Figure 2.8c). For the purposes of this paper, all faults and their folds are labelled on the structural map, starting with the frontal thrust A (Figure 2.4). Correlation of the thrust sheets from line to line was in places uncertain with so little crossline control, although the bathymetry proved helpful to determine structural trends. Thrust sheets were assumed to be relatively continuous through the study area, although some faults (such as Fault E) were only present in some of the lines. The changes in structural style, such as fault vergence, in lines 8 and 9 compared to the northern lines made correlation with faults in the southern area more difficult.

Throughout the entire survey, the frontal thrust is seaward dipping and landward vergent, and one of at least three well-developed landward vergent thrust sheets present in each line (Figures 2.7 and 2.8). With the exception of line 9, four or five well developed landward vergent thrust

sheets can be identified in each line. Line 9 contains doubly vergent thrust sheets, as well as some less well developed landward vergent sheets, although its frontal two thrusts have a similar deformation style to that seen in the more northern lines (Figure 2.9). The only dominantly seaward vergent fault is Fault G (and G') (Figure 2.4).

The outer wedge's width is fairly constant through the study area, with 27-33 kilometers between the deformation front and the Quinault Ridge. Some subtle changes in fault spacing are visible along strike. In the north, fault spacing for faults A, B, C, and D is between 4 to 6 km, although imbricate thrust sheets are more closely spaced, between 2.5 to 3 km. In the south, the first three thrusts (A, B, and C) are similarly spaced, but slightly farther apart: from ~4.5 to 7 km. Fault spacing between D and F narrows dramatically from north to south. In the northern lines (1-5), there is generally 6 to 9 km between the two faults. In lines 3, 4, 5, and 6, another thrust fault (fault E) is present between faults D and F. In the southern lines, fault spacing between D and F narrows to between ~2.75 to 4 km, and fault E is not present. Our estimates of shortening from line balancing in the COAST survey, as well as from plate motion models indicates that the amount of shortening taken up by the outer wedge is approximately 6 km ± 1 km since the initiation of sedimentation in the Pleistocene. Our estimates of ~15 to 20% tectonic shortening are similar to, if slightly lower than, those calculated from ORWELL survey lines, which predict 22-26% near the Grays Harbor area [*Adam et al.*, 2004; *Booth-Rea et al.*, 2008].

The bathymetric depth of the seafloor also increases from north to south: although the difference is not large, values on top of the wedge (excluding bathymetric highs of ridges and channel traces) in the north are all shallower than 2 km, between 1.8 and 1.9 km, whereas in the south all bathymetric values are ≥2km, between 2 and 2.3 km. Bathymetric highs formed by thrust sheets in the north are at an even shallower depth, between 1.7 and 1.8 km, where they can be seen

above slope basin cover. However, in the south, all ridges are also at a depth greater than 2 km, with the exception of thrust sheet B (1.9 km) and thrust sheet D (1.7 to 1.9 km). With the exception of line 9 and the trace of the Quinault Channel, the seafloor over the outer wedge is deepest over the seaward-most folds (A, B and C) of lines 6, 7 and 8. With the exception of the frontal thrust A and the continental slope, the seafloor is shallowest in the northern outer wedge and the lower slope terrace throughout the survey area (Figure 2.2). Line 9, along the trace of the Willapa Channel, has the deepest bathymetric values in the lower slope terrace and the outer wedge.

The wedge is subject to considerable supra-wedge sedimentation in mostly interconnected basins (Figures 2.2 and 2.3). Large basins overly the thrust sheets in several of the lines, so most of the thrusts are blind. The two frontal thrust sheets are mostly emergent at the seafloor throughout the study area, whereas the thrust sheets farther landward are often covered through portions of the study area, burying the folds entirely. Occasionally, submarine colluvial deposits, which are observed for thrust sheets globally (e.g. [*Moore and Karig*, n.d.; *McAdoo et al.*, 2004; *Moore et al.*, 2009; *Strasser et al.*, 2011]) can be seen buried below flat-lying basin reflectors (Figure 2.7b, gray areas, and Figure 2.10), and thrust sheets do show evidence of being eroded, indicating they were exposed at the seafloor before being buried (Figure 2.10c). Interpretation of these basin sediments shows evidence of deformation by continued thrusting of wedge deformation through different stages of deposition. Some of the faults that cut through the basins reach close to or deform the oceanic crust (Figure 2.10a and b), whereas others appear to deform the lowermost basin sediment and remain buried.

The internal deformation of the thrust sheets is much more pronounced to the north, with some single thrust sheets displaying two fold hinges, and some thrust faults splaying and/or duplexing

(Figures 2.7 and 2.8a,b). Secondary thrusting in the back limbs of folds is not uncommon, as are small faults near the crest of the folds. The seaward most thrust sheets in the south, however, are relatively internally undeformed when compared to their northern counterparts, and the thrusts have fewer splays (Figure 2.8c,d). In both the north and the south, a bright bottom simulating reflector (BSR) is present across the crests of many of the thrust sheets, as well as through some of the basins, indicating the presence of methane and methane hydrate, which has also been directly sampled by other methods (e.g [*Johnson et al.*, 2015]).

The lack of a consistent décollement reflector makes determining the depth and geometry by which the faults connect to the décollement ("sole out") somewhat difficult. In general, the faults sole near or into the top of the oceanic crust reflector, although there is not usually distinguishable offset of the reflector itself. Generally, faults in the northern lines (1-4) appear to sole into a level ~ 200 to 250 ms TWT above the oceanic crust (Figures 2.6a,b, 2.11 and 2.12a). In the south, the frontal thrust and faults B and C either sole directly into the top of oceanic crust or into a level <100 ms above it. Faults D and F sole into a higher level, ~225 ms above the oceanic crust (Figures 2.6c,d and 2.12b). In some lines, the sediment section above acoustic basement remains clearly undisturbed and flat-lying landward of the frontal thrust (Figure 2.12b). When fault reflectors cannot be traced to acoustic basement, there is not a clear décollement reflector. Below the fault soling level, reflectors cannot always be reliably identified, leading to a more acoustically blank layer beneath the outer wedge (e.g. Figure 2.8a,b). This layer may be representative of an underthrust sediment package, although the layer itself is generally <350 ms TWT when it is present.

2.4.3 Lower Slope Terrace

Between the outer wedge and the older accretionary wedge, there is an area that is termed here the lower slope terrace, although it has previously been referred to as the midslope terrace in most publications [*Flueh et al.*, 1998; *Fisher et al.*, 1999; *Adam et al.*, 2004; *Booth-Rea et al.*, 2008]. The basement is a faint and discontinuous reflector below this section. The deeper section of the lower slope terrace is not reliably well imaged, so identification of the oceanic crust can be uncertain. A continuation of the acoustically blank layer, possibly underthrust sediments, seen beneath the outer wedge may be observed but is not as distinct. This layer is thicker below the lower slope terrace than the outer wedge, usually measuring between 300 and 400 ms thick.

2.4.3.1 The Quinault Ridge

Throughout most of the survey, the lower slope terrace is separated from the outer wedge by a large symmetrical ridge structure with no internally coherent reflectors (see Figure 2.13),identified in bathymetry and named the Quinault Ridge by *Carson* [1978], and also referred to as an anticlinal ridge where it is identified in previous studies [*MacKay*, 1995; *Fisher et al.*, 1999]. The ridge generally parallels the deformation front, but trends slightly landward in the southern portion of the survey, and is not visible in the bathymetry at line 9, leading to some uncertainty in the correlation through this section. The Quinault Ridge is generally 5 to 7 km wide at its widest point through the survey. It is not emergent at the seafloor in line 5, where the top is eroded by the Quinault Channel (Figure 2.2). It is bounded by two thrust faults with opposite dip directions, with the trenchward (western) fault dipping seaward (fault G) and the landward (eastern) fault dipping landward (fault H). These are identified at the edges of the ridge where reflectors appear deformed and offset in the adjoining basin sediments (Figure 2.13). The

seaward fault is expressed clearly in the northern portion of the survey area, but becomes more indistinct in the south. The lack of coherent internal reflectors makes determining the structure of the ridge difficult. However, the Quinault Ridge correlates to a smaller, fold-like feature in line 1, similar to others seen in the lower slope terrace (see next section). In line 8, some reflectors can be seen, which resolve into a relatively undeformed doubly vergent thrust sheet in line 9 (Figure 2.9, CMPs 8500-10500). In addition, line 1 contains a large ridge that is not the Quinault Ridge (bordered by G' and H', Figure 2.4), and a smaller structure that correlates with the Quinault Ridge in the bathymetry. This proto-ridge structure appears as a possible fold, while the large ridge seen in line 1 dies out along strike to the south into what appears to be a smaller thrust sheet, akin to those seen in the lower slope terrace. This may indicate that the Quinault Ridge was originally a structure similar to those seen in the lower slope terrace that then continued to deform into a larger thrust sheet that developed a backthrust.

2.4.3.2 Basin and structures

Landward of this ridge, the lower slope terrace consists of a thick (~3 to 3.5 seconds TWT) sedimentary section with variable amounts of deformation, resulting in buried symmetrical fold-like structures within the terrace (Figures 2.13 (CMPs 203880-203480) and 2.14). These can vary in vergence, coherency, and size, but there are between one and three in each line. The structures are generally smaller in scale than those found in the corresponding seaward outer wedge, and are all entirely buried. Therefore, bathymetry cannot be used to correlate structures from line to line, as was done in the outer wedge. Similar structures were identified by *Fisher et al*. [1999], and identified as possible diapirs or isolated detachment folds. These structures show many of the characteristics previously interpreted, such as deformation of overlying sediments and incoherent internal reflectors.

The features can range in their deformation style (Figure 2.14). Clear fault plane reflectors are not usually identified, but sediment overlying and surrounding the features is deformed. Many have incoherent internal reflectors, further complicating the structural interpretation. More clearly imaged structures show doubly vergent thrust sheets, similar to those seen in line 9. Many of the structures appear symmetrical, and may accommodate some deformation by folding rather than faulting. The presence of some truncational unconformities in the basin indicates that there was a period of erosion during the basin's depositional history (Figure 2.14a, CMP ~12650). Some of the crests of the structures also show evidence of being eroded. Some of the structures appear to deform the sediment section near the surface, whereas others leave the uppermost sediments undisturbed (Figure 2.14).

The lower slope terrace abuts the slope; beneath this bathymetric break, the seismic reflectivity changes markedly, as the ordered reflectors of the lower slope terrace basin give way to the seismically chaotic landward wedge (Figure 2.15b). In some accretionary margins, such as the Nankai Trough and the Sunda margin, out of sequence thrust faults create high amplitude reflectors and mark the boundary between the outer, actively deforming wedge and the inner wedge (e.g. [*Kopp and Kukowski*, 2003; *Moore et al.*, 2007]). Interpretation of ORWELL seismic lines from offshore Grays Harbor [*Fisher et al.*, 1999; *Booth-Rea et al.*, 2008] have identified a seaward vergent thrust fault as the divider of the two tectonic domains. In the COAST data, the structure at the landward edge of the lower slope terrace is not a clear, high amplitude reflector. Furthermore, there is little to no reflectivity detected below the inner accretionary wedge, so the full extent of such a structure cannot be imaged. In the COAST data, as the slope taper angle increases, reflectors lose coherency so no single structure can be definitively interpreted as a spatially extensive out of sequence thrust fault.

2.4.4 Landward accretionary wedge

The landward continental slope portion of the wedge is very poorly imaged, with few to no coherent reflectors seen below the forearc basin. The forearc basin is in an extensional regime, containing large offset growth normal faults (Figure 2.15a). Structures interpreted here are similar to those interpreted by *McNeill et al*. [1997]. In the forearc basin sediments, two distinct stages of deposition can be imaged in certain lines, with a tilted package overlying a more chaotically imaged set of mostly horizontal reflectors. The forearc basin overlies a seismically chaotic package, the mélange broken formation (MBF) [*McNeill et al.*, 1997; *Flueh et al.*, 1998]. There is little to no evidence of an oceanic crust reflector below the inner accretionary wedge in these lines. Isolated patches of deeper coherent energy are present, but cannot be conclusively determined to be the oceanic plate reflector. As such, all plate geometry below the inner wedge is inferred. There is also no clear décollement reflector.

2.5 Discussion

The structures documented in the COAST study area, such as the dominance of landward vergent faults, the structures in the lower slope terrace, and possible décollement levels, agree broadly with those interpreted in earlier studies [*MacKay*, 1995; *Flueh et al.*, 1998; *Fisher et al.*, 1999; *Adam et al.*, 2004; *Booth-Rea et al.*, 2008]. However, the COAST survey's relatively close line spacing allows us to document spatial changes within the landward vergent zone of central Cascadia at a smaller scale. We relate the previous structural interpretations to the new data, document the variability of structural style, and propose possible processes for wedge development.

2.5.1 Underthrust sediment, fault soling, and the décollements

Interpretation of lines 103 and 107 collected as part of the 1998 ORWELL cruise just north of and at the Grays Harbor area, respectively, document an active basal décollement below the wedge [*Flueh et al.,* 1998; *Booth-Rea et al.,* 2008]. Offshore Oregon, in the landward vergent zone, a décollement 300 ms (~400 m) above oceanic crust is interpreted [*MacKay,* 1995]. Another interpretation has suggested two simultaneously active décollements: a basal décollement at the boundary with the crust, and a upper décollement higher in the stratigraphic section into which some faults sole [*Adam et al.,* 2004]. Our analysis of fault soling levels indicates that the level of the décollement varies spatially, both along strike and within the outer wedge in the dip direction. We document two active décollement levels in the COAST survey area: the basal décollement and an upper décollement. We also note that the décollement level can be correlated to the type of deformation that a thrust sheet experiences.

2.5.1.1 Estimates of underthrust sediment thickness

At the frontal thrust, different soling levels can be identified along strike in the survey (Figure 2.7). In the north, faults sole into the sediment section at a position clearly above the top of oceanic crust, indicating an active upper décollement. Reflectors from the incoming sediment section continue undisturbed below the frontal thrust. The thickness of sediment bypassing the frontal thrust corresponds to between ~175 to 250 ms of TWT (Figure 2.11). From velocity models used for depth and time migrations of seismic lines, velocities in the lower sediment section as it enters the trench vary from ~3.6 km/s to ~4.2 km/s, (e.g. Webb, Chapter 3, [*Flueh et al.*, 1998; *Everson,* 2014; *Fortin,* 2015]), giving estimates of underthrust sediment thickness between ~300 and 525 m. A maximum estimate for thickness is ~ 850 m (below fault F in line 1). In areas where the faults cut through the upper décollement and sole into the underthrust

package (Fault A, Line 2; Fault F, Line 3), the amount of underthrust sediment is ~150 m thick. However, in most cases the amount of sediment that is being underthrust is probably ≤500 m. Similar estimates were made in earlier interpretations offshore Oregon in the landward vergent area, where ~300 ms (corresponding to 400 m) of sediment is being underthrust [*MacKay*, 1995]. Offshore Washington, estimates of the location of the upper décollement are 500 to 530 m above oceanic crust [*Adam et al.*, 2004]. In the southern lines, faults sole into a basal décollement corresponding with the sediment-basement interface, and if any sediment is being underthrust, the thickness of the underthrust section cannot be resolved with the COAST seismic lines (Figure 2.11).

Hypotheses for the low taper angle of the wedge, as well as the presence of landward vergent faulting, often hinge on having low basal shear stress at the bottom of the wedge [*Seely*, 1977; *Davis and Hyndman*, 1989; *MacKay et al.*, 1992]. This is typically attributed to the presence of a fluid-rich underthrust overpressured layer, separated from the overlying outer wedge by a décollement. The low overall taper angle of the wedge is also generally associated with weaker underthrust sediments [*Saffer and Bekins*, 2006]. The amount of sediment underthrust here is similar to Barbados [*Bangs et al.*, 1990; *Shipley et al.*, 1990] or Muroto [*Tobin and Saffer*, 2009], where overpressured underthrust sediment is documented. Our analysis shows that there is an underthrust layer below most of the wedge, and overpressure in this layer could contribute to a low basal shear stress. However, we also document areas with landward vergent faulting where there is no seismically resolvable underthrust sediment. Also, in the case of Fault F in line 3, a large thrust fault cuts the upper décollement and may act as a conduit for fluids thereby potentially draining excess pore pressure.

2.5.1.2 Identification of the décollement

The best indications of the location of the upper décollement are the loss of fault plane reflectivity, acoustic blankness at depth, and analysis of the dip of reflectors (Figure 2.12). In the north, where the upper décollement appears to be active, fault reflectors cannot be interpreted through to the oceanic crust, and the underthrust section can be characterized in areas as more acoustically blank, although some reflectivity is present between the upper and lower décollements (Figure 2.8a, below faults C, D, and E). A similar acoustically blank package was noted in some of the earliest surveys of the margin as well, although much farther south [*Silver*, 1969]. Where the basal décollement is active, deformation of sediments and fault planes can be interpreted to reach the reflector at the top of acoustic basement, and reflectors are visible down to that level (Figure 2.8c).

A brighter reflector in the lower sections of the stratigraphic package offshore Oregon in the seaward vergent portion of the margin to the south of the COAST study area has been interpreted as a décollement due to reflector characteristics [*Gerdom et al.*, 2000]. However, in the COAST study area, although there are bright reflectors in the sediment package, the proto-décollement is not a prominent reflector in the incoming sediment section, and cannot be easily identified by reflector character alone.

Some drilling data is available in the incoming sediment section, albeit to the north and south of the COAST study area, or nearer the Juan de Fuca ridge [*Kulm et al.*, 1973a; *Westbrook et al.*, 1994; *Underwood et al.*, 2005]. At Site 174 offshore Oregon, distal Astoria fan turbidites were sampled (~284 m), as well as ~600 m of underlying Pliocene-Pleistocene turbidites, where Pliocene forams were found in the bottom 433 m of core [*Kulm et al.*, 1973b]. Assuming similar

deposition rates for Site 174 and the COAST study area, the décollement level would fall within the older Pliocene-Pleistocene silty clay turbidite section (see further discussion, Chapter 3).

2.5.1.3 Thrust sheet deformation and the spatial extent of the décollement

Below thrust sheets that exhibit backthrusts, internal deformation, and have higher bathymetric relief, faults generally, but not universally, sole into the upper décollement (Figure 2.11). In lines where the majority of faults sole into the upper décollement level (lines 1, 2, 3, and 4), some faults do appear to cross the upper décollement level and sole within the underthrust sediment package (Fault A, Line 2; Fault F, Line 3). Where thrust sheets display less internal deformation, faults sole into the basement décollement level and reflectors can still be imaged to the oceanic crust in areas with a basal décollement.

Evidence suggests that both décollements were active in the past as well as today, as landward faults within the wedge can sole into the upper and lower décollements. In lines 5, 6, 7, 8, and 9, older thrusts (D and F) sole into the upper décollement, indicating that there has been a temporal change in the active décollement in the south—that is, the upper décollement is active below faults D and F and was presumably active when they were frontal thrusts, but basal décollement is currently more active at the frontal thrust.

2.5.2 Deformation and out-of-sequence fault activity

2.5.2.1 The outer wedge and Quinault Ridge

Deformation of sedimentary basins overlying the accretionary wedge thrust faults can be used to construct a history of fault activity in the COAST study area. Although there is no drilling data through these basins to constrain absolute ages, basin deformation is used to determine timing of relative fault activity. The central portion of the wedge shows that even the youngest sediment

deposits are cut by some faults, indicating recent out of sequence thrust fault activity (Figure 2.10). The thrusts that show this clear deformation of the basins are faults C and D, which also indicates that there is continued movement on more than one fault in the outer wedge. Which of these faults deforms the overlying sediment most changes along strike in the wedge, indicating that the relative fault activity varies spatially.

Some folding and small offsets can be seen in the lowermost sediments in outer wedge basins as well (Figure 2.13, fault F), although the deformation is more subtle than that seen in Figure 2.10. The relative timing and amount of deformation is difficult to determine, although given the interconnected nature of the basins they are be assumed to have a relatively similar age along strike. Given the current level of seismic processing, some of the subtleties of the sediment-thrust sheet contacts may be obscured. Deformation of slope basin sediments, especially those that cover eroded slump deposits or eroded thrust sheets, indicates that there has been motion taken up by these faults during or after basin deposition—presumably after the fault is no longer the frontal thrust (Figure 2.10). The wide spacing of the faults and the amount of shortening taken up by the outer wedge in the COAST area suggest that the wedge may be relatively strong compared to the material at its base. Given critical wedge taper theory, the low taper angle would also indicate a relatively strong wedge overlying a relatively weak base.

Faults bounding the Quinault Ridge show evidence of recent movement, particularly fault G (Figure 2.13). The basin through which it cuts has evidence of different stages of deposition, seen in onlapping relationships. Fault F deforms the lower strata, whereas fault G deforms almost the entire sediment section. This suggests that the seaward fault G has also been active relatively recently Fault H, on the landward side of the Quinault Ridge, deforms sediments,

generally deeper in the section, but sometimes closer to the surface (Figure 2.13, CMP ~9000). How recent the fault activity is when the fault is more deeply buried is difficult to determine.

2.5.2.2 The lower slope terrace

2.5.2.2.1 Origin of structures

Fisher et al [1999] interpreted the lower slope terrace in an earlier reflection seismic survey, and suggested a possible diapiric origin for the lower slope terrace features, as well as an isolated detachment fold or strike-slip fault. Given that these features are seen along strike throughout the survey area, a strike-slip fault seems unlikely. Mud volcanoes and diapirs are documented on the surface at other locations in the Cascadia margin (e.g. [*Lewis and Cochrane*, 1990; *Brown and Orange*, 1993; *Suess et al.*, 2001]). The incoherent nature of some of the reflectors in the structures as well as the continued deformation of shallower sediment were identified as possible indications that fluidized mud was causing deformation. *Fisher et al*. [1999] also suggest that the diapirism was potentially short lived, due to the coherent nature of reflectors higher in the structure. A relatively rapid deformation history would be necessary to bury the mud so that fluid was not able to escape.

In the COAST lines, we see similar features to those documented by *Fisher et al*. [1999]. Incoherent reflectors are generally restricted to the lower portions of the structures, a patchy BSR can sometimes be seen, and the sediments above the features are often deformed in a symmetrical manner. Given the close spacing of the COAST lines, we image several structures in a relatively small area, and record a variety of different structural styles. The less deformed structures in the lower slope terrace most commonly resemble doubly vergent thrusts exemplified by those in line 9, or smaller, less developed thrust sheets similar to those seen in the outer wedge (Figures 2.9 and 2.14). Most of the deformation seems to have at least some

faulting associated with it, although symmetrical folds similar to detachment folds are seen in the lower slope terrace of line 9, and may be present in the more incoherent structures.

Evidence that diapirism is the driver for deformation in the lower slope terrace is inconclusive. The data here support *Fisher et al*. [1999]'s conclusions that if there was fluid movement, it is no longer deforming the structure. Where more chaotic reflectors are seen, they are generally restricted to the lower portion of the structures (Figure 2.14a,b), and continuous reflectors are seen across the crests of folds. Most of the deformation in this area seems to have been taken up by thrusting and folding, similar to, but at a smaller scale and more isolated, the deformation in the outer wedge, albeit at a smaller scale and more spatially isolated within the basin.

2.5.2.2.2 Stages of deformation

The lower slope terrace also shows evidence of deformation at several stages in its history. The style of deformation seen here results in fold-like structures that can be symmetrical, seaward, or landward vergent, and have few defined fault plane reflectors. An unconformity seen clearly in some lines can be used as a relative time marker (Figure 2.14, CMP ~12450), and indicates that the section was deforming during the Pleistocene. Timing of fault initiation and deformation is harder to constrain, given the flat-lying nature of the sediments and the relative isolation of the structures. Some reflectors near the top of the section appear to be deformed (Figure 2.14b, CMP 9520 to 9120), which may point to some later stage deformation in portions of the study area, although in other locations (Figure 2.14b, CMP 12250 to 12650) the sediments above deformed sections of the lower slope terrace basin are flat-lying.

2.5.3 Controls on wedge development

Several hypotheses have been put forward about the formation of the landward vergent zone in the Cascadia accretionary wedge. Changes in lithology, décollement level, and comparative wedge and basal strength due to overpressure have all been cited [*Silver*, 1972; *MacKay*, 1995; *Flueh et al.*, 1998; *Fisher et al.*, 1999; *Gerdom et al.*, 2000; *Adam et al.*, 2004]. *Adam et al* [2004], among others, suggest the influence of sedimentation rate, particularly high sedimentation during the Pleistocene, on the formation of the wedge. Post-glacial Holocene rates of deposition were much lower and are negligible at the seismic scale [*Barnard*, 1978; *Prytulak et al.*, 2006].

2.5.3.1 Supra-wedge sedimentation

Numerical and physical models have shown that increased sedimentation on top of an actively deforming fold and thrust belt can cause the deformation front to step forward into the incoming sediment section, often resulting in buried thrusts [*Storti and Mcclay*, 1995; *Mugnier et al.*, 1997; *Simpson*, 2006, 2010; *Pichot and Nalpas*, 2009; *Wu and McClay*, 2011; *Mannu et al.*, 2017]. This is observed in other areas, such as the Makran accretionary wedge and the Niger Delta [*Ellouz-Zimmermann et al.*, 2007; *Krueger and Grant*, 2011]. Moreover, doubly vergent thrust faults are documented in the low taper angle fold-and-thrust belt of the Niger Delta, suggesting some analogue to what we see here [*Bilotti and Shaw*, 2005; *Krueger and Grant*, 2011]. The introduction of a double décollement shows varying vergence in shallower faults in certain analogue models [*Pichot and Nalpas*, 2009]. A low wedge taper angle is also seen in models with high sediment influx (e.g. [*Simpson*, 2010; *Mannu et al.*, 2017]), leading to the suggestion that the wedge taper angle may be “supercritical” and due more to sediment influx than a reflection of mechanical weakness at the base of the wedge [*Storti and Mcclay*, 1995; *Simpson*,

2010]. Whether sediment is input from the trench or the hinterland also affects deformation, as does erosion and décollement strength [*Simpson*, 2010; *Wu and McClay*, 2011; *Mannu et al.*, 2017]. When sediment comes from the hinterland, the deformation front steps forward but two to three imbricate thrusts are observed at the front, rather than the singular thrust seen in models with trench input sediments [*Simpson*, 2010].

2.5.3.2 Sedimentation on the accretionary wedge in Cascadia

The submarine canyons that are present in this study area are all part of the Pleistocene to recent glacial sediment transport system that delivers a large amount of sediment to the Cascadia Basin [*Carson et al.*, 1974; *Barnard*, 1978], which likely had a profound impact on the structural evolution of the wedge, as has been suggested before [*Fisher et al.*, 1999; *Adam et al.*, 2004]. The presence of some truncations in the lower slope terrace and across line 9 indicates that there were periods of erosion along channel axes after fold development, indicating active erosion and deposition during deformation. The amount of inner deformation of thrust sheets, such as the development of backthrust or favored imbricate faulting, such as those seen from north to south, may also be partly due to sedimentation differences, although this is harder to determine from the evidence in the COAST seismic lines. The out of sequence faulting that is documented here has also been documented in numerical and analogue models of fold and thrust belts, where increased sedimentation can promote hinterland fault activity (e.g. [*Storti and Mcclay*, 1995; *Simpson*, 2010; *Mannu et al.*, 2016]). More deformation in the fault sheets is correlated not only to a higher décollement, but also to a larger amount of supra-wedge sedimentation. The northern outer wedge receives heavy supra-wedge sedimentation, mostly via trench parallel deposition, with the fold crests preventing much sedimentation directly into the trench. In the southern lines, basins between folds A, B, and C contain less sediment fill. The type of deformation seen in the

south also creates less accommodation space for supra-wedge sedimentation. Due to the traces of the Quinault and Willapa Channels through this area, more sediment may have bypassed the outer wedge in the southern portion of the survey. The amount of incoming sediment from the trench is similar throughout the survey.

2.5.3.3 Influence of the Quinault Ridge

Why thrust faults H/H' developed as landward vergent is unclear but their presence may have had an impact on the further development of the wedge. Line 9, along the axis of the Willapa Channel, does not have a Quinault Ridge, and instead contains doubly vergent thrusts and geometry such as that described by *Adam et al.* [2004] as a triangle zone, akin to that seen in the lower slope terrace. The presence of the Quinault Ridge as a well formed symmetrical ridge emergent at the seafloor is also not present in line 8, whose landward outer wedge deformation is a transition between deformation of northern lines and line 9. The development of the large Quinault Ridge thrust sheet may have enabled the formation of other large landward vergent thrust sheets of a similar style to develop seaward once the initial large thrust sheet was in place, whereas areas without the ridge have more doubly vergent thrust sheets. This difference may be a function of the presence of the Quinault Ridge, or may be a function of the mechanical or sedimentation conditions that allowed the Quinault Ridge to form, or, most likely, an interplay of the two factors.

2.5.3.4 Influence of sediment on wedge development

We propose a wedge development history that involves supra-wedge sedimentation, and is illustrated in Figure 2.16. An earlier, smaller Miocene accretionary wedge is assumed to have existed prior to the heavy Quaternary sedimentation on the margin (Figure 2.16, step 1). As heavy sedimentation began in the Pleistocene, the wedge deformation front may have "stepped

out" into the rapidly thickening incoming sediment section (Figure 2.16, step 4). The deformation in the lower slope terrace may reflect smaller steps forward of the deformation front, or continued deformation landward of the new frontal thrust (Step 3). The present day Quinault Ridge may have developed as the new frontal thrust, and influenced the deformation and the fault vergence of the outer wedge (Step 4). Through the development of thrusts D and F, deformation was likely similar throughout this area of the margin (Figure 2.16, Step 5 a and b), with the possible exception of line 9. Line 9 is along the axis of the Willapa Channel, lacks a Quinault Ridge feature, and appears to have deformed with doubly verging faults until the formation of fault B. As the wedge developed, continued ridge building and the development of the submarine canyons may have caused high levels of supra-wedge sedimentation in the north, and caused sediment bypass in the south. Most of the sediment into the south may have been from the trench, rather than both from the trench and trench parallel in the north. An active basal décollement mirrors locations with mostly trench sediment input and less deformed thrust sheets, whereas the upper décollement may be more active in areas where both trench and supra-wedge sedimentation are heavy.

Overall development of the Cascadia margin may be due to the relative strength of the wedge to the base, or possibly the presence of overpressure, but we suggest that some smaller spatial changes within the landward vergent area may be due to factors such as sediment supply and/or level of décollement. The influence of sediment in accretionary wedge development is non-negligible (e.g. [*Storti and Mcclay*, 1995; *Ellouz-Zimmermann et al.*, 2007; *Kimura et al.*, 2007; *Simpson*, 2010; *Mannu et al.*, 2017], and we posit that it played a significant role in the development of the Cascadia margin.

2.6 Conclusions

Using the COAST dataset, we document the tectonic variability on a small scale in the central, well developed landward vergent zone of the Cascadia subduction zone. Only one other seismic study has been collected at a similar line spacing as the COAST study, located offshore Oregon and straddling the landward-vergent/seaward-vergent transition [*MacKay et al.*, 1992]. The structures documented in this study are similar to those seen elsewhere in the landward vergent zone in Cascadia [*MacKay et al.*, 1992; *Tobin et al.*, 1993; *MacKay*, 1995; *Flueh et al.*, 1998; *Fisher et al.*, 1999; *Adam et al.*, 2004]. Here, we show that while the outer wedge is dominantly landward vergent throughout the survey area, the amount of internal thrust sheet deformation, depth of décollement and thrust fault soling, and fault geometry can vary. We see clear evidence for simultaneous activity on frontal and internal thrusts, with central outer wedge sediments showing evidence of recent deformation of overlying sediments. Our shortening estimates also indicate the presence of a relatively strong wedge. We identify two décollement levels, also consistent with earlier interpretations [*Flueh et al.*, 1998; *Fisher et al.*, 1999; *Adam et al.*, 2004]: an upper décollement above ~500 m of underthrust sediments, and a basal décollement at the sediment-basement interface. In the lower slope terrace, truncation of reflectors shows that some thrust faults were emergent at the seafloor before being buried, indicating that they were active during the Pleistocene. We do not see enough evidence to call the structures diapirs, but do detail the presence of some faulting and folding.

Adam et al. [2004] suggest that the initiation of an upper décollement was due to rapid sedimentation, which would alter effective stress at depth and allow for a shallower décollement. Analogue and numerical models have shown that supra-wedge sedimentation can impact structural deformation and wedge taper angle in fold and thrust belts (e.g. [*Storti and Mcclay*,

1995; *Simpson*, 2010; *Wu and McClay*, 2011; *Mannu et al.*, 2017]). We suggest that some of the changes in structural style from north to south in the COAST area may be linked to the amount of supra-wedge sedimentation, the presence of submarine canyons, and the development of the Quinault Ridge. The lower slope terrace, between the inner and outer wedges, may represent an area that was bypassed with relatively little deformation from a step-out of the deformation front during the Pleistocene. While many assumptions about Cascadia focus on the potentially weak base assumed from the wedge taper angle, we posit that the sedimentation on top of the wedge may be a driver for the types of deformation seen here.

Although there is a correlation between the amount of supra-wedge sedimentation, fault deformation style, and depth to décollement, the precise drivers for changes in deformation style cannot be absolutely resolved with the data here. Increased seismic coverage and drilling data could constrain the timing of events and help refine structural models of the development of deformation in Cascadia.

2.7 References

Adam, J., D. Klaeschen, N. Kukowski, and E. R. Flueh (2004), Upward delamination of Cascadia Basin sediment infill with landward frontal accretion thrusting caused by rapid glacial age material flux, *Tectonics*, *23*(3), doi:10.1029/2002TC001475.

Atwater, B. F., and D. K. Yamaguchi (1991), Sudden, probably coseismic submergence of Holocene trees and grass in coastal Washington State, *Geology*, *19*(7), 706–709, doi:10.1130/0091-7613(1991)019<0706:SPCSOH>2.3.CO;2.

Atwater, B. F., B. Carson, G. B. Griggs, P. P. Johnson, and M. S. Salmi (2014), Rethinking turbidite paleoseismology along the Cascadia subduction zone, *Geology*, *42*(9), 827–830, doi:10.1130/G35902.1.

Bangs, N. L. B., G. K. Westbrook, J. W. Ladd, and P. Buhl (1990), Seismic velocities from the Barbados Ridge complex: Indicators of high pore fluid pressures in an accretionary complex, *J. Geophys. …*, *95*(B6), 8767–8782.

Barnard, W. D. (1978), The Washington continental slope: Quaternary tectonics and sedimentation, *Mar. Geol.*, *27*(1–2), 79–114, doi:10.1016/0025-3227(78)90075-0.

Beeson, J. W. (2017), Investigating Plate Boundaries through New High-Resolution Bathymetry and Seismic Data; 2 Case Studies from the Cascadia Subduction Zone and San Andreas Fault, Oregon State University.

Benson, B. E., B. F. Atwater, D. K. Yamaguchi, L. J. Amidon, S. L. Brown, and R. C. Lewis (2001), Renewal of Tidal Forests in Washington State after a Subduction Earthquake in A.D. 1700, *Quat. Res.*, *56*, 139–147, doi:10.1016/j.yqres.2014.07.007.

Bilotti, F., and J. H. Shaw (2005), Deep-water Niger Delta fold and thrust belt modeled as a critical-taper wedge: The influence of elevated basal fluid pressure on structural styles, *Am. Assoc. Pet. Geol. Bull.*, *89*(11), 1475–1491, doi:10.1306/06130505002.

Booth-Rea, G., D. Klaeschen, I. Grevemeyer, and T. Reston (2008), Heterogeneous deformation in the Cascadia convergent margin and its relation to thermal gradient (Washington, NW USA), *Tectonics*, *27*(4), doi:10.1029/2007TC002209.

Brown, K. M., and D. L. Orange (1993), Structural aspects of diapiric melange emplacement: the Duck Creek Diapir, *J. Struct. Geol.*, *15*(7), 831–847.

Carson, B. (1973), Acoustic stratigraphy, structure, and history of Quaternary deposition in Cascadia Basin *, *Deep. Res.*, *20*(680), 387–396.

Carson, B., J. Yuan, P. B. Myers, and W. D. Barnard (1974), Initial deep-sea sediment deformation at the base of the Washington continental slope: A response to subduction, *Geology*, *2*(11), 561–564, doi:10.1130/0091-7613(1974)2<561:IDSDAT>2.0.CO;2.

Carson, B., E. T. Baker, B. M. Hickey, C. A. Nittrouer, D. J. DeMaster, K. W. Thorbjarnarson, and G. W. Snyder (1986), Modern sediment dispersal and accumulation in Quinault submarine canyon - A summary, *Mar. Geol.*, *71*(1–2), 1–13, doi:10.1016/0025-

3227(86)90030-7.

Clift, P., and P. Vannucchi (2004), Controls on tectonic accretion versus erosion in subduction zones: Implications for the origin and recycling of the continental crust, *Rev. Geophys.*, *42*(2), doi:10.1029/2003RG000127.

Clowes, R. M., and R. D. Hyndman (2002), Geophysical studies of the Northern Cascadia Subduction Zone off Western Canada and Their Implications for Great Earthquake Seismotectonics: A Review, in *Seismotectonics in Convergent Plate Boundary*, edited by Y. Fujinawa and A. Yoshida, pp. 1–23, Terra Scientific Publishing Company (TERRAPUB).

Davis, D., J. Suppe, and F. A. Dahlen (1983), Mechanics of Fold-and-Thrust Belts and Accretionary Wedges, *J. Geophys. Res.*, *88*(B2), 1153–1172.

Davis, E. E., and R. D. Hyndman (1989), Accretion and recent deformation of sediments along the northern Cascadia subduction zone, *Geol. Soc. Am. Bull.*, *101*, 1465–1480.

DeMets, C., R. G. Gordon, and D. F. Argus (2010), Geologically current plate motions, *Geophys. J. Int.*, *181*(1), 1–80, doi:10.1111/j.1365-246X.2009.04491.x.

Ellouz-Zimmermann, N., E. Deville, C. Muller, S. Lallemant, a B. Subhani, and a R. Tabreez (2007), Impact of sedimentation on convergent margin tectonics: Example of the Makran accretionary prism (Pakistan), *Thrust Belts Forel. Basins From Fold Kinemat. to Hydrocarb. Syst.*, 327–350, doi:Doi 10.1007/978-3-540-69426-7_17.

Everson, E. D. (2014), Seismic structure of the Costa Rican subduction system from active-source onshore-offshore seismic data and imaging plate boundary processes at the Cascadia subduction zone offshore Washington, University of Wyoming.

Fisher, M. A., E. R. Flueh, D. W. Scholl, T. Parsons, R. E. Wells, A. M. Tréhu, U. S. ten Brink, and C. S. Weaver (1999), Geologic processes of accretion in the Cascadia subduction zone west of Washington State, *Geodynamics*, *27*, 277–288.

Flueh, E. R., M. A. Fisher, J. Bialas, J. R. Childs, D. Klaeschen, N. Kukowski, T. Parsons, D. W. Scholl, A. M. Tréhu, and N. Vidal (1998), New seismic images of the Cascadia subduction zone from cruise SO108 — ORWELL, *Tectonophysics*, *293*, 69–84.

Fortin, W. F. J. (2015), Extracting physical parameters from marine seismic data: New methods in seismic oceanography and velocity inversion, University of Wyoming.

Frederik, M. C. G., S. P. S. Gulick, J. A. Austin, and N. L. B. Bangs (2015), What 2-D multichannel seismic and multibeam bathymetric data tell us about the North Sumatra wedge structure and coseismic response, , 1910–1926, doi:10.1002/2014TC003614.Received.

Gerdom, M., A. M. Trehu, E. R. Flueh, and D. Klaeschen (2000), The continental margin off Oregon from seismic investigations, *Tectonophysics*, *329*, 79–97, doi:10.1016/S0040-1951(00)00190-6.

Goldfinger, C. (2011), Submarine Paleoseismology Based on Turbidite Records, *Ann. Rev. Mar. Sci.*, *3*(1), 35–66, doi:10.1146/annurev-marine-120709-142852.

Goldfinger, C., L. D. Kulm, R. S. Yeats, L. Mcneill, and C. Hummon (1997), Oblique strike-slip faulting of the central Cascadia, *J. Geophys. Res.*, *102*(B4), 8217–8243.

Goldfinger, C., C. H. Nelson, and J. E. Johnson (2003), Deep-water turbidites as Holocene earthquake proxies: the Cascadia subduction zone and Northern San Andreas Fault systems, *Ann. Geophys.*, *46*(5), 1169–1194, doi:10.4401/ag-3452.

Griggs, G. B., and L. D. Kulm (1970), Sedimentation in cascadia deep-sea channel, *Bull. Geol. Soc. Am.*, *81*(5), 1361–1384, doi:10.1130/0016-7606(1970)81[1361:SICDC]2.0.CO;2.

Griggs, G. B., A. G. Carey, and L. D. Kulm (1969), Deep-sea sedimentation and sediment-fauna interaction in Cascadia Channel and on Cascadia Abyssal Plain, *Deep Sea Res. Oceanogr. Abstr.*, *16*(2), 157–170, doi:10.1016/0011-7471(69)90071-0.

Gulick, S. P. S., A. M. Meltzer, and S. H. Clarke (1998), Seismic structure of the southern Cascadia subduction zone and accretionary prism north of the Mendocino triple junction, *J. Geophys. Res.*, *1031*(98), 27207–27222.

Gutscher, M.-A., D. Klaeschen, E. R. Flueh, and J. Malavieille (2001), Non-Coulomb wedges, wrong-way thrusting, and natural hazards in Cascadia, *Geology*, *29*(5), 379–382.

Han, S., S. M. Carbotte, J. P. Canales, M. R. Nedimovic, H. Carton, J. C. Gibson, and G. W. Horning (2016), Seismic reflection imaging of the Juan de Fuca plate from ridge to trench: New constraints on the distribution of faulting and evolution of the crust prior to subduction, *J. Geophys. Res. B Solid Earth*, *121*(3), 1849–1872, doi:10.1002/2015JB012416.Received.

Holbrook, W. S., G. M. Kent, K. Keranen, H. P. Johnson, H. J. Tobin, J. Caplan-Auerbach, and J. Beeson (2012), Cascadia Fore Arc Seismic Survey: Open-Access Data Available, *Eos (Washington. DC).*, *93*(50), 521–522.

von Huene, R., and D. W. Scholl (1991), Observations at convergent margins concerning sediment subduction, subduction erosion, and the growth of continental crust, *Rev. Geophys.*, *29*(3), 279–316, doi:10.1029/91RG00969.

von Huene, R., D. Klaeschen, M. Gutscher, and J. Fruehn (1998), Mass and fluid flux during accretion at the Alaskan margin, *GSA Bull.*, *110*(4), 468–482.

Hyndman, R. D., K. Wang, T. Yuan, and G. D. Spence (1993), Tectonic Sediment Thickening, Fluid Expulsion, and the Thermal Regime of Subduction Zone Accretionary Prisms: The Cascadia Margin off Vancouver Island, *J. Geophys. Res.*, *98*(B12), 21865–21876.

Johnson, H. P., U. K. Miller, M. S. Salmi, and E. A. Solomon (2015), Analysis of bubble plume distributions to evaluate methane hydrate decomposition on the continental slope, *Geochemistry, Geophys. Geosystems*, *16*(11), 3825–3839, doi:10.1002/2015GC005955.

Kimura, G., Y. Kitamura, A. Yamaguchi, and H. Raimbourg (2007), Links among mountain building, surface erosion, and growth of an accretionary prism in a subduction zone—An example from southwest Japan, *Geol. Soc. Am. Spec. Pap. 436, 2436*.

Kopp, H., and N. Kukowski (2003), Backstop geometry and accretionary mechanics of the Sunda margin, *Tectonics*, *22*(6), doi:10.1029/2002TC001420.

Krueger, S. W., and N. T. Grant (2011), The Growth History of Toe Thrusts of the Niger Delta and the Role of Pore Pressure, in *Thrust fault-related folding: AAPG Memoir 94*, pp. 357–390.

Kulm, L. D. et al. (1973a), Introduction, in *Initial reports of the Deep Sea Drilling Project, covering Leg 18 of the cruises of the drilling vessel Glomar Challenger, Honolulu, Hawaii to Kodiak, Alaska May-July 1971*, edited by L. D. Kulm et al., pp. 5–8, Ocean Drilling Program, College Station, TX.

Kulm, L. D. et al. (1973b), Site 174, in *Initial reports of the Deep Sea Drilling Project, covering Leg 18 of the cruises of the drilling vessel Glomar Challenger, Honolulu, Hawaii to Kodiak, Alaska May-July 1971*, edited by L. D. Kulm et al., College Station, TX.

Lewis, B. T. R., and G. C. Cochrane (1990), Relationship between the location of chemosynthetic benthic communities and geologic structure on the Cascadia Subduction Zone, *J. Geophys. Res.*, *95*, 8783–8793.

MacKay, M. E. (1995), Structural variation and landward vergence at the toe of the Oregon accretionary prism, *Tectonics*, *14*(5), 1309–1320.

MacKay, M. E., G. F. Moore, G. R. Cochrane, J. Casey Moore, and L. D. Kulm (1992), Landward vergence and oblique structural trends in the Oregon margin accretionary prism: Implications and effect on fluid flow, *Earth Planet. Sci. Lett.*, *109*, 477–491, doi:10.1016/0012-821X(92)90108-8.

MacKay, M. E., G. F. Moore, D. Klaeschen, and R. von Huene (1995), The case against porosity change: Seismic velocity decrease at the toe of the Oregon accretionary prism, *Geology*, *23*, 827–830, doi:10.1130/0091-7613(1995)023<0827.

Mannu, U., K. Ueda, S. D. Willett, T. V Gerya, and M. Strasser (2016), Impact of sedimentation on evolution of accretionary wedges: Insights from high-resolution thermomechanical modeling, *Tectonics*, 2828–2846, doi:10.1002/2016TC004239.

Mannu, U., K. Ueda, S. D. Willett, T. V Gerya, and M. Strasser (2017), Stratigraphic signatures of forearc basin formation mechanisms, *Geochemistry, Geophys. Geosystems*, *18*, doi:10.1002/2017GC006810.Received.

McAdoo, B. G., M. K. Capone, and J. Minder (2004), Seafloor geomorphology of convergent margins: Implications for Cascadia seismic hazard, *Tectonics*, *23*(6), n/a-n/a, doi:10.1029/2003TC001570.

McNeill, L. C., K. A. Piper, C. Goldfinger, L. D. Kulm, and R. S. Yeats (1997), Listric normal faulting on the Cascadia continental margin, *J. Geophys. Res.*, *102*(B6), 12123–12138.

Moore, G. F., and D. E. Karig (n.d.), Development of sedimentary basins on the lower trench slope, , 1–5.

Moore, G. F., N. L. B. Bangs, A. Taira, S. Kuramoto, E. Pangborn, and H. J. Tobin (2007), Three-dimensional splay fault geometry and implications for tsunami generation, *Science (80-.).*, *318*(5853), 1128–1131, doi:10.1126/science.1147195.

Moore, G. F. et al. (2009), Structural and seismic stratigraphic framework of the NanTroSEIZE

Stage 1 transect, in *Proceedings of the Integrated Ocean Drilling Program, Volume 314/315/316*, vol. 314/315/31, edited by M. Kinoshita, H. J. Tobin, J. Ashi, G. Kimura, S. Lallemant, E. J. Screaton, D. Curewitz, H. Masago, K. T. Moe, and E. 314/315/316 Scientists.

Mugnier, J. L., P. Baby, B. Colleta, P. Vinour, P. Bale, and P. Leturmy (1997), Thrust geometry controlled by erosion and sedimentation: A view from analogue models, *Geology*, *25*(5), 427–430.

Pichot, T., and T. Nalpas (2009), Influence of synkinematic sedimentation in a thrust system with two decollement levels; analogue modelling, *Tectonophysics*, *473*(3–4), 466–475, doi:10.1016/j.tecto.2009.04.003.

Prytulak, J., J. D. Vervoort, T. Plank, and C. Yu (2006), Astoria Fan sediments, DSDP site 174, Cascadia Basin: Hf-Nd-Pb constraints on provenance and outburst flooding, *Chem. Geol.*, *233*(3–4), 276–292, doi:10.1016/j.chemgeo.2006.03.009.

Saffer, D. M., and B. A. Bekins (2006), An evaluation of factors influencing pore pressure in accretionary complexes: Implications for taper angle and wedge mechanics, *J. Geophys. Res. Solid Earth*, *111*(4), 1–21, doi:10.1029/2005JB003990.

Seely, D. R. (1977), The significance of landward vergence and oblique structural trends on trench inner slopes, *Isl. arcs Deep sea trenches back-arc basins*, *1*, 187–198.

Shipley, T. H., G. F. Moore, N. L. B. Bangs, J. C. Moore, and P. L. Stoffa (1990), Seismically inferred dilatancy distribution, northern Barbados Ridge decollement: Implications for fluid migration and fault strength, *Geology*, *22*(411–414).

Silver, E. A. (1969), Late Cenozoic Underthrusting of the Continental Margin off Northernmost California, *Science (80-.).*, *166*(3910), 1265–1266.

Silver, E. A. (1972), Pleistocene tectonic accretion of the continental slope off Washington, *Mar. Geol.*, *13*, 239–249.

Simpson, G. D. H. (2004), A dynamic model to investigate coupling between erosion, deposition, and three-dimensional (thin-plate) deformation, *J. Geophys. Res.*, *109*(F2), 1–12, doi:10.1029/2003JF000078.

Simpson, G. D. H. (2006), Modelling interactions between fold-thrust belt deformation, foreland flexure and surface mass transport, *Basin Res.*, *18*(2), 125–143, doi:10.1111/j.1365-2117.2006.00287.x.

Simpson, G. D. H. (2010), Formation of accretionary prisms influenced by sediment subduction and supplied by sediments from adjacent continents, *Geology*, *38*(2), 131–134, doi:10.1130/G30461.1.

Storti, F., and K. Mcclay (1995), Influence of syntectonic sedimentation on thrust wedges in analogue models, , (11), 999–1002.

Strasser, M., G. F. Moore, G. Kimura, A. J. Kopf, M. B. Underwood, J. Guo, and E. J. Screaton (2011), Slumping and mass transport deposition in the Nankai fore arc: Evidence from IODP drilling and 3-D reflection seismic data, *Geochemistry, Geophys. Geosystems*, *12*(5),

n/a-n/a, doi:10.1029/2010GC003431.

Suess, E. et al. (2001), Sea Floor Methane Hydrates at Hydrate Ridge, Cascadia Margin, in *Natural Gas Hydrates: Occurrence, Distribution, and Detection, Geophysical Monograph 124*, pp. 87–98.

Tobin, H. J., and D. M. Saffer (2009), Elevated fluid pressure and extreme mechanical weakness of a plate boundary thrust, Nankai Trough subduction zone, *Geology*, *37*(8), 679–682, doi:10.1130/G25752A.1.

Tobin, H. J., J. C. Moore, M. E. MacKay, D. L. Orange, and L. D. Kulm (1993), Fluid flow along a strike-slip fault at the toe of the Oregon accretionary prism: Implications for the geometiy of frontal accretion, *Geol. Soc. Am. Bull.*, *105*(5), 569–582, doi:10.1130/0016-7606(1993)105<0569.

Tréhu, A. M., J. Braunmiller, and J. L. Nabelek (2008), Probable low-angle thrust earthquakes on the Juan de Fuca-North America plate boundary, *Geology*, *36*(2), 127–130, doi:10.1130/G24145A.1.

Tréhu, A. M., R. J. Blakely, and M. C. Williams (2012), Subducted seamounts and recent earthquakes beneath the central Cascadia forearc, *Geology*, *40*(2), 103–106, doi:10.1130/G32460.1.

Underwood, M. B., K. D. Hoke, A. T. Fisher, E. E. Davis, E. Giambalvo, L. Zuhlsdorff, and G. A. Spinelli (2005), Provenance, Stratigraphic Architecture, and Hydrogeologic Influence of Turbidites on the Mid-Ocean Ridge Flank of Northwestern Cascadia Basin, Pacific Ocean, *J. Sediment. Res.*, *75*(1), 149–164, doi:10.2110/jsr.2005.012.

Wang, K., and A. M. Tréhu (2016), Invited review paper : Some outstanding issues in the study of great megathrust earthquakes — The Cascadia example, *J. Geodyn.*, *98*, 1–18, doi:10.1016/j.jog.2016.03.010.

Wang, K., R. E. Wells, S. Mazzotti, R. D. Hyndman, and T. Sagiya (2003), A revised dislocation model of interseismic deformation of the Cascadia subduction zone, *J. Geophys. Res.*, *108*(B1), doi:10.1029/2001JB001227.

Westbrook, G. K., B. Carson, and Shipboard Scientific Party (1994), Summary of Cascadia Drilling Results, in *Proceedings of the Ocean Drilling Program, Initial Reports*, vol. 146, edited by G. K. Westbrook, B. Carson, R. J. Musgrave, and E. Al, pp. 389–396.

Williams, M. C., A. M. Tréhu, and J. Braunmiller (2011), Seismicity at the Cascadia Plate Boundary beneath the Oregon Continental Shelf, *Bull. Seismol. Soc. Am.*, *101*(3), 940–950, doi:10.1785/0120100198.

Wu, J. E., and K. McClay (2011), Two-dimensional Analog Modeling of Fold and Thrust Belts: Dynamic Interactions with Syncontractional Sedimentation and Erosion, *AAPG Mem.*, *94*, 301–333, doi:10.1306/13251343M9450.

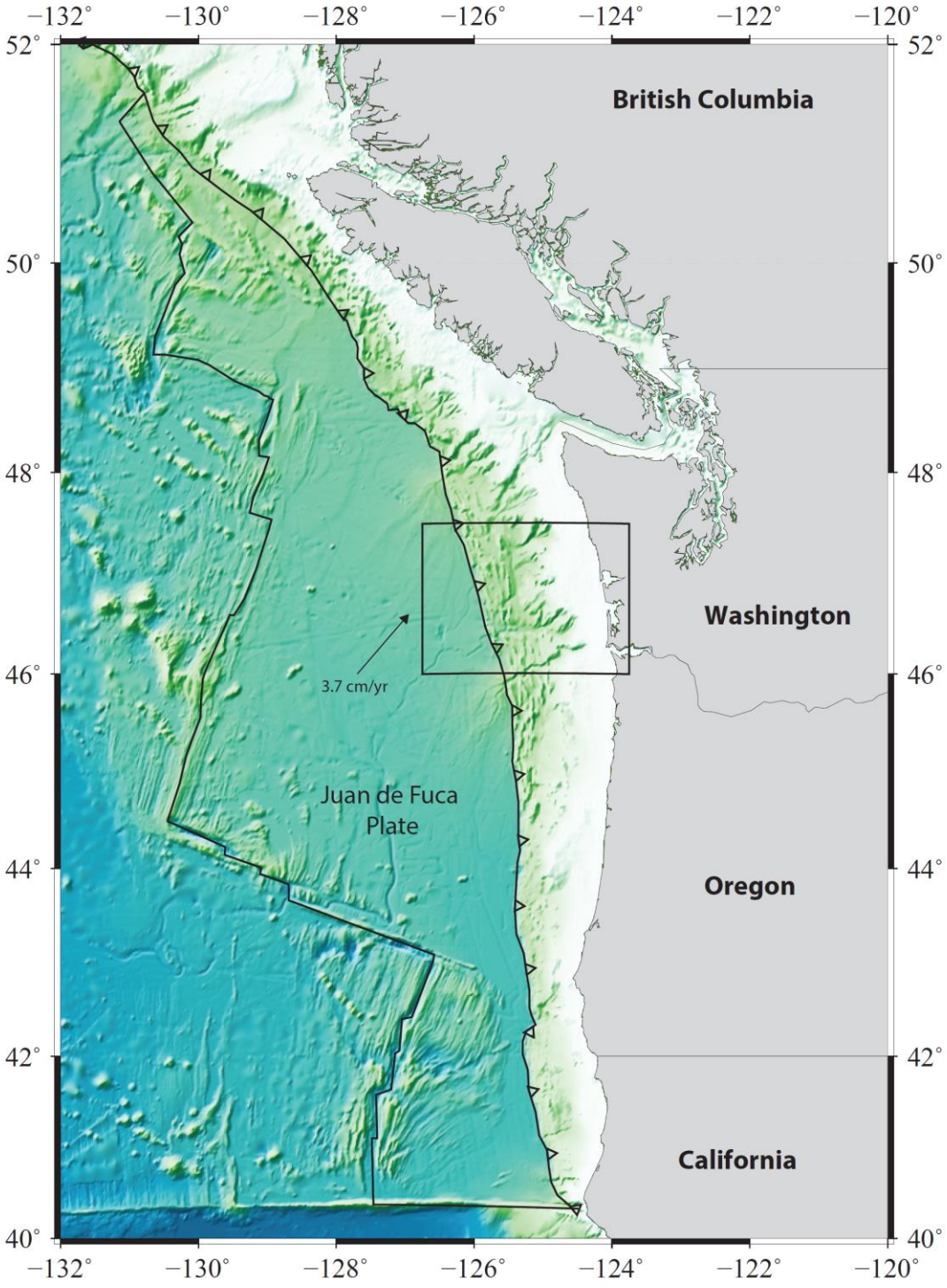

Figure 2.1: Map of the Cascadia subduction zone, with regional bathymetry from GeoMapApp. The Juan de Fuca plate subducts obliquely underneath North America, forming a relatively narrow prism in the north and the south of the subduction zone, with a wider, flatter prism visible in the bathymetry offshore Washington and northern Oregon. The relative lack of bathymetric features on the Juan de Fuca plate near the subduction zone is due to the deposition of large sediment fans into the Cascadia Basin. The black box indicates the location of Figure 2.2, a close-up of the Cascadia Open Access Seismic Transect (COAST) survey area.

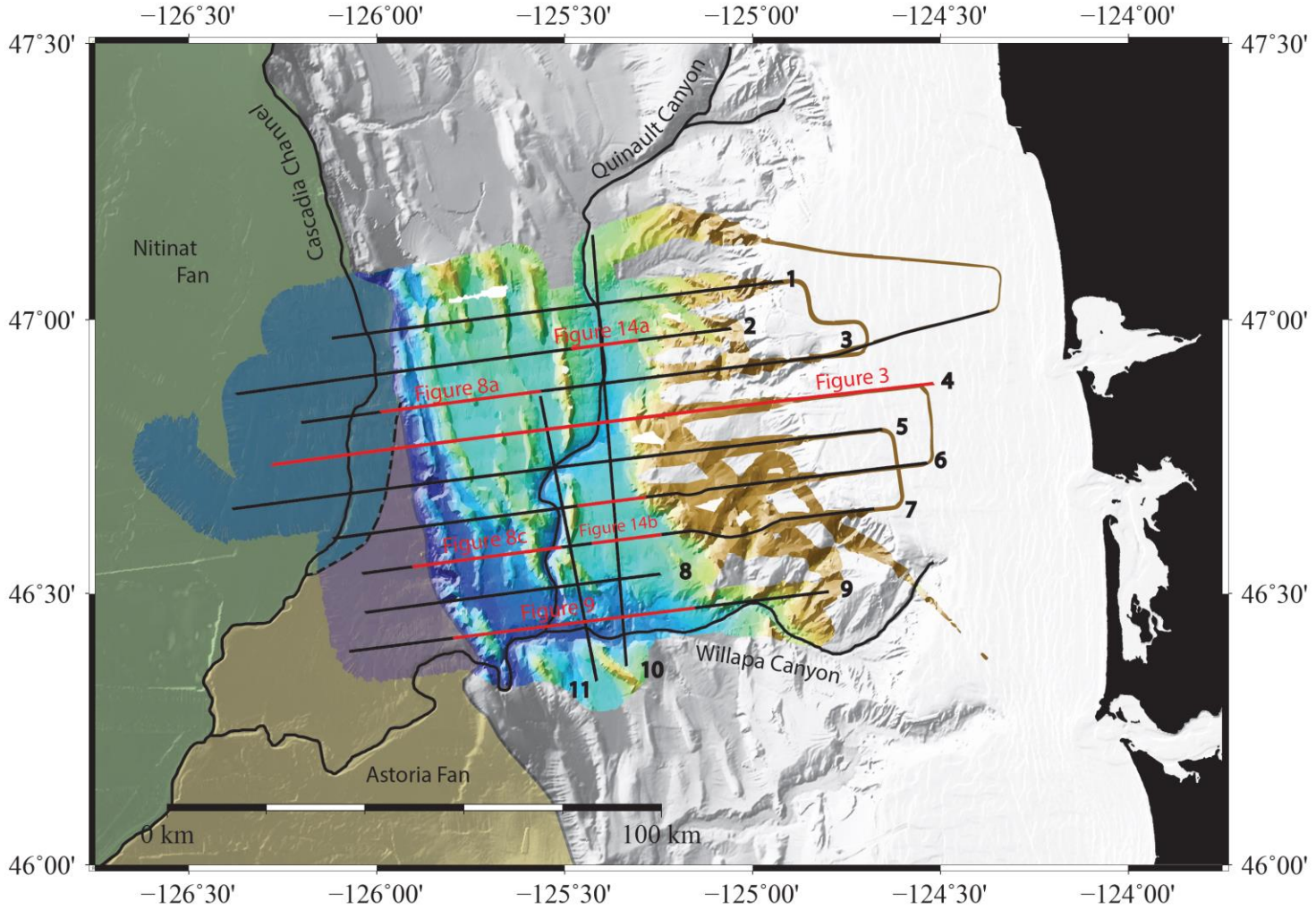

Figure 2.2: A close-up of the COAST survey location, with high resolution multibeam bathymetry overlain on the lines, labelled 1 through 11. The Quinault, Willapa, and Cascadia Channels have all been outlined, as well as the rough boundaries of the Nitinat and Astoria fans, from Underwood et al., 2005. Locations of seismic data in figures are marked in red.

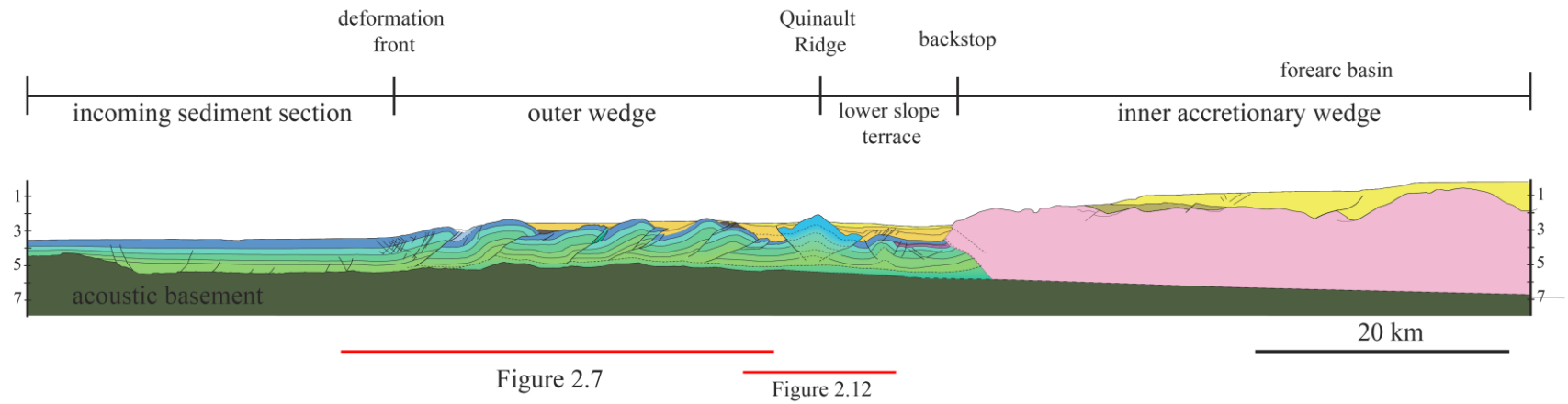

Figure 2.3: Simplified interpretation of line 4, showing general tectonic domains of the Cascadia subduction zone discussed in this paper. The incoming sediment section is a thick (~2.5 seconds TWT) section that is relatively undeformed, except for some small normal faults in the lower section. The incoming sediment is separated from the outer wedge by the deformation front, where small reverse conjugate faults form at the hinge point for the first large thrust sheet (frontal thrust). The outer wedge is characterized by large, landward vergent thrust sheets, some of which are buried by basins filled with supra-wedge sediment. The Quinault Ridge separates the outer wedge from the lower slope terrace. The taper angle of the wedge increases on the shelf slope, and the inner accretionary wedge is overlain by a forearc basin, which is normally faulted.

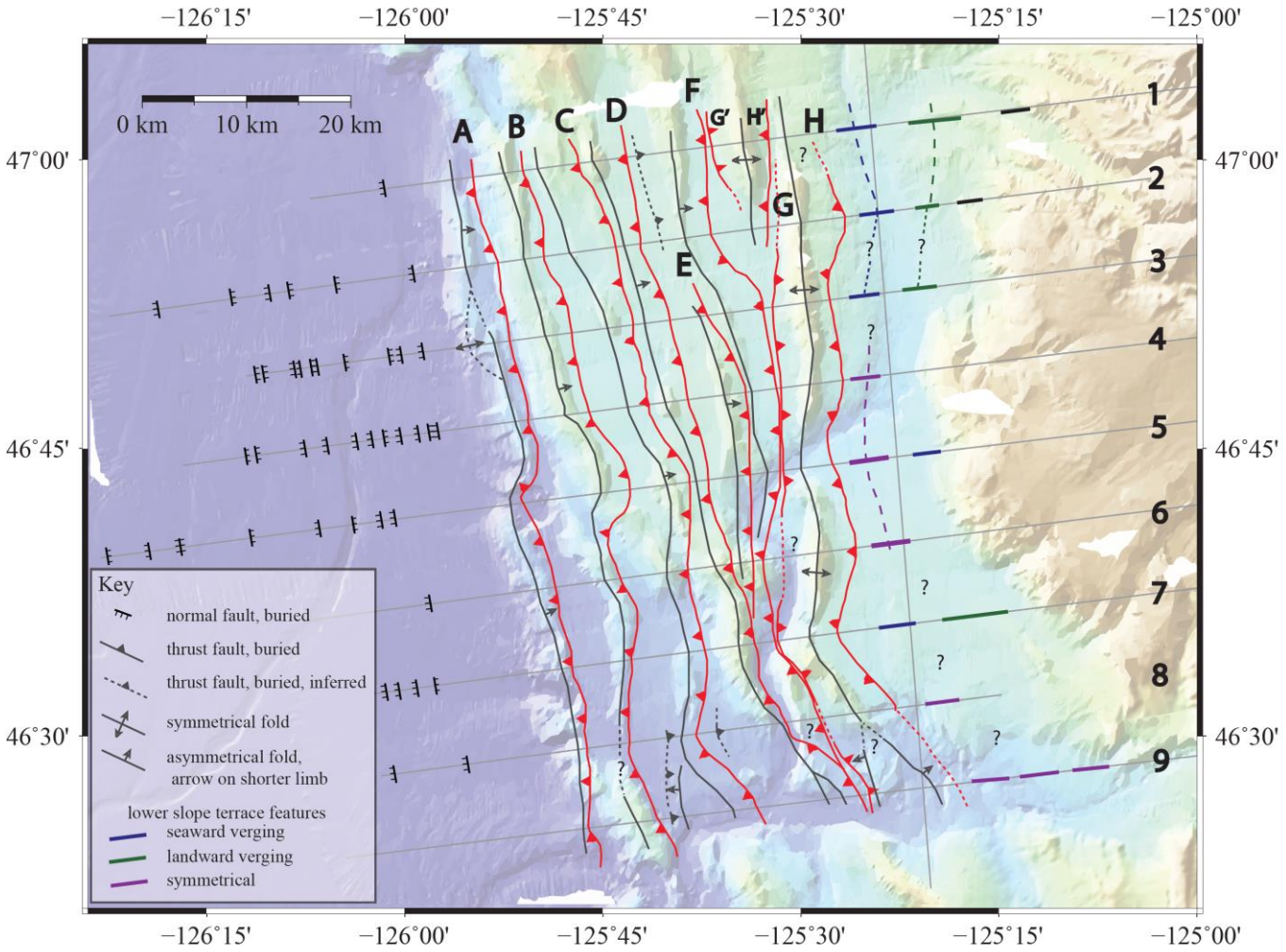

Figure 2.4: Simplified structural map of the COAST study area showing major thrust faults and fold axes, as well as the locations of deformation in the lower slope terrace and location of normal faults in the incoming sediment section. Faults and folds are labelled by letters used to refer to them throughout the paper, starting with frontal thrust A. Correlation between lines is done using bathymetry when crosslines are not available. Given the lack of bathymetric relief in the lower slope terrace, correlation between structures is difficult. The Quinault Ridge is located between faults G and H.

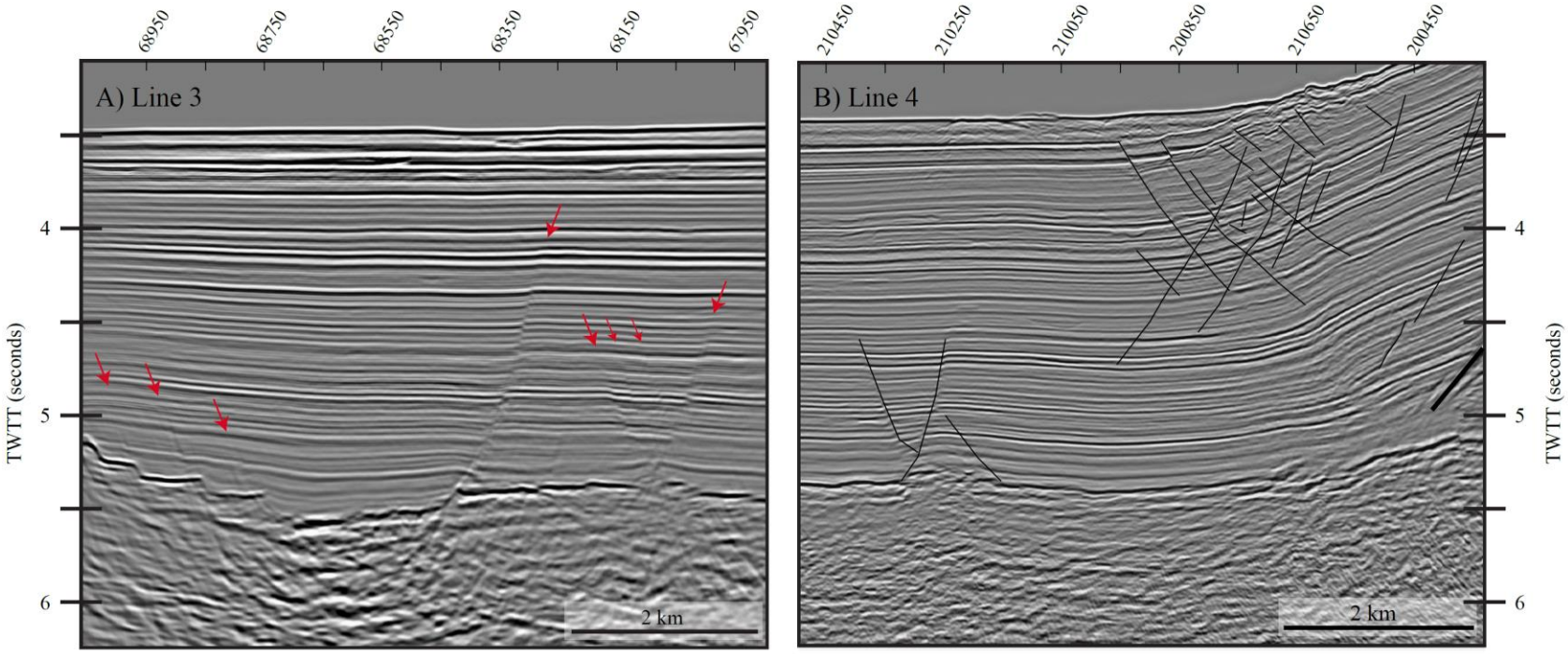

Figure 2.5: Incoming sediment section in A) line 3 and B) line 4. Red arrows on A) show the normal faults, some of which offset the acoustic basement reflector, at the base of the incoming sediment section, before it reaches the deformation front. Conjugate faults are interpreted on B) as the incoming section is incorporated into the outer wedge at the deformation front. Some smaller normal faults can still be seen between CMPs 210450 and 210250.

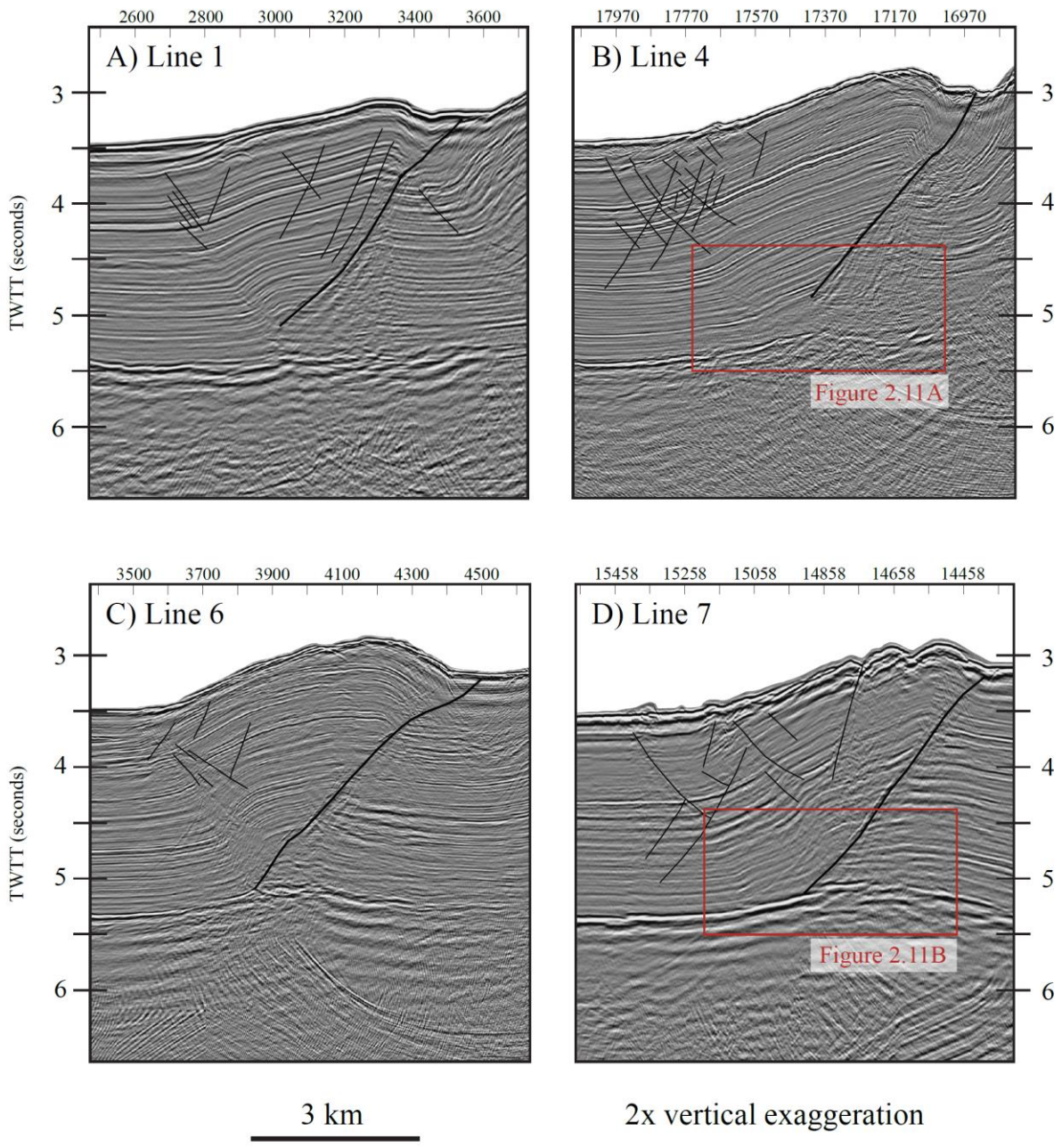

Figure 2.6: Frontal thrusts of A) line 1, B) line 4, C) line 6, and D) line 7. All show evidence of the conjugate faults found in the hinge zone. Lines 1 and 4 are northern lines, where the frontal thrust soles into an upper decollement in the sediment section. Lines 6 and 7 sole into the basal decollement, and the following thrust sheets are nor as deformed. In lines 1 and 4, however, tilting and deformation due to the second thrust sheet is visible almost immediately behind the frontal thrust. In B) a small fault scarp is seen where the frontal thrust displaces the seafloor. Red boxes show the location of Figure 2.11A and Figure 2.11B.

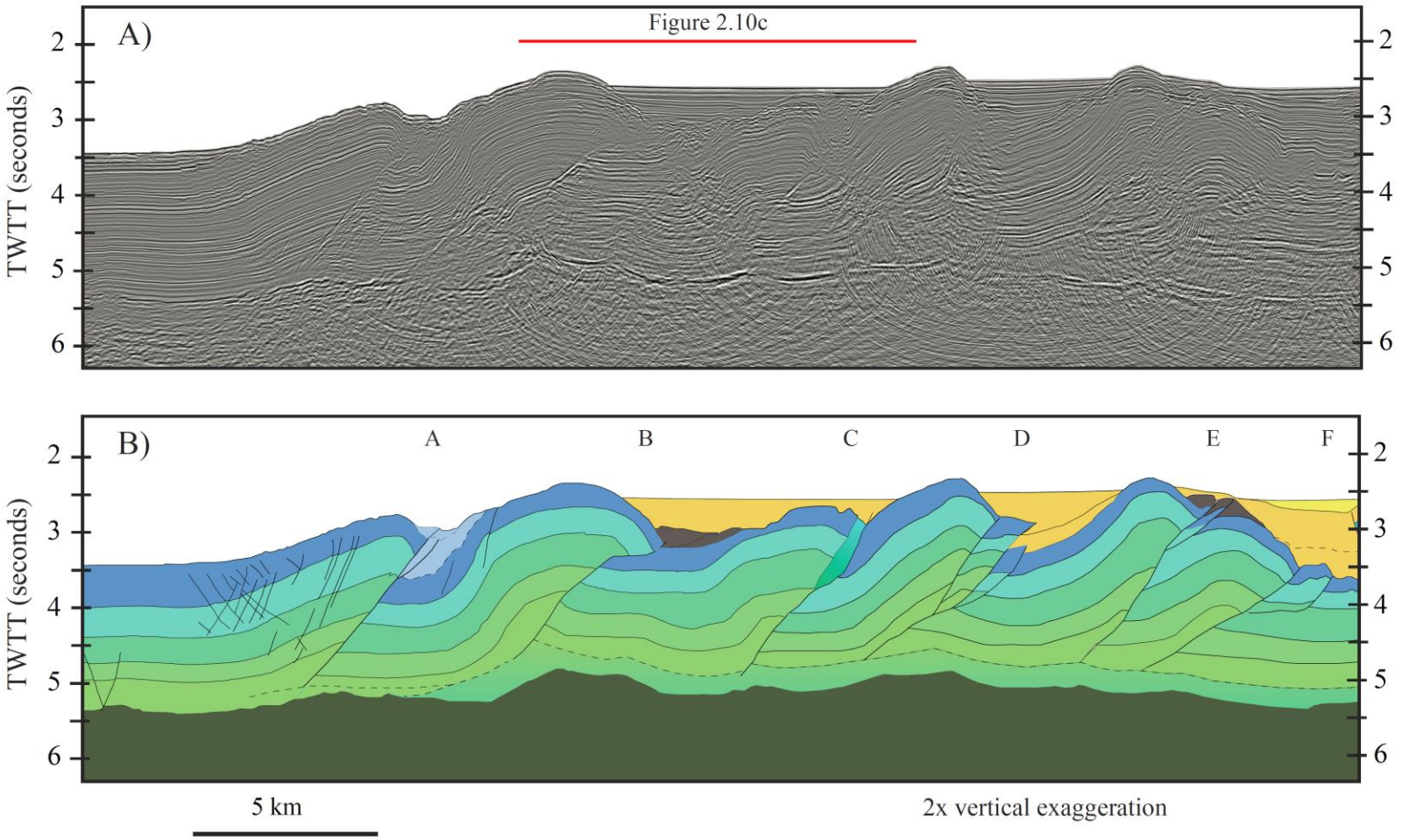

Figure 2.7: Simplified interpretation of Line 4; PSTM processing by GeoTrace. Horizons are interpreted to show general structure, with emphasis on the thrust faults. Faults sole into the upper decollement. Basins are shown in yellow, while gray sections are interpreted as chaotic deposits, possibly from the erosion of thrust sheets. Light blue is probably a combination of these slump deposits with some minor slope basin sedimentation, but is difficult to differentiate. Faults are labelled to correspond with Figure 2.4.

Figure 2.8, A and B:

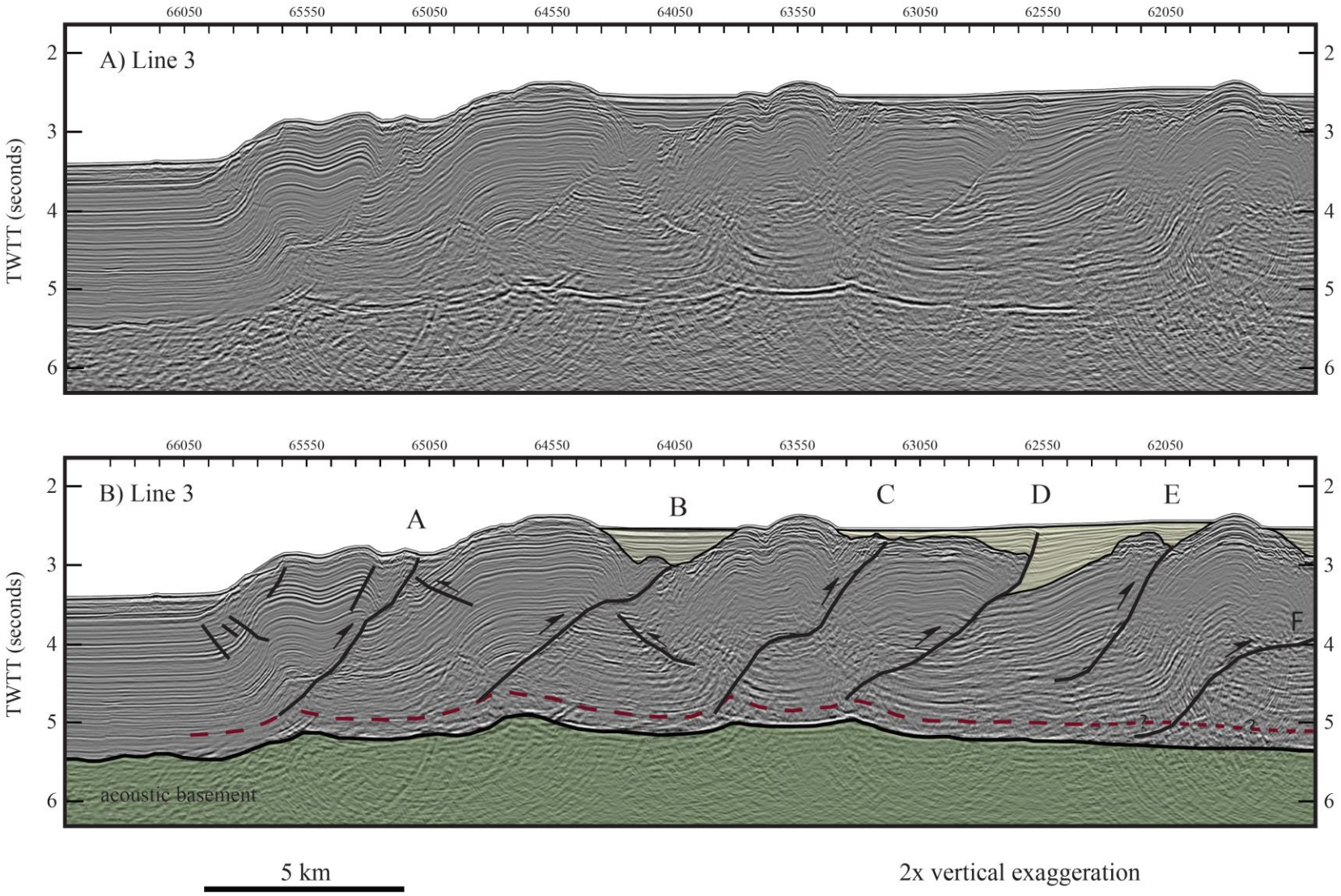

Figure 2.8, C and D:

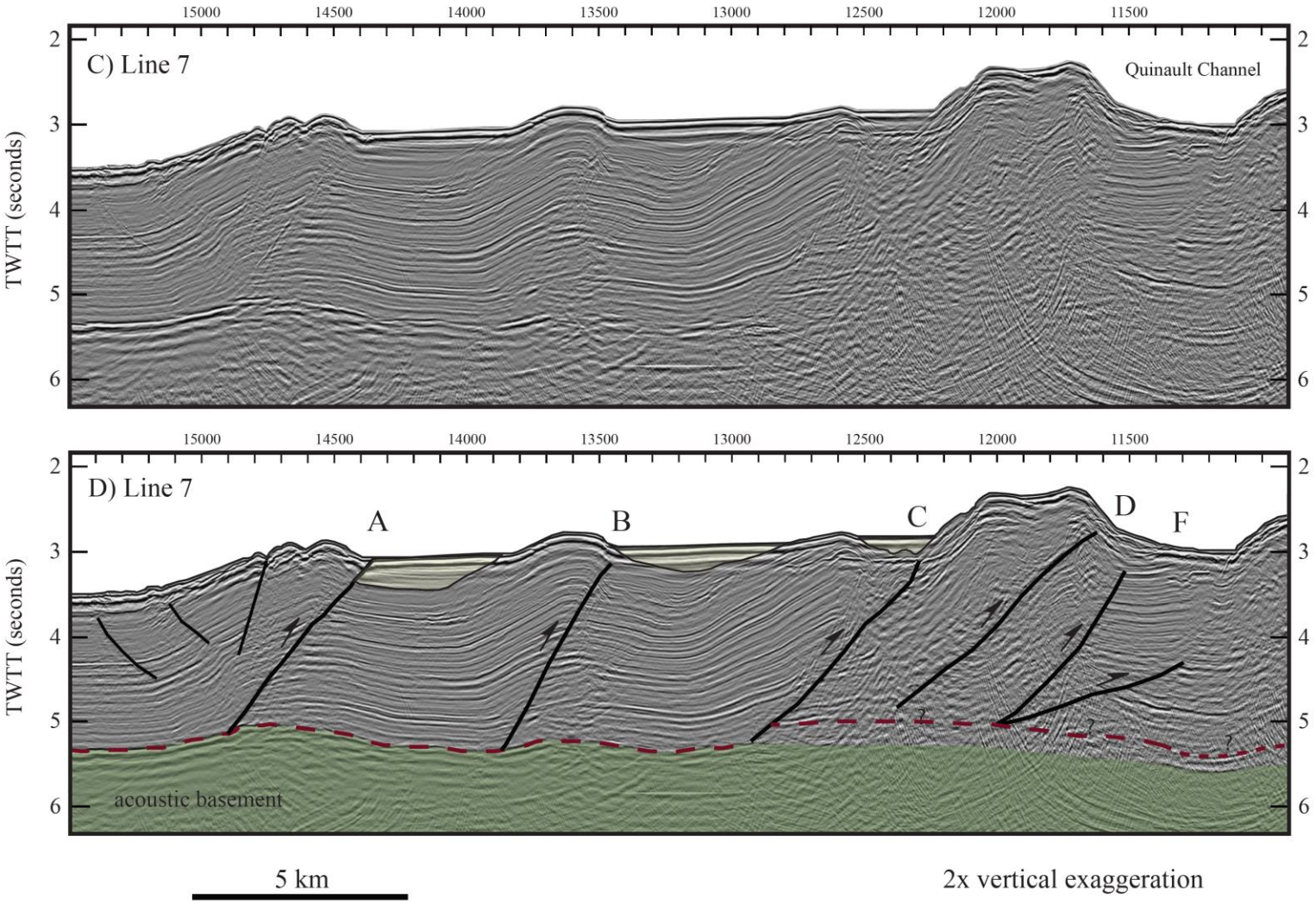

Figure 2.8: Uninterpreted sections (A, B) and the simplified interpretation (B, D) of the outer wedge of lines 3 and 7. Line 3 is an example of the northern style of deformation, with variable soling depths, as well as an underthrust section underlying the entire outer wedge. Faults in line 7 sole into the crust until fault C, at which point data quality complicates the interpretation of decollement level. The trace of the Quinault Channel can be seen in line 7. Slope basins are lightly shaded, and the decollement level is shown with the red dashed line. The underthrust sediment below Line 3, particularly beneath thrust sheets C and D, exhibits some acoustically blank characteristics, where reflectors are difficult to trace.

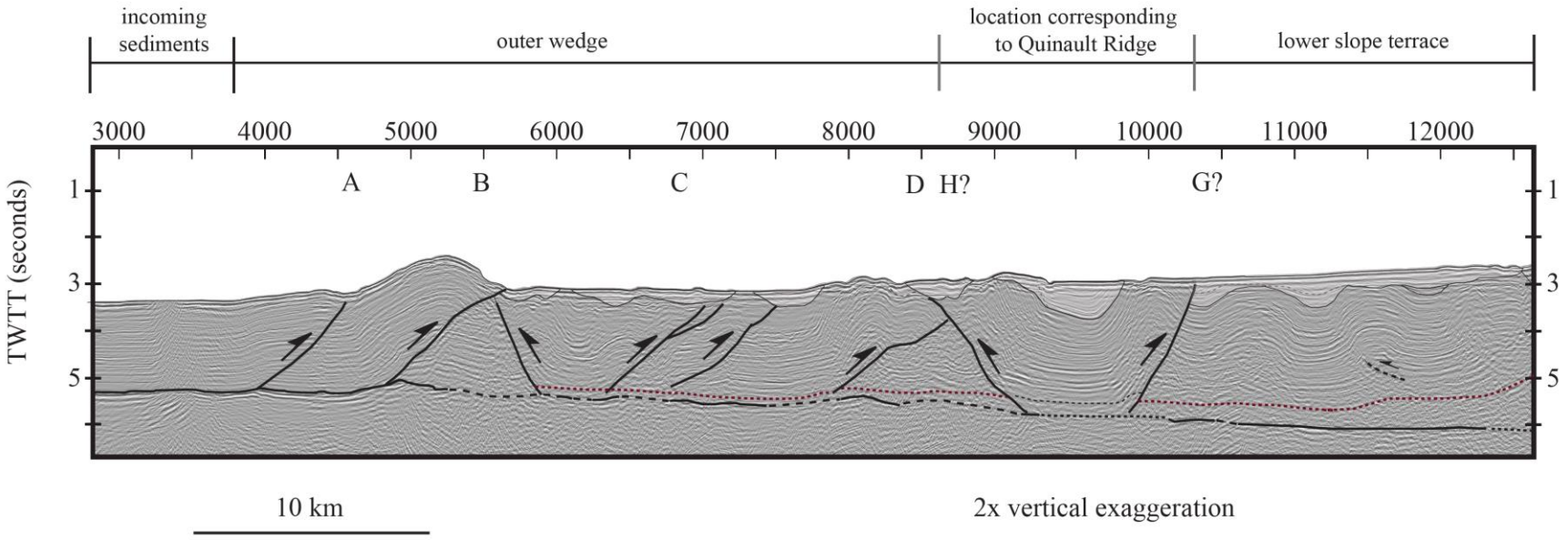

Figure 2.9: Simplified fault and basin interpretation of line 9. Line 9 contains doubly vergent thrust sheets, as well as variable fault soling depths and evidence of various stages of erosion and deposition. The frontal thrusts sole into the sediment-basement interface, but if underthrust sediment is present, it is not a thick layer, until the lower slope terrace, where distinct folding deformation can be seen. The doubly verging thrust sheet that corresponds spatially with the Quinault Ridge to the north is marked. Lighter gray areas indicate basins with supra-wedge sedimentation. The irregular shape of the thrust sheets below the basins from CMP ~5500 to 7000 are erosive surfaces.

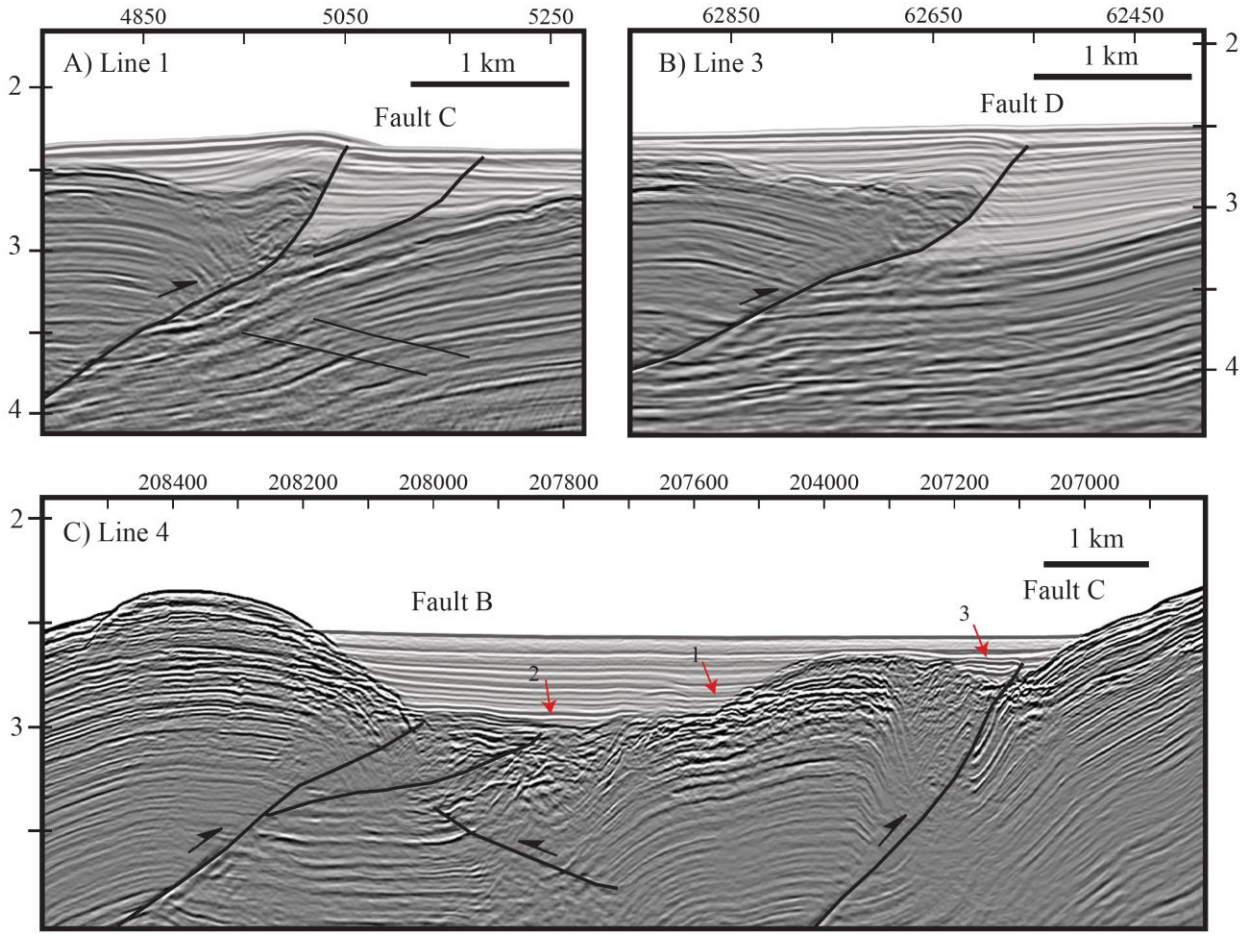

Figure 2.10: Slope basin deformation in A) Line 1, B) Line 3 and C) Line 4. Slope basin sediments are shown in a lighter gray. In A) fault C deforms the overlying sediments and deforms the seafloor. In B) fault D deforms the sediments but does not cut the seafloor. C) shows several characteristics seen in slope basins and over the top of buried thrusts. 1 marks the location of erosion over the top of a now buried thrust, which led to the deposition of chaotic slump deposits (2), which have now been partially deformed by fault B. 3 indicates where there has been minor deformation of the slope basin sediments from fault C, which is more typical of the slope basin deformation by the thrust faults seen in this study area. The deformation of these slope sediments indicates at least some out of sequence thrusting in the outer wedge.

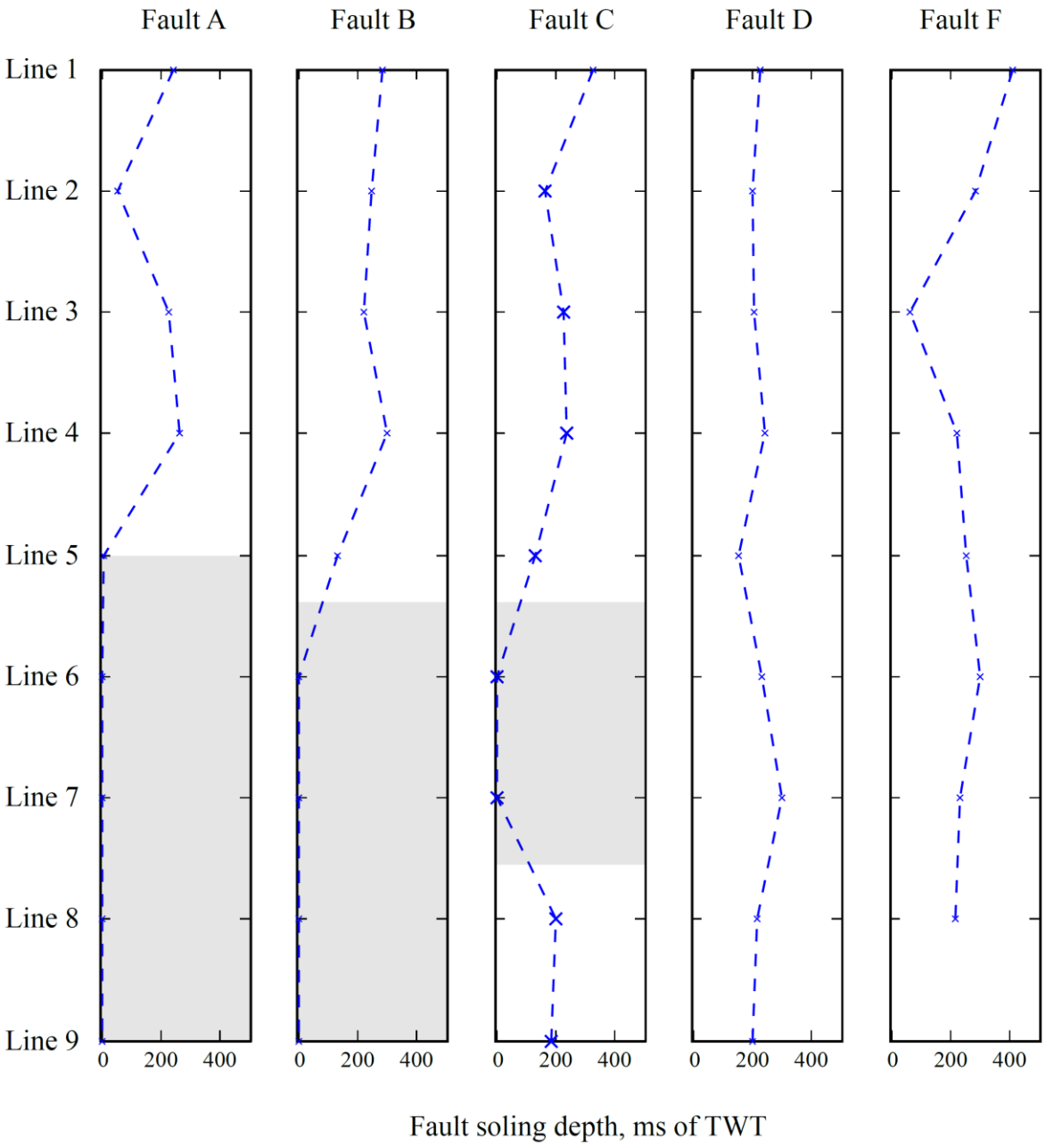

Figure 2.11: TWT to detachment for the outer wedge thrust faults A-D and F for each inline in the COAST survey. Fault E is not shown as it does not span the entire study area. Areas shaded in grey indicate locations where the basal detachment is active, as the faults sole into the basement, within seismic resolution. Elsewhere, the upper detachment is active. Fault F is not interpreted to extend to line 9, and thus does not have a data point there.

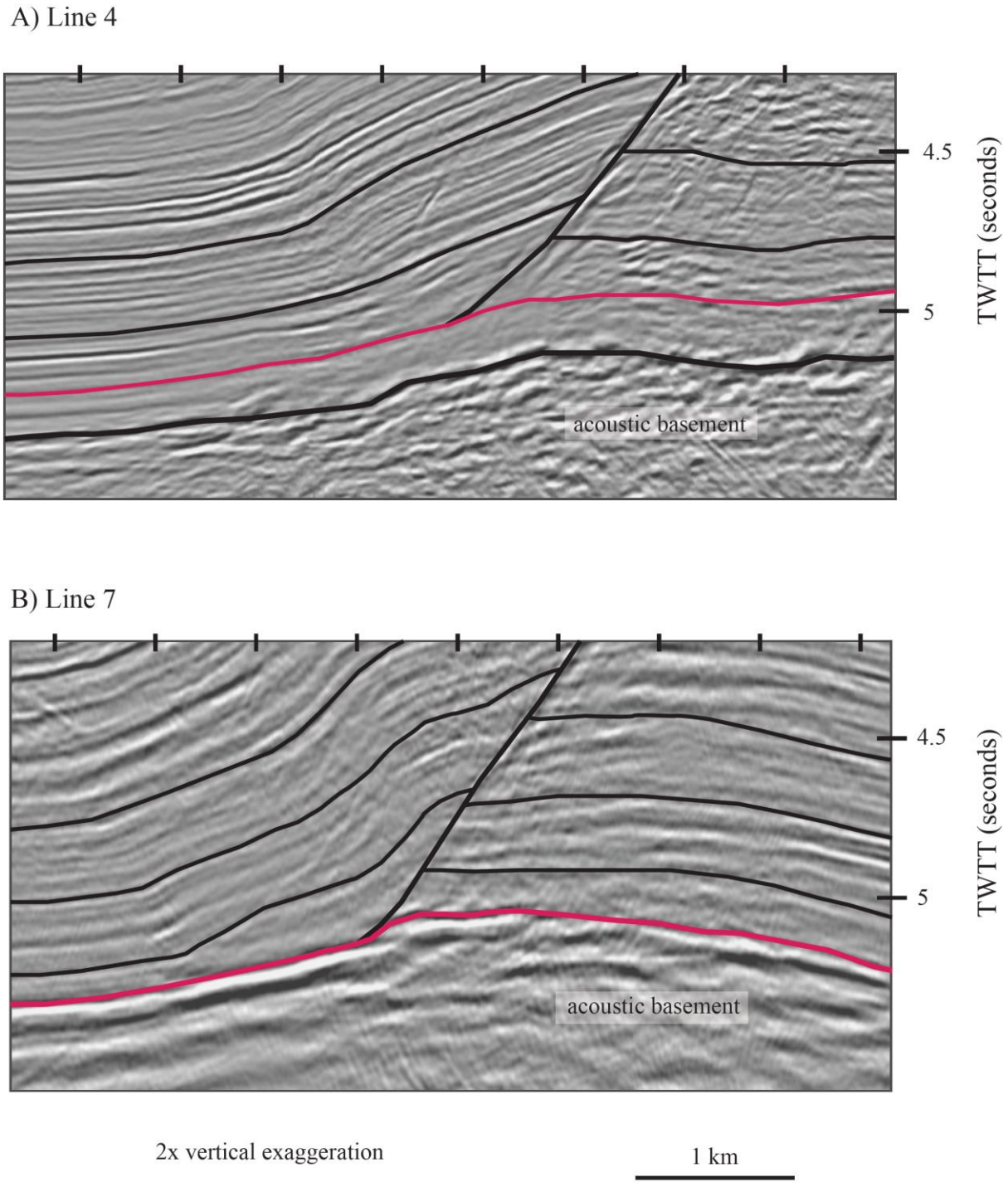

Figure 2.12: Comparison of the lowest section of the frontal thrust from A) Line 4, in the north, and B) Line 7, in the south. The decollement (and proto-decollement) are marked in red. In A), the frontal thrust soles into the sediment section above acoustic basement, into the upper decollement, while in line 7 (B), the basal decollement is active.

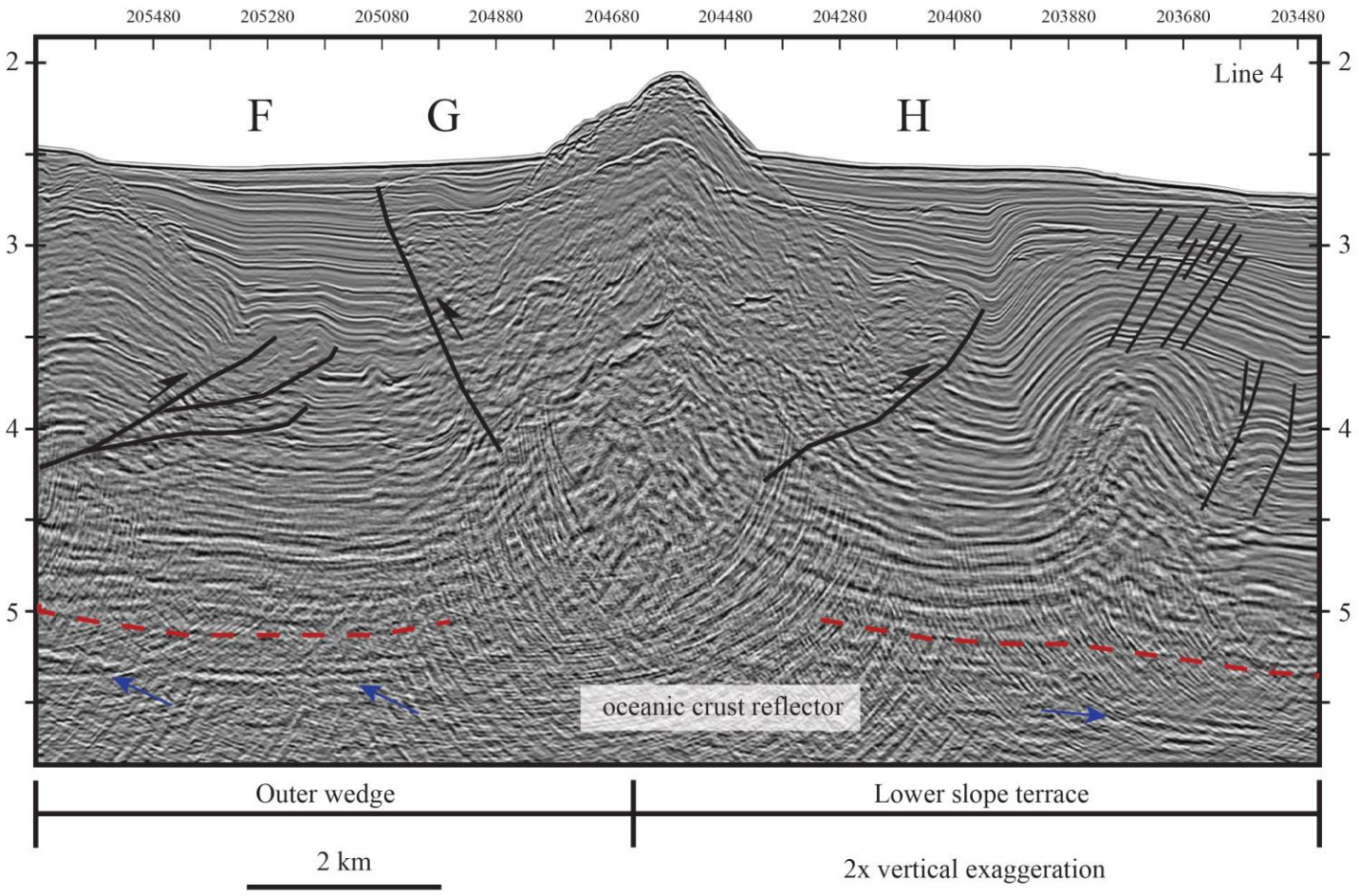

Figure 2.13: The symmetrical Quinault Ridge imaged in line 4, bordered by faults G and H. A strong BSR can be seen over the crest of the ridge, but internal reflectors are generally incoherent. From CMP 20980 to 203480, deformation of the lower slope terrace by another symmetrical feature can also be seen, along with attendant faults. Chaotic reflectors are only seen in the lower portions of the structure (~4.25 to 5 s), which would indicate that if there was any movement of fluidized mud, it did not disrupt the upper reflectors. The patchy nature of the oceanic crust can also be seen. Fault F can be seen deforming the lower sediment section on the lefthand side of the basin. The incoherent reflectors of the Quinault Ridge complicate the interpretation of faults G and H, but deformation of overlying basin sediments can be seen near CMPs 205080 and 204080. The decollement is shown in red, with blue arrows pointing to the locations where the oceanic crust reflector can be seen.

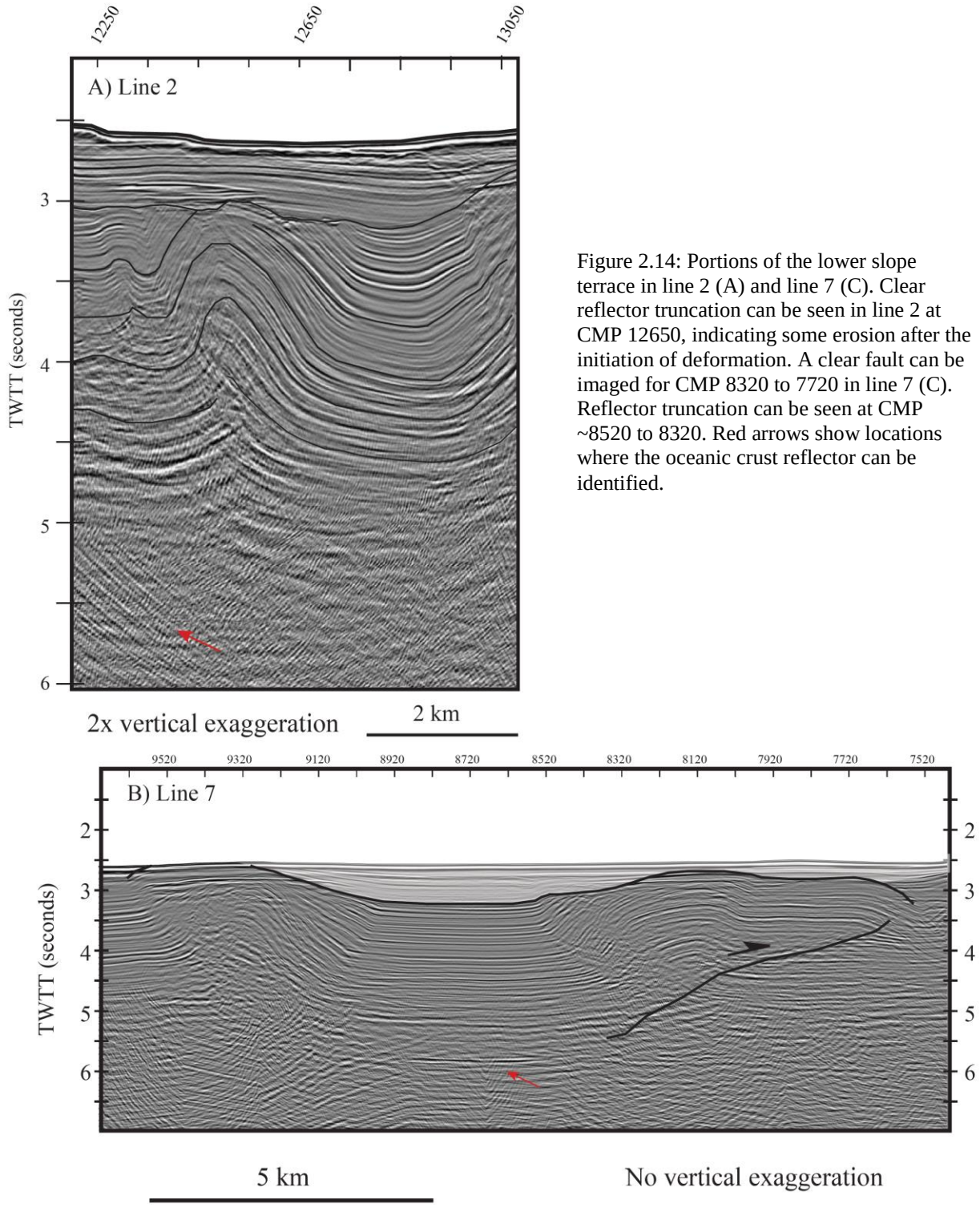

Figure 2.14: Portions of the lower slope terrace in line 2 (A) and line 7 (C). Clear reflector truncation can be seen in line 2 at CMP 12650, indicating some erosion after the initiation of deformation. A clear fault can be imaged for CMP 8320 to 7720 in line 7 (C). Reflector truncation can be seen at CMP ~8520 to 8320. Red arrows show locations where the oceanic crust reflector can be identified.

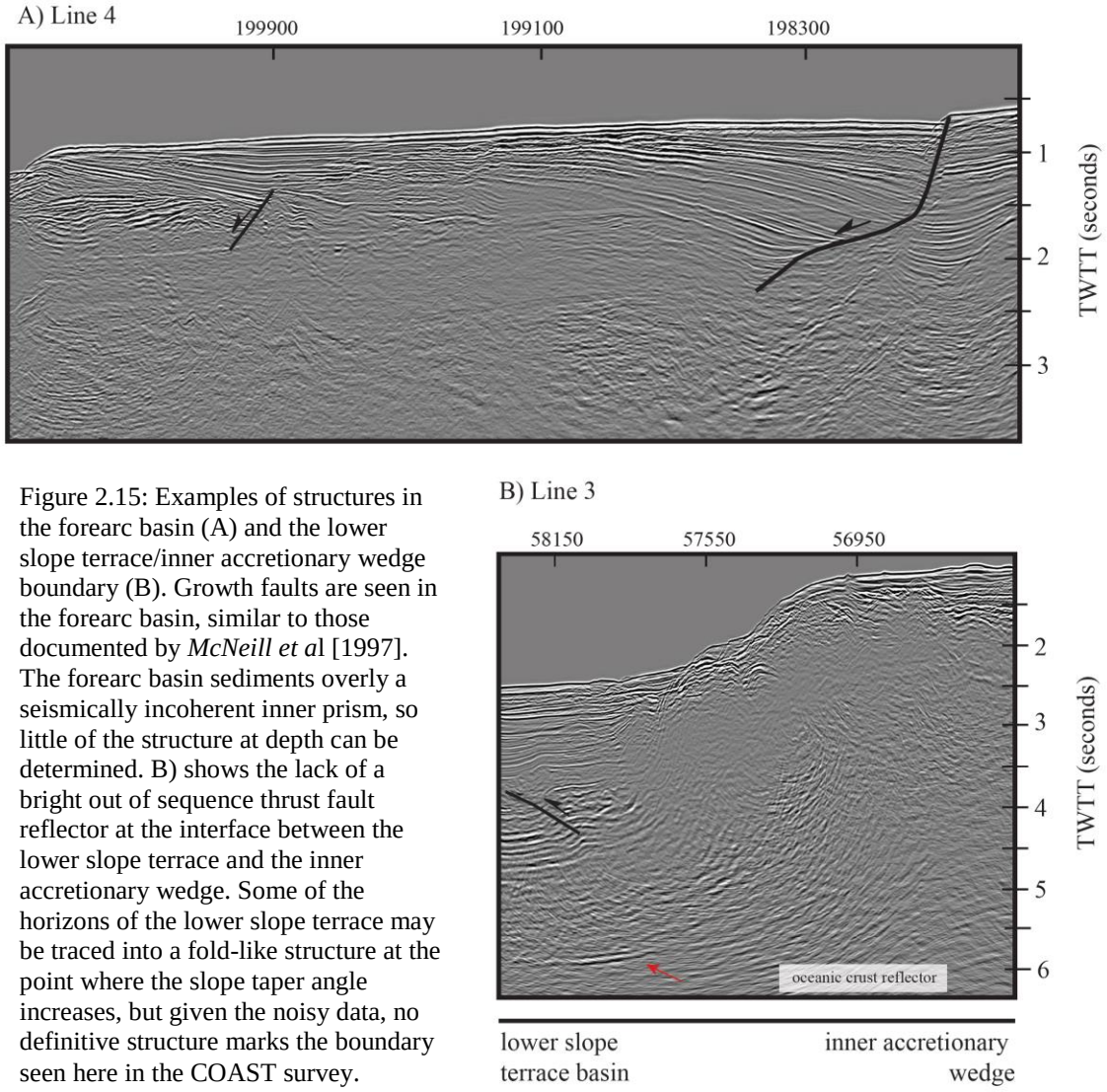

Figure 2.15: Examples of structures in the forearc basin (A) and the lower slope terrace/inner accretionary wedge boundary (B). Growth faults are seen in the forearc basin, similar to those documented by *McNeill et a*l [1997]. The forearc basin sediments overly a seismically incoherent inner prism, so little of the structure at depth can be determined. B) shows the lack of a bright out of sequence thrust fault reflector at the interface between the lower slope terrace and the inner accretionary wedge. Some of the horizons of the lower slope terrace may be traced into a fold-like structure at the point where the slope taper angle increases, but given the noisy data, no definitive structure marks the boundary seen here in the COAST survey.

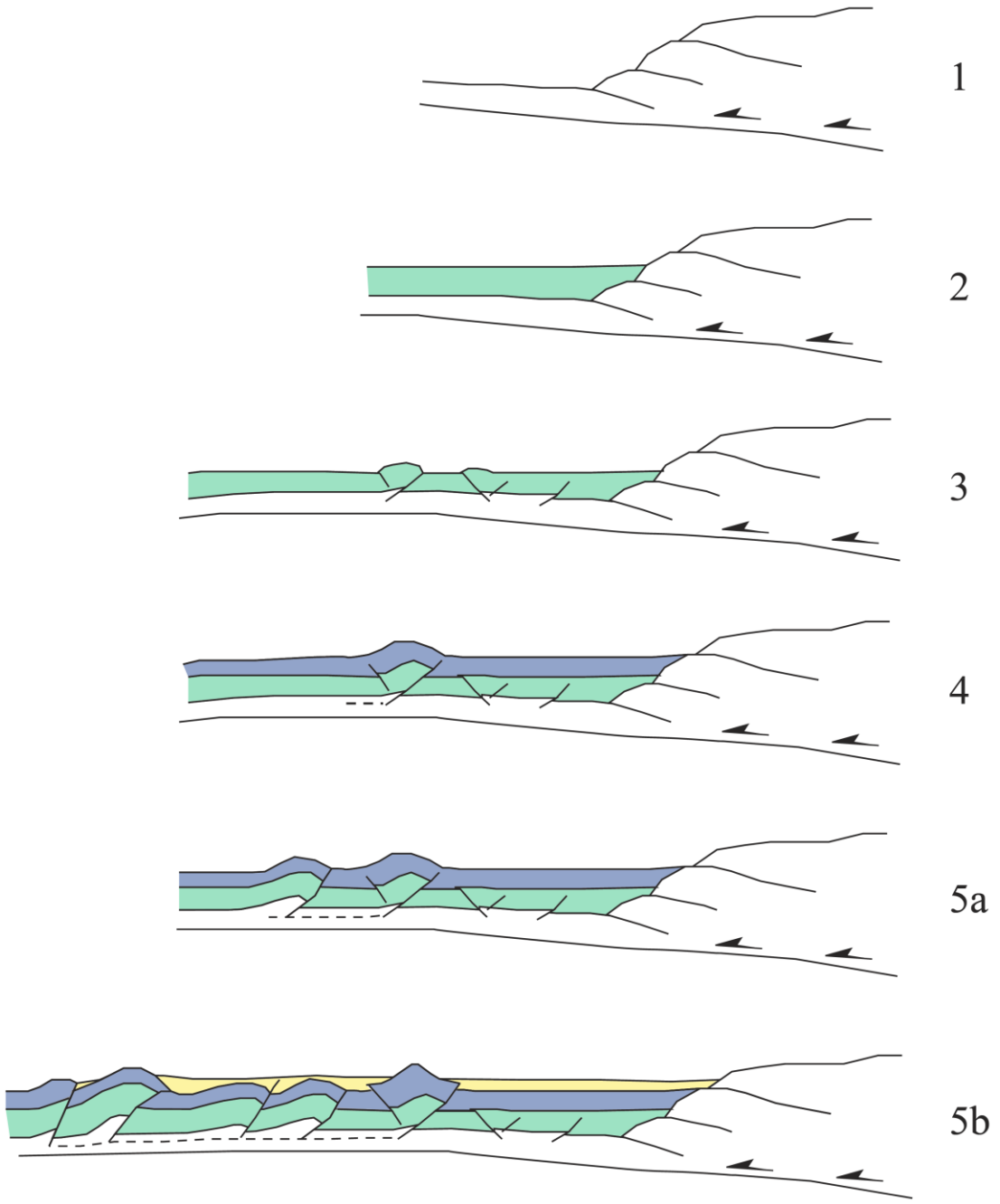

Figure 2.16: Proposed model for how supra-wedge sedimentation may influence development of the Cascadia margin structure. Step 1: Miocene accretionary prism, assumed to be seaward vergent. Step 2: Initial influx of sediment in the Pleistocene. Step 3: Incipient deformation, dormation of the décollement (dashed line); doubly vergent faulting in the lower slope terrace region. Step 4: Landward vergent fault of the proto-Quinault Ridge becomes the new frontal thrust. Steps 5 a and b: Wedge continues to develop as landward vergent, with continued supra-wedge sedimentation in basins, which may promote out of sequence fault activity.

3 Constraints on accretionary wedge porosity and pore fluid pressure from velocity models in the central Cascadia subduction zone

Abstract

In the central Cascadia subduction zone, the relative lack of interplate seismicity has made the definition of the upper limit of the locked zone difficult to resolve. Additionally, the central portion of the margin is characterized by a very low wedge taper angle and a landward vergent thrust belt, both of which have been attributed to low basal shear stress, possibly due to overpressure. Pore fluid pressure at depth in accretionary wedges is linked to structure as well as to the updip limit of the seismogenic zone beneath the wedge. In this study, porosity and pore pressure are estimated along three seismic reflection lines offshore Grays Harbor, Washington, using velocity models developed for pre-stack depth migration. No indication of strong overpressure or high excess pore pressure is seen within or below the outer wedge, with excess pore pressure <5 MPa, and overpressure ratios < 0.15. Excess pore pressure values are concentrated in the footwalls of thrust faults in the outer wedge, and in the incoming sediment section. The lack of pore pressure anomalies in the hanging walls and a decrease in excess pore pressure as sediments enter the outer wedge indicates that the wedge is draining efficiently, and may be mechanically strong. The entire interpreted underthrust sediment section (~500 m) is not overpressured, although mechanical properties of the sediments at depth or a seismically unresolvable layer of overpressure could contribute to low basal shear stress. The analysis presented here, although it cannot constrain the updip limit of the seismogenic zone, supports the presence of a strong, drained wedge, and does not preclude the potential of a weak base, both of which have been called upon to explain the low wedge taper angle and landward vergent faulting at Cascadia.

3.1 Introduction

The potential of subduction zones to rupture in large tsunamigenic megathrust earthquakes leads to significant interest in constraining the seismic hazard posed by these margins. The spatial extent of the seismogenic zone and the geometry and structure of the accretionary wedge are

influenced by pore pressure, material properties, and the relative strength of materials within and below the wedge. The updip limit of the locked seismogenic is correlated with the loss of elevated pore pressure in underthrust sediments [*Saffer and Tobin*, 2011]. Above the updip limit, excess pore pressure is also thought to contribute to the weakness of plate boundary fault zones found beneath the wedge, as well as the weakness of materials that make up the wedge itself (e.g. [*Hubbert and Rubey*, 1959b; *Suppe*, 2007]). Overpressure is not the only factor influencing seismic hazard in subduction zones. Material properties at depth and within the wedge can also impact the coseismic deformation of the wedge and the propagation of rupture, as well as the structures and wedge taper angle seen in the outer wedge (e.g [*Saffer and Bekins*, 2002; *Gulick et al.*, 2011; *Lotto et al.*, 2017]).

Based on critical wedge taper theory the geometry of accretionary wedges is linked to low basal shear strength of the underlying detachment and the strength of the material at the base of the wedge relative to the overriding material [*Hubbert and Rubey*, 1959c; *Davis et al.*, 1983]. Low basal shear stress can be caused by high pore fluid pressure in undrained underthrust sediment. Underthrust sediment is often assumed to be weaker and more fluid-rich, as there are fewer escape pathways for the fluids as they are subducted beneath the wedge [*Moore*, 1989; *Moore and Vrolijk*, 1992; *Saffer and Bekins*, 2002; *Gamage et al.*, 2011]. Low velocity anomalies at depth, sometimes associated with bright seismic reflectors, are often attributed to the presence of overpressured sediments in underthrust sections (e.g. [*Ranero et al.*, 2008; *Bangs et al.*, 2009; *Park et al.*, 2010]). Velocity models can be used to estimate porosity (e.g. [*Bangs et al.*, 1990; *Cochrane et al.*, 1994; *Adam et al.*, 2004; *Calahorrano et al.*, 2008; *Tsuji et al.*, 2008]) from empirically derived velocity-porosity relationships. This porosity can be used to estimate effective stress and pore fluid pressure at depth when compared to a lithostatic model, and thus

identify whether or not overpressure is present (e.g. [*Saffer*, 2003; *Tobin and Saffer*, 2009; *Kitajima and Saffer*, 2012; *Rowe et al.*, 2012]). However, deformation in the wedge can affect the fluid budget by either providing a path for fluids to drain, or by inhibiting fluid expulsion [*Saffer and Bekins*, 2002; *Screaton et al.*, 2009]. The type of deformation the wedge develops is determined not only by pore fluid pressure but by the intrinsic material properties of the sediments within the wedge.

The material properties of the outer wedge and extent of the locked zone beneath it can govern how far updip rupture will propagate and how much the wedge will deform coseismically, which in turn informs tsunami risk [*Wang and Tréhu*, 2016; *Lotto et al.*, 2017]. Previous large, devastating tsunamigenic earthquakes have been associated with slip near the toe of the accretionary wedge (e.g [*Gulick et al.*, 2011; *Ito et al.*, 2011; *Kodaira et al.*, 2012; *Yue et al.*, 2014]). During the 2004 M_w 9.1 Sumatra earthquake, the wedge is posited to have move coseismically as a whole due to the relative strength of overriding and basal materials, generating a large tsunami [*Frederik et al.*, 2015]. The frictional properties of the materials at the detachment below the wedge at both the Japan Trench and Sumatra are linked to the propagation of rupture through shallow sediments near the trench during the large 2011 M_w 9.0 and 2004 M_w 9.1 earthquakes at those margins [*Dean et al.*, 2010; *Gulick et al.*, 2011; *Chester et al.*, 2013]. Samples from the Japan Trench fault zone are mechanically weak and, despite exhibiting velocity-strengthening behavior, may have facilitated slip to the trench in the Tohoku earthquake, resulting in a tsunami [*Chester et al.*, 2013; *Ikari et al.*, 2015].

Determining a possible updip limit of locking is useful when assessing seismic hazard in the Cascadia margin area, as it can influence the potential for coseismic deformation of the wedge during a large subduction zone earthquake. The seismic hazard associated with the Cascadia

margin is high, as both the most populous cities and the capitols of British Columbia, Washington and Oregon are located near the coast (Figure 3.3.1). *Wang and Tréhu* [2016] describe several possible scenarios for coseismic deformation of the outer wedge that could be seen in Cascadia, similar to the Sumatra and Tohoku earthquakes. However, determining how the wedge would deform is complicated by the lack of recent seismicity and the atypical accretionary wedge structure observed in central Cascadia [*Wang and Tréhu*, 2016].

In this study, we present an analysis of velocity models used in pre-stack depth migration of active source seismic data at the Cascadia margin. Our goal is to analyze the porosity and pore fluid pressure estimated from velocity models and investigate the implications these results have for the conditions inside and below the outer wedge, the development of structure in the wedge, the identification of the updip limit of the seismogenic zone, and the potential for slip beneath the outer wedge.

3.2 Geologic setting and seismic history

At the Cascadia margin, which extends from northern California to British Columbia, the Juan de Fuca, Gorda, and Explorer plates subduct beneath North America at a rate of ~36 to 40 mm/year [*DeMets et al.*, 2010] (Figure 3.3.1). Unlike other more seismically active subduction zones, Cascadia exhibits a near total lack of interplate seismicity [*Wang et al.*, 2003; *Tréhu et al.*, 2008; *Williams et al.*, 2011]. Although there have been no recent earthquakes, turbidite paleoseismology and changes in the level of the coastline show that the margin has ruptured in large magnitude earthquakes in the past [*Adams*, 1990; *Atwater and Yamaguchi*, 1991; *Goldfinger et al.*, 2003, 2008; *Witter et al.*, 2003; *Goldfinger*, 2011; *Atwater et al.*, 2014].

The last known large subduction zone earthquake occurred on 26 January 1700 and is believed to have been approximately magnitude 9, based on the evidence seen in studies of ghost forests and records of orphan tsunami in Japan [*Satake et al.,* 1996; *Benson et al.,* 2001]. Thirteen turbidites identified in sediment cores and linked to large earthquakes have occurred since a volcanic eruption dated at ~7500 years [*Goldfinger et al.,* 2003]. This study, coupled with other paleoseismological studies, give a recurrence interval of between ~350-600 years along the Cascadia margin [*Adams,* 1990; *Goldfinger et al.,* 2016]. There is variation in recurrence interval along the margin with a shorter interval between earthquakes at the southern end of the margin compared to the northern end [*Wang et al.,* 2003; *Goldfinger et al.,* 2016]. Investigation of tidal forests on the coast of Washington and Oregon indicates that many of these large earthquakes dropped the coastline level and were accompanied by large tsunamis [*Atwater and Yamaguchi*, 1991; *Benson et al.,* 2001; *Atwater et al.,* 2014].

Episodic tremor and slip has been observed at depths of 30-40 km in the subduction zone at what is inferred to be the transition zone at the downdip limit of the seismogenic zone [*Dragert et al.,* 2001, 2004, *Ghosh et al.,* 2009, 2010; *Wech et al.,* 2009; *Dragert and Wang,* 2011]. These slow slip events also migrate at depth along the plate boundary [*Ghosh et al.,* 2010; *Dragert and Wang*, 2011]. *Brudzinski and Allen* [2007] separate the Cascadia margin into three sections based on the recurrence time of their episodic tremor and slip events: the Wrangellia zone, north of 47 degrees north, with a recurrence interval of 14 ± 2 months, the Siletzia zone, between 47 and 43 degrees north, with a recurrence interval of 19 ± 4 months, and the Klamath zone south of 43 degrees north, with a recurrence interval of 10 ± 2 months.

Due to the lack of contemporary interplate earthquake activity, the spatial extent of the seismogenic zone is difficult to determine. Geodetic and thermal models indicate that there is a

degree of locking and stress buildup along the plate boundary with the widest portion of the locked zone located in the central portion of the subduction zone and narrowing along the edges. [*Hyndman and Wang*, 1995; *Oleskevitch et al.*, 1999; *Wang et al.*, 2003; *McCaffrey et al.*, 2007; *Calkins et al.*, 2011; *Schmalzle et al.*, 2014]. The Juan de Fuca plate is relatively young (<10 Ma) and hot, and subducts at a shallow angle, making the potential locked zone broader than expected for a colder, more steeply dipping plate [*Dragert et al.*, 1994; *Nicholson et al.*, 2005; *Calkins et al.*, 2011]. Geodetic models suggest the locked seismogenic zone extends into the offshore portions of Cascadia, under the accretionary wedge [*McCaffrey et al.*, 2000; *Nedimovic et al.*, 2003; *Wang et al.*, 2012]. However, the amount of locking is not constant along the margin, but varies from north to south. Recent models show the potential the locking may not be as strong beneath the central Cascadia margin as to the north and the south [*Mccaffrey et al.*, 2013; *Schmalzle et al.*, 2014] and the amount of coastal uplift during past earthquakes may have been relatively low [*McAdoo and Watts*, 2004]. Central Cascadia also has a small number of recorded slow slip events, and it has been posited that it may be creeping, possibly due to high pore fluid pressure along the plate-boundary fault [*Schmalzle et al.*, 2014].

3.3 Accretionary wedge structure

The study area for this analysis is within the central section of the Cascadia subduction margin, which has unique structural features. The northern and southern sections of the margin have predominantly seaward vergent faults but the central portion, offshore Washington and northern Oregon, is dominated by landward vergent faults which is atypical for accretionary wedges (e.g. [*Silver*, 1972; *MacKay*, 1995; *Flueh et al.*, 1998; *Fisher et al.*, 1999; *Adam et al.*, 2004]). Input to the trench is a thick sedimentary package, mostly deposited rapidly during the Pleistocene

[*Griggs et al.*, 1969; *Griggs and Kulm*, 1970; *Barnard*, 1978; *Underwood et al.*, 2005]. The upper sediments are sandier, whereas the lowermost >600 m of the section is more clay-rich [*Kulm et al.*, 1973b]. The active source seismic data used as part of this study is located wholly in the landward vergent zone, offshore Grays Harbor, Washington.

The outer wedge of the accretionary wedge consists of a large fold and thrust belt with predominantly landward vergent faults, a low wedge taper angle, and a broad, relatively undeformed basin termed the lower slope terrace (Figure 3.3.2a). Analysis of fault soling and structure indicates that the majority or all of the sediment is accreting with a small (~500m thick) underthrust section identified in some lines (Figure 3.3.2b,c). A higher detachment is present, generally in the more northern lines, but clear fault soling into the oceanic crust in those lines and in southern lines indicates a basement detachment is active throughout the survey. These interpretations are broadly consistent with earlier work done in central Cascadia (e.g. [*MacKay*, 1995; *Flueh et al.*, 1998; *Fisher et al.*, 1999; *Gerdom et al.*, 2000; *Gutscher et al.*, 2001; *Adam et al.*, 2004]), but do highlight the variable nature of the detachment and the amount of sediment that is underthrust.

Thrust fault spacing and detachment show some spatial differences, with more internally deformed thrust sheets generally soling into an upper detachment in the northern portion of the survey, and less deformed thrust sheets soling into acoustic basement in the southern lines [Webb, Chapter 2]. Structural interpretation has identified some out of sequence thrust faulting and buried structures in the lower slope terrace show evidence of reactivation. The outer wedge and the lower slope terrace are separated by a roughly symmetrical feature first identified in bathymetry by *Barnard* [1978] and named the Quinault Ridge. The interior of the structure is

generally seismically incoherent although it is bounded by faults that appear to have been recently active.

Both the low taper angle and landward vergent faulting seen in Cascadia have been attributed to very low basal shear stress beneath the wedge. An overpressure ratio (the ratio of pore fluid pressure to lithostatic pressure) of 0.9 at depth has been estimated from the low taper angle [*Davis et al.*, 1983]. High overpressure resulting in a weak basal layer, possibly aided by material properties, has also been cited as a cause for landward vergent faulting in Cascadia and Sumatra [*MacKay,* 1995; *Flueh et al.*, 1998; *Gutscher et al.*, 2001; *Frederik et al.*, 2015]. Rapid sedimentation on top of the wedge in the Pleistocene is also thought to have contributed to the deformation seen here, possibly by forming the lower slope terrace due to a step out of the deformation front, increasing overpressure at the base of the sediment section, or by allowing the formation of landward vergent faults similar to those seen in numerical and analog models [*Storti and Mcclay,* 1995; *Fisher et al.*, 1999; *Adam et al.*, 2004; *Simpson,* 2010; *Mannu et al.*, 2017]. Results from these models also suggest that the wedge taper angle may be due to the high rates of sedimentation rather than solely due to the conditions at the base of the wedge that would influence calculations of the overpressure ratio [*Simpson,* 2010].

3.4 Data

3.4.1 Drilling Data

The Cascadia margin has been the focus of one Deep Sea Drilling Program (DSDP) and one Ocean Drilling Program (ODP) expedition. DSDP Leg 18 drilled three sites offshore Oregon: site 174 in the incoming sediment section, site 175 in the lower slope offshore Oregon, and site 176 on the continental shelf [*Kulm et al.*, 1973a]. ODP Leg 146 drilled site 888 in the incoming

sediments, sites 889 and 890 offshore Vancouver, and sites 891 and 892 on the accretionary wedge offshore Oregon [*Westbrook et al.,* 1994]. Measurements taken on samples from these expeditions have been used to calibrate porosity-velocity relationships for Cascadia, as well as to estimate fluid pressure at depth [*Tobin et al.,* 1993; *Jarrard et al.*, 1995; *Jarrard*, 1997]. Although there is no core or log data available within this study area, there is some data on the properties of the material entering the subduction zone and becoming part of the accretionary wedge.

The incoming sediment section sampled at site 174 consisted of a 284 meter interval of Pleistocene turbidites of the distal Astoria Fan [*Kulm et al.,* 1973b]. Underlying these more sand-rich layers is ~600 m of Plio-Pleistocene age silty clays and silts, also identified as turbidite deposits, albeit much finer grained with increased carbonate content [*Kulm et al.,* 1973b]. Site 175 sampled two units between the frontal and second thrust of the outer wedge offshore Oregon. The upper unit consisted of 120 m of Pleistocene silty clay with some fine sand layers, while the underlying unit also consisted of Pleistocene age silty clay with some increased carbonate [*Kulm et al.*, 1973c]. Although the incoming sections are far from the study area, we assume that the general stratigraphy is similar—that is, a section of more clay-rich Pliocene and early Pleistocene sediments overlain by sandier fan deposits.

3.4.2 Seismic Data

The seismic data used in this study was collected as part of the Cascadia Open Access Seismic Transect (COAST) cruise on the *Marcus G. Langseth* in July 2012 (Figure 3.3.1b) [*Holbrook et al.*, 2012]. The data collected includes nine trench-perpendicular and two trench-parallel active source seismic reflection lines as well as high resolution multibeam bathymetry. Four strings of 9 airguns and an 8 km long streamer with 636 geophone channels spaced 12.5 meters apart were

used to collect data at a sample rate of 2 ms. For lines 2, 3A, 4, 6, 8, 9A, 9C, and 10 the streamer tow depth was 9 m, and for lines 1, 3, 5, 7, 9, and 11 the tow depth was 15 m. Equipment failure and the presence of marine mammals led to some portions of the survey being collected with only a mitigation gun source or no data being collected at all. Areas of variable data quality can be seen in the stacked lines [*Holbrook et al.*, 2012]. Data from lines 3, 4, and 5 are used in this study.

Shipboard stacked time migrated lines are available for interpretation, as are commercially migrated time domain lines provided by GeoTrace for lines 3 and 4. These two lines have undergone proprietary multiple suppression processes and give a clearer image. The time stacks, their velocity models, and the time-migrated gathers were made available by GeoTrace.

3.5 Pre-stack depth migration processing

A subset of the lines from the COAST cruise are available in the depth domain as well as the time domain. The two GeoTrace lines were scaled into depth using a time-depth conversion with the two velocity models that GeoTrace provided. These are used primarily as a guide for future velocity model adjustment and processing. Some of the lines have been migrated into depth at the University of Wyoming and the University of Wisconsin using three methods.

All of the line gathers have undergone initial pre-processing and multiple suppression in preparation for pre-stack depth migration following a protocol established by collaborators at the University of Wyoming [*Everson*, 2014]. Lines were initially sorted into CMP gathers, and edited to remove bad traces, of which there were several mostly due to mechanical problems encountered during the survey collection. The seafloor multiple is a strong signal throughout the

dataset, and is produced when energy reflected off the seafloor from the initial shot returns to the surface, bounces off the sea surface and is directed downward again and reflects from the seafloor again. In much of the COAST survey, the arrival of the seafloor multiple coincides with the arrival of a signal from the basement interface, making identification and interpretation of deeper structures more challenging. In an attempt to mitigate the effect of the multiple, a workflow designed for use on prior data collected on the *Marcus G. Langseth* was employed [*Lester and McIntosh*, 2012; *Everson*, 2014]. This involved surface-related multiple attenuation as well as radon transform multiple attenuation. Gathers were also filtered to remove noise [*Everson*, 2014].

Initially, two methods of pre-stack depth migration were performed: an iterative picking process based on velocity residual moveout and full waveform inversion [*Everson*, 2014; *Fortin*, 2015]. Lines 3, 4, 5, and 6 underwent the residual moveout process, while lines 5 and 9 underwent inversion. The velocity model for line 4 was used as a starting point for the horizon-based tomography on that line that was performed at the University of Wisconsin.

Horizon-based tomography incorporated geological features of the lines to refine the velocity models with a focus on improving imaging. Initial velocity values were taken from the PSDM models provided by University of Wyoming colleagues. Horizons were interpreted on the lines and semblance was calculated from the data, allowing for refinement of the picked velocities. Five formations, along with the seafloor, oceanic crust, and model base, were used to construct the model. Each horizon's velocity values were used as a base to that formation, which graded into the velocity values of the ones above it. Lateral and vertical smoothing was applied as unsmoothed models caused artefacts in the image from abrupt changes in the velocity values at depth. The velocities were assumed to be increasing downward through the section, although

some models were run where a low velocity zone was inserted below the wedge to gauge the effect on the imaging and migration. The insertion of low velocity values below the wedge did not appear to alter the resultant image, although the lack of a consistent identifiable oceanic crust reflector below portions of the wedge complicated the analysis of whether the image changed. In lower sections of the wedge the uncertainty in velocity values is approximately 10% as changes of more than that amount began significantly altering the location of migrated reflectors. Estimates of velocity in the inner accretionary wedge cannot be verified since there are no coherent reflectors at depth to flatten in the gathers.

The velocity models derived for Cascadia have relatively high velocity values near the base of the wedge, generally greater than 4000 m/s above the oceanic crust (Figure 3.3.3a, above the shaded oceanic crust, generally between 0 and 30 km from the deformation front). There are no large visible velocity inversions below the wedge although small localized inversions can be seen below thrust faults (e.g. Figure 3.3.3, between 10 to 30 meters behind the deformation front). Velocity values below the wedge are higher than those estimated for the Muroto Transect of the Nankai Trough, which range between 2300 and 2500 in the underthrust sediment section [*Costa Pisani et al.,* 2005]. At the Kumano Basin region of the Nankai Trough, the velocities directly above the oceanic crust reflector in the wedge are between 3500 m/s and 4000 m/s [*Park et al.*, 2010]. Velocities are also higher (~4000 m/s) below the wedge in Sumatra, which is also a heavily sedimented margin [*Gulick et al.,* 2011].

Previous work done on the incoming sediment section offshore Oregon shows similar velocity values in the incoming section [*Cochrane et al.*, 1994; *MacKay et al.*, 1995]. *Cochrane et al.* [1994] report a velocity decrease in the sediment below the proto-décollement in a seaward

vergent section of the margin. A velocity increase is documented by *MacKay et al.* [1995] in the lowermost layers as they are incorporated into the frontal landward vergent thrust.

3.6 Methods and calculation of excess pore fluid pressure

We use the velocity models from pre-stack depth migrations to estimate porosity, and thus effective stress and overpressure ratio in the outer wedge. The calculations were completed for three lines: line 3 (one model from *Everson* [2014]), line 4 (one model from *Everson* [2014], one from horizon-based tomography) and line 5 (one model from *Everson* [2014], one inversion-based model from *Fortin* [2015]).

Empirical velocity-porosity relationships have been derived for a variety of locations and sediments. *Erickson and Jarrard* [1998] used data from the Amazon fan to develop two least squares fits—one for sediment that is normally compacting:

$$V_p = 0.739 + 0.552\phi + \frac{0.305}{(\phi + 0.13)^2 + 0.0725} + 0.61(v_{sh}\text{-}1.123)[X_1 - |X_1|] \qquad 6.1$$

$$X_1 = \tanh[40(\phi\text{-}0.31)] \qquad 6.2$$

and another for sediment that experiences high compaction in its early history:

$$V_p = 1.11 + 0.178\phi + \frac{0.305}{(\phi + 0.135)^2 + 0.0775} + 0.61(v_{sh} - 1.123)[X_1 - |X_1|] \qquad 6.3$$

$$X_1 = \tanh[20(\phi - 0.39)] \qquad 6.4$$

The least squares fit relies on certain parameters, usually derived from logging data. The numbers are empirically derived constants and v_{sh} is estimated from the gamma ray as a proxy for the amount of shale (or clay minerals) present in the section. The 0.31 and 0.39 in the X_1 term are referred to as the "critical porosity". *Hoffman and Tobin* [2004] used the same least squares method to fit core and log data from the incoming sediment section at the Muroto Transect, offshore Japan:

$$V_p = A + B\phi + \frac{0.305}{\left[(\phi + C)^2 + \frac{0.305}{1.51 - A - B} - C^2 - 2C - 1\right]} + 0.61(v_{sh} - 1.123)[X_m] \qquad 6.5$$

$$X_m = \tanh\left[40\left(\phi - \phi_c\right)\right] - |\tanh[40\left(\phi - \phi_c\right)]| \qquad 6.6$$

To fit the Muroto Transect data, the critical porosity, ϕ_c, is fixed at 29.5 and the v_{sh} at 1.057. Both the *Erickson and Jarrard* [1998] and the *Hoffman and Tobin* [2004] curves have two parts, assuming different compaction trends above and below the critical porosity. Other velocity-

porosity relationships assume only normal compaction such as the *Hyndman et al* [1993] curve, also derived for sediments offshore Japan. The fit is a simpler polynomial curve:

$$\phi = -1.180 + 8.607\left(\frac{1}{V_p}\right) - 17.89\left(\frac{1}{V_p}\right)^2 + 13.94\left(\frac{1}{V_p}\right)^3 \quad 6.7$$

Drilling data have been used to calibrate empirical curves to specific areas, including Alaska and Cascadia [*Jarrard et al.*, 1995; *von Huene et al.*, 1998]. Cascadia data were fit with two curves, one for unfractured samples and the other for fractured samples [*Jarrard et al.*, 1995; *Jarrard*, 1997]:

$$V_p = 3.48 - 5.42\phi + 3.69\phi^2 \quad 6.8$$

$$\frac{1}{V_p} = 0.351 + 0.406\phi \quad 6.9$$

However, these equations for Cascadia are presented with the caveat that they are only valid for porosities ranging from 38% to 79% and 38% to 68%, respectively [*Jarrard et al.*, 1995; *Jarrard*, 1997]. This introduces some problems when projecting the relationships deeper into the sedimentary section, as negative porosities are produced at velocities higher than ~3000 m/s, which can occur within the incoming sediment section and do occur in the outer wedge (Figure 3.3.3a). Given the lack of constraints on the v_{sh} term for the *Erickson and Jarrard* [1998] transforms, as well as the anomalously low porosities given by the Cascadia specific transforms,

we decided to use the *Hoffman and Tobin* [2004] and *Hyndman et al* [1993] transforms for estimates of porosity.

In order to estimate the excess pore pressure at depth, a model of the expected lithostatic stress with depth must be constricted. The lithostatic model is made based on the assumption that incoming sediment sections to subduction zones are compacting normally down to the oceanic crust.

Athy [1930] lays out the exponential equation for loss of porosity with depth in sediments due to normal compaction:

$$\phi = \phi_i e^{-\beta z} \qquad 6.10$$

Given an initial porosity, ϕ_i, the porosity, ϕ, will decrease exponentially as the sediment is buried to a depth, *z*. Usually, the normal compaction curve is calibrated to core or logging data obtained from undisturbed incoming sediments, which helps determine the β value [*Wang et al.*, 1993; *Saffer and Bekins*, 1998; *Kopp and Kukowski*, 2003; *Gamage and Screaton*, 2006; *Gamage et al.*, 2011].

Pore fluid pressure, P_f, is related to the effective stress (σ') and the normal stress (σ) by the following equation as framed in *Saffer and Tobin* [2011] from *Hubbert and Rubey* [1959a]:

$$\sigma' = \sigma - P_f \qquad 6.11$$

The porosities from the velocity-porosity transforms can be used to calculate a model of assumed stress, which is then compared to the hydrostatic and lithostatic gradients at a given point in space and depth. If the pore fluid pressure rises above hydrostatic, it is excess pore fluid pressure, and the section is said to be overpressured. Any anomalies in pore pressure will plot between the hydrostat and the lithostat, indicating a deviation from normally drained conditions (ex. [*Tobin and Saffer*, 2009]). The closer the excess pore fluid pressure is to lithostatic, the higher the overpressure at depth. Another way to relate the amount of overpressure to the normally compacting lithostatic model is through the overpressure ratio, λ*, defined as follows by *Screaton et al* [2002]:

$$\lambda^* = \frac{P^*}{P_L^*} = \frac{P_f - P_H}{P_L - P_H} \qquad 6.12$$

where P^* is the excess pore pressure, and P_L^* is the excess lithostatic pressure.

Given the limits of the drilling data available to calibrate our lithostatic models, we considered the following three cases for Athy fits in the incoming sediments to construct lithostatic stress models, which were then carried forward through the effective stress and overpressure ratio calculations.

In the first case, we use the Athy fit derived from the Shikoku Basin sediments sampled in the Muroto drilling transect of the Nankai Trough, offshore Japan [*Screaton et al.*, 2002]:

$$\phi = 0.77e^{-0.0011z} \qquad 6.13$$

This allows comparison of the incoming sediments to an independent Athy curve that is not derived from a set of porosities estimated from the velocity models. In the second case, we use the best fit exponential curve to the incoming sediments in the line 5 inversion model:

$$\phi = 0.5609e^{-0.000728z} \quad 6.14$$

We assume that the fit to the inversion models is less affected by assumptions about the geology and velocity values through the incoming sediment section, as the methods used to make other velocity models that are picked for lines 3 and 4 rely more heavily on interpretation than the inversion method. In the third case, each sediment section is assumed to be normally compacting and an individual exponential fit is made from a selection of CMPs spanning ~12.5 km in the incoming sediment section of each velocity-porosity model (Figure 3.3.4).

Each of the three Athy cases (Muroto Transect, inversion fit, and incoming sediment fit) are used to calculate the background lithostatic stress that is compared to the effective stress calculated using the two porosity sections (from *Hoffman and Tobin* [2004] and *Hyndman et al.* [1993]).

Uncertainties also occur with the use of the Athy curves. Both the second and third Athy curve cases are constructed by assuming that the entire incoming sediment section is normally compacting. This may not be true given the heavy sedimentation that the margin experienced in the Pleistocene (e.g. [*Griggs and Kulm*, 1970; *Barnard*, 1978; *Carson et al.*, 1986]). Work done on more distal cores nearer the Juan de Fuca Ridge has suggested that fluid movement up from the oceanic crust is inhibited by the overlying sediment, possibly resulting in overpressure [*Underwood et al.*, 2005]. As the first case Athy fit is derived from wholly independent data, it

does not assume that the porosities estimated here represent normal compaction. This curve is, however, derived from an area with sediment inputs of a less sandy composition than those seen in the Cascadia Basin, which will also affect the fit of the Athy curve. There is also some uncertainty in the calculated overpressure values in the outer wedge as velocity-porosity transforms were derived from sediments that have not undergone tectonic stresses. However, given the relatively undeformed nature of the sediments and the lack of an alternative, we carry our calculations through the outer wedge.

3.7 Results

No large areas of excess pore pressure or large overpressure ratios are observed beneath the outer wedge in the porosity models considered here, independent of the velocity-porosity transform or Athy curve used for the analysis. The magnitude of the observed excess pore pressure values and overpressure ratios does vary given the velocity-porosity transform and Athy curve used, but the overall patterns observed are similar in each model.

3.7.1 Porosity and excess pore pressure

The *Hoffman and Tobin* [2004] and the *Hyndman et al* [1993] velocity-porosity transforms provide similar values in the shallow portions of the incoming sediment section, outer wedge and lower slope terrace (Figures 3.5, 3.6). The *Hoffman and Tobin* [2004] velocity-porosity transform provides higher porosity values at depth within the wedge, whereas the resultant porosity model from the *Hyndman et al.* [1993] velocity-porosity transform often reaches a porosity value of 0% above the acoustic basement (Figures 3.3a, 3.5, 3.6). The influence of the horizon-based tomography method's geological interpretations can be clearly seen in the both the

velocity and porosity models (Figure 3.3.3), where gradients follow the interpreted fault planes much more closely than the other models.

For porosity models estimated from either *Hoffman and Tobin* [2004] or *Hyndman et al.* [1993] transforms, the highest amount of excess pore pressure occurs when the porosities are compared to the Muroto Transect Athy fit, regardless of the velocity model type, although the amount of excess pore pressure is small, <5 MPa, and usually ranging between 0 and 3 MPa (Figures 3.7, 3.8a,c,e, 3.9a,c,e, 3.10a,c,e). Some excess pore pressure, generally below 2 MPa, is seen in the incoming sediment section in most sections. The largest excess pore pressure anomalies (4-5 MPa) are seen within the outer wedge in the horizon-based tomography models, focused below the interpreted fault planes (Figure 3.3.7). A small concentrated anomaly (~3 MPa) is seen in the Line 4 residual moveout section near the frontal thrust (Figure 3.11). A higher excess pore pressure (~3 MPa) exists inside the Quinault Ridge in the residual moveout model of line 4 (Figure 3.8, ~32 km landward of the deformation front), but given the chaotic nature of the reflectors inside the structure, whether that anomaly is real or not cannot be easily determined. The residual moveout sections (Figures 3.8, 3.9) have smaller areas with anomalies, but they are more concentrated than the inversion method section anomalies (Figure 3.10). The inversion method sections have more diffuse and lower excess pore pressure values (<2 MPa), where present in the outer wedge and lower slope terrace (Figure 3.10). All models appear to have no excess pore pressure in the upper sediment sections, and values of zero are seen in all models throughout the outer wedge and lower slope terrace.

The amount of excess pore pressure in the underthrust sediments is variable. In the line 4 model using the horizon-based tomography method, ~3 MPa of excess pore pressure exists below the two frontal thrusts but no anomaly is visible below the central portion of the wedge (Figure 3.7).

Seaward in the outer wedge (~25 km from the deformation front), another smaller anomaly can be seen. The residual moveout model shows none of these excess pore pressure values, with the exception of a small anomaly below the frontal thrust, but above the underthrust sediment section. The Line 5 inversion model has low (maximum <2.5 MPa) excess pore pressure below the frontal thrusts, and the residual moveout model on line 5 has some patchy excess pore pressure values that do not exceed 1 MPa below the frontal thrusts, although this is mostly seen when using the Muroto Transect Athy fit.

3.7.2 Overpressure ratio

The largest overpressure ratio (λ^*) values observed in any of the models are generally <0.15, which corresponds to relatively low overpressure (Figures 3.11, 3.8b,d,f, 3.9b,d,f, 3.10b,d,f). The highest ratios are seen in the horizon-based tomography model for Line 4, concentrated below fault planes where small velocity inversions occur (Figure 3.11). No overpressure ratio values corresponding to highly overpressured underthrust sediments can be identified below the thrust sheets in the wedge, and there are no values anywhere that correspond with the 0.90 suggested by *Davis et al.* [1983] given the Cascadia accretionary wedge's taper angle. The incoming sediment section consistently shows low overpressure ratios (<0.125). The overpressure ratios for the shallow incoming sediment section, as well as the upper portion of the thrust sheets, are near or below zero, which implies overcompaction, where the values obtained are consistent with a depth lower than the present burial depth of the sediment.

Low values of λ^* below the wedge can be seen most clearly in the Line 4 horizon-based tomography model (Figure 3.8) and the Line 5 inversion model (Figure 3.10b,d,f). The residual moveout models result in negative values below the wedge in all cases except when the Hoffman-Tobin velocity-porosity transform is used with the Muroto Transect Athy relationship

(Figures 3.9b,d,f, 3.10b,d,f). In Figures 3.12 and 3.13, the overpressure ratios were extracted from the sections at a point 200 m above the oceanic crust, within what would be the underthrust section interpreted from the seismic reflection profiles. Figure 3.12 shows the overpressure ratios extracted from the *Hoffman and Tobin* [2004] overpressure sections. Figure 3.13 shows the profiles extracted when using the *Hyndman et al.* [1993] velocity-porosity transform, which results in negative overpressure ratios below the wedge in all cases except two for the horizon-based tomography model. The input sections generally show positive overpressure ratio values in all lines. The residual moveout sections (Figures 3.12a,c,d) show consistently lower values under the wedge. Both the inversion model (Figure 3.12e) and the horizon-based tomography model (Figure 3.12b) show positive values for two of the transforms (the Muroto Transect and the inversion model Athy fit) but values are <0.05, which correspond with very low overpressure. These two models also show an area of positive λ^* under the first two thrust sheets (first ~10 km landward of the deformation front). All models show negative values below the lower slope terrace (~30 km landward of the deformation front).

3.8 Discussion

Structure and taper angle in the Cascadia wedge have often been attributed to a large mechanical contrast, often assumed to be due to a low velocity, high porosity overpressured underthrust section below a relatively stronger wedge. Analysis of velocity models shows only low to moderate excess pore pressure inside or below the wedge. Below, we outline the possible reasons for the presence or absence of excess pore pressure in the wedge, and the implications this may have for shallow coseismic slip.

3.8.1 Model assumptions

These model analyses assume initial normal consolidation conditions and attribute all changes in velocity to porosity loss. These are simplified assumptions, especially in an active accretionary margin. The outer wedge is subject to tectonic compressional stress, which indicates that the sediment undergoes a different stress path than simple normal compaction. Deformation in the outer wedge, such as large thrust faults, can impact the fluid budget of the wedge by providing pathways for fluid escape from depth, as well as altering the velocity by fracturing the material itself (e.g. [*Screaton et al.*, 2009]).

Diagenesis, particularly cementation, can also alter velocity and hence, porosity values. The shallow sections of wedge in both the incoming section and the outer wedge show negative overpressure ratios which could be interpreted as overcompaction. However, samples taken in the shallow portion of the wedge show carbonate cementation [*Kopf et al.*, 1995; *Jarrard*, 1997], which would alter the incoming sediment's shallow velocities, possibly resulting in apparent overcompaction.

Although the magnitude of the models' excess pore pressure and overpressure ratio values differ widely, anomalies are all concentrated in the lower portion of the incoming sediment section and the outer wedge, no matter the method used to construct the initial velocity model. The excess pore pressure seen in the outer wedge is concentrated in the footwalls of the interpreted faults. The horizon-based tomography model gives the largest excess pore pressure values and only the inversion method has excess pore pressure above 0 below most of the outer wedge. Although the magnitude of the high porosity values is variable, the location of positive excess pore pressures in the models is similar. We may not be able to definitively gauge the magnitude of

excess pore pressure in the wedge, but we can use the locations of the areas of excess pore pressure to examine the general state of overpressure in the wedge.

3.8.2 The incoming sediment section

The higher excess pore pressure and λ^* values in the lower incoming sediment section may indicate that the initial assumption of normal compaction through this section is not correct. *Underwood et al* [2005] suggested that given the high rate of sedimentation in the Cascadia Basin, the lower sediment section may not be able to adequately drain, leading to overpressure at depth in the sediment section covering the Juan de Fuca plate. Heat flow studies have also suggested that the toe of the accretionary wedge is above the temperature for the smectite-to-illite transition [*Johnson et al.*, 2013], which releases mineral bound water and can lead to overpressure at depth (e.g. [*Moore and Saffer*, 2001; *Gamage et al.*, 2011; *Saffer et al.*, 2012]). If this reaction is occurring seaward of the deformation front, the incoming sediment would be more likely to be overpressured, due to the undeformed nature of the sediments and the lack of faults to act as fluid conduits.

A fluid-rich section entering the wedge would lead to a lower effective stress at the toe of the wedge. The deformation due to the thrust sheets, particularly the frontal thrust, may act as pathway for fluid escape, increasing the effective stress at depth as the sediment section is incorporated into the wedge (e.g. [*Screaton et al.*, 2009]). If the incoming sediments do indeed have a higher porosity than expected from normal compaction, determining the initial conditions is complicated further, compounding issues cited earlier with respect to cementation of upper layers. Using the Athy compaction curve fits to incoming sediment sections for each line generally gives low overpressure ratio estimates for the incoming section as well as negative values below the outer wedge. The prevalence of slightly elevated λ^* in the incoming section

may support the suggestion that the incoming section is overpressured, which may have implications for the fluid budget of the study area. However, an overpressured incoming section that is assumed to be normally compacting would lead to incorrect assumptions about the amount of overpressure below the wedge. Although using the Muroto Transect Athy fit produces fewer low or unrealistic excess pore pressure values, it does introduce a compositional problem, as it was fit to more clay-rich material than has been observed at Cascadia.

3.8.3 The outer wedge

The largest excess pore pressure values from the models are seen in the outer wedge, focused in the footwalls of the thrust faults, but also occurring across the lower sections of the thrust sheets. These areas of excess pore pressure can have an impact on wedge strength and be a source of fluid in the accretionary wedge.

The deformation of sediments entering a subduction zone can increase permeability by introducing fluid pathways along faults that are a result of brittle deformation and fracture dilation, but also decrease permeability when faults act at barriers to fluid and pore volumes rapidly decrease under tectonic stress (e.g. [*Bray and Karig*, 1985; *Moore and Vrolijk*, 1992]). Active fluid seeps have been documented on the seafloor on the Cascadia subduction zone margin, observed from submersible dives, indicating fluid is expelled both along faults and along stratigraphic horizons in this margin (e.g [*Lewis and Cochrane*, 1990; *Moore et al.*, 1990; *Tobin et al.*, 1993]).

Zones of high porosity in the lower thrust sheets below faults may indicate areas that have not been fully drained, but excess pore pressure in the footwalls of thrust faults suggests that the anomalies are caused by lithostatic loading from the thrust faults. The localization of anomalies

below the thrust faults suggests that the faults are preventing fluids from escaping from the footwall. The frontal thrust sheet does not show evidence of high excess pore fluid pressure, nor do the hanging walls of any of the faults. As the incoming sediment section is incorporated into the wedge, a decrease in excess pore pressure is seen indicating that the frontal thrust may be draining fluid from the incoming sediment section in the hanging wall of the thrust. In the COAST seismic reflection profiles for lines 3 and 4, the fault plane reflectors are high amplitude through the central portion of the wedge in both the time and depth domains, an indication of the possibility that the faults may be acting as a conduit for fluids.

If the wedge is efficiently draining, it is likely to be mechanically strong. The wedge does not show much thickening or extensive deformation in the thrust sheets, and the low wedge taper angle is consistent with a strong wedge [*Davis et al.*, 1983]. Given the evidence for high temperatures in the incoming sediment section [*Johnson et al.*, 2013], metamorphic reactions that produce fluid may have already occurred, and are unlikely to add to the fluid budget in the wedge, keeping the wedge relatively strong.

3.8.4 The underthrust section

. The low basal shear stress that has been invoked to explain landward-vergent faulting is often attributed to overpressure. We do not document high porosity or excess pore pressure in the interpreted section below the wedge, indicating that the entire underthrust section is not overpressured below the wedge. This would indicate that if there is low basal shear stress below the wedge, it may be due to mechanical properties of the underthrust material itself.

We cannot discount the possibility that an overpressured section could be present, but below seismic resolution. The structurally interpreted underthrust section is ~500 m thick where it is

imaged, and velocity models were initially constructed with the assumption that velocity increased with depth. Accurate migration at depth below the wedge is complicated by the patchy nature of the oceanic crust reflector and the presence of a strong multiple. However, none of the migration methods, including the inversion method, result in a low velocity zone beneath the wedge. Given the initial assumption that velocity increases with depth and the resolution of the current processing, an overpressured section may be present but not resolved. In addition, the presence of two detachments, one in the sediment section and another at the acoustic basement (e.g. Webb, Chapter 2; [*Adam et al.*, 2004]), may indicate that areas with overpressure may not extend spatially throughout the entire survey.

Another explanation for the structures observed in Cascadia could be a difference in the physical properties of the sediments above and below the plate boundary. Core through the incoming sedimentary section at ODP site 174 showed that the lowermost ~600 m consists of Plio-Pleistocene silty clays, in contrast with the sandier Pleistocene fan deposits above them [*Kulm et al.*, 1973b], and the upper décollement is within this layer (Webb, Chapter 2). The presence of a ductile carbonate layer, combined with high overpressure, underlying the incoming sediment section has been posited as the reason for landward vergence, with analogue models indicating it spans the lower third of the incoming section [*Gutscher et al.*, 2001]. However, the core descriptions from ODP site reports [*Kulm et al.*, 1973b], indicate that although there is an increase in the amount of carbonate in the lower section, the lithology is generally silty clay, and does not seem to indicate a large carbonate section at depth with a radical difference in material properties. The larger amount of clay in the deeper sediments may lead to a weaker interval at the base of the sediment section, between the stronger oceanic crust and the sandier fan sediments. The material property differences could contribute to the landward vergence and low

taper angle seen in the outer wedge. Presence of both an active upper and lower detachment suggests that there may be different weak layers into which the faults sole, making their correlation to the core more difficult. These layers could potentially be very thin, and not visible as a large reflector within or at the top of the underthrust section. Velocity models developed for PSDM in the Japan Trench do not show a low velocity zone [*Nakamura et al.*, 2014], but in the aftermath of the 2011 Tohoku earthquake the fault zone was sampled and subsequent experiments on the clays sampled showed a relatively weak layer between two stronger wall rock layers [*Chester et al.*, 2013; *Ikari et al.*, 2015].

If the incoming sediment section is overpressured and some pore fluid is released as deformation begins, it could drain and strengthen the outer wedge, beginning with the frontal thrust. The strengthening of the wedge would increase the contrast in mechanical properties between the stronger accreted and weaker underthrust material.

3.8.5 Implications for the updip limit of the seismogenic zone

The extent of the seismogenic zone beneath the outer wedge at Cascadia impacts the extent of expected rupture and tsunami hazard estimates. The updip limit of seismogenesis is often correlated with the transition from low to high effective stress due to porosity loss and fluid expulsion in underthrust sediments.

If the thrust faults at Cascadia are draining overpressured incoming sediments, this would call for an updip limit to the seismogenic zone near or at the toe of the accretionary wedge, extending under the entire outer wedge. Slip to the trench increases tsunami hazard, as the wedge is more likely to displace and deform the overlying water column. The draining of the wedge could also

lead to its relative strengthening, possibly increasing the likelihood that the outer wedge would deform as a whole coseismically.

If the updip limit of the locked seismogenic zone is governed by a thin overpressured section or contrast in material properties at depth, its extent below the wedge cannot be determined from this dataset. The propagation of rupture is also tied to the rate-dependent strength or weakness of sediments. Laboratory tests on clays from subduction zone settings have shown that they are generally velocity strengthening (e.g. [*Kopf and Brown*, 2003; *Saffer and Marone*, 2003; *Ikari et al.*, 2010; *Ikari and Saffer*, 2011]). This would lead to the inhibition of rupture within this clay-rich layer. However, if the surrounding sediment were velocity-weakening or the amount of energy released was sufficient, rupture could still propagate. From this analysis, it is possible that rupture could extend to the trench during a large subduction zone earthquake.

3.9 Conclusions

Different empirical velocity-porosity relationships, as well as Athy compaction curves, were used to estimate porosity, and thus excess pore pressure and overpressure ratio for three lines in the COAST survey, offshore Grays Harbor, Washington. Results varied but showed consistent modest excess pore fluid pressure concentrated in the footwalls of thrust faults in the outer wedge, as well as slight overpressure in the incoming sediment section. Changes in velocity from factors other than porosity (such as cementation of shallow sediments) as well as the assumption of a normal compaction state across the entire wedge can impact the values estimated in this study, but the areas showing overpressure were consistent regardless of the method used to construct the velocity model. The *Hoffman and Tobin* [2004] velocity-porosity transform, coupled with an Athy fit to Muroto Transect sediments [*Screaton et al.*, 2002] show the highest

values of excess pore pressure and overpressure ratio, although they are below 5 MPa and 0.10, respectively. These values correspond to low to moderate overpressure in the incoming sediments and outer wedge at Cascadia.

The thick incoming sediment section may be slightly overpressured, but the pore fluid appears to be draining as it enters the frontal thrust. The lack of excess pore pressure in the hanging walls of thrust faults, as well as the decrease in overpressure ratio of the incoming sediment section as it is deformed by the frontal thrust, suggest that the outer wedge is relatively well drained. A well drained wedge is likely to be stronger and would result in a low wedge taper angle, which is observed in Cascadia. No low velocity anomaly related to overpressure is detected in the ~500 m of underthrust sediment, suggesting that if overpressure is present, it is below seismic resolution. Weakness at the base of the outer wedge could also be due to the mechanical properties of the sediments, which may not have a signal in the velocity models. A stronger wedge may be more likely to deform coseismically in a large megathrust earthquake, but the extent of the seismogenic zone beneath the wedge is still uncertain. If the incoming section is overpressured and the frontal thrust drains some of that fluid, a change in effective stress may occur near the trench.

In this analysis, we do document the potential for a strong, drained wedge and the lack of an entirely overpressured underthrust sediment section. Low basal shear stress may be possible due to the mechanical properties of sediments, or a thin overpressured layer. The lack of a large overpressured section at depth complicates assumptions made about the underthrust sediments and the décollement, which are often assumed to be overpressured. A stronger wedge may inhibit rupture in a large earthquake (e.g. [*Wang and Tréhu*, 2016]) or possibly deform as a whole, which would increase tsunami risk (e.g. [*Gulick et al.*, 2011]. If the area beneath the

wedge has low basal shear stress due to material properties, these may not be identifiable in seismic data. Further investigation and higher resolution methods may be necessary to determine what the conditions at depth are below Cascadia.

3.10 References

Adam, J., D. Klaeschen, N. Kukowski, and E. R. Flueh (2004), Upward delamination of Cascadia Basin sediment infill with landward frontal accretion thrusting caused by rapid glacial age material flux, *Tectonics*, *23*(3), doi:10.1029/2002TC001475.

Adams, J. (1990), Paleoseismicity of the Cascadia Subduction Zone: Evidence from turbidites off the Oregon-Washington Margin, *Tectonics*, *9*(4), 569–583, doi:10.1029/TC009i004p00569.

Athy, L. F. (1930), Density, porosity, and compaction of sedimentary rocks, *Bull. Am. Assoc. Pet. Geol.*, *14*(1), 468–470, doi:10.1126/science.51.1323.468.

Atwater, B. F., and D. K. Yamaguchi (1991), Sudden, probably coseismic submergence of Holocene trees and grass in coastal Washington State, *Geology*, *19*(7), 706–709, doi:10.1130/0091-7613(1991)019<0706:SPCSOH>2.3.CO;2.

Atwater, B. F., B. Carson, G. B. Griggs, P. P. Johnson, and M. S. Salmi (2014), Rethinking turbidite paleoseismology along the Cascadia subduction zone, *Geology*, *42*(9), 827–830, doi:10.1130/G35902.1.

Bangs, N. L. B., G. K. Westbrook, J. W. Ladd, and P. Buhl (1990), Seismic velocities from the Barbados Ridge complex: Indicators of high pore fluid pressures in an accretionary complex, *J. Geophys. …*, *95*(B6), 8767–8782.

Bangs, N. L. B., G. F. Moore, S. P. S. Gulick, E. M. Pangborn, H. J. Tobin, S. Kuramoto, and A. Taira (2009), Broad, weak regions of the Nankai Megathrust and implications for shallow coseismic slip, *Earth Planet. Sci. Lett.*, *284*(1–2), 44–49, doi:10.1016/j.epsl.2009.04.026.

Barnard, W. D. (1978), The Washington continental slope: Quaternary tectonics and sedimentation, *Mar. Geol.*, *27*(1–2), 79–114, doi:10.1016/0025-3227(78)90075-0.

Benson, B. E., B. F. Atwater, D. K. Yamaguchi, L. J. Amidon, S. L. Brown, and R. C. Lewis (2001), Renewal of Tidal Forests in Washington State after a Subduction Earthquake in A.D. 1700, *Quat. Res.*, *56*, 139–147, doi:10.1016/j.yqres.2014.07.007.

Bray, C. J., and D. E. Karig (1985), Porosity of sediments in accretionary prisms and some implications for dewatering processes, *J. Geophys. Res. Solid …*, *90*(4), 768–778, doi:doi:10.1029/JB090iB01p00768.

Brudzinski, M. R., and R. M. Allen (2007), Segmentation in episodic tremor and slip all along Cascadia, *Geology*, *35*(10), 907–910, doi:10.1130/G23740A.1.

Calahorrano, A., V. Sallares, J.-Y. Collot, F. Sage, and C. R. Ranero (2008), Nonlinear variations of the physical properties along the southern Ecuador subduction channel: Results from depth-migrated seismic data, *Earth Planet. Sci. Lett.*, *267*(3–4), 453–467, doi:10.1016/j.epsl.2007.11.061.

Calkins, J. A., G. A. Abers, G. Ekström, K. C. Creager, and S. Rondenay (2011), Shallow structure of the Cascadia subduction zone beneath western Washington from spectral

ambient noise correlation, *J. Geophys. Res.*, *116*(B7), doi:10.1029/2010JB007657.

Carson, B., E. T. Baker, B. M. Hickey, C. A. Nittrouer, D. J. DeMaster, K. W. Thorbjarnarson, and G. W. Snyder (1986), Modern sediment dispersal and accumulation in Quinault submarine canyon - A summary, *Mar. Geol.*, *71*(1–2), 1–13, doi:10.1016/0025-3227(86)90030-7.

Chester, F. M. et al. (2013), Structure and composition of the plate-boundary slip zone for the 2011 Tohoku-Oki earthquake, *Science (80-.).*, *342*, 1208–1112.

Cochrane, G. R., J. C. Moore, M. E. MacKay, and G. F. Moore (1994), Velocity and inferred porosity model of the Oregon accretionary prism from multichannel seismic reflection data: Implications on sediment dewatering and overpressure, *J. Geophys. Res.*, *99*(B4), 7033–7043, doi:doi:10.1029/9; http://dx.doi.org/10.1029/93JB03206.

Costa Pisani, P., M. Reshef, and G. F. Moore (2005), Targeted 3-D prestack depth imaging at Legs 190-196 ODP drill sites (Nankai Trough, Japan), *Geophys. Res. Lett.*, *32*(20), doi:10.1029/2005GL024191.

Davis, D., J. Suppe, and F. A. Dahlen (1983), Mechanics of Fold-and-Thrust Belts and Accretionary Wedges, *J. Geophys. Res.*, *88*(B2), 1153–1172.

Dean, S., L. C. McNeill, T. J. Henstock, J. M. Bull, S. P. S. Gulick, J. A. Austin, N. L. B. Bangs, Y. S. Djajadihardja, and H. Permana (2010), Contrasting decollement and prism properties over the Sumatra 2004-2005 earthquake rupture boundary, *Science (80-.).*, *329*, 207–211.

DeMets, C., R. G. Gordon, and D. F. Argus (2010), Geologically current plate motions, *Geophys. J. Int.*, *181*(1), 1–80, doi:10.1111/j.1365-246X.2009.04491.x.

Dragert, H., and K. Wang (2011), Temporal evolution of an episodic tremor and slip event along the northern Cascadia margin, *J. Geophys. Res.*, *116*, doi:10.1029/2011JB008609.

Dragert, H., R. D. Hyndman, G. C. Rogers, and K. Wang (1994), Current deformation and the width of the seismogenic zone of the northern Cascadia subduction thrust, *J. Geophys. Res.*, *99*(B1), 653–668.

Dragert, H., K. Wang, and T. S. James (2001), A Silent Slip Event on the Deeper Cascadia Subduction Interface, *Science (80-.).*, *292*(5521), 1525–1528, doi:10.1126/science.1060152.

Dragert, H., K. Wang, and G. Rogers (2004), Geodetic and seismic signatures of episodic tremor and slip in the northern Cascadia subduction zone, *Earth Planets Sp.*, *56*, 1143–1150.

Everson, E. D. (2014), Seismic structure of the Costa Rican subduction system from active-source onshore-offshore seismic data and imaging plate boundary processes at the Cascadia subduction zone offshore Washington, University of Wyoming.

Fisher, M. A., E. R. Flueh, D. W. Scholl, T. Parsons, R. E. Wells, A. M. Tréhu, U. S. ten Brink, and C. S. Weaver (1999), Geologic processes of accretion in the Cascadia subduction zone west of Washington State, *Geodynamics*, *27*, 277–288.

Flueh, E. R., M. A. Fisher, J. Bialas, J. R. Childs, D. Klaeschen, N. Kukowski, T. Parsons, D. W.

Scholl, A. M. Tréhu, and N. Vidal (1998), New seismic images of the Cascadia subduction zone from cruise SO108 — ORWELL, *Tectonophysics*, *293*, 69–84.

Fortin, W. F. J. (2015), Extracting physical parameters from marine seismic data: New methods in seismic oceanography and velocity inversion, University of Wyoming.

Frederik, M. C. G., S. P. S. Gulick, J. A. Austin, and N. L. B. Bangs (2015), What 2-D multichannel seismic and multibeam bathymetric data tell us about the North Sumatra wedge structure and coseismic response, , 1910–1926, doi:10.1002/2014TC003614.Received.

Gamage, K., and E. J. Screaton (2006), Characterization of excess pore pressures at the toe of the Nankai accretionary complex, Ocean Drilling Program sites 1173, 1174, and 808: Results of one-dimensional modeling, *J. Geophys. Res.*, *111*, B04103, doi:10.1029/2004JB003572.

Gamage, K., E. J. Screaton, B. A. Bekins, and I. Aiello (2011), Permeability–porosity relationships of subduction zone sediments, *Mar. Geol.*, *279*(1–4), 19–36, doi:10.1016/j.margeo.2010.10.010.

Gerdom, M., A. M. Trehu, E. R. Flueh, and D. Klaeschen (2000), The continental margin off Oregon from seismic investigations, *Tectonophysics*, *329*, 79–97, doi:10.1016/S0040-1951(00)00190-6.

Ghosh, A., J. E. Vidale, J. R. Sweet, K. C. Creager, and A. G. Wech (2009), Tremor patches in Cascadia revealed by seismic array analysis, *Geophys. Res. Lett.*, *36*(17), doi:10.1029/2009GL039080.

Ghosh, A., J. E. Vidale, J. R. Sweet, K. C. Creager, A. G. Wech, H. Houston, and E. E. Brodsky (2010), Rapid, continuous streaking of tremor in Cascadia, *Geochemistry, Geophys. Geosystems*, *11*(12), 1–10, doi:10.1029/2010GC003305.

Goldfinger, C. (2011), Submarine Paleoseismology Based on Turbidite Records, *Ann. Rev. Mar. Sci.*, *3*(1), 35–66, doi:10.1146/annurev-marine-120709-142852.

Goldfinger, C., C. H. Nelson, and J. E. Johnson (2003), Holocene Earthquake Records from the Cascadia Subduction Zone and Nothern San Andreas Fault Based on Precise Dating of Offshore Turbidites, *Annu. Rev. Earth Planet. Sci.*, *31*(1), 555–577, doi:10.1146/annurev.earth.31.100901.141246.

Goldfinger, C. et al. (2008), Late Holocene Rupture of the Northern San Andreas Fault and Possible Stress Linkage to the Cascadia Subduction Zone, *Bull. Seismol. Soc. Am.*, *98*(2), 861–889, doi:10.1785/0120060411.

Goldfinger, C., S. Galer, J. Beeson, T. Hamilton, B. Black, C. Romsos, J. Patton, C. H. Nelson, R. Hausmann, and A. Morey (2016), The importance of site selection, sediment supply, and hydrodynamics: A case study of submarine paleoseismology on the northern Cascadia margin, Washington USA, *Mar. Geol.*, (2016), doi:10.1016/j.margeo.2016.06.008.

Griggs, G. B., and L. D. Kulm (1970), Sedimentation in cascadia deep-sea channel, *Bull. Geol. Soc. Am.*, *81*(5), 1361–1384, doi:10.1130/0016-7606(1970)81[1361:SICDC]2.0.CO;2.

Griggs, G. B., A. G. Carey, and L. D. Kulm (1969), Deep-sea sedimentation and sediment-fauna

interaction in Cascadia Channel and on Cascadia Abyssal Plain, *Deep Sea Res. Oceanogr. Abstr.*, *16*(2), 157–170, doi:10.1016/0011-7471(69)90071-0.

Gulick, S. P. S., J. A. A. Jr, L. C. Mcneill, N. L. B. Bangs, K. M. Martin, T. J. Henstock, J. M. Bull, S. Dean, and Y. S. Djajadihardja (2011), Updip rupture of the 2004 Sumatra earthquake extended by thick indurated sediments, *Nat. Geosci.*, *4*(7), 453–456, doi:10.1038/ngeo1176.

Gutscher, M.-A., D. Klaeschen, E. R. Flueh, and J. Malavieille (2001), Non-Coulomb wedges, wrong-way thrusting, and natural hazards in Cascadia, *Geology*, *29*(5), 379–382.

Holbrook, W. S., G. M. Kent, K. Keranen, H. P. Johnson, H. J. Tobin, J. Caplan-Auerbach, and J. Beeson (2012), Cascadia Fore Arc Seismic Survey: Open-Access Data Available, *Eos (Washington. DC).*, *93*(50), 521–522.

Hubbert, M. K., and W. W. Rubey (1959a), Role of Fluid Pressure in Mechanics of Overthrust Faulting, , *70*(February), 115–166.

Hubbert, M. K., and W. W. Rubey (1959b), Role of Fluid Pressure in Mechanics of Overthrust Faulting I: Mechanics of Fluid-Filled Porous Solids and Its Application to Overthrust Faulting, *Geol. Soc. Am. Bull.*, *70*, 116–186, doi:10.1130/0016-7606(1959)70.

Hubbert, M. K., and W. W. Rubey (1959c), Role of fluid pressure in mechanics of overthrust faulting I. Mechanics of fluid-filled porous solids and its application to overthrust faulting, *Bull. Geol. Soc. Am.*, *70*, 115–166.

von Huene, R., D. Klaeschen, M. Gutscher, and J. Fruehn (1998), Mass and fluid flux during accretion at the Alaskan margin, *GSA Bull.*, *110*(4), 468–482.

Hyndman, R. D., and K. Wang (1995), The rupture zone of Cascadia great earthquake from current deformation and the thermal regime, *J. Geophys. Res.*, *100*(B11), 22133–22154, doi:http://dx.doi.org/10.1029/95JB01970.

Ikari, M. J., and D. M. Saffer (2011), Comparison of frictional strength and velocity dependence between fault zones in the Nankai accretionary complex, *Geochemistry, Geophys. Geosystems*, *12*(4), n/a-n/a, doi:10.1029/2010GC003442.

Ikari, M. J., C. Marone, and D. M. Saffer (2010), On the relation between fault strength and frictional stability, *Geology*, *39*(1), 83–86, doi:10.1130/G31416.1.

Ikari, M. J., J. Kameda, D. M. Saffer, and A. J. Kopf (2015), Strength characteristics of Japan Trench borehole samples in the high-slip region of the 2011 Tohoku-Oki earthquake, *Earth Planet. Sci. Lett.*, *412*, 35–41, doi:10.1016/j.epsl.2014.12.014.

Ito, Y., T. Tsuji, Y. Osada, M. Kido, D. Inazu, Y. Hayashi, H. Tsushima, R. Hino, and H. Fujimoto (2011), Frontal wedge deformation near the source region of the 2011 Tohoku-Oki earthquake, *Geophys. Res. Lett.*, *38*(7), doi:10.1029/2011GL048355.

Jarrard, R. D. (1997), Origins of porosity and velocity variations at Cascadia accretionary prism, *Geophys. Res. Lett.*, *24*(3), 325–328.

Jarrard, R. D., M. E. MacKay, G. K. Westbrook, and E. J. Screaton (1995), Log-based porosity

of ODP sites on the Cascadia Accretionary Prism, in *Proceedings of the Ocean Drilling Program, Scientific Results, Vol 146*, vol. 146, edited by B. Carson, G. K. Westbrook, R. J. Musgrave, and E. Suess, pp. 313–335.

Johnson, H. P., E. A. Solomon, R. N. Harris, M. S. Salmi, and R. D. Berg (2013), Heat Flow and Fluid Flux in Cascadia's Seismogenic Zone, *Eos (Washington. DC).*, *94*(48), 457–468, doi:10.1029/2009GC002957.Salmi.

Kitajima, H., and D. M. Saffer (2012), Elevated pore pressure and anomalously low stress in regions of low frequency earthquakes along the Nankai Trough subduction megathrust, *Geophys. Res. Lett.*, *39*(L23301), doi:10.1029/2012GL053793.

Kodaira, S., T. No, Y. Nakamura, T. Fujiwara, Y. Kaiho, S. Miura, N. Takahashi, Y. Kaneda, and A. Taira (2012), Coseismic fault rupture at the trench axis during the 2011 Tohoku-oki earthquake, *Nat. Geosci. Lett.*, *5*(9), 646–650, doi:10.1038/ngeo1547.

Kopf, A., J. C. Sample, P. Bauer, J. H. Behrmann, and H. Erlenkeuser (1995), Diagenetic carbonates from Cascadia Margin; textures, chemical compositions, and oxygen and carbon stable isotope signatures, *Proc. Ocean Drill. Program; Sci. results, Part 1, Cascadia Margin; Cover. Leg 146 cruises Drill. Vessel JOIDES Resolut. Victoria, Canada, to San Diego, California, sites 888-892, 20 Sept. Novemb. 1992.*, *146 Part 1*, 117–136.

Kopf, A. J., and K. M. Brown (2003), Friction experiments on saturated sediments and their implications for the stress state of the Nankai and Barbados subduction thrusts, *Mar. Geol.*, *202*(3–4), 193–210, doi:10.1016/S0025-3227(03)00286-X.

Kopp, H., and N. Kukowski (2003), Backstop geometry and accretionary mechanics of the Sunda margin, *Tectonics*, *22*(6), doi:10.1029/2002TC001420.

Kulm, L. D. et al. (1973a), Introduction, in *Initial reports of the Deep Sea Drilling Project, covering Leg 18 of the cruises of the drilling vessel Glomar Challenger, Honolulu, Hawaii to Kodiak, Alaska May-July 1971*, edited by L. D. Kulm et al., pp. 5–8, Ocean Drilling Program, College Station, TX.

Kulm, L. D. et al. (1973b), Site 174, in *Initial reports of the Deep Sea Drilling Project, covering Leg 18 of the cruises of the drilling vessel Glomar Challenger, Honolulu, Hawaii to Kodiak, Alaska May-July 1971*, edited by L. D. Kulm et al., College Station, TX.

Kulm, L. D. et al. (1973c), Site 175, in *Initial reports of the Deep Sea Drilling Project, covering Leg 18 of the cruises of the drilling vessel Glomar Challenger, Honolulu, Hawaii to Kodiak, Alaska May-July 1971al reports of the Deep Sea Drilling Project, covering Leg 18 of the cruises of the d*, edited by L. D. Kulm et al., College Station, TX.

Lester, R., and K. McIntosh (2012), Multiple attenuation in crustal-scale imaging: examples from the TAIGER marine reflection data set, *Mar. Geophys. Res.*, *33*(4), 289–305, doi:10.1007/s11001-012-9149-1.

Lewis, B. T. R., and G. C. Cochrane (1990), Relationship between the location of chemosynthetic benthic communities and geologic structure on the Cascadia Subduction Zone, *J. Geophys. Res.*, *95*, 8783–8793.

Lotto, G. C., E. M. Dunham, T. N. Jeppson, and H. J. Tobin (2017), The effect of compliant

prisms on subduction zone earthquakes and tsunamis, *Earth Planet. Sci. Lett.*, *458*, 1–23, doi:10.1016/j.epsl.2016.10.050.

MacKay, M. E. (1995), Structural variation and landward vergence at the toe of the Oregon accretionary prism, *Tectonics*, *14*(5), 1309–1320.

MacKay, M. E., G. F. Moore, D. Klaeschen, and R. von Huene (1995), The case against porosity change: Seismic velocity decrease at the toe of the Oregon accretionary prism, *Geology*, *23*, 827–830, doi:10.1130/0091-7613(1995)023<0827.

Mannu, U., K. Ueda, S. D. Willett, T. V Gerya, and M. Strasser (2017), Stratigraphic signatures of forearc basin formation mechanisms, *Geochemistry, Geophys. Geosystems*, *18*, doi:10.1002/2017GC006810.Received.

McAdoo, B. G., and P. Watts (2004), Tsunami hazard from submarine landslides on the Oregon continental slope, *Mar. Geol.*, *203*, 235–245, doi:10.1016/S0025-3227(03)00307-4.

Mccaffrey, R., R. W. King, S. J. Payne, and M. Lancaster (2013), Active tectonics of northwestern U . S . inferred from GPS-derived surface velocities, , *118*(October 2012), 709–723, doi:10.1029/2012JB009473.

McCaffrey, R., M. D. Long, C. Goldfinger, P. C. Zwick, J. L. Nabelek, C. K. Johnson, and C. Smith (2000), Rotation and plate locking at the Southern Cascadia Subduction Zone, *Geophys. Res. Lett.*, *27*(19), 3117–3120, doi:10.1029/2000GL011768.

McCaffrey, R., A. I. Qamar, R. W. King, R. Wells, G. Khazaradze, C. A. Williams, C. W. Stevens, J. J. Vollick, and P. C. Zwick (2007), Fault locking, block rotation and crustal deformation in the Pacific Northwest, *Geophys. J. Int.*, *169*(3), 1315–1340, doi:10.1111/j.1365-246X.2007.03371.x.

Moore, J. C. (1989), Tectonics and hydrogeology of accretionary prisms: role of the decollement zone, *J. Struct. Geol.*, *11*(1), 95–106.

Moore, J. C., and D. M. Saffer (2001), Updip limit of the seismogenic zone beneath the accretionary prism of southwest Japan: An effect of diagenetic to low-grade metamorphic processes and increasing effective stress, *Geology*, *29*(2), 183–186.

Moore, J. C., and P. Vrolijk (1992), Fluids in Accretionary Prisms, *Rev. Geophys.*, *30*(2), 113–135.

Moore, J. C., D. L. Orange, and L. D. Kulm (1990), Interrelationship of Fluid Venting and Structural Evolution: Alvin Observations From the Frontal Accretionary Prism, Oregon, *J. Geophys. Res.*, *95*, 8795–8808.

Nakamura, Y., S. Kodaira, B. J. Cook, T. Jeppson, T. KASAYA, Y. Yamamoto, Y. Hashimoto, M. Yamaguchi, K. Obana, and G. Fujie (2014), Seismic imaging and velocity structure around the JFAST drill site in the Japan Trench: low Vp, high Vp/ Vs in the transparent frontal prism, *Earth*, *66*(1), 121, doi:10.1186/1880-5981-66-121.

Nedimovic, M. R., R. D. Hyndman, K. Ramachandran, and G. D. Spence (2003), Reflection signature of seismic and aseismic slip on the northern Cascadia subduction interface, *Lett. to Nat.*, *424*, 416–419, doi:10.1038/nature01828.

Nicholson, T., M. Bostock, and J. F. Cassidy (2005), New constraints on subduction zone structure in northern Cascadia, *Geophys. J. Int.*, *161*, 849–859, doi:10.1111/j.1365-246X.2005.02605.x.

Oleskevitch, D. A., R. D. Hyndman, and K. Wang (1999), The updip and downdip limits to great subduction earthquakes: Thermal and structural models of Cascadia, south Alaska, SW Japan, and Chile, *J. Geophys. Res.*, *104*(B7), 14965–14991.

Park, J.-O., G. Fujie, L. Wijerathne, T. Hori, S. Kodaira, Y. Fukao, G. F. Moore, N. L. B. Bangs, S. Kuramoto, and A. Taira (2010), A low-velocity zone with weak reflectivity along the Nankai subduction zone, *Geology*, *38*(3), 283–286, doi:10.1130/G30205.1.

Ranero, C. R., I. Grevemeyer, H. Sahling, U. Barckhausen, C. Hensen, K. Wallmann, W. Weinrebe, P. Vannucchi, R. Von Huene, and K. McIntosh (2008), Hydrogeological system of erosional convergent margins and its influence on tectonics and interplate seismogenesis, *Geochemistry, Geophys. Geosystems*, *9*(3), doi:10.1029/2007GC001679.

Rowe, K. T., E. J. Screaton, and S. Ge (2012), Coupled fluid flow and deformation modeling of the frontal thrust region of the Kumano Basin transect, Japan: Implications for fluid pressures and decollement downstepping, *Geochemistry, Geophys. Geosystems*, *13*(3), n/a-n/a, doi:10.1029/2011GC003861.

Saffer, D. M. (2003), Pore pressure development and progressive dewatering in underthrust sediments at the Costa Rican subduction margin: Comparison with northern Barbados and Nankai, *J. Geophys. Res.*, *108*(B5), 2261, doi:10.1029/2002JB001787.

Saffer, D. M., and B. A. Bekins (1998), Episodic fluid flow in the Nankai accretionary complex: Timescale, geochemistry, flow rates, and fluid budget, *J. Geophys. Res.*, *103*(B12), 30351–30370.

Saffer, D. M., and B. A. Bekins (2002), Hydrologic controls on the mechanics and morphology of accretionary wedges and thrust belts, *Geology*, *30*(3), 271–274, doi:10.1130/0091-7613(2002)030<0271:HCOTMA>2.0.CO;2.

Saffer, D. M., and C. Marone (2003), Comparison of smectite- and illite-rich gouge frictional properties: Application to the updip limit of the seismogenic zone along subduction megathrusts, *Earth Planet. Sci. Lett.*, *215*(1–2), 219–235, doi:10.1016/S0012-821X(03)00424-2.

Saffer, D. M., and H. J. Tobin (2011), Hydrogeology and Mechanics of Subduction Zone Forearcs: Fluid Flow and Pore Pressure, *Annu. Rev. Earth Planet. Sci.*, *39*, 157–186, doi:10.1146/annurev-earth-040610-133408.

Saffer, D. M., D. A. Lockner, and A. Mckiernan (2012), Effects of smectite to illite transformation on the frictional strength and sliding stability of intact marine mudstones, *Geophys. Res. Lett.*, *39*, doi:10.1029/2012GL051761.

Satake, K., K. Shimazaki, Y. Tsuji, and K. Ueda (1996), Time and size of a giant earthquake in Cascadia inferred from Japanese tsunami records of January 1700, *Nature*, *379*(6562), 246–249, doi:10.1038/379246a0.

Schmalzle, G., R. McCaffrey, and K. C. Creager (2014), Central Cascadia subduction zone

creep, *Geochemistry, Geophys. Geosystems*, *15*, 1515–1532, doi:10.1002/2013GC005172.Received.

Screaton, E. J., D. M. Saffer, P. Henry, and S. Hunze (2002), Porosity loss within the underthrust sediments of the Nankai accretionary complex: Implications for overpressures, *Geology*, *30*(1), 19–22, doi:10.1130/0091-7613(2002)030<0019:PLWTUS>2.0.CO;2.

Screaton, E. J. et al. (2009), Interactions between deformation and fluids in the frontal thrust region of the NanTroSEIZE transect offshore the Kii Peninsula, Japan: Results from IODP Expedition 316 Sites C0006 and C0007, *Geochemistry Geophys. Geosystems*, *10*, doi:10.1029/2009GC002713.

Silver, E. A. (1972), Pleistocene tectonic accretion of the continental slope off Washington, *Mar. Geol.*, *13*, 239–249.

Simpson, G. D. H. (2010), Formation of accretionary prisms influenced by sediment subduction and supplied by sediments from adjacent continents, *Geology*, *38*(2), 131–134, doi:10.1130/G30461.1.

Storti, F., and K. Mcclay (1995), Influence of syntectonic sedimentation on thrust wedges in analogue models, , (11), 999–1002.

Suppe, J. (2007), Absolute fault and crustal strength from wedge tapers, *Geology*, *35*(12), 1127–1130, doi:10.1130/G24053A.1.

Tobin, H. J., and D. M. Saffer (2009), Elevated fluid pressure and extreme mechanical weakness of a plate boundary thrust, Nankai Trough subduction zone, *Geology*, *37*(8), 679–682, doi:10.1130/G25752A.1.

Tobin, H. J., J. C. Moore, M. E. MacKay, D. L. Orange, and L. D. Kulm (1993), Fluid flow along a strike-slip fault at the toe of the Oregon accretionary prism: Implications for the geometiy of frontal accretion, *Geol. Soc. Am. Bull.*, *105*(5), 569–582, doi:10.1130/0016-7606(1993)105<0569.

Tréhu, A. M., J. Braunmiller, and J. L. Nabelek (2008), Probable low-angle thrust earthquakes on the Juan de Fuca-North America plate boundary, *Geology*, *36*(2), 127–130, doi:10.1130/G24145A.1.

Tsuji, T., H. Tokuyama, P. Costa Pisani, and G. F. Moore (2008), Effective stress and pore pressure in the Nankai accretionary prism off the Muroto Peninsula, southwestern Japan, *J. Geophys. Res.*, *113*, doi:10.1029/2007JB005002.

Underwood, M. B., K. D. Hoke, A. T. Fisher, E. E. Davis, E. Giambalvo, L. Zuhlsdorff, and G. A. Spinelli (2005), Provenance, Stratigraphic Architecture, and Hydrogeologic Influence of Turbidites on the Mid-Ocean Ridge Flank of Northwestern Cascadia Basin, Pacific Ocean, *J. Sediment. Res.*, *75*(1), 149–164, doi:10.2110/jsr.2005.012.

Wang, K., and A. M. Tréhu (2016), Invited review paper : Some outstanding issues in the study of great megathrust earthquakes — The Cascadia example, *J. Geodyn.*, *98*, 1–18, doi:10.1016/j.jog.2016.03.010.

Wang, K., R. D. Hyndman, and E. E. Davis (1993), Thermal Effects of Sediment Thickening and

Fluid Expulsion in Accretionary Prisms: Model and Parameter Analysis, *J. Geophys. Res.*, *98*(B6), 9975–9984.

Wang, K., R. E. Wells, S. Mazzotti, R. D. Hyndman, and T. Sagiya (2003), A revised dislocation model of interseismic deformation of the Cascadia subduction zone, *J. Geophys. Res.*, *108*(B1), doi:10.1029/2001JB001227.

Wang, K., Y. Hu, and J. He (2012), Deformation cycles of subduction earthquakes in a viscoelastic Earth, *Nature*, *484*(7394), 327–32, doi:10.1038/nature11032.

Wech, A. G., K. C. Creager, and T. I. Melbourne (2009), Seismic and geodetic constraints on Cascadia slow slip, *J. Geophys. Res.*, *114*, doi:10.1029/2008JB006090.

Westbrook, G. K., B. Carson, and Shipboard Scientific Party (1994), Summary of Cascadia Drilling Results, in *Proceedings of the Ocean Drilling Program, Initial Reports*, vol. 146, edited by G. K. Westbrook, B. Carson, R. J. Musgrave, and E. Al, pp. 389–396.

Williams, M. C., A. M. Tréhu, and J. Braunmiller (2011), Seismicity at the Cascadia Plate Boundary beneath the Oregon Continental Shelf, *Bull. Seismol. Soc. Am.*, *101*(3), 940–950, doi:10.1785/0120100198.

Witter, R. C., H. M. Kelsey, and E. Hemphill-Haley (2003), Great Cascadia earthquakes and tsunamis of the past 6700 years, Coquille River estuary, southern coastal Oregon, *Geol. Soc. Am. Bull.*, *115*(10), 1289–1306, doi:10.1130/B25189.1.

Yue, H., T. Lay, L. Rivera, C. An, C. Vigny, and X. Tong (2014), Localized fault slip to the trench in the 2010 Maule, Chile Mw = 8.8 earthquake from joint inversion of high-rate GPS, teleseismic body waves, InSAR, campaign GPS, and tsunami observations, *J. Geophys. Res. Solid Earth*, *119*, 7786–7804, doi:10.1002/2014JB011340.Received.

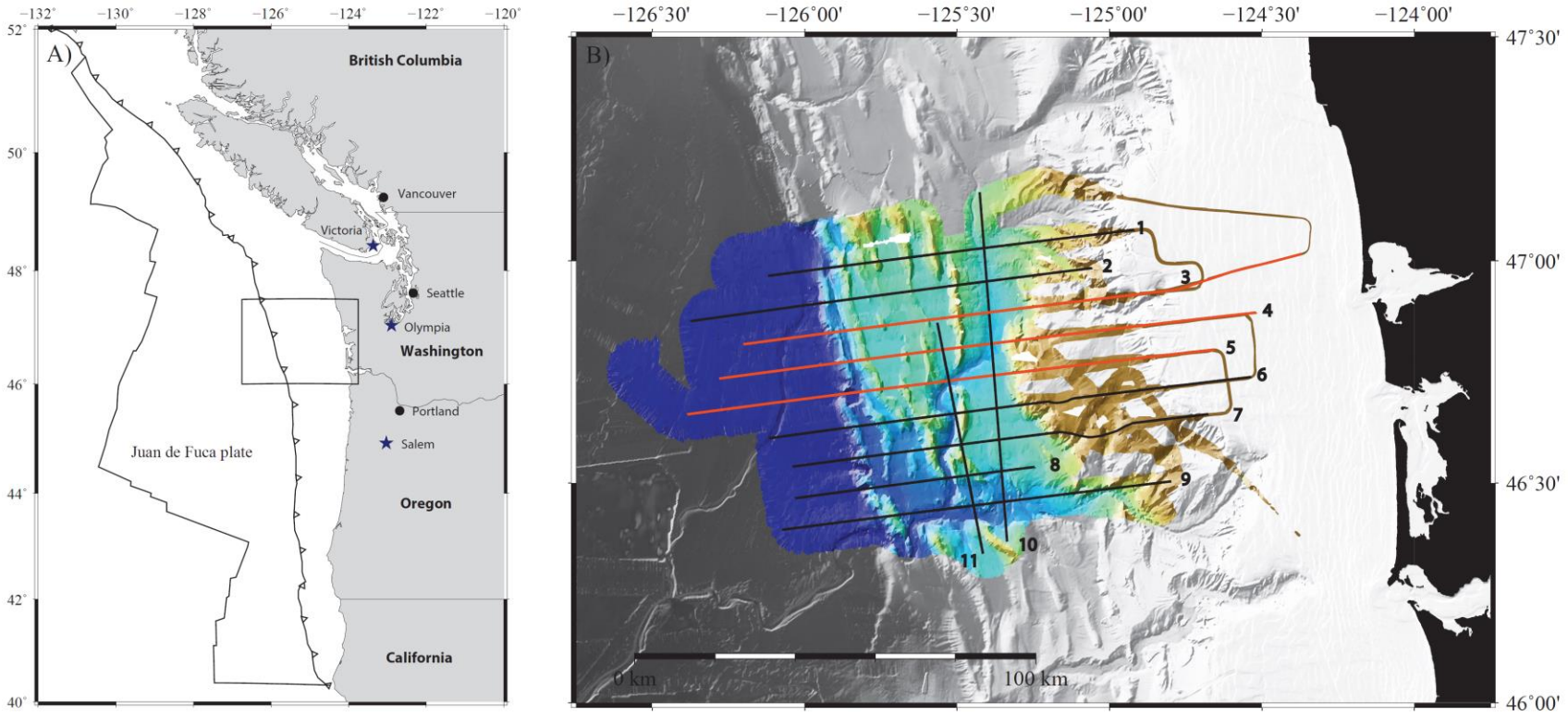

Figure 3.1: A) Regional map of the Cascadia subduction zone, where the Juan de Fuca plate subducts under North America. State/provincial capitols are marked with a star and most populous cities with a circle. Box shows inset location of B, the COAST survey. B) COAST survey lines, shown on top of multibeam bathymetry. Lines 3, 4 and 5, highlighted in orange, were used in this paper.

Figure 3.2:

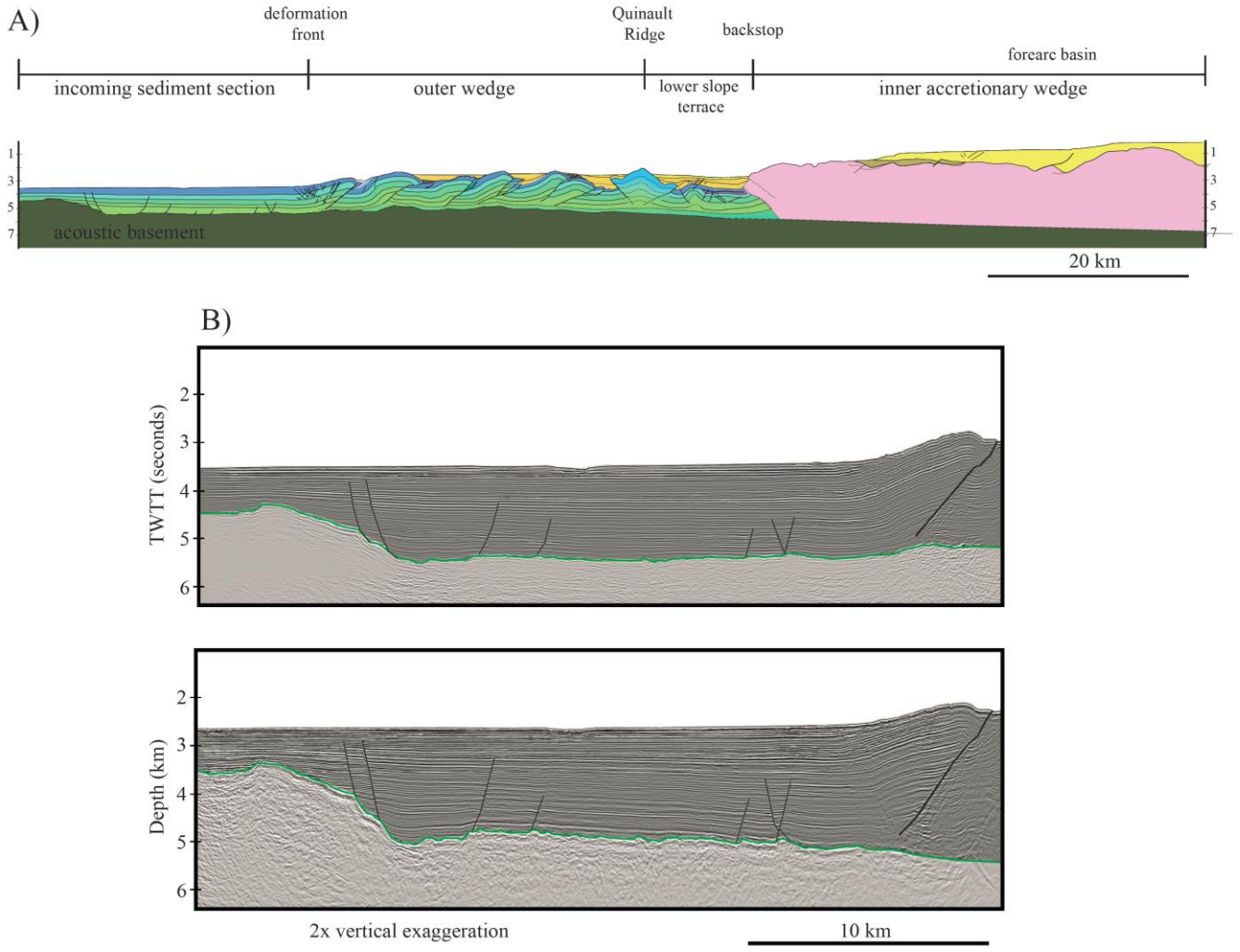
A)
deformation front
Quinault Ridge
backstop
forearc basin
incoming sediment section
outer wedge
lower slope terrace
inner accretionary wedge
1
3
5
7
acoustic basement
20 km
B)
TWTT (seconds)
2
3
4
5
6
Depth (km)
2x vertical exaggeration
10 km

Figure 3.2

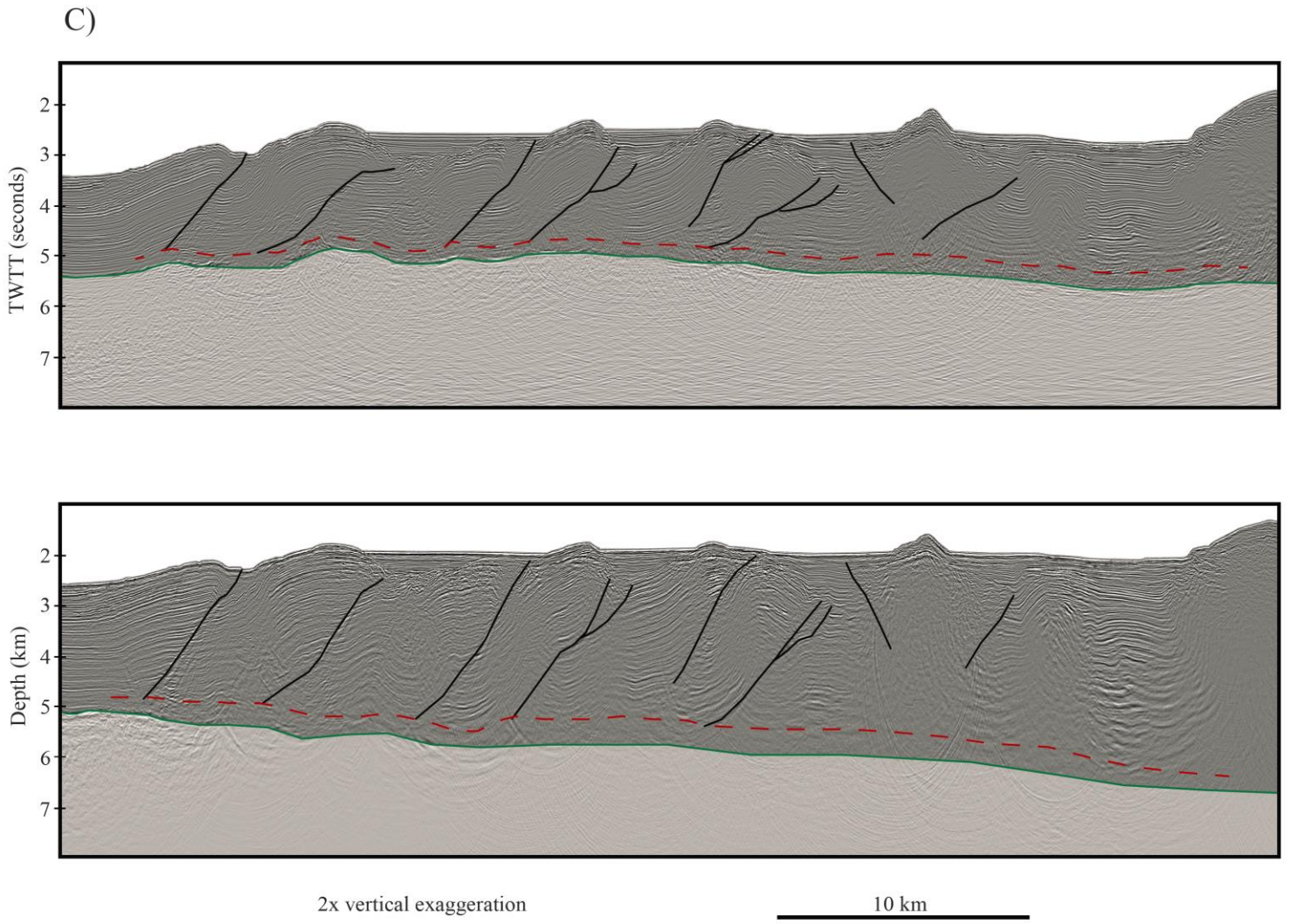
C)
TWTT (seconds)
2
3
4
5
6
7
Depth (km)
2
3
4
5
6
7
2x vertical exaggeration
10 km

Figure 3.2: A) Simplified interpretation of line 4, showing general tectonic domains of the Cascadia subduction zone seen in the COAST dataset. Incoming sediments are thick, but relatively undeformed except for small normal faults at the bottom of the section. B is line 4 in time and depth, showing interpretation of the faults in the incoming sediment section. C shows the interpreted faults of the outer wedge in the time domain and the depth domain. In both B and C, the acoustic basement is shown as shaded, with a green line at its top. Faults are shown in black, and the interpreted underthrust section is shown with a dashed red line. Deformation is mostly in the form of large landward vergent thrust faults, underlain by an interpreted underthrust section, above acoustic basement. The Quinault Ridge separates the outer wedge from the lower slope terrace. The inner accretionary prism is less seismically coherent, and is not analyzed in this study.

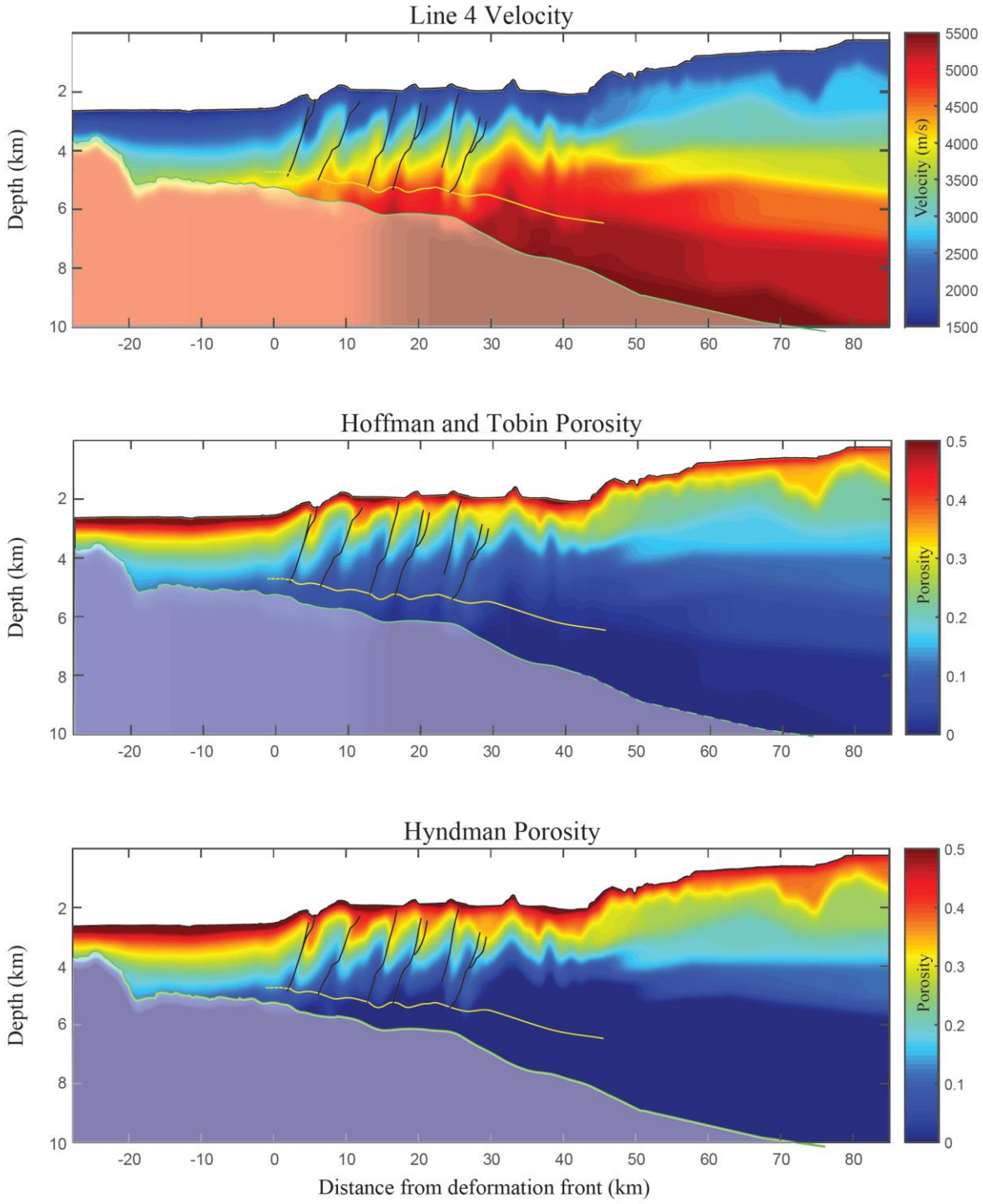

Figure 3.3: A) Horizon-based tomography velocity model of line 4. Incorporation of the thrust faults can be seen in the outer wedge, as can the relatively high velocity values below those thrust sheets. B) Porosity from the velocity model in A using the *Hoffman and Tobin* [2004] velocity-porosity transform. C) Porosity from the velocity model in A using the *Hyndman et al* [1990] porosity model. Values using the Hyndman model go to 0 relatively quickly below the wedge, indicating that the estimates at depth may not be as reliable.

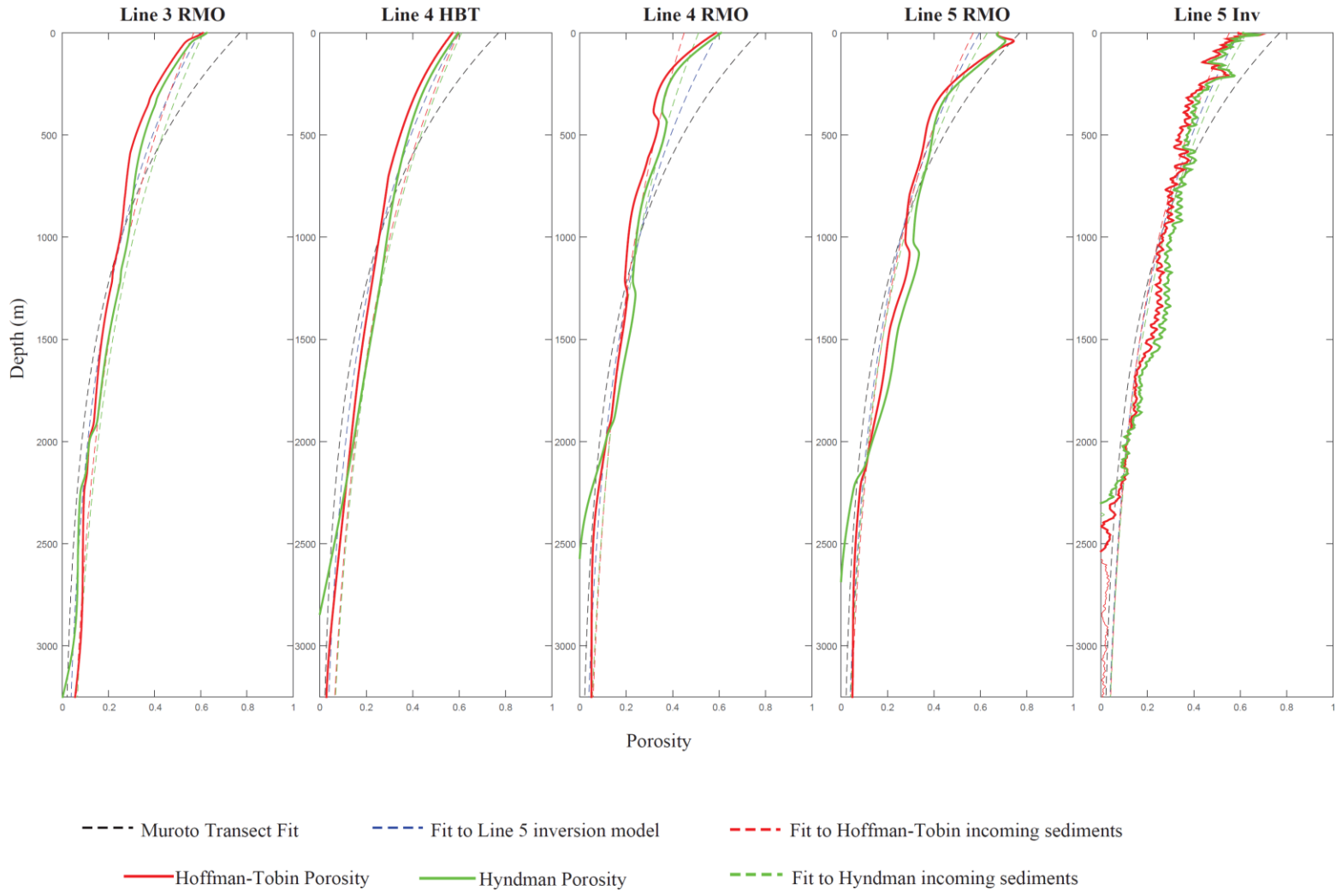

Figure 3.4: Incoming sediment porosites from both the *Hoffman and Tobin* [2004] and *Hyndman et al* [1993] models, plotted with the fit from each of the Athy curves. The Muroto Transect Athy curve has significantly higher inital porosity values than those fit to the sediment sections here. RMO = residual moveout models, HBT = horizon-based tomography model, Inv = inversion model

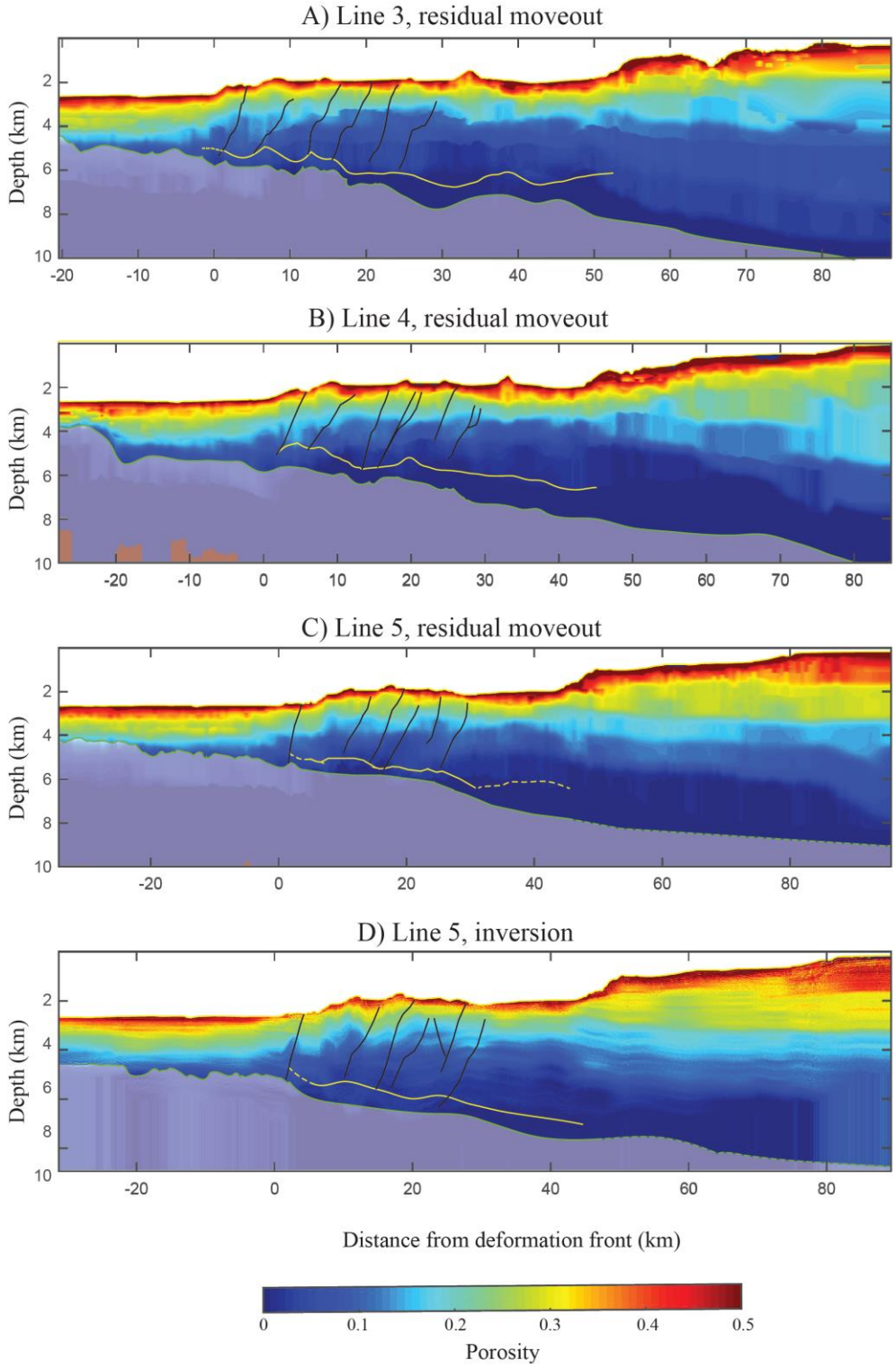

Figure 3.5: Porosity models from residual moveout velocity models (A,B,C) and an inversion model (C). Porosity values are from the *Hoffman and Tobin* [2004] velocity-porosity transform. Black lines are faults interpreted from the seismic reflection sections in depth with the top of the interpreted underthrust package shown in yellow.

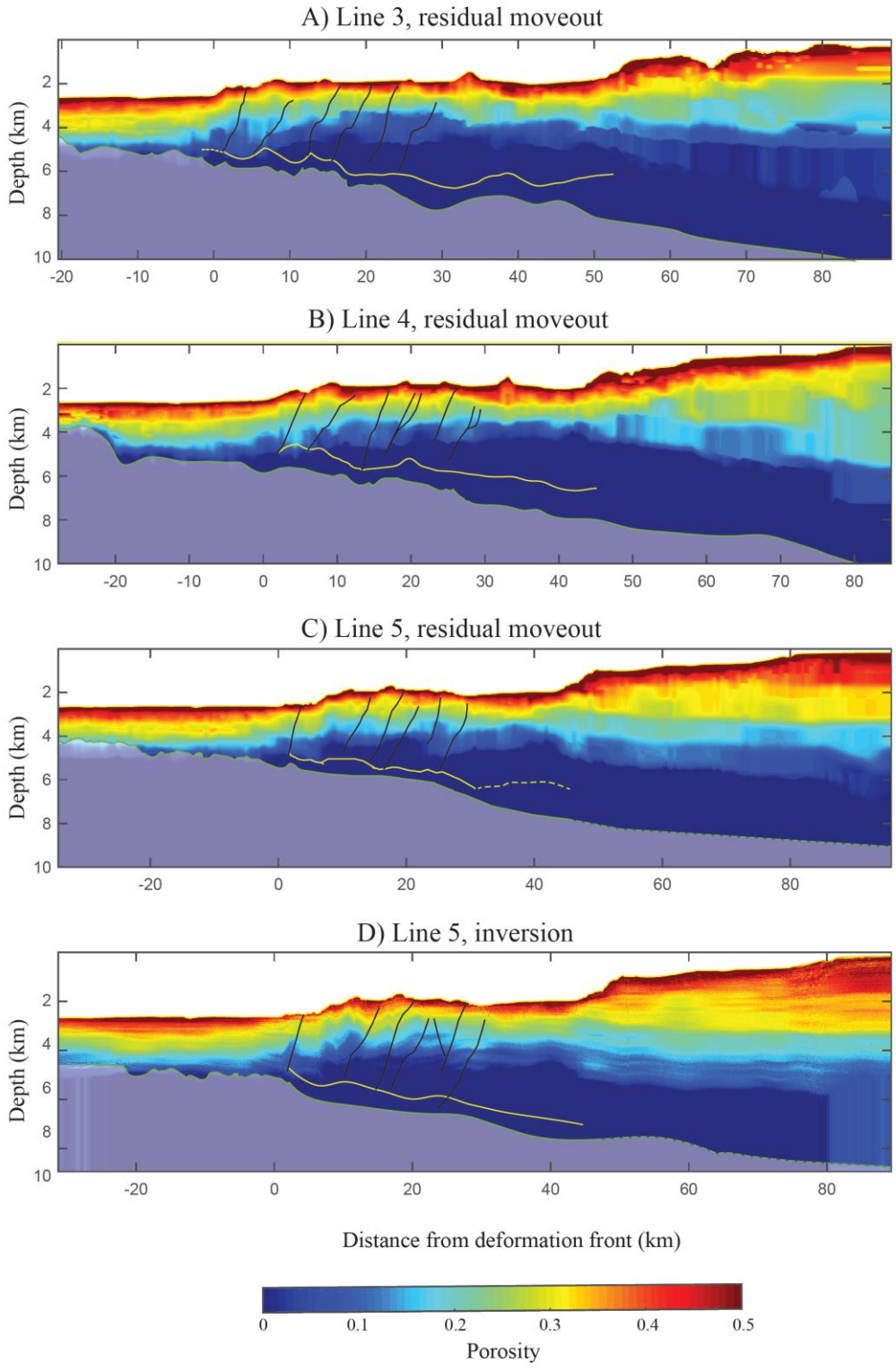

Figure 3.6: Porosity models from residual moveout velocity models (A,B,C) and an inversion model (C). Porosity values are from the *Hyndman et al* [1993] velocity-porosity transform. Black lines are faults interpreted from the seismic reflection sections in depth with the top of the interpreted underthrust package shown in yellow.

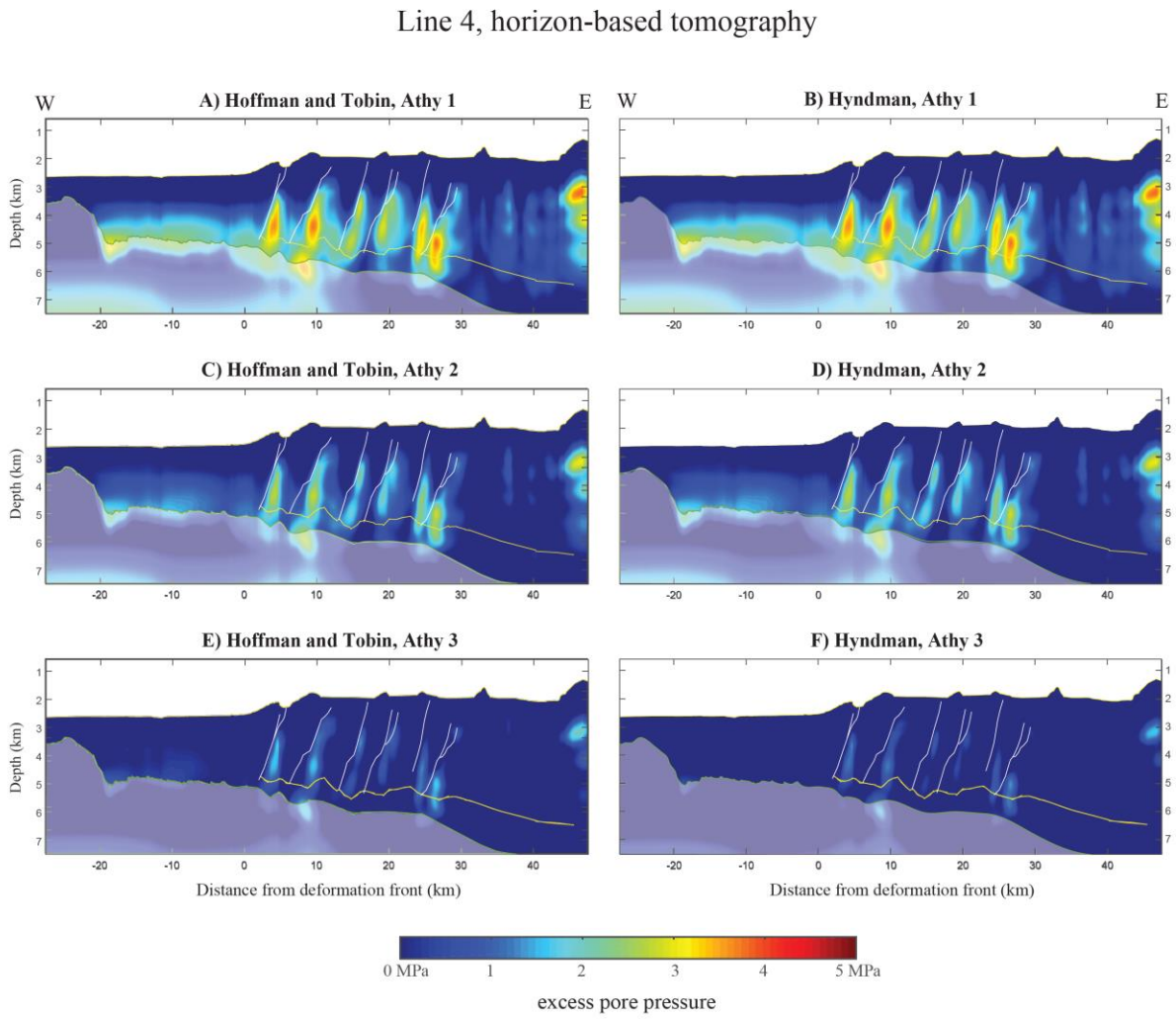

Figure 3.7: Excess pore pressure sections for the incoming sediment section, outer wedge and lower slope terrace of Line 4, horizon-based tomography velocity model. A, C, and E use *the Hoffman and Tobin* [2004] velocity-porosity transform, and B, D, and F use the *Hyndman et al* [1993] velocity-porosity transform. A and B use the Muroto Transect compaction curve, from Screaton et al [2002]. C and D use the compaction curve derived from the inversion model porosity. E and F are from the compaction curves fit to the particular line and velocity-porosity transform.

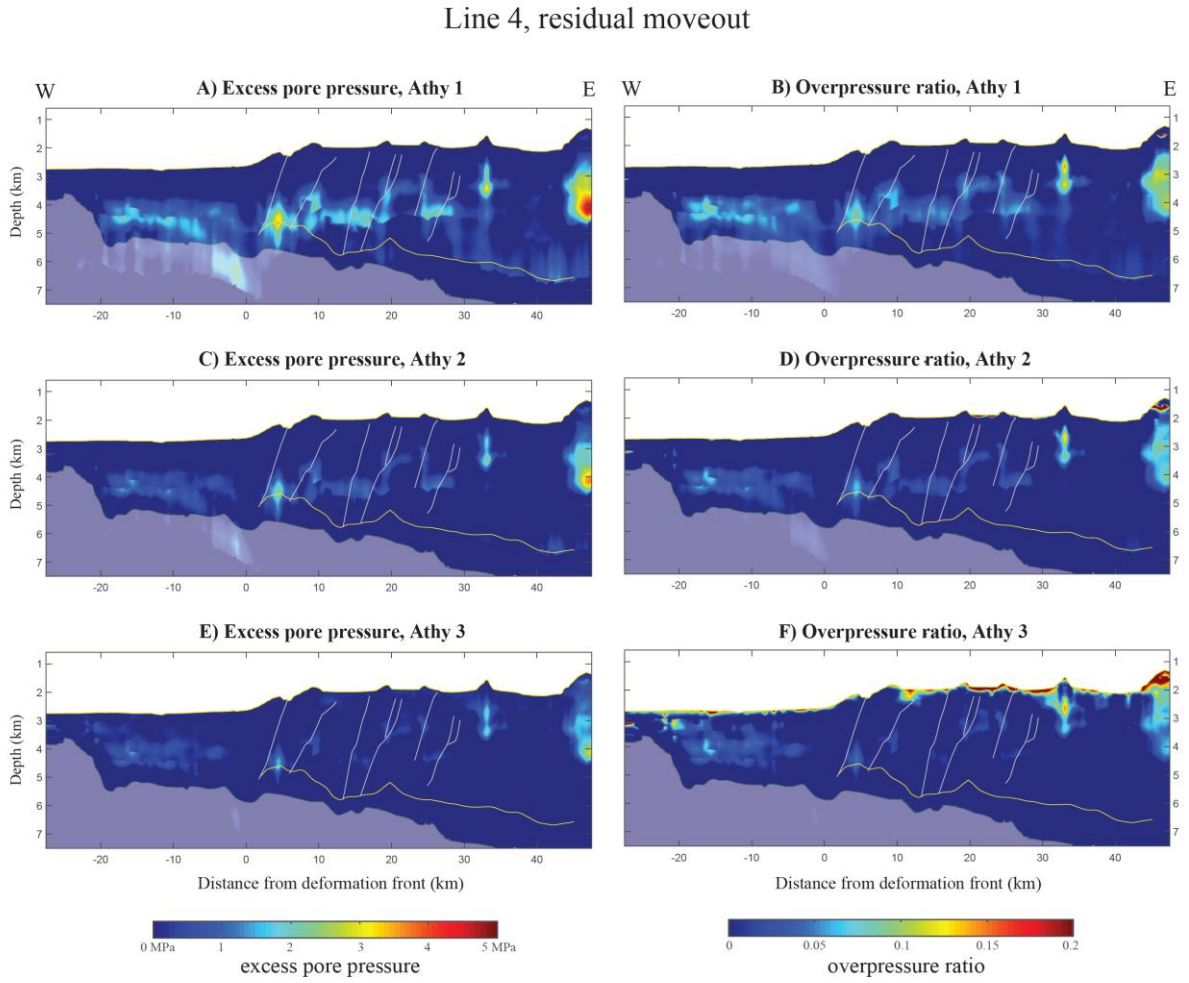

Figure 3.8: Excess pore pressure (A, C, E) and overpressure ratio (B, D, F) sections for the incoming sediment section, outer wedge, and lower slope terrace of Line 4, residual moveout model. Faults are shown in gray and the top of the underthrust section is shown in yellow. A small area of relatively high excess pore pressure value can be seen in the shallow Quinault Ridge (~32 km landward from the deformation front)--the only non-zero value that can be seen in the ridge.

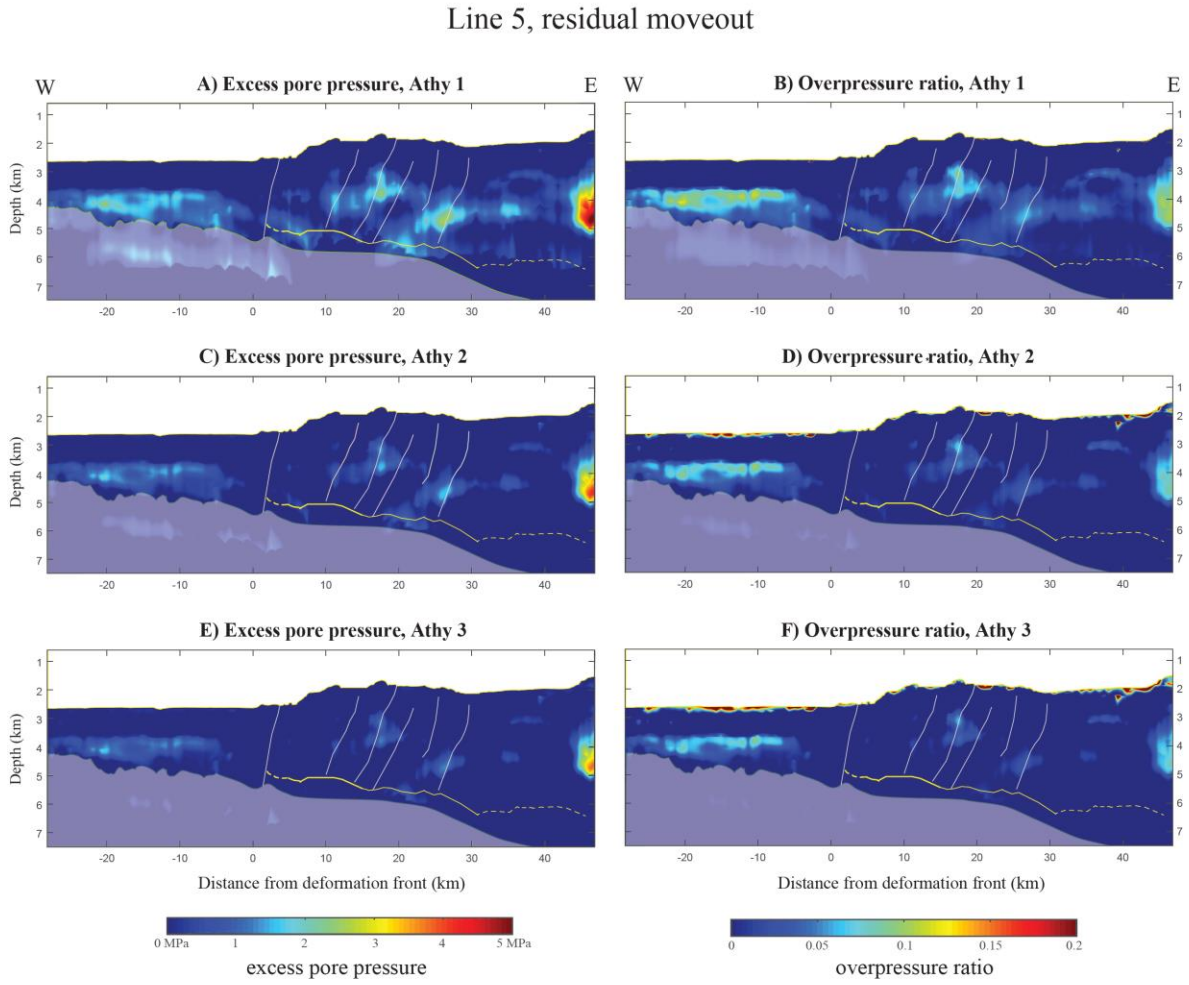

Figure 3.9: Excess pore pressure sections (A, C, E) and overpressure ratio sections (B, D, F) for the incoming sediment section, outer wedge, and lower slope terrace of Line 5 residual moveout velocity models. As with other figures, interpreted faults are shown in gray and the top of the interpreted underthrust sediment section is yellow. Line 5's frontal thrust soles into the oceanic crust, showing an active basal decollement.

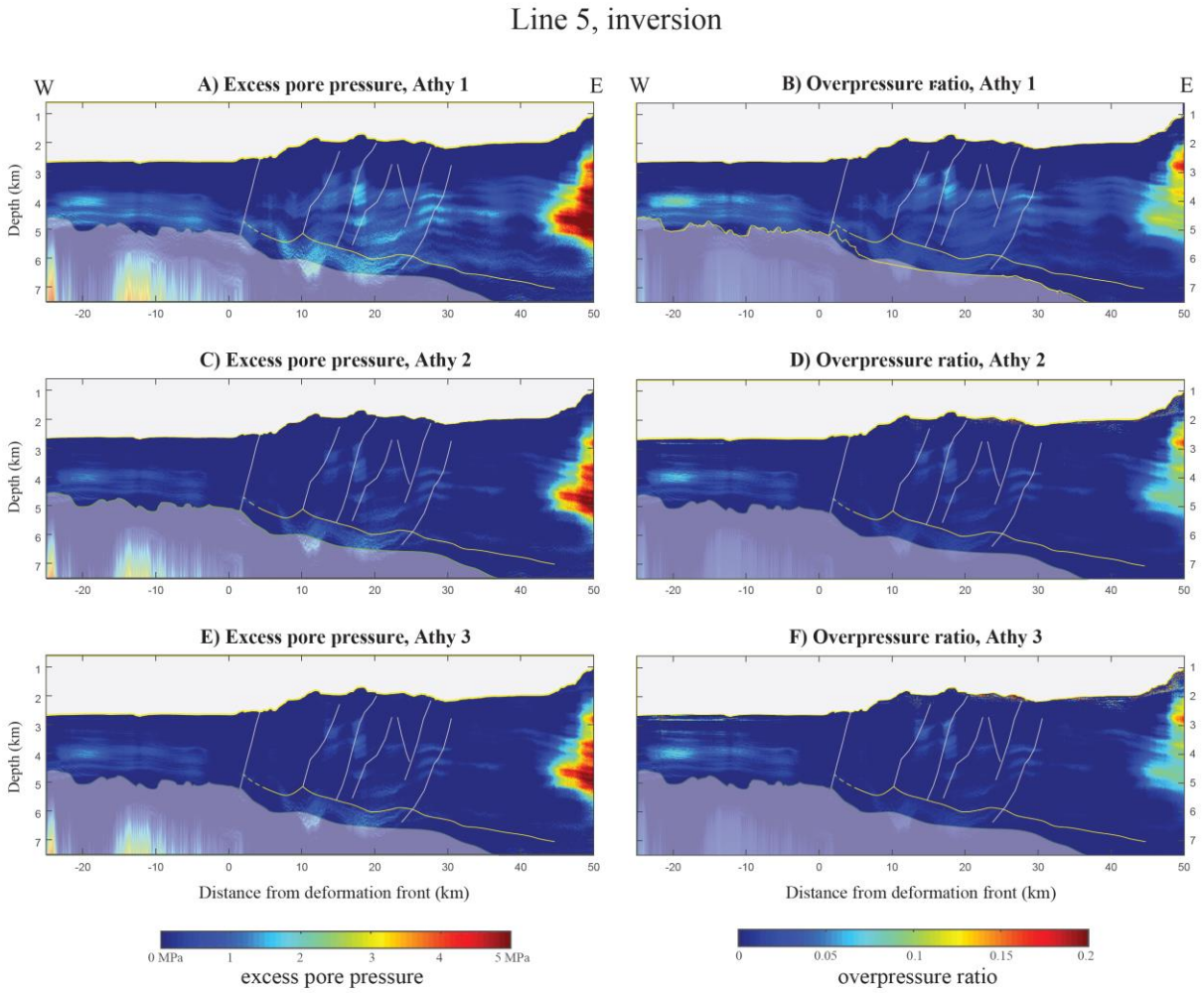

Figure 3.10: Companion figure to line 10, but with Line 5 using the inversion method. Positive values for excess pore pressure and overpressure ratio are more diffuse, but there are no strong individual anomalies.

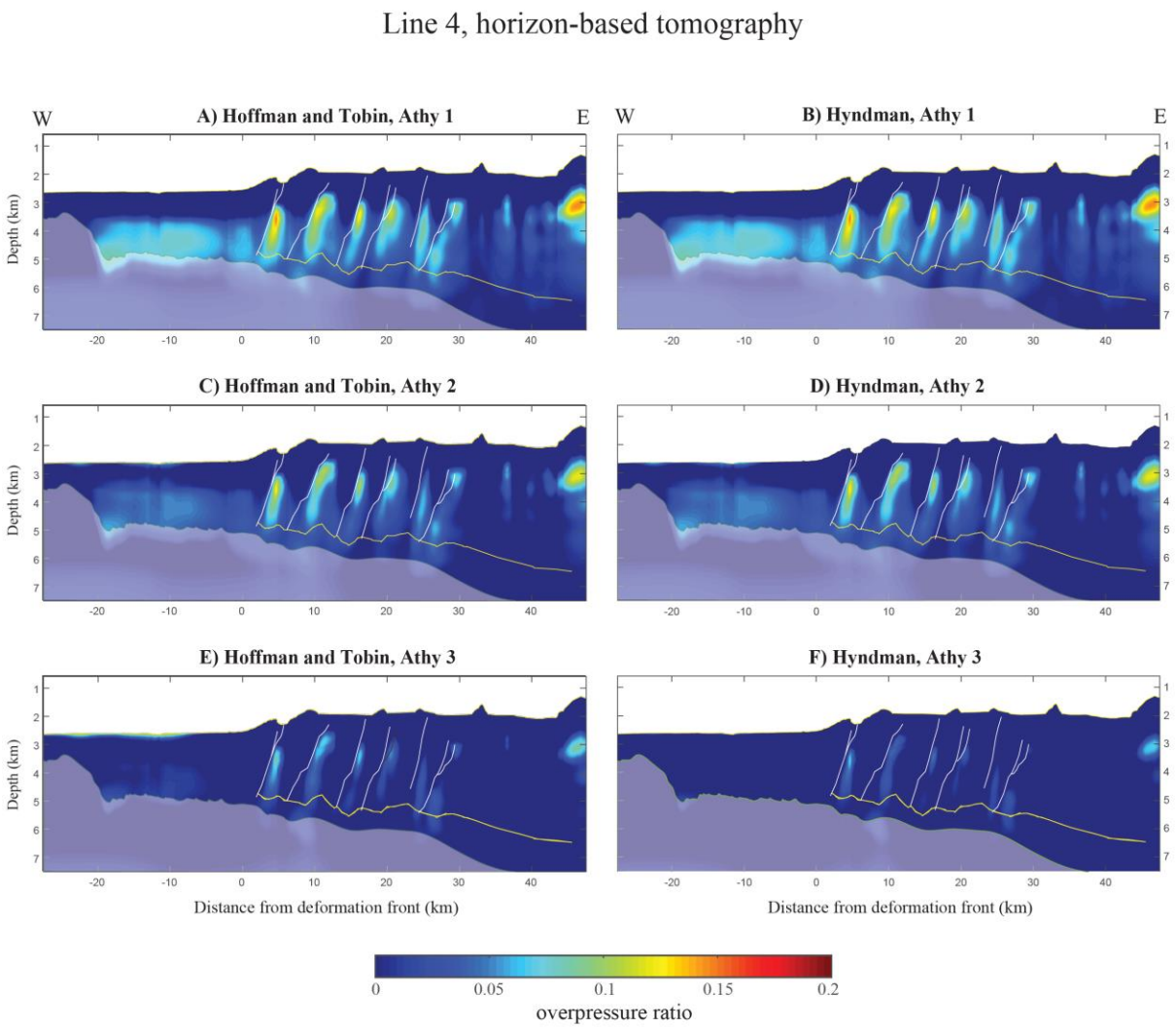

Figure 3.11: Overpressure ratios for Line 4, horizon-based tomography model. A, C, and D use the *Hoffman and Tobin* [2004] velocity-porosity transform, and B, D, and F use the *Hyndman et al* [1993] transform. A and B use the Muroto Transect compaction curve, from *Screaton et al* [2009]. C and D use the compaction curve derived from the inversion model porosity. E and F are from the compaction curves fit to the particular line and velocity-porosity transform. The horizon-based tomography model shows evidence of anomalies at faults, and some very low overpressure ratios at the base of the wedge.

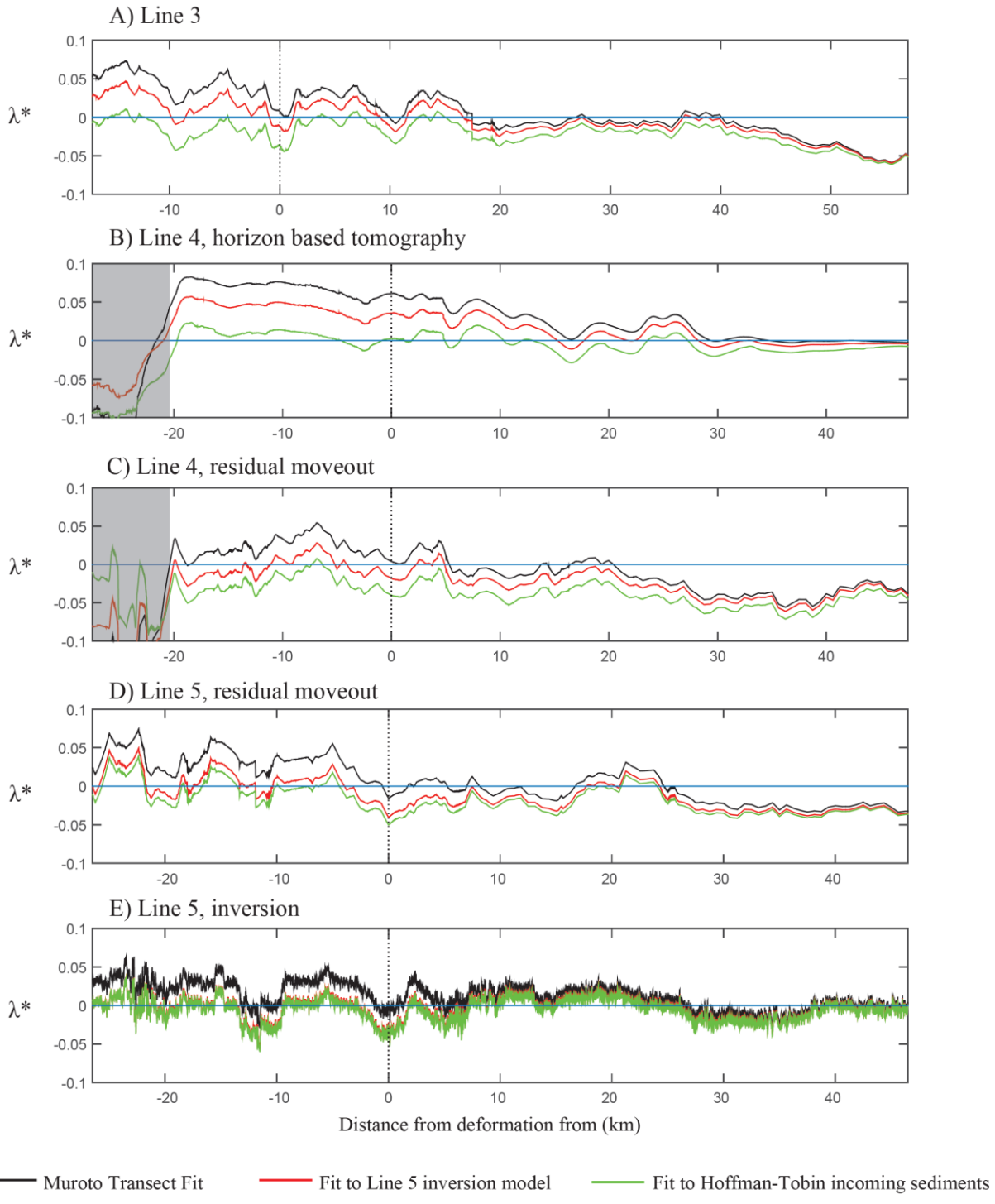

Figure 3.12: Extracted overpressures from 200 m above the oceanic crust through the incoming sediment section and outer wedge, calculated using the *Hoffman and Tobin* [2004] velocity-porosity transform. The vertical dashed line indicates the deformation front. The three curves represent the three Athy curves used in the analysis. The fit to the incoming sediment section of each individual model (green curve) generally gives unrealistic values. Overpressure ratios indicate very low overpressure at depth. The gray box indicates the location of a basement high in line 4.

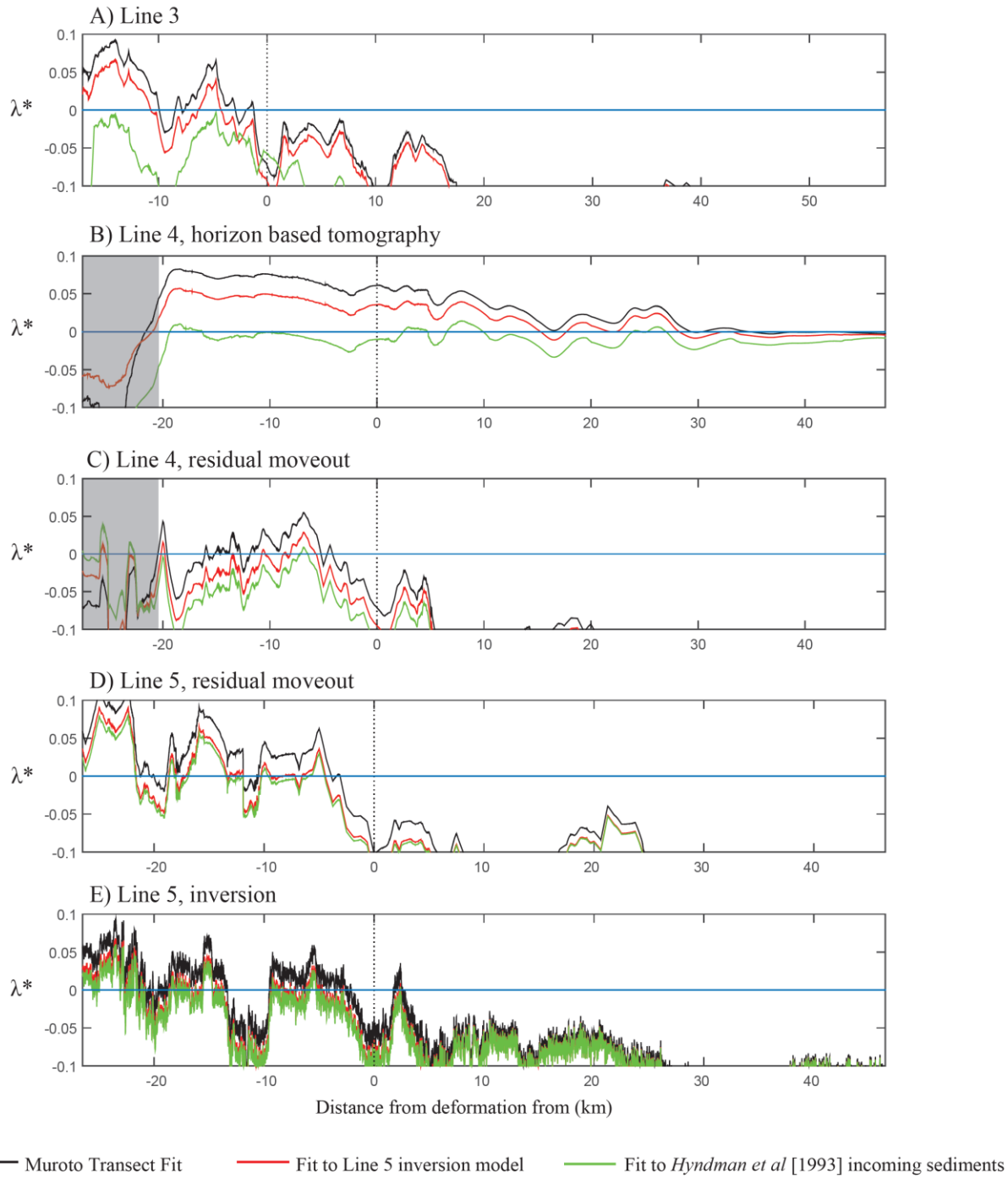

Figure 3.13: Extracted overpressures from 200 m above the oceanic crust through the incoming sediment section and outer wedge, calculated using the *Hyndman et al* [1993] velocity-porosity transform. The vertical dashed line indicates the deformation front. The three curves represent the three Athy curves used in the analysis. The Hyndman curve quickly goes to zero porosity below the outer wedge, giving unrealistic values at depth. The gray box indicates the location of a basement high in line 4.

4 Log-based evaluation of properties of the deeper inner accretionary wedge above the megasplay fault, Nankai Trough, Japan

Abstract

Recent drilling has sampled the inner accretionary wedge of the Nankai Trough, Japan to a depth of 3 km below the sea floor, revealing a silty claystone, dubbed Unit V, that extends for over a kilometer in depth with a remarkably homogeneous log response. The inner wedge is poorly imaged in the seismic data, so well logs, drill cuttings, and very limited core sampling are relied upon for structural and lithologic information at depth. Here, sonic waveforms from both monopole and dipole logging tools are processed to produce both compressional and shear wave velocities through this previously unsampled unit of the inner wedge. These reprocessed values are then used to estimate the bulk and shear moduli at depth. The calculated moduli are similar to those experimentally determined for clays elsewhere. The moduli values indicate that the wedge is at least partially constructed of compliant material, which has implications for the extent of rupture in an earthquake and the potential of wedge deformation and tsunamigenesis. Attempts to correlate changes in log values to specific deformed zones proved unsuccessful, so all structural information relies on the interpretation of resistivity images. The log sonic velocity is constant with depth. One interpretation of this signal would be an estimate of low overpressure in the wedge. However, the core and cuttings samples show decreasing porosity with depth, following a normal compaction trend, which would not support the low overpressure hypothesis. This trend in porosity may indicate that the sediment is currently experiencing its peak load, which would imply an isolation from tectonic stresses earlier in its history, when it was incorporated into the accretionary wedge.

4.1 Introduction

Subduction zones are the location of very large magnitude earthquakes. These earthquakes have the potential to cause tsunami and be very damaging, as seen in Sumatra, Japan, and Chile within the last fifteen years (e.g. [*Lay et al.*, 2005; *Ito et al.*, 2011; *Yue et al.*, 2014; *Lay*, 2015]). Stress

state, pore pressure distribution, friction, and other material properties in the subduction zone are important factors controlling earthquake nucleation, propagation, and rupture area [*Scholz*, 1998; *Moore and Saffer*, 2001; *Bangs et al.*, 2009; *Ikari and Saffer*, 2011; *Ikari et al.*, 2015; *Chang and Song*, 2016; *Lotto et al.*, 2017]. Frictional properties of materials can govern the slip behavior of faults, either promoting stick-slip or stable sliding [*Kopf and Brown*, 2003; *Saffer and Marone*, 2003; *Ikari et al.*, 2010]. Rapid underthrusting of high porosity sediments in a subduction zone can lead to high pore fluid pressure at depth, which is correlated to the updip limit for seismogenesis [*Bekins et al.*, 1994; *Screaton et al.*, 2002; *Brown et al.*, 2003; *Saffer*, 2003; *Bangs et al.*, 2009]. Dehydration reactions at depth can also lead to increased pore fluid pressure [*Bekins et al.*, 1994; *Saffer and Bekins*, 1998; *Moore and Saffer*, 2001; *Saffer and Tobin*, 2011]. Low velocity zones at depth are seen within subduction zones that have ruptured in large earthquakes, and the downdip edge of the low velocity zone is often correlated with the updip limit of the seismogenic zone (e.g. [*Oleskevitch et al.*, 1999; *Moore and Saffer*, 2001; *Ge and Screaton*, 2005; *Ranero et al.*, 2008; *Bangs et al.*, 2009; *Hung et al.*, 2009; *Wallace et al.*, 2009]). Material properties of the wedge may also impact the extent of rupture. In models of dynamic rupture, the inclusion of a more compliant wedge causes rupture to slow below the wedge, but shallower slip and tsunami generation is more likely [*Lotto et al.*, 2017].

Given the complex deformation history of sediments at convergent margins, as well as their current burial depths, determining the conditions and properties at depth can be difficult. Seismic data typically images the outer wedges of these subduction zones relatively well, allowing for detailed structural interpretation (e.g. [*Barnes and de Lepinay*, 1997; *Adam et al.*, 2004; *Moore et al.*, 2009a; *Wallace et al.*, 2009; *Kington*, 2012]). However, the older, landward sections of these subduction zones can be more difficult to interpret based on seismic data,

typically because they are more strongly deformed. Tomographic velocity models can be used to estimate conditions at depth and within the acoustically chaotic portion of the wedge [*Tsuji et al.*, 2014]. Shallow (<1.5 km) sites have been drilled at convergent margins, allowing inferences to be made about shallow conditions there and extrapolated to depth (e.g. [*Screaton et al.*, 2002; *Bangs and Gulick*, 2005; *Ask and Morgan*, 2010; *Hashimoto et al.*, 2010; *Raimbourg et al.*, 2011; *Schumann et al.*, 2014]). Direct sampling of areas that are not well imaged can help inform our understanding of the lithology and structural history within the older portions of the wedge, as well as help refine our estimates of physical properties and stress states at depth.

In the Nankai Trough, Japan, recent drilling on Integrated Ocean Drilling Program (IODP) Expeditions 338 and 348 has sampled the deep inner accretionary wedge above the megathrust, a plate boundary fault that is thought to have ruptured during past earthquakes [*Strasser et al.*, 2014a; *Tobin et al.*, 2015a]. Using logging-while-drilling (LWD) data, supplemented by core and cuttings analysis, the properties of the inner wedge at depth can be examined. In this study, we have: 1) reprocessed velocity logs to improve P-wave data and develop an S-wave log, 2) investigated whether structural domains can be identified using logging data, 3) used the reprocessed sonic log to estimate bulk moduli and physical properties at depth, and 4) integrated findings with possible structural histories of the inner wedge. These constraints can be used test assumptions and improve understanding of material properties of the plate boundary zone, including the overlying hanging wall wedge.

4.2 The Nankai Trough

4.2.1 Setting and Structure

The Nankai Trough is located offshore the southwestern coast of Japan, where the Philippine Sea plate subducts obliquely under Japan at a rate of approximately 6 cm/yr [*DeMets et al.*, 2010]. This area has been the focus of several Ocean Drilling Program (ODP) and Integrated Ocean Drilling Program (IODP) expeditions over three transects (Figure 4.4.1a): the Ashizuri and Muroto transects offshore Shikoku Island, and the Kumano Basin transect offshore the Kii Peninsula, Honshu Island [*Moore et al.*, 1990, 2001; *Tobin et al.*, 2009]. The most recent drilling in the Kumano Basin area (Figure 4.4.1b) is part of the Nankai Trough Seismogenic Zone Experiment (NanTroSEIZE), whose ultimate goal is to sample and instrument the seismogenic zone of an active subduction zone plate-boundary fault at depth [*Tobin and Kinoshita*, 2006; *Tobin et al.*, 2009, 2015a; *Underwood et al.*, 2010; *Strasser et al.*, 2014a].

The Nankai Trough has an extensive record of subduction zone earthquakes that span 1300 years [*Ando*, 1975]. The two most recent earthquakes, a M8.2 in 1944 and a M8.3 in 1946, were both accompanied by large tsunami [*Ando*, 1975; *Tanioka and Satake*, 2001]. A large out of sequence thrust fault, termed the megasplay, is thought to have slipped coseismically in the 1944 event, as well as other past earthquakes [*Cummins and Kaneda*, 2000; *Baba and Cummins*, 2005; *Kodaira et al.*, 2006]. Very low frequency earthquakes along the plate boundary and slow slip events have also been observed; slow slip appears to be associated with low stress drops, and the very low frequency earthquakes are associated with areas of inferred high pore pressure and low stress [*Obara and Ito*, 2005; *Ito and Obara*, 2006; *Kitajima and Saffer*, 2012; *Sugioka et al.*, 2012].

The availability of 3D seismic data has allowed for detailed structural interpretation in the Kumano Basin area (Figure 4.4.2) [*Bangs et al.*, 2006; *Kimura et al.*, 2007, 2011, *Moore et al.*, 2007, 2009a, 2009b; *Nakanishi et al.*, 2008; *Gulick et al.*, 2010; *Park et al.*, 2010; *Kington*, 2012]. The incoming oceanic plate is covered by more than 1 km Shikoku Basin hemipelagic sediments [*Pickering et al.*, 1993, 2013; *Underwood and Guo*, 2013]. Lower Shikoku Basin sediments are subducted and the upper Shikoku Basin and trench fill sediments are accreted to form an outer wedge fold and thrust belt, consisting of imbricate seaward-vergent faults overlain by slope sediment basins. The outer wedge is separated from the Miocene inner accretionary wedge by the megasplay [*Park et al.*, 2002]. The inner accretionary wedge appears chaotic, with few to no lateral seismic reflectors, which makes structural or sedimentary features difficult to resolve at depth. The wedge is overlain by the Kumano forearc basin, which has undergone several phases of deposition and deformation [*Gulick et al.*, 2004; *Martin et al.*, 2010; *Kington*, 2012; *Moore et al.*, 2015].

A low-velocity zone beneath the megasplay and plate boundary fault is observed in velocity models, and hypothesized to be fluid-rich and therefore weak [*Brown et al.*, 2003; *Tsuji et al.*, 2008; *Bangs et al.*, 2009; *Park et al.*, 2010; *Kamei et al.*, 2012]. Calculations performed on Muroto transect velocity models show a pore pressure ~75% of lithostatic within the underthrust sediments [*Tobin and Saffer*, 2009]. Evidence for less-than-normal compaction, potentially due to overpressure, is also seen in estimates of physical properties from the underthrust sediment at the toe of the accretionary wedge in the Kumano Basin area [*Screaton et al.*, 2002].

4.2.2 Borehole logging datasets

IODP Site C0002 has been sampled intensively over the course of several expeditions, and is the location of the deepest holes drilled into any accretionary wedge (Figure 4.4.1b, c). Hole C0002

is the deepest scientific drill hole anywhere in the world ocean. In 2007, Expeditions 314/315/316 collected log and core data through the forearc basin and into the Miocene inner accretionary wedge [*Tobin et al.*, 2009]. A large suite of logging data is available for hole C0002A, which goes through Units I, II and III of the Kumano Basin and into Unit IV of the inner wedge (Figure 4.4.3). Hole C0002B was cored through these four units as well. Recently, in 2012 and 2014, Expeditions 338 and 348 drilled further into the deeper, older inner accretionary wedge at Site C0002 and collected a suite of LWD data as well as core and cuttings data [*Strasser et al.*, 2014a; *Tobin et al.*, 2015a]. Expedition 338 drilled hole C0002F, sampling Kumano Basin sediments (Unit III) before reaching Units IV and V of the inner accretionary wedge, reaching a total depth of 2004 mbsf (Figure 4.4.3). Expedition 348 sidetracked from C0002F to drill C0002N, which reached a depth of 2330 mbsf. Hole C0002P continued in Unit V, reaching a final depth of 3058 mbsf. LWD gamma ray and resistivity logs were collected in all holes, with a sonic tool added in C0002F and C0002P (Figure 4.4.3). Resistivity image logs were also collected in C0002F and C0002P to analyze the structure of the inner wedge. Logging data were acquired by two service companies. Schlumberger logged hole C0002F with arcVISION (gamma ray, azimuthal resistivity, pressure and temperature), geoVISION (natural gamma ray and resistivity), sonicVISION (sonic), and TeleScope instruments. Halliburton logged holes C0002N with the EWR-PHASE4 (gamma ray and resistivity) and C0002P with EWR-M5 (gamma ray and resistivity), AFR (azimuthal resistivity), and XBAT (sonic). Technical specifications are available at http://www.halliburton.com/en-US/ps/sperry/drilling/lwd.page?node-id=hfyjrqtw. Cuttings were collected and analyzed on board the ship during both expeditions, and core samples from 2163-2218.5 mbsf were collected in C0002P.

One other site, C0009, was drilled through the Kumano Basin and reached Unit IV in the inner accretionary wedge [*Expedition 319 Scientists*, 2010a]. Wireline logs were acquired in C0009, including P- and S-wave velocities as well as neutron density and porosity. However, the caliper from these wireline runs indicates extremely poor hole quality in the inner wedge, so the data quality reliability of those logs may be questionable.

4.3 Data processing

4.3.1 Sonic log processing

Both monopole and dipole waveforms were collected in hole C0002P by Halliburton using the X-Bimodal AcousTic (XBAT). The XBAT has four transmitters and four azimuthal arrays of six receivers, and a source frequency between 2 and 25 kHz was used in data collection [*Tobin et al.*, 2015a]. Final sonic logs delivered by the contractor included P-wave and S-wave slowness values, but the logs showed different trends than initial shipboard slowness logs. We reprocessed the raw waveform data and obtained new P-wave and S-wave slownesses.

In order to reprocess the P-wave and S-wave monopole and dipole data, the raw waveforms were loaded into Geolog, the well logging application that is part of the Paradigm interpretation software package. Waveforms were sorted according to the tool geometry into source-receiver arrays (A, B, C, D), and inspected for missing values before a bandpass filter was applied to remove noise. Velocity logs were picked using slowness-time semblance plots constructed from each of the source-receivers sets (e.g. [*Haldorsen et al.*, n.d.; *Kimball and Marzetta*, 1984; *Barton et al.*, 1989]). Semblance was calculated using the Create Semblance Module in Geolog. For the monopole, each source-receivers set was analyzed independently, and then averaged. Dipole data were processed as individual arrays, but also processed in the X and Y direction.

Initial slowness seed values were used to guide initial computer-based picking for both P- and S-wave slowness logs. The initial automatically picked slowness values were inspected and manually edited. We then used the edited slowness log as a guide for a second set of automatic picks. We repeated this process until the slowness log values corresponded to the semblance peak at the each depth. Some areas required more manual editing than others, as the strength of the signal was not consistent through the borehole.

The P-wave signal was clearest on the monopole data, whereas the better quality S-wave was seen in the dipole semblance plots. The signal for the shear wave in the dipole tool often had two separate high semblance peaks. Test logs were individually picked on each of these highs to determine the slowness values associated with each peak. This spreading out of signal is most likely due to frequency dispersion, which was partially mitigated by processing the dipole in the X and Y direction. When analyzing sonic log data from a dipole, the low frequency signal produces a more reliable estimate of the S-wave velocity through the formation, as it samples more of the formation and is less affected by the presence of the borehole. This low frequency signal, corresponding to the first peak, will provide lower slowness (higher velocity) values that more accurately reflect the S-wave velocity through the formation. The final S-wave slowness was picked on the first peak of double peak semblance areas.

The data quality was variable but overall there was enough coherent signal for reliable picks of the P-wave in the monopole data and the S-wave in the dipole data, at a finer resolution than the logs previously available. Both the monopole P-wave and the dipole S-wave slownesses were converted to velocity logs, which were used in the following analysis (Figure 4.4).

4.3.2 Resistivity image processing and structural interpretation

Both bedding and fractures can be picked as sinusoids on resistivity images, so their orientation and dip can be recorded [*e.g.* [*McNeill et al.*, 2004; *Ienaga et al.*, 2006]. Azimuthal resistivity images were collected on both Expeditions 338 and 348, in holes C0002F and C0002P. Shipboard interpretation of bedding and fractures was carried out for both holes [*Moore et al.*, 2013; *Tobin et al.*, 2015a]. Resistivity image data were loaded into Geolog and processed to obtain both statically (with absolute resistivity image values throughout the borehole) and dynamically (where the resistivity images are normalized over a moving window) normalized images. Fracture and bedding dips were then interpreted (see bedding and fracture dips, Figure 4.5). The bedding and fracture surfaces picked here are consistent with those seen in the shipboard data as well as those published in *Boston et al.* [2016].

4.4 Log description

The focus of this work was the inner accretionary wedge at Site C0002, which encompasses Unit IV and Unit V. Shipboard logging units were defined based on log properties. Logging units for holes C0002F and C0002P were defined during both Expeditions 338 and 348 (Figure 4.5): Unit III in the Kumano Basin, and Units IV and V in the inner accretionary wedge. Unit IV is beneath an unconformity that delineates the base of the Kumano Basin [*Expedition 314 Scientists*, 2009a]. Unit IV was logged in holes C0002A, C0002F, and C0002P and Unit V was logged in holes C0002F, C0002N, and C0002P. The boundary between Units IV and V in hole C0002F is characterized by an increase in velocity and resistivity values, as well as a concentration of fractures interpreted from resistivity images [*Moore et al.*, 2013]. Unit IV and Unit V were further subdivided into subunits that shared similar log values and trends. The

gamma ray shows variation from ~40 to 150 API (standardized American Petroleum Institute unit for gamma ray logs, calibrated to a standard) through Unit IV, consistent with both sandy and clay-rich fragments seen in cuttings (Figure 4.4a) [*Tobin et al.*, 2015a]. Resistivity and velocity increase downhole through Unit IV until reaching the formation boundary with Unit V at 1638.5 mbsf and 1665.5 mbsf in holes C0002F and C0002N, respectively.

Logs through Unit V show remarkably little variation across three holes and a depth range of over 1 km (Figure 4.5b). The gamma ray values are high, indicating high clay content, which is corroborated by analysis of cuttings and core samples [*Underwood and Song*, 2016a, 2016b; *Underwood*, 2017b]. In hole C0002P there are few excursions of the resistivity, especially deeper in the hole; these excursions are typically associated with small increases (~200-300 m/s) in the sonic log values. In hole C0002P there is more variability in the upper portion of the borehole, above ~2366 mbsf, where the boundary for shipboard units Vc' and Vd was picked. This includes the section that was cored prior to logging, which may have compromised borehole quality and log data [*Expedition 348 Scientists and Participants*, 2014].

4.4.1 Results of velocity analysis

Our P-wave values are similar to the non-shipboard log values provided by Halliburton. Our dipole S-wave picks result in lower velocity values than those provided by Halliburton. Both the P- and S-wave velocities picked at Wisconsin and by Halliburton remain nearly constant over the depth of almost one kilometer, instead of continuing to increase as the velocity logs do through the Kumano Basin and Unit IV of the upper inner accretionary wedge (Figures 4.4 and 4.6). Unit V has a very homogenous velocity when logged in both C0002F and C0002P (Figure 4.5). These velocity values remain relatively constant despite the continued decrease of porosity

measured shipboard on cuttings samples during the expeditions (Figure 4.6) [*Moore et al.*, 2013; *Expedition 348 Scientists and Participants*, 2014].

The largest identified anomaly is present at ~2610 to 2660 mbsf in the S-wave velocity log, where the values decrease ~200 m/s (Figure 4.4). The sonic caliper does not indicate a large change in borehole size in this interval, it does correspond with a more resistive zone. There does not seem to be a comparable decrease in the P-wave velocity, leading to a higher v_p/v_s ratio through this section (Figure 4.7). The fracture density does increase slightly through this interval, although poor data quality limits structural interpretation (Figure 4.4). The difficulty in making picks may have led to less accurate S-wave values through this section, so this excursion may be an artifact rather than a real low velocity zone; however, lower S-wave velocity is potentially consistent with higher fracture content.

Velocity values from models used in pre-stack depth migration (PSDM) in this region are similar to those obtained from the reprocessed sonic logs (~3000-3500 m/s) [*Moore et al.*, 2007]. However, these values increase linearly through depths that correspond with the logged Unit V, so do not match the almost constant velocities in the well. Velocity values from tomographic models, while increasing slightly, remain much more constant with an increase of only ~250 m/s over the depths identified as Unit V in holes C0002F and C0002P [*Kamei et al.*, 2012]. In hole C0002F, log velocity values are slightly higher than tomography values, but both the tomography and the velocity log record values between ~3200 and 3300 at the base of hole C0002P. In general, however, the velocity values from the logging data are within the range of both PSDM and tomography velocity models, although only the tomographic model shows a more constant velocity value with depth consistent with the values from the logs.

4.4.2 Log crossplots

In addition to the visual interpretation of the logs, we crossplot log data to investigate features of logged intervals (Figure 4.8). The differences between logging units in the gamma ray can be clearly identified in the crossplots (Figure 4.8). For Unit IV, gamma ray values are generally between 40 and 100 API, consistent with those of the Kumano Basin (Figure 4.8a). However, Unit V has a shift to consistently higher gamma ray values, between 90 and 120 API. Velocity values in Unit V vary by less than about 1000 m/s through the unit, compared to a range of 2250 m/s in the overlying units (Figure 4.8). Increased velocity generally corresponds to increased resistivity through Units IV and V in hole C0002P (Figure 4.8b), although a wider range of resistivity is seen at lower velocities when C0002A is added to the crossplots (Figure 4.8c). The boundary between Unit IV and Unit V is clearly seen in the gamma ray-velocity crossplot plotted in gray, due to the rapid velocity increase (Figure 4.8a).

4.4.3 Wedge Structure

Given the lack of coherent seismic imaging through the inner accretionary wedge, structural information at this depth is interpreted from logging data [*Expedition 314 Scientists*, 2009b; *Strasser et al.*, 2014b; *Tobin et al.*, 2015b; *Boston et al.*, 2016]. The steeply dipping bedding and numerous fractures indicate that both units in the inner accretionary wedge have undergone deformation (Figure 4.5). Beds within the inner accretionary wedge have high dips (>60 degrees). The resistivity images also record fractures throughout both holes C0002F and C0002P, further indicating the deformed nature of the inner accretionary wedge. Unit IV has been identified at Site C0002 and Site C0009, although its degree of deformation varies, with more fractures and higher bedding dips interpreted at Site C0002 [*Expedition 319 Scientists*, 2010b]. *Boston et al.* [2016] carried out an analysis of the structure in the wedge, identifying

areas where large changes in bedding dip or azimuth occur and interpreting these sections as deformed, either faults or folds.

4.5 Physical property and stress estimates

4.5.1 Elastic moduli and ratios

Data from shallower holes with core and sonic and/or density/porosity logs have been used to measure the elastic moduli in the Nankai Trough, e.g.[*Hashimoto et al.*, 2010; *Raimbourg et al.*, 2011; *Schumann et al.*, 2014]. Having log values of both P- and S-wave velocities for hole C0002P, elastic moduli can be estimated for the inner accretionary wedge as follows:

$$V_p = \sqrt{\frac{\kappa + \frac{4}{3}\mu}{\rho}} \qquad 5.1.1$$

$$V_s = \sqrt{\frac{\mu}{\rho}} \qquad 5.1.2$$

V_p is the P-wave velocity, V_s is the S-wave velocity, ρ is the density, κ is the bulk modulus, and μ is the shear modulus. Velocity ratio, bulk and shear moduli, and Poisson's ratio were calculated for the inner accretionary wedge using the re-picked P- and S-wave velocity values. Density for the modulus calculations was estimated from an exponential shipboard fit to the cuttings and core based porosity and density [*Expedition 348 Scientists and Participants*, 2014].

Given the relatively small variation in the velocity values within the wedge, the moduli values also do not vary extensively (Figure 4.7).

The velocity ratio (V_p/V_s) through this section of Unit V is approximately 2. The bulk modulus ranges from ~12 to 23 GPa, and the shear modulus falls between ~ 4.5 and 6.5 GPa. Poisson's ratio ranges between ~0.3 and 0.4, within the expected range for clay-rich sediments.

4.5.2 Overpressure

We also calculated overpressure for the wedge, in order to see what trends emerged. Overpressure can be estimated in the wedge by converting velocity to porosity through one of the available experimentally derived transforms, then using the porosity to estimate effective stress and pore fluid pressure at depth. However, a caveat of using these transforms is that they directly attribute changes in velocity to changes in porosity. If there is a loss of porosity with depth despite the velocity remaining the same, overpressure estimates would not be valid. The *Hoffman and Tobin* [2004] and *Hyndman et al.* [1993] transforms are based on sediments from the Muroto transect of the Nankai Trough. *Tudge and Tobin* [2013] used NanTroSEIZE sediment samples to tailor fits to certain tectonic domains in the Kumano Basin area. *Erickson and Jarrard* [1998] also provided two global transforms that are termed "high compaction" and "normal compaction." . The *Hoffman and Tobin* [2004], *Erickson and Jarrard* [1998], and *Tudge and Tobin* [2015] equations are least squares fit to data, and take the form as follows:

$$V_p = \mathrm{A} + \mathrm{B}\phi + \frac{0.305}{\left[(\phi + \mathrm{C})^2 + \frac{0.305}{1.51 - \mathrm{A} - \mathrm{B}} - \mathrm{C}^2 - 2\mathrm{C} - 1\right]} + 0.61(v_{sh} - 1.123)[X_m] \quad 5.1.3$$

$$X_m = \tanh\left[40\left(\phi - \phi_c\right)\right] - \left|\tanh\left[40\left(\phi - \phi_c\right)\right]\right| \qquad 5.1.4$$

where V_p *is* the compressional wave velocity, v_{sh} is the shale "volume", or fraction of clay in the sediments, ϕ is the porosity, and A, B, and C are parameters to fit the data. The shale volume value is usually estimated from the gamma ray log values, where the lowest value is assumed to be a clay-poor sandstone, and the higher values are assumed to be a clay-rich shale. However, the lack of variation in the gamma ray through Unit V prevents the baselining of a "clean sandstone" value through that section. To determine the best v_{sh} value, I crossplotted the porosity from the core and cuttings with velocity, and compared these values to those predicted from published velocity-porosity relationships (Figure 4.9a). Given the high clay content of Unit V [*Tobin et al.*, 2015a; *Underwood*, 2017a], a fit to higher v_{sh} values was expected, but the best v_{sh} values to fit the data were between 0.2 and 0.6 . However, given that fits to data have resulted in v_{sh} values that are physically unrealistic before (i.e. v_{sh} of >1 in *Hoffman and Tobin* [2004]), these low numbers are not entirely unexpected. Here, we use a v_{sh} of 0.3 with the *Erickson and Jarrard* [1998] high compaction model to make our estimations of pore pressure (Figure 4.9a).

Given these porosity estimates from velocity, we can calculate the pore pressure, P_f:

$$P_f = \sigma_n - \sigma_n' \qquad 5.1.7$$

where σ_n is the normal (lithostatic) stress, and σ_n' is the effective stress. Lithostatic pressure was calculated using density values calculated from the shipboard derived Athy porosity curve. The assumption made for these calculations is that the Kumano Basin overlying the accretionary wedge is normally compacting and does not experience any overpressure—that is, pore pressures in the Kumano Basin should fit the hydrostat.

If this estimate for overpressure is used, it indicates that the overpressure in the wedge is low (Figure 4.9b), as values do not rise significantly above the hydrostat until the base of Unit V. However, the assumptions made in this calculation must be reconciled with core and cuttings data (see section 4.6.2), so may not provide an accurate estimate of conditions at depth.

4.6 Discussion

Elastic moduli, velocity ratio, and Poisson ratio were estimated for the inner accretionary wedge of the Nankai Trough from logging data available as part of the NanTroSEIZE project. In order to put these calculated parameters in context, they are compared to values measured elsewhere. The log analysis and synthesis is used to hypothesize some potential structural histories that the inner wedge may have experienced.

4.6.1 Elastic moduli and a potentially compliant wedge

The material properties of an accretionary wedge have been hypothesized to be a factor that influences tsunami hazard, as a compliant wedge is thought to allow more displacement at the seafloor [*Tanioka and Satake*, 1996; *Lotto et al.*, 2017]. The elastic properties presented here are the first available for the deeper inner accretionary wedge anywhere. The values are high compared to those measured on core samples elsewhere in Nankai, which is expected given the

shallow depth at which the other samples were collected [*Hashimoto et al.*, 2011; *Raimbourg et al.*, 2011; *Schumann et al.*, 2014]. The values found here fall in the range of elastic moduli calculated for fault gouges measured in laboratory experiments at higher pressures [*Jeppson and Tobin*, 2015]. The relatively little variability seen in the elastic moduli is a reflection of the velocity values, which also show little variability with depth.

The only other inner wedge shear wave velocity data available is from wireline logs in Unit IV at Site C0009, which also results in a velocity ratio of ~2 when used in conjunction with the compressional sonic log [*Expedition 319 Scientists*, 2010b]. However, the hole quality through this section is poor, which introduces uncertainty to the values of the P- and S-wave velocities. V_p/V_s ratios have also been estimated through the wedge from ocean bottom seismometer tomography [*Tsuji et al.*, 2008, 2011]. They estimate V_p/V_s for the inner wedge from 1.6 to 2. The higher estimates from this method are similar to the values of ~2 estimated here. Overall, the values seen in the well logs are slightly higher than those seen in ocean bottom seismometer data, but the tomographic models are sampling a larger area at a larger scale than the well logs, and may average out values that are reflected in the finer scaled wireline log measurements.

These elastic moduli indicate that the material making up the sampled section of the inner wedge is relatively compliant compared to crystalline rocks (e.g. [*Lockner et al.*, 1991; *Lockner*, 1995] and references therein). Clay materials from the inner wedge at much shallower depths have been sampled and their frictional properties measured, indicating that they are velocity-strengthening [*Ikari et al.*, 2009]. This would imply that the material in the wedge would slow rupture, perhaps inhibiting the ability of rupture to the shallow portions of the megasplay. Unfortunately, given the limited data available for the wedge, the extent to which material properties extend through the wedge, and how much they can be laterally extrapolated, is not

known. The presence of a large (>1 km) section of material with the properties estimate here indicates that at least a portion of the wedge is relatively compliant.

4.6.2 Velocity log-porosity discussion

The sonic log's near constant values through Unit V are a departure from the trend seen in the shallower accretionary wedge (Figure 4.6). Through the Kumano Basin and Unit IV, sonic velocity increases with depth. However in Unit V the sonic log varies very little, despite sampling ~1 km of the inner accretionary wedge. This log response may be due to a problem with the measurement, overpressure, the structural history of the inner wedge, or the composition of the sediments.

4.6.2.1 Tool measurements

One possibility is that the sonic log is affected by the consistently high dips in Unit V, traveling along the dip plane rather than the borehole wall [*Rider*, 2002; *Ellis and Singer*, 2008]. However, we do not see a relationship between bedding dip and velocity in either C0002F or C0002P (discussed in section 4.6.2). One section with a concentration of lower dips in C0002P does not correspond consistently with V_p and V_s changes. Also, Unit IV in hole C0002F has steeply dipping bedding, but the sonic log within that unit does show variation in values. High bedding dip is probably not responsible for the consistent velocity values in Unit V.

4.6.2.2 Overpressure

Deviations from a normal velocity-depth compaction trend are often attributed to overpressure, at a variety of scales (e.g. [*Bangs et al.*, 1990; *Cochrane et al.*, 1994; *Calahorrano et al.*, 2008; *Conin et al.*, 2012]). Overpressure calculations, such as those performed above, would indicate overpressure not much above hydrostatic in the wedge. However, the velocity log's constant

values cannot be reconciled with the porosity data that are also seen in the wedge (Figure 4.6). If the sediment was overpressured, the porosity values should also remain elevated above a normal compaction trend. Porosity measured in shipboard cuttings and core follows an exponential curve, similar to sections that have experienced normal compaction (Figure 4.6) [*Athy*, 1930]. As the porosity and velocity trends cannot be directly reconciled through assumptions of overpressure, other parameters may influence the observed trends. In addition, estimates of overpressure in the inner accretionary wedge relying solely on the velocity log are a potentially inaccurate reflection of conditions at depth.

4.6.2.3 Structural history

The structurally complex nature of the inner wedge makes determining the original position of the Units IV and V relative to each other difficult. Preservation of fossils is low, so the ages are difficult to determine [*Tobin et al.*, 2015a]. The unit boundary between Unit IV and Unit V is characterized by high P-wave velocity, as well as difficult to interpret, high resistivity intervals that may point to a structural boundary between the two units (Figure 4.5a). The difference may also be lithological, with Unit IV seeing more influence from a terrestrial sediment source, but the relative location of these two units to each other during deposition may not be resolvable.

The velocity-porosity data trend may be due to structural effects. The porosity data from core and cuttings appear to follow a normal compaction trend. If these sediments were incoming hemipelagic sediments that were incorporated into what was the outer wedge in the Miocene, they may have experienced normal compaction when being deposited on the incoming plate. The model of the out of sequence thrust fault development proposed by *Strasser et al.* [2009] shows a relatively small taper angle on the wedge, and the incorporation of much of the incoming section into the imbricate fault zone. After incorporation into the outer wedge, the

sediments would have experienced tectonic loading and compression. Given the present day structure interpreted from resistivity image logs, the sediment package has undergone tilting and fracturing, which is consistent with deformation in the outer wedge of the accretionary wedge. While there is a possibility that porosity loss due to normal compaction could be preserved, an overprint from some of the tectonic loading could be expected as well, which would cause deviation from the curve defined by the exponential porosity decrease.

However, the preservation of this porosity-depth trend implies that the thrust sheet did not experience intensive tectonic loading. The current stress state in the inner wedge is either normal or strike-slip, not compressional [*Chang and Song*, 2016]. If this is the case, the thrust sheet may not have been exposed to extensive tectonic loading. If the thrust sheet was landward of the developing megathrust, and overlying a weak fault at the plate boundary megathrust below, it would have been isolated from strong tectonically derived lateral stress.

The normal compaction trend of the porosity as well as the velocity through Unit IV does extend from the Kumano Basin into the accretionary wedge. The ability to fit an exponential curve to the porosity data through not only the basin but the underlying accretionary wedge would indicate, in the absence of other information, that the entire section was undergoing normal compaction at the present position and configuration. If it was not, a change in the trend might be expected at the interface with the inner accretionary wedge. However, if the assumption that the sediment section experienced a large amount of loading in its history is not correct, this normal compaction trend may indicate the sediment section is currently experiencing the highest total stress it has been exposed to. This suggests that the sediments of the inner wedge, while tilted and fractured/faulted, may have been relatively uncompacted when they were separated from the outer wedge by the out of sequence megasplay fault.

These structural scenarios, with their isolated tectonic effects, seem somewhat unlikely in an actively deforming accretionary wedge. Each structural scenario requires a very specific set of processes, and even then cannot always account for the log responses seen here. Despite the fact that sediments have clearly been deformed, a solely deformation-based explanation is not satisfactory to explain the velocity-porosity trends seen here. A third factor to explore is lithologic composition.

4.6.3 Effect of sediment composition on log properties

Although both Unit IV and Unit V are classified as silty claystones [*Strasser et al.*, 2014b; *Tobin et al.*, 2015b], there is a greater proportion of sand in Unit IV, reflected in the gamma ray response (Figure 4.5a). The clay content of the clay fraction in Unit IV and V has a similar mineral signature, but the addition of more sand in Unit IV indicates a possible change in sediment source [*Tobin et al.*, 2015a; *Underwood and Song*, 2016a, 2016b].

The current sedimentary section tectonically input into the Nankai Trough is the Shikoku Basin, which has higher smectite concentrations than those observed in the inner wedge [*Underwood and Guo*, 2013; *Underwood*, 2017a]. *Pickering et al.* [2013] hypothesize that the migration of a triple junction past the Nankai Trough implies that the earlier sediment incorporated into the wedge was not that of the Shikoku Basin. Furthermore, *Underwood* [2017a] has suggested that the sediment source for the clay-rich inner accretionary wedge is not the Shikoku Basin sediments that are input to the trench today, but rather the marine sediments that were present before the migration of the triple junction through the Nankai Trough area. This may explain why the velocity-porosity relationships tailored to Shikoku Basin sediments (e.g. [*Tudge and Tobin*, 2013]), do not provide the best fit for the porosity data collected in the inner accretionary

wedge. It may also complicate extrapolation from shallower, Shikoku Basin facies to the inner wedge.

Recent work on the composition of clays in the cuttings from C0002P reveals that there is a marked increase of illite and a decrease in the amount of smectite deeper within hole C0002P [*Underwood*, 2017a]. Analysis of cuttings in C0002N and core in C0002P indicate that Unit V is predominantly silty claystone and fine silty claystone [*Tobin et al.*, 2015b; *Ramirez and Milliken*, 2016]. Cuttings in C0002N and C0002P contain both smectite and illite, with smectite comprising about 40% of the clay in Unit V, and illite about 35% in the upper portion of Unit V [*Underwood and Song*, 2016a, 2016b; *Underwood*, 2017b]. There is a shift to higher illite concentrations lower in the hole, in subunit Vb [*Underwood*, 2017a].

Relationships between clay mineralogy and velocity are difficult to determine in these data. Changes in clay mineralogy correspond to very slight shifts in velocity values seen deeper in the hole. Smectite decreases as illite increases beginning near 2355 mbsf [*Underwood*, 2017a], which corresponds to the change from a (relatively) more variable velocity log to the section with the most constant velocity. Near this depth, a decrease in velocity values from ~3400 m/s to 3200 m/s begins. In the lower portions of the hole (~2625 mbsf), when the lithological definition changes from silty claystone to fine silty claystone, the amount of smectite decreases to the lowest value seen in the inner accretionary wedge, whereas the illite increases slightly [*Underwood*, 2017a]. Below this depth, a small (~200 m/s) decrease in the velocity log values occurs, but may or may not be due to the lithological change.

Also, *Underwood* [2017a] indicates that the illite in the deepest samples of Unit V is a result of diagenetic reactions in situ. This would indicate that it may be from a relatively shallow section, rather than deeply buried to a depth where the entire section has already undergone diagenesis.

It may suggest that while Unit V seems lithologically homogenous, there may be subtler structural contacts within the units, as well as compositional changes. The bottom part of Unit V may also represent a different depositional environment than the upper portion.

Although many of these links to lithology are intriguing, we cannot definitively point to a lithological change contributing to changes in the velocity log. The in situ diagenesis suggests that the sediment may have come from relatively shallow in a sediment section. Shallow sediments would experience less compression from burial when deposited and may not have developed much of a compaction trend before reaching their current location. This could support the theory that the sediments are currently experiencing peak loading.

4.7 Conclusions

Reprocessed sonic data, combined with other available data, allows for detailed analysis and estimates of physical properties at depth in the Nankai Trough, Japan. Elastic moduli in the clay-rich accretionary wedge estimated from logs are similar to those experimentally determined for clays that have experienced similar burial depths, although higher than moduli values calculated for shallower IODP/ODP sites. Unit IV and Unit V are both classified as silty claystones [*Tobin et al.*, 2015a], but their log responses are markedly different. Unit IV generally follows Kumano Basin trends of variable gamma ray and increasing velocity with depth, despite high bedding dips and the presence of fractures. Unit V is characterized by almost constant log values with depth. Structurally, both display consistently high dips, indicating that they probably underwent similar deformation paths through at least a portion of their history.

The constant velocity values in Unit V might be interpreted as indicators of modest overpressure in the wedge, perhaps due to the impermeability of the clays. However, the almost constant velocity log coupled with a normally compacting porosity trend measured from core and cuttings poses more of a challenge to interpret, and suggests that overpressure may not be responsible for the velocity log response. This relatively simple porosity trend may indicate a simpler loading history than what may be expected for material incorporated into an accretionary wedge. The sediment may be recording an earlier period of deformation with relatively low amounts of tectonic loading, or may be experiencing a peak load at its current depth. If it is at its peak load, it may have been incorporated into a shallower level in the wedge before being buried by the ~1 km of Kumano Basin sediments, and is now experiencing a normal compaction trend. . The role that clays play in the signal is more enigmatic. Changing clay mineralogy can be linked to small variations in the logs, but no definitive correlations can be determined at this time. In the inner wedge, log values are possibly reflecting a deformation history of relatively light tectonic loading, but other factors such as lithology cannot be discounted as affecting the log response.

Further drilling and collection of log data would help narrow possible scenarios for deformation, and may help determine to what extent clay composition acts as a control. More samples would also illuminate how homogeneous the composition of the wedge is. Lab-based measurements of physical properties could also help constrain the log-based elastic moduli estimates. This would help in estimates of the material properties even deeper in the wedge, including the area immediately above the megasplay fault.

4.8 References

Adam, J., D. Klaeschen, N. Kukowski, and E. R. Flueh (2004), Upward delamination of Cascadia Basin sediment infill with landward frontal accretion thrusting caused by rapid glacial age material flux, *Tectonics*, *23*(3), doi:10.1029/2002TC001475.

Ando, M. (1975), Source mechanisms and tectonic significance of historical earthquakes along the nankai trough, Japan, *Tectonophysics*, *27*(2), 119–140, doi:10.1016/0040-1951(75)90102-X.

Ask, M. V. S., and J. K. Morgan (2010), Projection of mechanical properties from shallow to greater depths seaward of the Nankai accretionary prism, *Tectonophysics*, *482*(1–4), 50–64, doi:10.1016/j.tecto.2009.08.023.

Athy, L. F. (1930), Density, porosity, and compaction of sedimentary rocks, *Bull. Am. Assoc. Pet. Geol.*, *14*(1), 468–470, doi:10.1126/science.51.1323.468.

Baba, T., and P. R. Cummins (2005), Contiguous rupture areas of two Nankai Trough earthquakes revealed by high-resolution tsunami waveform inversion, *Geophys. Res. Lett.*, *32*(8), doi:10.1029/2004GL022320.

Bangs, N. L. B., and S. P. S. Gulick (2005), Physical Properties along the Developing Decollement in the Nankai Trough: Inferences from 3-D Seismic Reflection Data Inversion and Leg 190 and 196 Drilling Data, *Proc. Ocean Drill. Program, Initial Reports Vol. 190/196*, *190/196*.

Bangs, N. L. B., G. K. Westbrook, J. W. Ladd, and P. Buhl (1990), Seismic velocities from the Barbados Ridge complex: Indicators of high pore fluid pressures in an accretionary complex, *J. Geophys. …*, *95*(B6), 8767–8782.

Bangs, N. L. B., S. P. S. Gulick, and T. H. Shipley (2006), Seamount subduction erosion in the Nankai Trough and its potential impact on the seismogenic zone, *Geology*, *34*(8), 701–704, doi:10.1130/G22451.1.

Bangs, N. L. B., G. F. Moore, S. P. S. Gulick, E. M. Pangborn, H. J. Tobin, S. Kuramoto, and A. Taira (2009), Broad, weak regions of the Nankai Megathrust and implications for shallow coseismic slip, *Earth Planet. Sci. Lett.*, *284*(1–2), 44–49, doi:10.1016/j.epsl.2009.04.026.

Barnes, P. M., and B. M. de Lepinay (1997), Rates and mechanics of rapid frontal accretion along the very obliquely convergent southern Hikurangi margin , New Zealand, *J. Geophys. Res.*, *102*(B11), 24,931-24,952.

Barton, C., D. Moos, and J.-P. Blangy (1989), Analysis of full waveform acoustic logging data at ODP Site 642—outer Vøring Plateau, in *Proceedings of the Ocean Drilling Program, Scientific Results, Vol 104*, vol. 104, edited by O. Eldholm, J. Thiede, and E. Taylor.

Bekins, B. A., A. M. McCaffrey, and S. J. Dreiss (1994), Influence of kinetics on the smectite to illite transition in the Barbados accretionary prism, *J. Geophys. Res.*, *99*(B9), 18,147-18,158.

Boston, B. B., G. F. Moore, M. J. Jurado, and H. Sone (2016), Deformation of the Nankai Trough inner accretionary prism: The role of inherited structures, *Geochemistry, Geophys. Geosystems*, *17*(2), 485–500, doi:10.1002/2015GC006185.

Brown, K. M., A. J. Kopf, M. B. Underwood, and J. L. Weinberger (2003), Compositional and fluid pressure controls on the state of stress on the Nankai subduction thrust: A weak plate boundary, *Earth Planet. Sci. Lett.*, *214*(3–4), 589–603, doi:10.1016/S0012-821X(03)00388-1.

Calahorrano, A., V. Sallares, J.-Y. Collot, F. Sage, and C. R. Ranero (2008), Nonlinear variations of the physical properties along the southern Ecuador subduction channel: Results from depth-migrated seismic data, *Earth Planet. Sci. Lett.*, *267*(3–4), 453–467, doi:10.1016/j.epsl.2007.11.061.

Chang, C., and I. Song (2016), Present-day stress states underneath the Kumano basin to 2 km below seafloor based on borehole wall failures at IODP site C0002, Nankai accretionary wedge, *Geochemistry Geophys. Geosystems*, *17*, 4289–4307, doi:10.1002/2016GC006406.

Cochrane, G. R., J. C. Moore, M. E. MacKay, and G. F. Moore (1994), Velocity and inferred porosity model of the Oregon accretionary prism from multichannel seismic reflection data: Implications on sediment dewatering and overpressure, *J. Geophys. Res.*, *99*(B4), 7033–7043, doi:doi:10.1029/9; http://dx.doi.org/10.1029/93JB03206.

Conin, M., P. Henry, S. Bourlange, H. Raimbourg, and T. Reuschlé (2012), Interpretation of porosity and LWD resistivity from the Nankai accretionary wedge in light of clay physicochemical properties: Evidence for erosion and local overpressuring, *Geochemistry, Geophys. Geosystems*, *12*(3), 1–17, doi:10.1029/2010GC003381.

Cummins, P. R., and Y. Kaneda (2000), Possible splay fault slip during the 1946 Nankai earthquake, *Geophys. Res. Lett.*, *27*(17), 2725–2728.

DeMets, C., R. G. Gordon, and D. F. Argus (2010), Geologically current plate motions, *Geophys. J. Int.*, *181*(1), 1–80, doi:10.1111/j.1365-246X.2009.04491.x.

Ellis, D. V., and J. M. Singer (2008), *Well Logging for Earth Scientists*, 2nd ed., Springer Netherlands, Dordrecht.

Erickson, S. N., and R. D. Jarrard (1998), Velocity-porosity relationships for water-saturated sediments, *J. Geophys. Res.*, *103*(B12), 30385–30406.

Expedition 314 Scientists (2009a), Expedition 314 Site C0002, in *Proceedings of the Integrated Ocean Drilling Program*, vol. 314/315/31, edited by M. Kinoshita, H. J. Tobin, G. Kimura, S. Lallemant, E. J. Screaton, D. Curewitz, H. Masago, K. T. Moe, and Expedition 314/315/316 Scientists, Integrated Ocean Drilling Program.

Expedition 314 Scientists (2009b), Expedition 314 Site C0002, edited by M. Kinoshita, H. J. Tobin, J. Ashi, G. Kimura, S. Lallemant, E. J. Screaton, D. Curewitz, H. Masago, K. T. Moe, and E. 314/315/316 Scientists, *Proc. Integr. Ocean Drill. Progr.*, *314/315/31*, doi:10.2204/iodp.proc.314315316.114.2009.

Expedition 319 Scientists (2010a), Expedition 319 summary, in *Proceedings of the Integrated Ocean Drilling Program*, vol. 319, edited by D. M. Saffer, L. C. McNeill, T. B. Byrne, E.

Araki, S. Toczko, N. Eguchi, K. Takahashi, and E. 319 Scientists, Integrated Ocean Drilling Program.

Expedition 319 Scientists (2010b), Site C0009, in *Proceedings of the Integrated Ocean Drilling Program*, vol. 319, edited by D. M. Saffer, L. C. McNeill, T. B. Byrne, E. Araki, S. Toczko, N. Eguchi, K. Takahashi, and Expedition 319 Scientists, Integrated Ocean Drilling Program.

Expedition 348 Scientists and Participants (2014), Expedition 348 Preliminary Report, *Integr. Ocean Drill. Progr. Prelim. Reports*, *348*, doi:10.2204/iodp.pr.348.2014.

Ge, S., and E. J. Screaton (2005), Modeling seismically induced deformation and fluid flow in the Nankai subduction zone, *Geophys. Res. Lett.*, *32*(17), L17301, doi:10.1029/2005GL023473.

Gulick, S. P. S., N. L. B. Bangs, T. H. Shipley, Y. Nakamura, G. F. Moore, and S. Kuramoto (2004), Three-dimensional architecture of the Nankai accretionary prism's imbricate thrust zone off Cape Muroto, Japan: Prism reconstruction via en echelon thrust propagation, *J. Geophys. Res.*, *109*(B2), B02105, doi:10.1029/2003JB002654.

Gulick, S. P. S., N. L. B. Bangs, G. F. Moore, J. Ashi, K. M. Martin, D. S. Sawyer, H. J. Tobin, A. Taira, and S. Kuramoto (2010), Rapid forearc basin uplift and megasplay fault development from 3D seismic images of Nankai Margin off Kii Peninsula, Japan, *Earth Planet. Sci. Lett.*, *300*(1–2), 55–62, doi:10.1016/j.epsl.2010.09.034.

Haldorsen, J. B. U., D. L. Johnson, T. Plona, H.-P. Valero, and K. Winkler (n.d.), Borehole Acoustic Waves, *Oilf. Rev.*, 34–43.

Hashimoto, Y., H. J. Tobin, and M. Knuth (2010), Velocity-porosity relationships for slope apron and accreted sediments in the Nankai Trough Seismogenic Zone Experiment, Integrated Ocean Drilling Program Expedition 315 Site C0001, *Geochemistry, Geophys. Geosystems*, *11*(12), doi:10.1029/2010GC003217.

Hashimoto, Y., H. J. Tobin, M. Knuth, and A. Harada (2011), Data report: compressional and shear wave velocity measurements on sediment in the hanging wall and footwall of megasplay fault , NanTroSEIZE Stage 1, in *Proceedings of the Integrated Ocean Drilling Program*, vol. 314/315/31, edited by M. Kinoshita, H. J. Tobin, J. Ashi, G. Kimura, S. Lallemant, E. J. Screaton, D. Curewitz, H. Masago, K. T. Moe, and E. 314/315/316 Scientists.

Hoffman, N. W., and H. J. Tobin (2004), An Empirical Relationship between Velocity and Porosity for Underthrust Sediments in the Nankai Trough Accretionary Prism, in *Proceedings of the Ocean Drilling Program, Scientific Results, Volume 190/196*, vol. 190/196, edited by H. Mikada, G. F. Moore, A. Taira, K. Becker, J. C. Moore, and A. Klaus.

Hung, J.-H., K.-F. Ma, C.-Y. Wang, H. Ito, W. Lin, and E.-C. Yeh (2009), Subsurface structure, physical properties, fault-zone characteristics and stress state in scientific drill holes of Taiwan Chelungpu Fault Drilling Project, *Tectonophysics*, *466*(3–4), 307–321, doi:10.1016/j.tecto.2007.11.014.

Hyndman, R. D., G. F. Moore, and K. Moran (1993), Velocity, porosity, and pore-fluid loss from the Nankai subduction zone accretionary prism, in *Proceedings of the Ocean Drilling Program, Scientific Results*, vol. 131, edited by I. A. Hill, A. Taira, J. V. Firth, and E. Al, pp. 211–220.

Ienaga, M., L. C. McNeill, H. Mikada, S. Saito, D. Goldberg, and J. C. Moore (2006), Borehole image analysis of the Nankai Accretionary Wedge, ODP Leg 196: Structural and stress studies, *Tectonophysics*, *426*(1–2), 207–220, doi:10.1016/j.tecto.2006.02.018.

Ikari, M. J., and D. M. Saffer (2011), Comparison of frictional strength and velocity dependence between fault zones in the Nankai accretionary complex, *Geochemistry, Geophys. Geosystems*, *12*(4), n/a-n/a, doi:10.1029/2010GC003442.

Ikari, M. J., D. M. Saffer, and C. Marone (2009), Frictional and hydrologic properties of a major splay fault system, Nankai subduction zone, *Geophys. Res. Lett.*, *36*(20), 1–5, doi:10.1029/2009GL040009.

Ikari, M. J., C. Marone, and D. M. Saffer (2010), On the relation between fault strength and frictional stability, *Geology*, *39*(1), 83–86, doi:10.1130/G31416.1.

Ikari, M. J., J. Kameda, D. M. Saffer, and A. J. Kopf (2015), Strength characteristics of Japan Trench borehole samples in the high-slip region of the 2011 Tohoku-Oki earthquake, *Earth Planet. Sci. Lett.*, *412*, 35–41, doi:10.1016/j.epsl.2014.12.014.

Ito, Y., and K. Obara (2006), Very low frequency earthquakes within accretionary prisms are very low stress-drop earthquakes, *Geophys. Res. Lett.*, *33*(9), doi:10.1029/2006GL025883.

Ito, Y., T. Tsuji, Y. Osada, M. Kido, D. Inazu, Y. Hayashi, H. Tsushima, R. Hino, and H. Fujimoto (2011), Frontal wedge deformation near the source region of the 2011 Tohoku-Oki earthquake, *Geophys. Res. Lett.*, *38*(7), doi:10.1029/2011GL048355.

Jeppson, T. N., and H. J. Tobin (2015), San Andreas fault zone velocity structure at SAFOD at core, log, and seismic scales, *J. Geophys. Res.*, 1–15, doi:10.1002/2015JB012043.Received.

Kamei, R., R. G. Pratt, and T. Tsuji (2012), Waveform tomography imaging of a megasplay fault system in the seismogenic Nankai subduction zone, *Earth Planet. Sci. Lett.*, *317–318*, 343–353, doi:10.1016/j.epsl.2011.10.042.

Kimball, C. V, and T. L. Marzetta (1984), Semblance processing of borehole acoustic array data, *Geophysics*, *49*(3), 274–281.

Kimura, G., Y. Kitamura, Y. Hashimoto, A. Yamaguchi, T. Shibata, K. Ujiie, and S. Okamoto (2007), Transition of accretionary wedge structures around the up-dip limit of the seismogenic subduction zone, *Earth Planet. Sci. Lett.*, *255*(3–4), 471–484, doi:10.1016/j.epsl.2007.01.005.

Kimura, G., G. F. Moore, M. Strasser, E. J. Screaton, D. Curewitz, C. Streiff, and H. J. Tobin (2011), Spatial and temporal evolution of the megasplay fault in the Nankai Trough, *Geochemistry, Geophys. Geosystems*, *12*(3), doi:10.1029/2010GC003335.

Kington, J. D. (2012), The Structure and Kinematics of the Nankai Trough Accretionary Prism, Japan, University of Wisconsin-Madison.

Kitajima, H., and D. M. Saffer (2012), Elevated pore pressure and anomalously low stress in regions of low frequency earthquakes along the Nankai Trough subduction megathrust, *Geophys. Res. Lett.*, *39*(L23301), doi:10.1029/2012GL053793.

Kodaira, S., T. Hori, A. Ito, S. Miura, G. Fujie, J.-O. Park, T. Baba, H. Sakaguchi, and Y. Kaneda (2006), A cause of rupture segmentation and synchronization in the Nankai trough revealed by seismic imaging and numerical simulation, *J. Geophys. Res.*, *111*(B9), doi:10.1029/2005JB004030.

Kopf, A. J., and K. M. Brown (2003), Friction experiments on saturated sediments and their implications for the stress state of the Nankai and Barbados subduction thrusts, *Mar. Geol.*, *202*(3–4), 193–210, doi:10.1016/S0025-3227(03)00286-X.

Lay, T. (2015), The surge of great earthquakes from 2004 to 2014, *Earth Planet. Sci. Lett.*, *409*, 133–146, doi:10.1016/j.epsl.2014.10.047.

Lay, T. et al. (2005), The Great Sumatra-Anadaman Earthquake of 26 December 2004, *Science (80-.).*, *308*(May), 1127–1133, doi:10.1126/science.1112250.

Lockner, D. A. (1995), Rock Failure, in *Rock Physics and Phase Relations*, edited by T. J. Ahrens.

Lockner, D. A., J. . Byerlee, V. Kuksenko, A. Ponomarev, and A. Sidorin (1991), Quasi-static frault growth and shear fracture energy in granite, *Nature*, *350*.

Lotto, G. C., E. M. Dunham, T. N. Jeppson, and H. J. Tobin (2017), The effect of compliant prisms on subduction zone earthquakes and tsunamis, *Earth Planet. Sci. Lett.*, *458*, 1–23, doi:10.1016/j.epsl.2016.10.050.

Martin, K. M., S. P. S. Gulick, N. L. B. Bangs, G. F. Moore, J. Ashi, and J.-O. Park (2010), Possible strain partitioning structure between the Kumano fore-arc basin and the slope of the Nankai Trough accretionary prism, *Geochemistry Geophys. Geosystems*, *11*, 1–15, doi:10.1029/2009GC002668.

McNeill, L. C., M. Ienaga, H. J. Tobin, S. Saito, D. Goldberg, J. C. Moore, and H. Mikada (2004), Deformation and in situ stress in the Nankai Accretionary Prism from resistivity-at-bit images, ODP Leg 196, *Geophys. Res. Lett.*, *31*(2), L02602, doi:10.1029/2003GL018799.

Moore, G. F., T. H. Shipley, P. L. Stoffa, D. E. Karig, A. Taira, S. Kuramoto, H. Tokuyama, and K. Suyehiro (1990), Structure of the Nankai Trough Accretionary Zone from Multichannel Seismic Reflection Data, *J. Geophys. Res.*, *95*, 8753–8765.

Moore, G. F. et al. (2001), New insights into deformation and fluid flow processes in the Nankai Trough accretionary prism: Results of Ocean Drilling Program Leg 190, *Geochemistry Geophys. Geosystems*, *2*, 1–15.

Moore, G. F., N. L. B. Bangs, A. Taira, S. Kuramoto, E. Pangborn, and H. J. Tobin (2007), Three-dimensional splay fault geometry and implications for tsunami generation, *Science (80-.).*, *318*(5853), 1128–1131, doi:10.1126/science.1147195.

Moore, G. F. et al. (2009a), Structural and seismic stratigraphic framework of the NanTroSEIZE Stage 1 transect, in *Proceedings of the Integrated Ocean Drilling Program, Volume*

314/315/316, vol. 314/315/31, edited by M. Kinoshita, H. J. Tobin, J. Ashi, G. Kimura, S. Lallemant, E. J. Screaton, D. Curewitz, H. Masago, K. T. Moe, and E. 314/315/316 Scientists.

Moore, G. F. et al. (2009b), Structural and seismic stratigraphic framework of the NanTroSEIZE Stage 1 transect 1, , *314*, doi:10.2204/iodp.proc.314315316.102.2009.

Moore, G. F., K. Kanagawa, and M. Strasser (2013), Expedition 338 Preliminary Report NanTroSEIZE Stage 3 : NanTroSEIZE plate boundary deep riser 2 1 October 2012 – 13 January 2013, , (October 2012), doi:10.2204/iodp.pr.338.2013.

Moore, G. F., B. B. Boston, M. Strasser, M. B. Underwood, and R. A. Ratliff (2015), Evolution of tectono-sedimentary systems in the Kumano Basin, Nankai Trough forearc, *Mar. Pet. Geol.*, *67*, 604–616, doi:10.1016/j.marpetgeo.2015.05.032.

Moore, J. C., and D. M. Saffer (2001), Updip limit of the seismogenic zone beneath the accretionary prism of southwest Japan: An effect of diagenetic to low-grade metamorphic processes and increasing effective stress, *Geology*, *29*(2), 183–186.

Nakanishi, A., S. Kodaira, S. Miura, A. Ito, T. Sato, J.-O. Park, Y. N. Kido, and Y. Kaneda (2008), Detailed structural image around splay-fault branching in the Nankai subduction seismogenic zone: Results from a high-density ocean bottom seismic survey, *J. Geophys. Res.*, *113*(B3), B03105, doi:10.1029/2007JB004974.

Obara, K., and Y. Ito (2005), Very low frequency earthquakes excited by the 2004 off the Kii peninsula earthquakes: A dynamic deformation process in the large accretionary prism, *Earth Planets Sp.*, *57*, 321–326.

Oleskevitch, D. A., R. D. Hyndman, and K. Wang (1999), The updip and downdip limits to great subduction earthquakes: Thermal and structural models of Cascadia, south Alaska, SW Japan, and Chile, *J. Geophys. Res.*, *104*(B7), 14965–14991.

Park, J.-O., T. Tsuru, S. Kodaira, P. R. Cummins, and Y. Kaneda (2002), Splay fault branching along the Nankai subduction zone, *Science (80-.).*, *297*(5584), 1157–1160, doi:10.1126/science.1074111.

Park, J.-O., G. Fujie, L. Wijerathne, T. Hori, S. Kodaira, Y. Fukao, G. F. Moore, N. L. B. Bangs, S. Kuramoto, and A. Taira (2010), A low-velocity zone with weak reflectivity along the Nankai subduction zone, *Geology*, *38*(3), 283–286, doi:10.1130/G30205.1.

Pickering, K. T., M. B. Underwood, and A. Taira (1993), Stratigraphic synthesis of the DSDP-ODP sites in the Shikoku Basin, Nankai Trough, and accretionary prism, in *Proceedings of the Ocean Drilling Program, Scientific Results, Volume 131*, vol. 131, edited by I. A. Hill, A. Taira, J. V. Firth, and E. Al., pp. 313–330.

Pickering, K. T., M. B. Underwood, S. Saito, H. Naruse, S. Kutterolf, R. Scudder, J. O. Park, G. F. Moore, and A. Slagle (2013), Depositional architecture, provenance, and tectonic/eustatic modulation of Miocene submarine fans in the Shikoku Basin: Results from Nankai Trough Seismogenic Zone Experiment, *Geochemistry, Geophys. Geosystems*, *14*(6), 1722–1739, doi:10.1002/ggge.20107.

Raimbourg, H., Y. Hamano, S. Saito, M. Kinoshita, and A. J. Kopf (2011), Acoustic and

mechanical properties of Nankai accretionary prism core samples, *Geochemistry, Geophys. Geosystems*, *12*(4), n/a-n/a, doi:10.1029/2010GC003169.

Ramirez, S. G., and K. L. Milliken (2016), Data report: atlas of lithic grain types at Site C0002; reference for petrographic provenance analysis in the Kumano Basin and upper Nankai accretionary prism, in *Proceedings of the Integrated Ocean Drilling Program*, vol. 338, edited by M. Strasser, B. Dugan, K. Kanagawa, G. F. Moore, S. Toczko, L. Maeda, and E. 338 Scientists, Integrated Ocean Drilling Program.

Ranero, C. R., I. Grevemeyer, H. Sahling, U. Barckhausen, C. Hensen, K. Wallmann, W. Weinrebe, P. Vannucchi, R. Von Huene, and K. McIntosh (2008), Hydrogeological system of erosional convergent margins and its influence on tectonics and interplate seismogenesis, *Geochemistry, Geophys. Geosystems*, *9*(3), doi:10.1029/2007GC001679.

Rider, M. (2002), The Geological Interpretation of Well Logs, *Rider-French Consult. Ltd*, 290.

Saffer, D. M. (2003), Pore pressure development and progressive dewatering in underthrust sediments at the Costa Rican subduction margin: Comparison with northern Barbados and Nankai, *J. Geophys. Res.*, *108*(B5), 2261, doi:10.1029/2002JB001787.

Saffer, D. M., and B. A. Bekins (1998), Episodic fluid flow in the Nankai accretionary complex: Timescale, geochemistry, flow rates, and fluid budget, *J. Geophys. Res.*, *103*(B12), 30351–30370.

Saffer, D. M., and C. Marone (2003), Comparison of smectite- and illite-rich gouge frictional properties: Application to the updip limit of the seismogenic zone along subduction megathrusts, *Earth Planet. Sci. Lett.*, *215*(1–2), 219–235, doi:10.1016/S0012-821X(03)00424-2.

Saffer, D. M., and H. J. Tobin (2011), Hydrogeology and Mechanics of Subduction Zone Forearcs: Fluid Flow and Pore Pressure, *Annu. Rev. Earth Planet. Sci.*, *39*, 157–186, doi:10.1146/annurev-earth-040610-133408.

Scholz, C. H. (1998), Earthquakes and friction laws, *Nature*, *391*(6662), 37–42, doi:10.1038/34097.

Schumann, K., M. Stipp, J. H. Behrmann, D. Klaeschen, and D. Schulte-Kortnack (2014), P and S wave velocity measurements of water-rich sediments from the Nankai Trough, Japan, *J. Geophys. Res. Solid Earth*, 1–15, doi:10.1002/2014JB010978.Received.

Screaton, E. J., D. M. Saffer, P. Henry, and S. Hunze (2002), Porosity loss within the underthrust sediments of the Nankai accretionary complex: Implications for overpressures, *Geology*, *30*(1), 19–22, doi:10.1130/0091-7613(2002)030<0019:PLWTUS>2.0.CO;2.

Strasser, M. et al. (2009), Origin and evolution of a splay fault in the Nankai accretionary wedge, *Nat. Geosci. Lett.*, *2*, doi:10.1038/NGEO609.

Strasser, M. et al. (2014a), Expedition 338 summary, in *Proceedings of the Integrated Ocean Drilling Program*, vol. 338, edited by M. Strasser, B. Dugan, K. Kanagawa, G. F. Moore, S. Toczko, L. Maeda, and Expedition 338 Scientists, Integrated Ocean Drilling Program.

Strasser, M. et al. (2014b), Site C0002, in *Proceedings of the Integrated Ocean Drilling*

Program, vol. 338, edited by M. Strasser, B. Dugan, K. Kanagawa, G. F. Moore, S. Toczko, L. Maeda, and Expedition 338 Scientists, Integrated Ocean Drilling Program.

Sugioka, H., T. Okamoto, T. Nakamura, Y. Ishihara, A. Ito, K. Obana, M. Kinoshita, K. Nakahigashi, M. Shinohara, and Y. Fukao (2012), Tsunamigenic potential of the shallow subduction plate boundary inferred from slow seismic slip, *Nat. Geosci. Lett.*, *5*(6), 414–418, doi:10.1038/ngeo1466.

Tanioka, Y., and K. Satake (1996), Tsunami generation by horizontal displacement of ocean bottom, *Geophys. Res. Lett.*, *23*(8), 861–864.

Tanioka, Y., and K. Satake (2001), Coseismic slip distribution of the 1946 Nankai earthquake and aseismic slips caused by the earthquake, *Earth Planets Sp.*, *53*, 235–241.

Tobin, H. J., and M. Kinoshita (2006), NanTroSEIZE: The IODP Nankai Trough Seismogenic Zone Experiment, *Sci. Drill.*, (2), 23–27, doi:10.2204/iodp.sd.2.06.2006.

Tobin, H. J., and D. M. Saffer (2009), Elevated fluid pressure and extreme mechanical weakness of a plate boundary thrust, Nankai Trough subduction zone, *Geology*, *37*(8), 679–682, doi:10.1130/G25752A.1.

Tobin, H. J., M. Kinoshita, J. Ashi, S. Lallemant, G. Kimura, E. J. Screaton, K. T. Moe, H. Masago, D. Curewitz, and Expedition 314/315/316 Scientists (2009), NanTroSEIZE Stage 1 expeditions: introduction and synthesis of key results, in *Proceedings of the Integrated Ocean Drilling Program*, vol. 314/315/31, edited by M. Kinoshita, H. J. Tobin, J. Ashi, G. Kimura, S. Lallemant, E. J. Screaton, D. Curewitz, H. Masago, K. T. Moe, and Expedition 314/315/316 Scientists, Integrated Ocean Drilling Program.

Tobin, H. J. et al. (2015a), Expedition 348 summary, in *Proceedings of the Integrated Ocean Drilling Program*, vol. 348, edited by H. J. Tobin, T. Hirose, D. M. Saffer, S. Toczko, L. Maeda, Y. Kubo, and Expedition 348 Scientists, Integrated Ocean Drilling Program.

Tobin, H. J. et al. (2015b), Site C0002, in *Proceedings of the Integrated Ocean Drilling Program*, vol. 348, edited by H. J. Tobin, T. Hirose, D. M. Saffer, S. Toczko, L. Maeda, Y. Kubo, and Expedition 348 Scientists, Integrated Ocean Drilling Program.

Tsuji, T., H. Tokuyama, P. Costa Pisani, and G. F. Moore (2008), Effective stress and pore pressure in the Nankai accretionary prism off the Muroto Peninsula, southwestern Japan, *J. Geophys. Res.*, *113*, doi:10.1029/2007JB005002.

Tsuji, T. et al. (2011), In situ stress state from walkaround VSP anisotropy in the Kumano basin southeast of the Kii Peninsula, Japan, *Geochemistry, Geophys. Geosystems*, *12*(9), n/a-n/a, doi:10.1029/2011GC003583.

Tsuji, T., R. Kamei, and R. G. Pratt (2014), Pore pressure distribution of a mega-splay fault system in the Nankai trough subduction zone: Insight into up-dip extent of the seismogenic zone, *Earth Planet. Sci. Lett.*, *396*, 165–178, doi:10.1016/j.epsl.2014.04.011.

Tudge, J., and H. J. Tobin (2013), Velocity-porosity relationships in smectite-rich sediments: Shikoku Basin, Japan, *Geochemistry, Geophys. Geosystems*, *14*(12), 5194–5207, doi:10.1002/2013GC004974.

Underwood, M. B. (2017a), Data report: clay mineral assemblages and illite/smectite diagenesis in cuttings from Hole C0002P, IODP Expedition 348, Nankai Trough accretionary prism, in *Proceedings of the Integrated Ocean Drilling Program*, vol. 348, edited by H. J. Tobin, T. Hirose, D. M. Saffer, S. Toczko, L. Maeda, Y. Kubo, and Expedition 348 Scientists, Integrated Ocean Drilling Program, College Station, TX.

Underwood, M. B. (2017b), Data report: clay mineral assemblages in cuttings from Hole C0002N, IODP Expedition 348, upper Nankai Trough accretionary prism, in *Proceedings of the Integrated Ocean Drilling Program*, vol. 348, edited by H. J. Tobin, T. Hirose, D. M. Saffer, S. Toczko, L. Maeda, Y. Kubo, and E. 348 Scientists, Integrated Ocean Drilling Program.

Underwood, M. B., and J. Guo (2013), Data report: clay mineral assemblages in the Shikoku Basin, NanTroSEIZE subduction inputs, IODP Sites C0011 and C0012, in *Proceedings of the Integrated Ocean Drilling Program*, vol. 322, edited by S. Saito, M. B. Underwood, Y. Kubo, and Expedition 322 Scientists, Integrated Ocean Drilling Program.

Underwood, M. B., and C. Song (2016a), Data report: clay mineral assemblages in cores from Hole C0002P, IODP Expedition 348, upper Nankai Trough accretionary prism, in *Proceedings of the Integrated Ocean Drilling Program*, vol. 348, edited by H. J. Tobin, T. Hirose, D. M. Saffer, S. Toczko, L. Maeda, Y. Kubo, and E. 348 Scientists.

Underwood, M. B., and C. Song (2016b), Data report: clay mineral assemblages in cuttings from Hole C0002F, IODP Expedition 338, upper Nankai Trough accretionary prism, in *Proceedings of the Integrated Ocean Drilling Program*, vol. 338, edited by M. Strasser, B. Dugan, K. Kanagawa, G. F. Moore, S. Toczko, L. Maeda, and E. 338 Scientists.

Underwood, M. B., S. Saito, Y. Kubo, and Expedition 322 Scientists (2010), Expedition 322 summary, in *Proceedings of the Integrated Ocean Drilling Program*, vol. 322, edited by S. Saito, M. B. Underwood, Y. Kubo, and Expedition 322 Scientists, Integrated Ocean Drilling Program.

Wallace, L. M. et al. (2009), Characterizing the seismogenic zone of a major plate boundary subduction thrust: Hikurangi Margin, New Zealand, *Geochemistry Geophys. Geosystems*, *10*(10), doi:10.1029/2009GC002610.

Yue, H., T. Lay, L. Rivera, C. An, C. Vigny, and X. Tong (2014), Localized fault slip to the trench in the 2010 Maule, Chile Mw = 8.8 earthquake from joint inversion of high-rate GPS, teleseismic body waves, InSAR, campaign GPS, and tsunami observations, *J. Geophys. Res. Solid Earth*, *119*, 7786–7804, doi:10.1002/2014JB011340.Received.

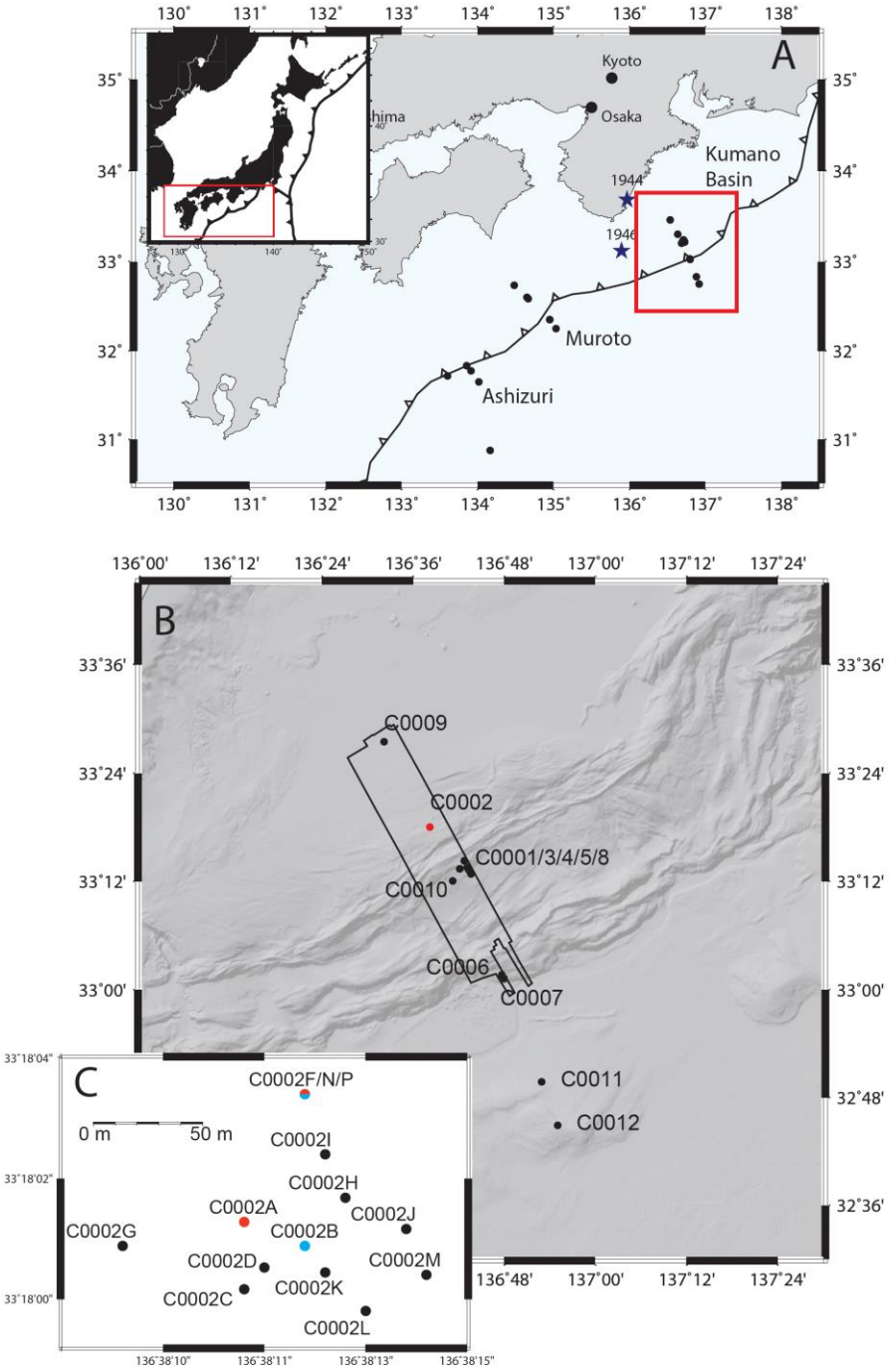

Figure 4.1: Map of the Nankai Trough offshore Shikoku and Honshu, Japan. A) Drill sites for the Ashizuri, Muroto, and Kumano Basin transects drilled by ODP and IODP. Red box shows the location of B. Stars show the locations of the epicenters of the 1944 and 1946 earthquakes. B) Outline of the 3D seismic survey collected in the Kumano Basin study area as part of NanTroSEIZE. Well sites drilled by D/V Chikyu are also shown. Site C0002 (in red) is the focus of this study. C) Close-up map showing the relative locations of the holes at Site C0002. Logging data from C0002A (in red) and core data from C0002B (in blue) are used in this study. Logging, core, and cuttings data are used from holes C0002F, C0002N, and C0002P (in red and blue).

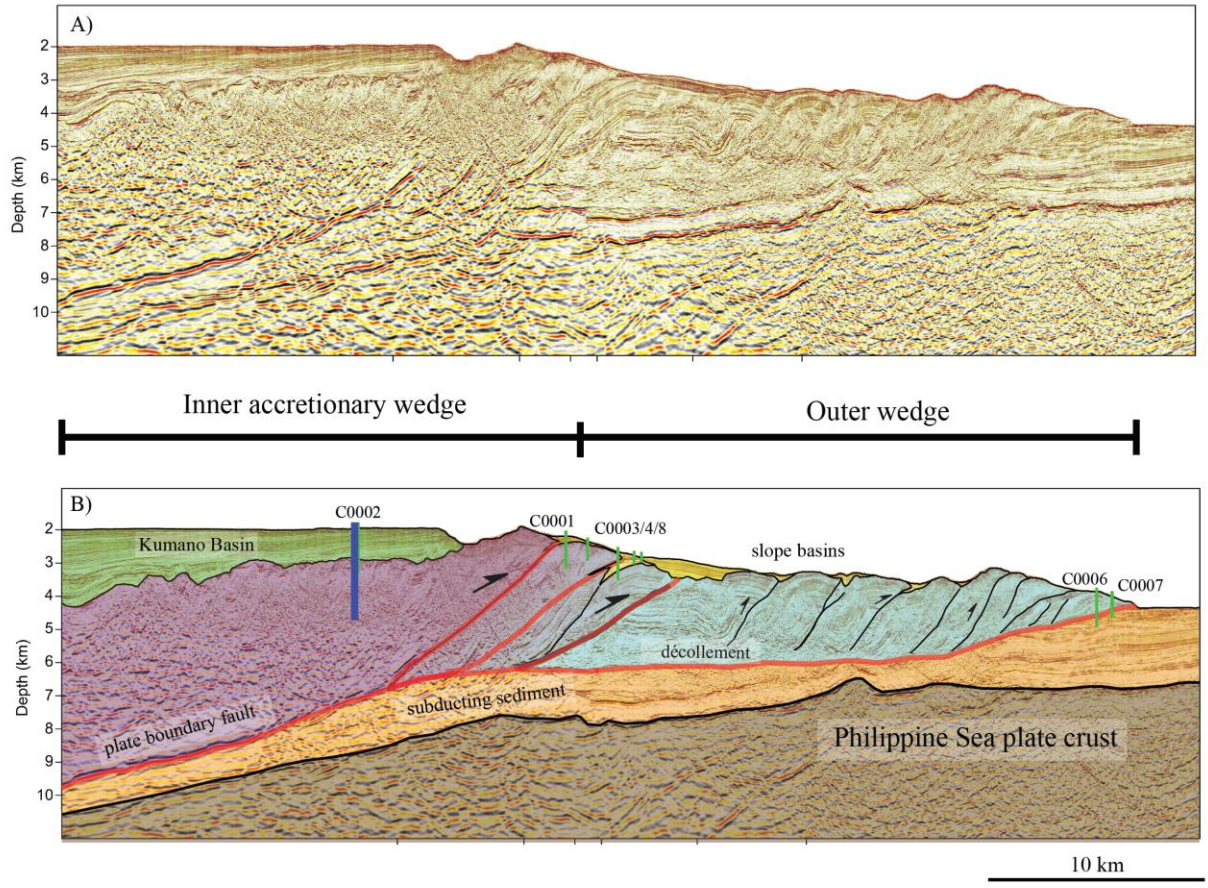

Figure 4.2: Multi-channel sesimic section extracted from 3D seismic volume (A), adapted from Moore et al (2009) and Tobin et al (2015), with drilling sites and major tectonic features marked. Site C0002 is shown in blue.

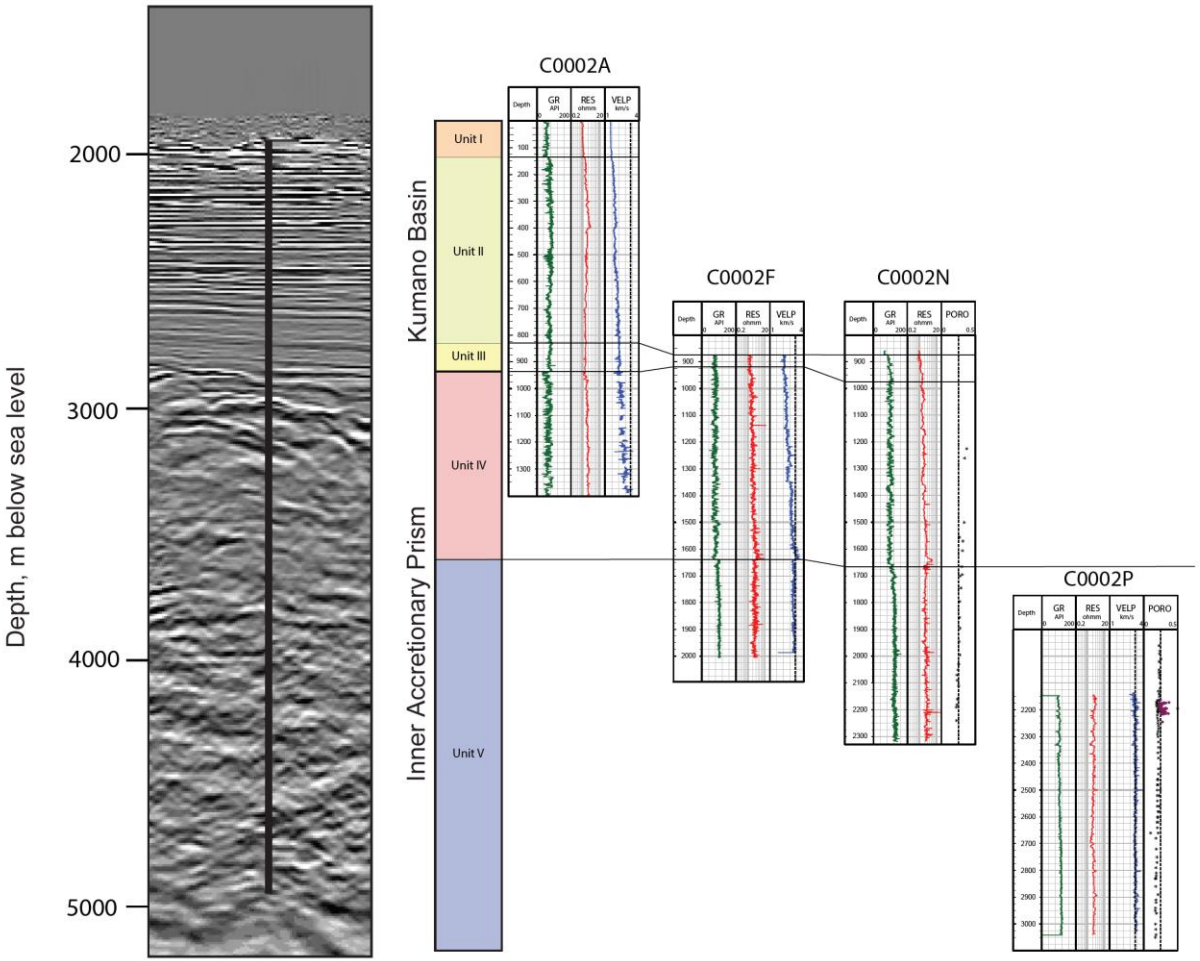

Figure 4.3: Seismic section of a cross line through sire C0002, showing the Kumano Basin and the inner accretionary prism. Unites defined on IODP expeditions (I, II, II, IV, V) are shown, as well as log data from various wells used in this study. The green log (GR) is the gamma ray, in API units. Resistivity in ohm is shown in red, and compressional sonic velocity, VELP, is shown in blue in units of km/s. The dashed baseline on the sonic data is shown at 3250 m/s, and all logs are shown on the same scale across all wells. Wells C0002N and C0002P have porosity from cuttings (x-es) and core (circles shown as well. The dashed porosity baseline is at 0.25.

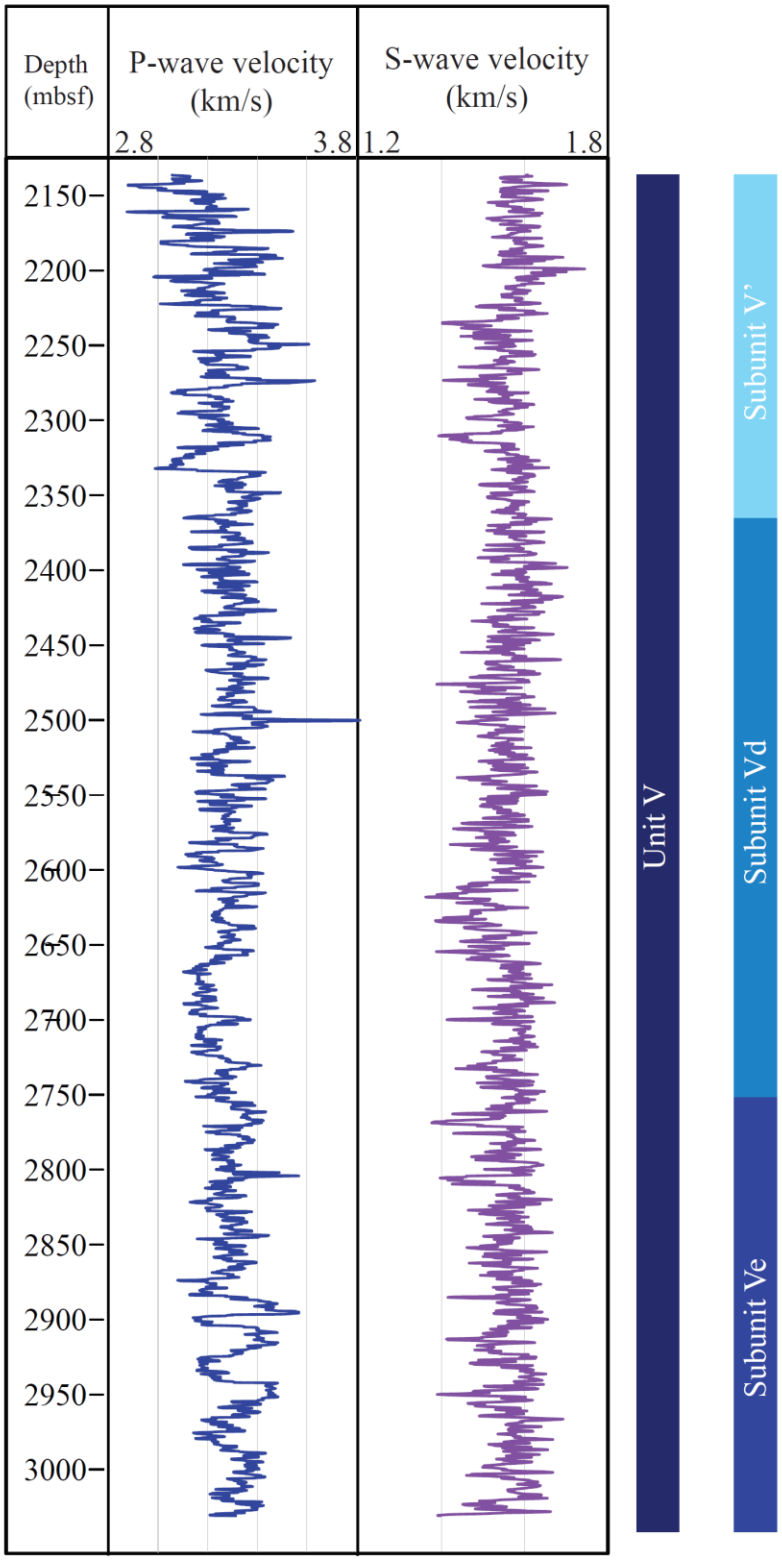

Figure 4.4: P-wave velocity and S-wave velocity logs, reprocessed and picked from raw waveforms collected by Halliburton's XBAT tool in hole C0002P during IODP Expedition 348.

Figure 4.5 A: C0002F

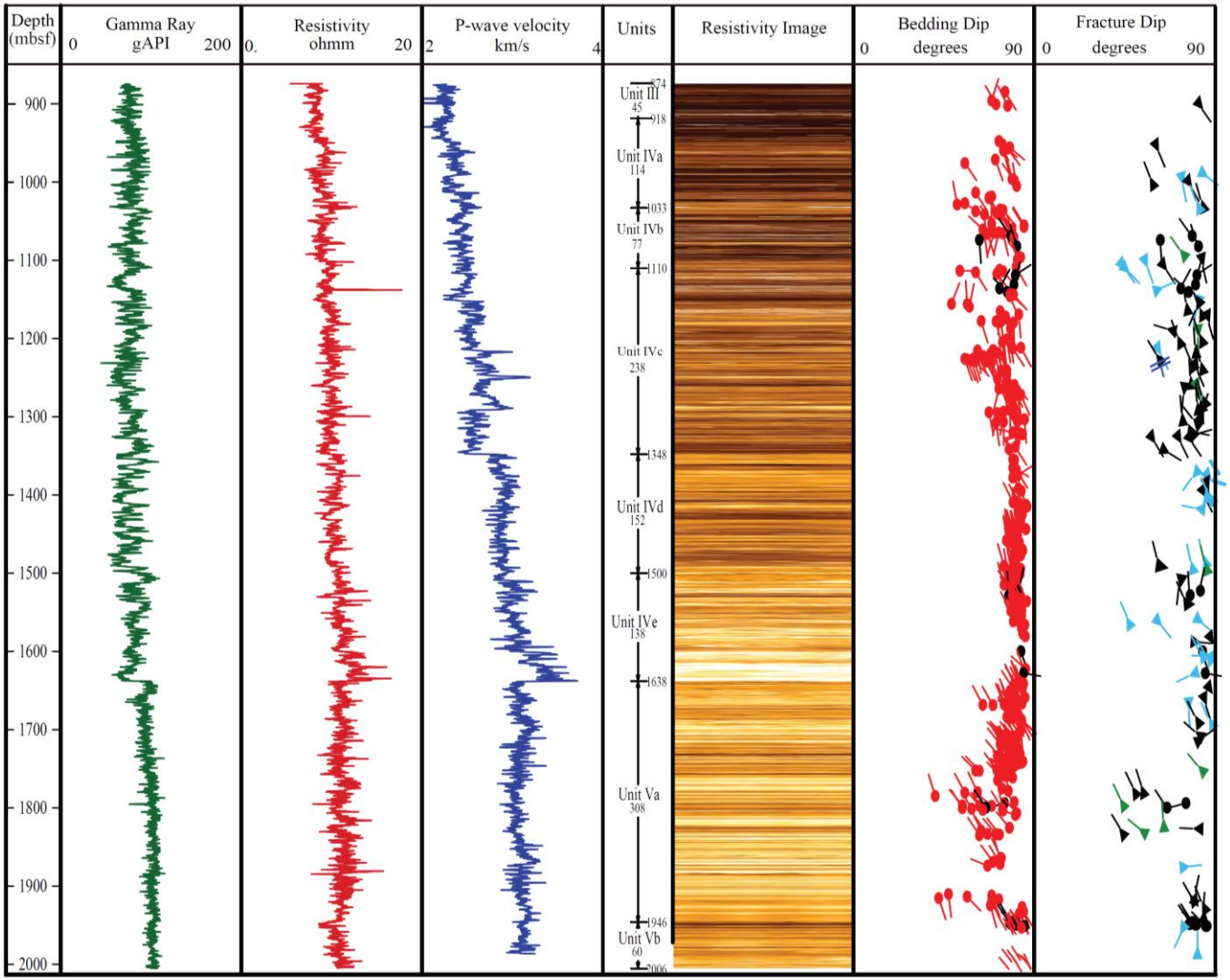

Figure 4.5 B: C0002P

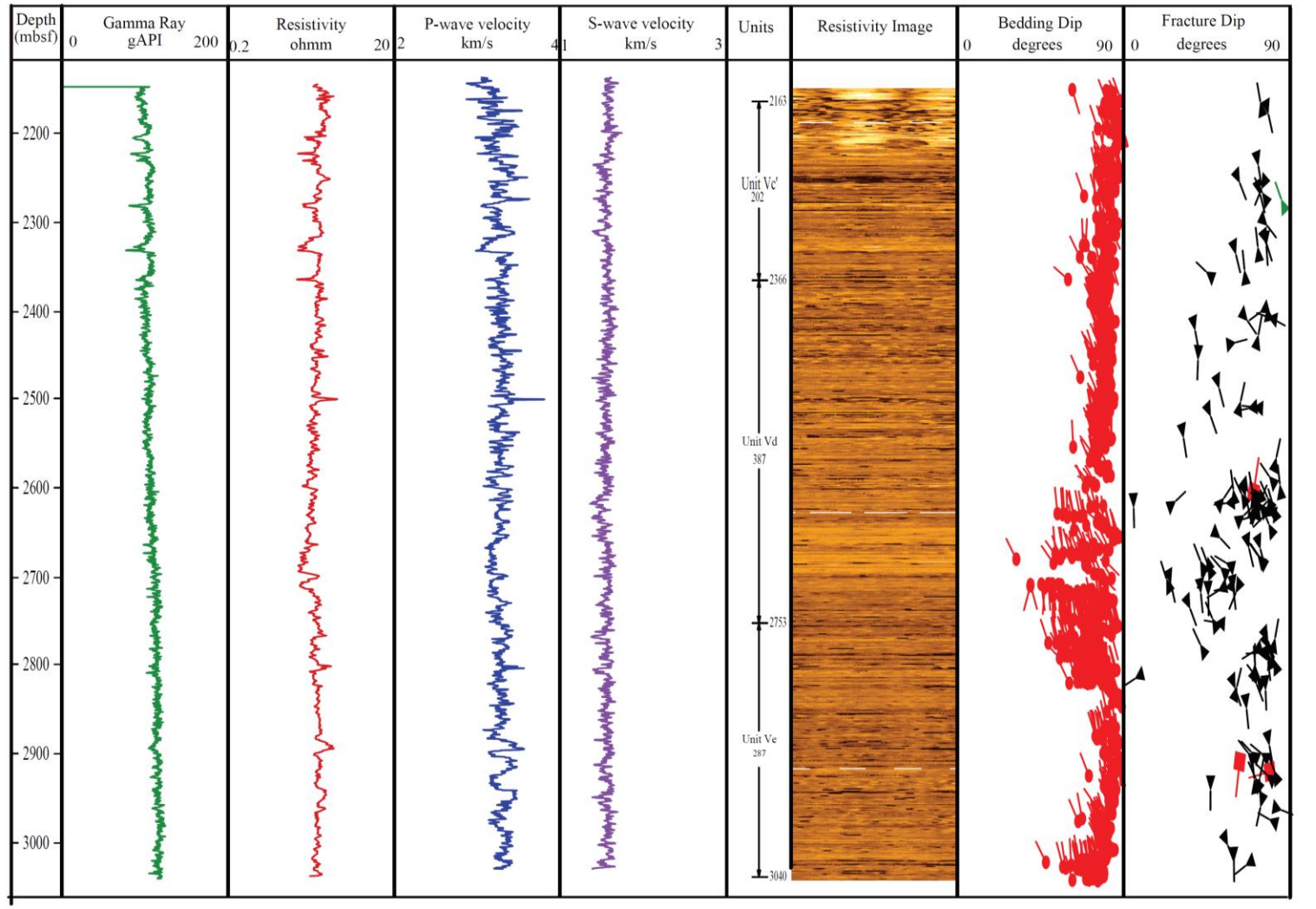

Figure 4.5: Selected LWD logs from C0002F (A) and C0002P (B). Logs shown are gamma ray, deep resistivity, p-wave velocity, s-wave velocity (C0002P only), as well as the resistivity image and the bedding and fracture dips.

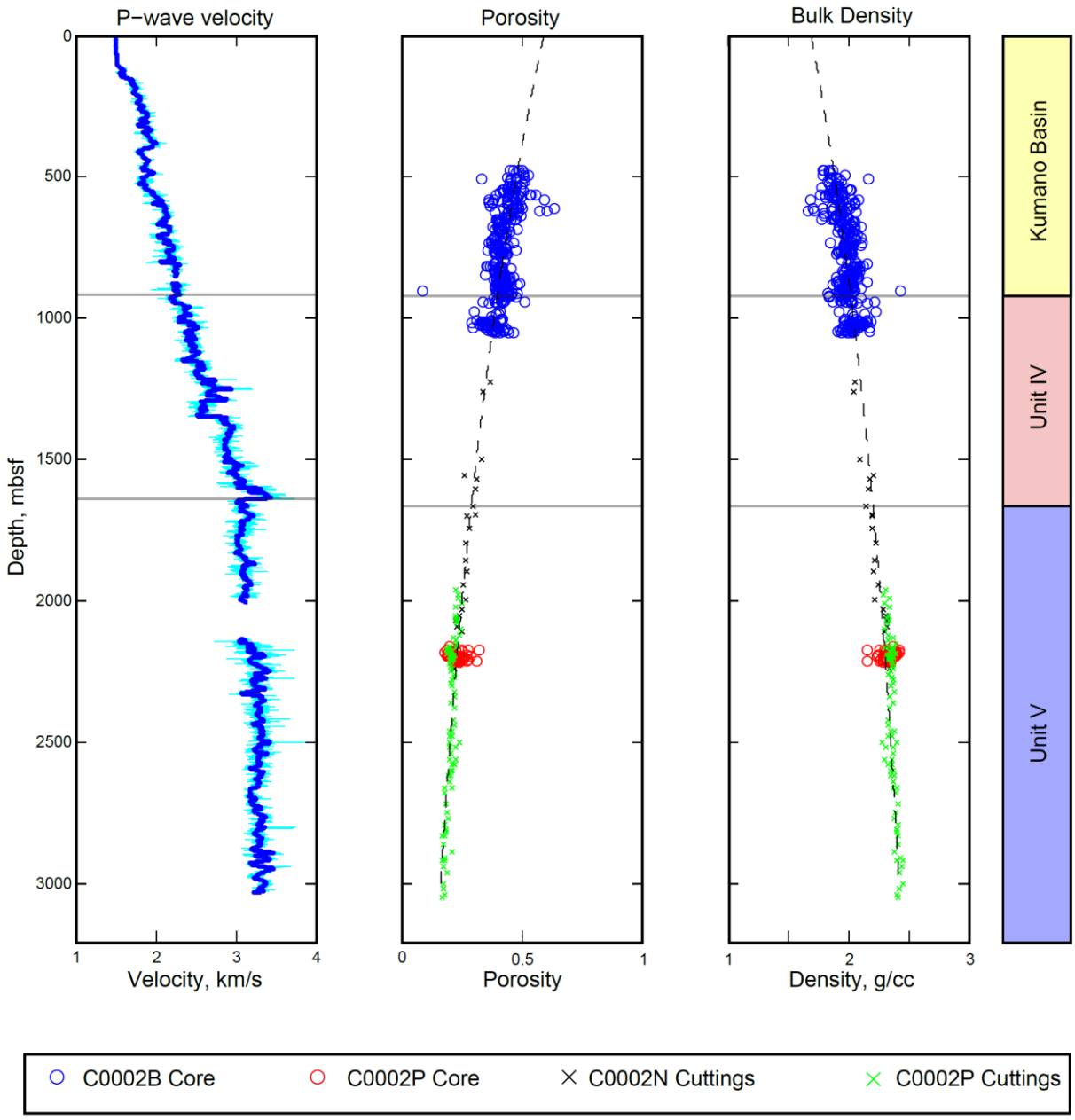

Figure 4.6: Comparison of sonic velocity log, with core and cuttings based porosity and calculated bulk density through Site C0002. Smoothed velocity seen in dark blue. Dashed lines are the Athy fits to both porosity and density.

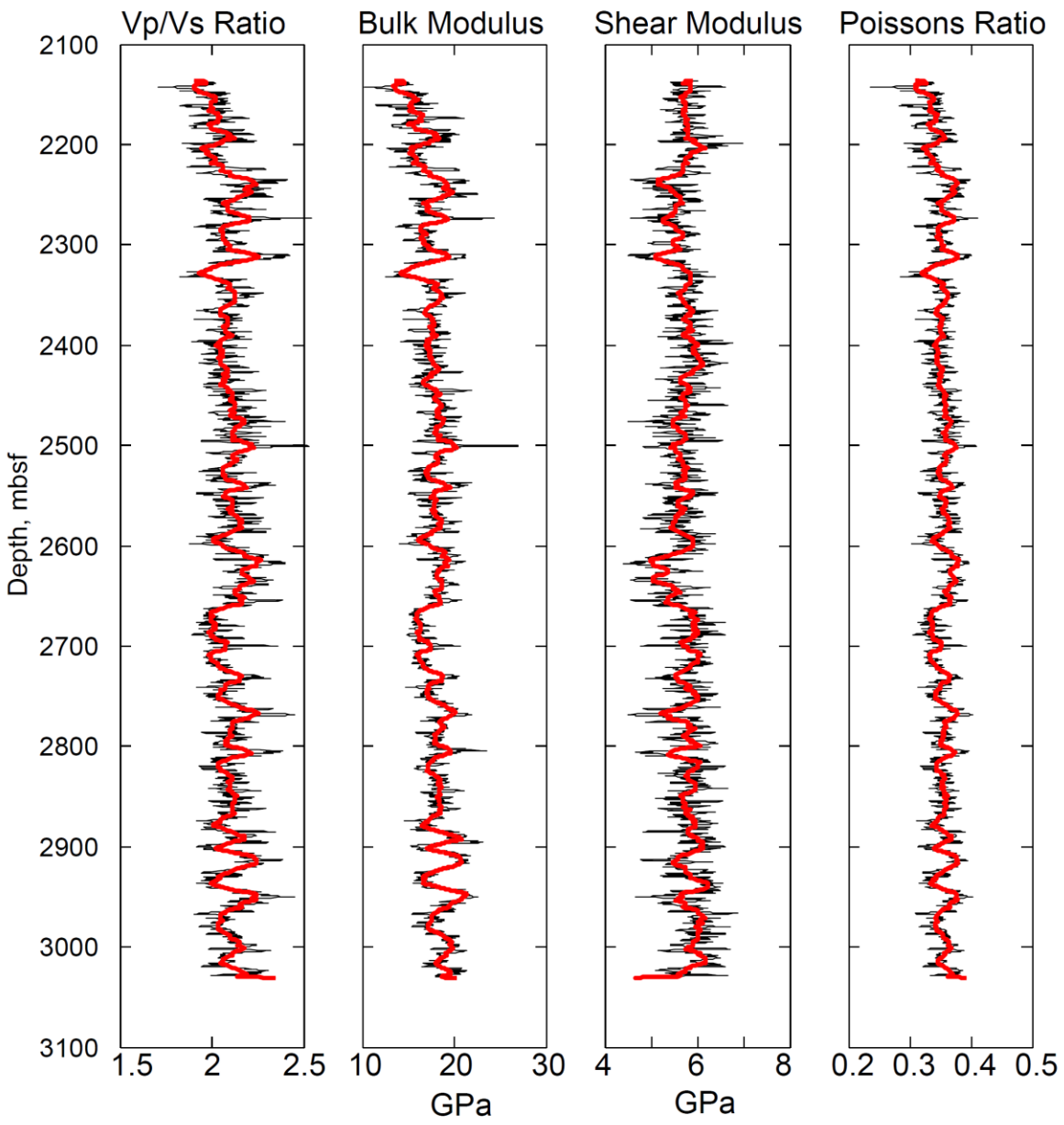

Figure 4.7: Plot of bulk modulus, shear modulus, velocity ratio and Poisson's ratio calculated from velocity logs through well C0002P. Black lines are at the sampling depth of the velocity logs. Red lines are smoothed over a 10 m interval.

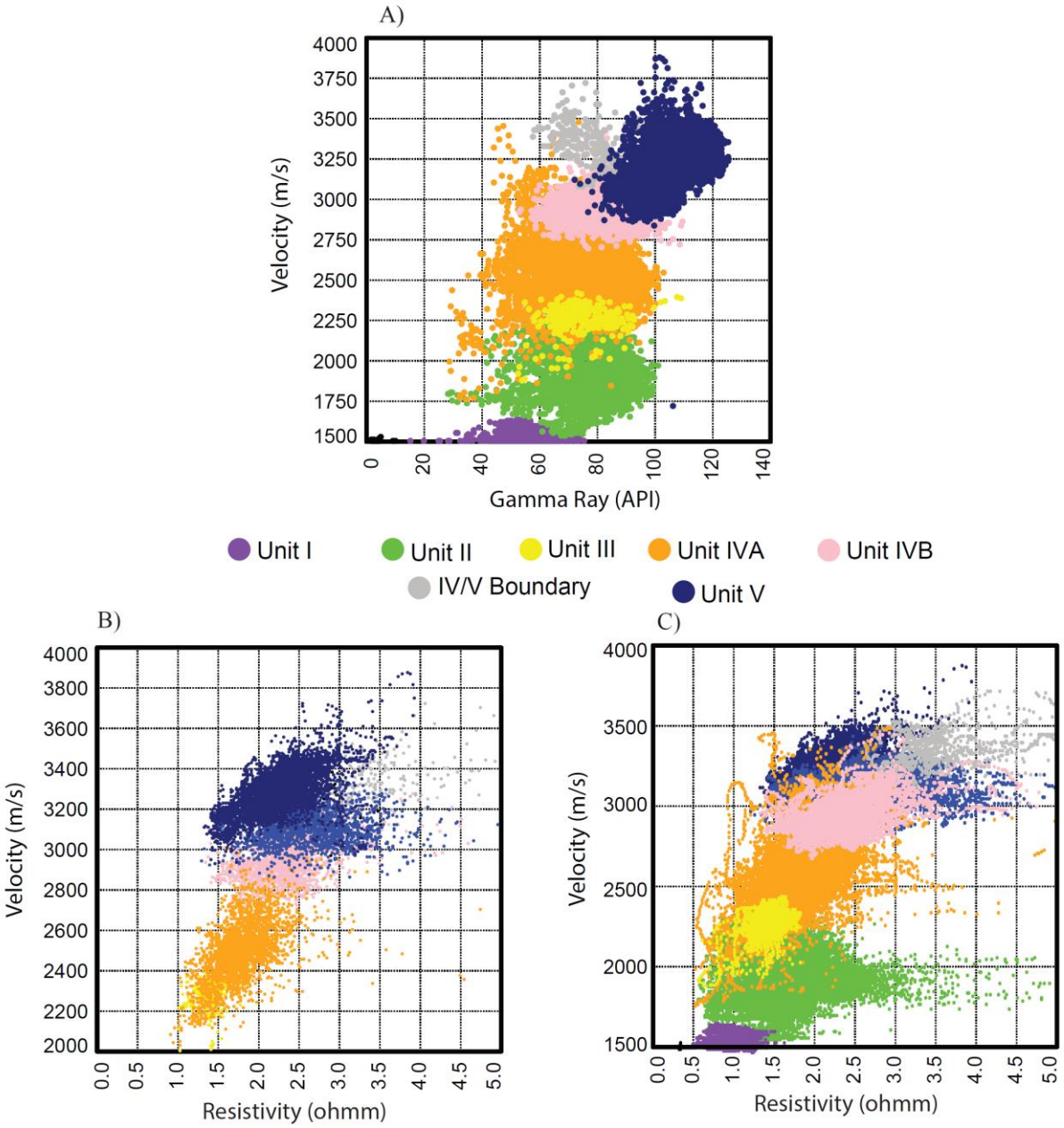

Figure 4.8: Cross plots of gamma ray versus velocity (A) and resistivity vs velocity, without C0002A (B) and with C0002A (C). All plots are coloured by shipboard defined unit, with Unit IV broken into two sections (A and B, above and below ~1280 mbsf, respectively) to highlight the separation in the units seen in C0002F (B).

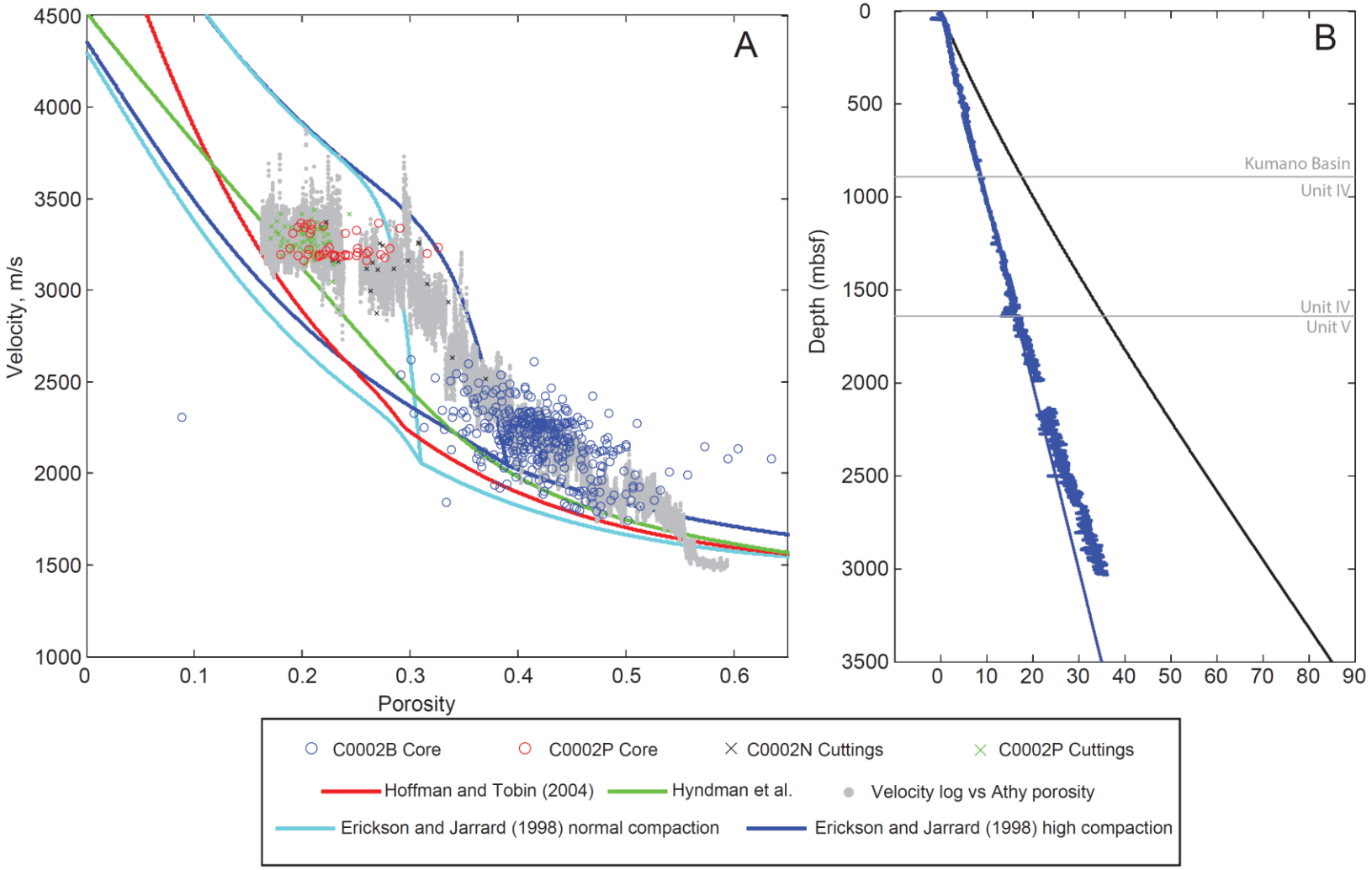

Figure 4.9: A) Comparison of the porosity versus velocity of the core and cuttings at Site C0002 with the empirically established relationships of velocity and porosity. For the *Erickson and Jarrard* [1998] relationships, the upper and lower bounds above the crictical porosity are shown. The grey points plot the velocity against the shipboard Athy porosity. B) Estimate of overpressure through Site C0002, estimated from using the *Erickson and Jarrard* [1998] high compaction with a v_{sh} term of 0.3. Hydrostat in blue, lithostat in black. The term used was the one that best fit the hydrostat through the upper portion of the hole.